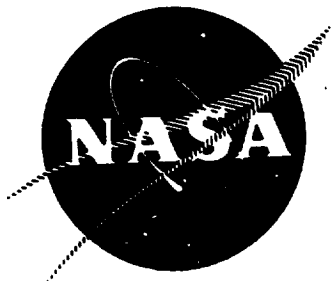


2 mid

N74-23343



NASA CR-72965
R-8494-1



ROTATING AND POSITIVE-DISPLACEMENT PUMPS
FOR
LOW-THRUST ROCKET ENGINES

FINAL REPORT
VOLUME I
EVALUATION AND DESIGN

(NASA-CR-72965) ROTATING AND
POSITIVE-DISPLACEMENT PUMPS FOR LOW-THRUST
ROCKET ENGINES. VOLUME I: PUMP
EVALUATION AND DESIGN (Rocketdyne) Final Report
227 P HC
2/3

ROCKETDYNE DIVISION
ROCKWELL INTERNATIONAL
CANOGA PARK, CALIFORNIA



prepared for

NATIONAL AERONAUTICS AND SPACE ADMINISTRATION

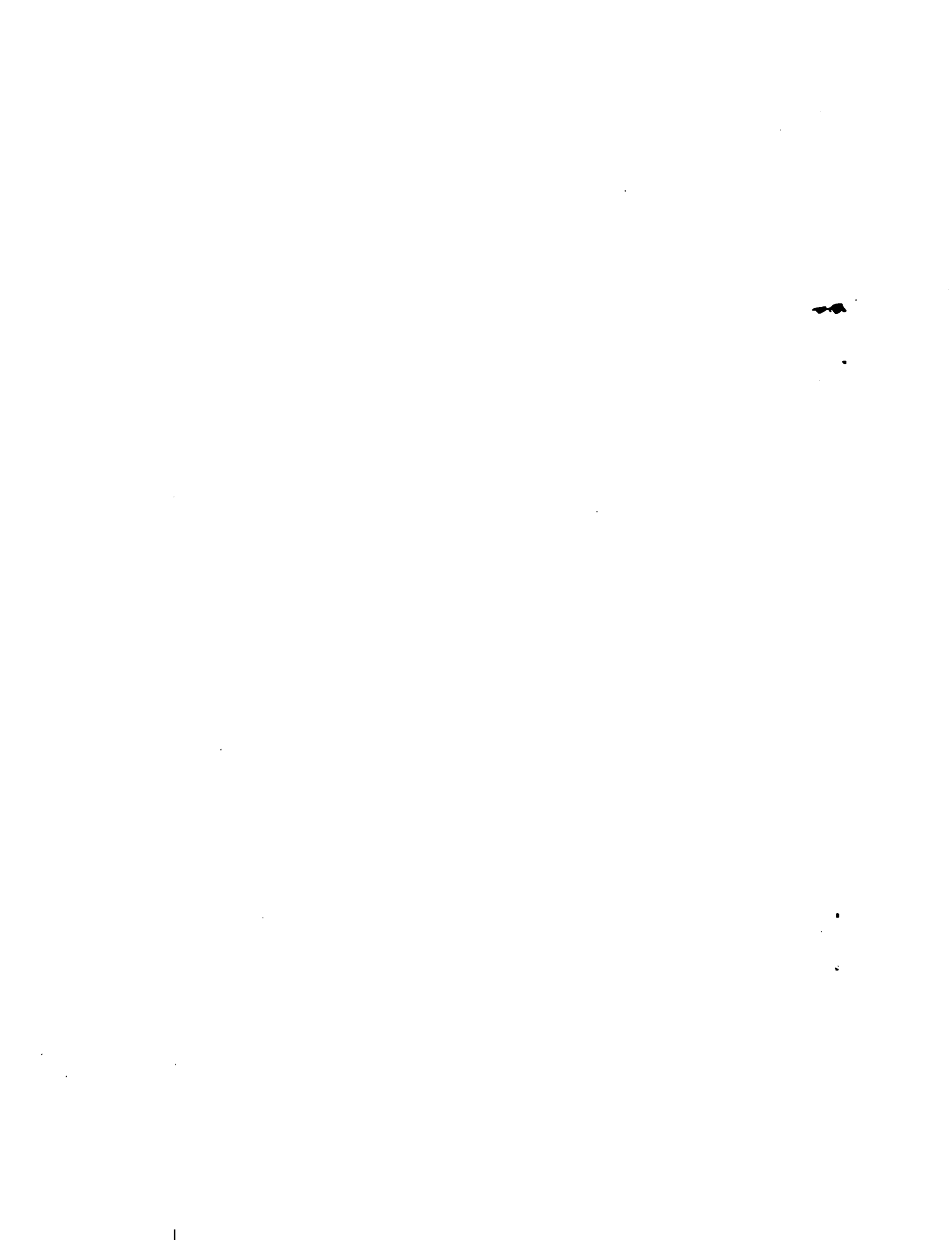
NASA-Lewis Research Center
Contract NAS3-12022
Werner Britsch, Project Manager

Reproduced by
**NATIONAL TECHNICAL
INFORMATION SERVICE**
U.S. Department of Commerce
Springfield, VA 22151

PRICES SUBJECT TO CHANGE

1. Report No. NAS CR-72965	2. Government Accession No.	3. Recipient's Catalog No.	
4. Title and Subtitle ROTATING AND POSITIVE-DISPLACEMENT PUMPS FOR LOW-THRUST ROCKET ENGINES Final Report, Volume I, Pump Evaluation and Design		5. Report Date February 1974	
		6. Performing Organization Code	
7. Author(s) C. MacGregor and A. Csomor		8. Performing Organization Report No. R-849d-1	
9. Performing Organization Name and Address Rocketdyne Division, Rockwell International Canoga Park, California 91304		10. Work Unit No.	
		11. Contract or Grant No. NAS3-12022	
12. Sponsoring Agency Name and Address National Aeronautics and Space Administration Washington, D.C. 20546		13. Type of Report and Period Covered Contractor Report	
		14. Sponsoring Agency Code	
15. Supplementary Notes Technical Manager, Werner Britsch, NASA-Lewis Research Center, Cleveland, Ohio			
16. Abstract Rotating and positive displacement pumps of various types were studied for pumping liquid fluorine for low-thrust, high-performance rocket engines. Included in the analysis were: centrifugal, pitot, Barske, Tesla, drag, gear, vane, axial piston, radial piston, diaphragm, and heliotor pump concepts. The centrifugal pump and the gear pump were selected and these were carried through detailed design and fabrication. Mechanical difficulties were encountered with the gear pump during the preliminary tests in Freon-12. Further testing and development was therefore limited to the centrifugal pump. Tests on the centrifugal pump were conducted in Freon-12 to determine the hydrodynamic performance and in liquid fluorine to demonstrate chemical compatibility.			
17. Key Words (Suggested by Author(s)) Pumping Methods Evaluation Pump Design Pump Performance Fluorine Pumping		18. Distribution Statement	
19. Security Classif. (of this report) Unclassified	20. Security Classif. (of this page) Unclassified	21. No. of Pages 216	22. Price*

* For sale by the National Technical Information Service, Springfield, Virginia 22151



FOREWORD

This technical report presents the results of an investigation of rotating and positive displacement pumps for low thrust rocket engines. The program conducted by Rocketdyne, a Division of North American Rockwell, during the period of July 1968 to March 1971, was authorized by the Lewis Research Center of the National Aeronautics and Space Administration (NASA) under Contract NAS3-12022. The NASA project manager was Mr. W. Britsch.

This report is submitted as Rocketdyne report number R-8494, in two volumes:

- I. Pump Evaluation and Design
- II. Pump Fabrication and Testing

CONTENTS

Foreword	ii
Abstract	iii
Acknowledgments	iv
Introduction	1
Summary	5
Task I: Rotating Pump Evaluation	7
Centrifugal Pump	11
Pitot Pump	22
Baske Pump	40
Tesla Pump	50
Drag Pump	63
Pump Evaluation (Rotating)	70
Task II: Rotating Pump Design	75
Hydrodynamic Design	75
Mechanical Design	84
Drive Design	90
Stress and Dynamic Analysis	93
Rotordynamic Analysis	98
Reduction in Power Losses Using Gas Cavities	101
Bearing and Seal Power Losses	114
Task V: Positive Displacement Pump Evaluation	121
Gear Pump	123
Vane Pump	136
Piston Pump	142
Helirotor Pump	150
Diaphragm Pump	161
Pump Evaluation	165
Task VI: Positive Displacement Pump Design	175
Gear Design	175
Materials Selection	180

Axial Thrust	180
Mechanical Design	182
Stress and Dynamic Analysis	184
Nomenclature	191
References	197
<u>Appendix A</u>	
Derivations	201

ILLUSTRATIONS

1. N_s - D_s Diagram for Pumps	10
2. Hydraulic Efficiency as a Function of Impeller Diameter	14
3. Effect of Impeller Size on Pump Efficiency	16
4. LF_2 Centrifugal Pump Loss Breakdown Preliminary Design	17
5. Centrifugal Pump-Preliminary Design	19
6. Volute Friction and Momentum Loss as a Function of Flow Coefficient	21
7. Schematic of Pitot Pump	23
8. Typical Values for Drag Coefficient	28
9. Relative Eddy Within the Pitot Pump	28
10. N_s - D_s Diagram for the Pitot Pump With a Single Pitot	31
11. N_s - D_s Diagram for the Pitot Pump With a Double Pitot	33
12. N_s - D_s Diagram for the Pitot Pump With a Double Pitot	34
13. Efficiency vs Specific Speed for Pitot Pump With Double Pitot	35
14. Efficiency vs Specific Speed for Pitot Pump With a Double Pitot	36
15. N_s - D_s Diagram for the Pitot Pump With a Double Pitot	37
16. Efficiency vs Specific Speed - Comparison of the Single and Double Pitot Pumps	38
17. Optimum Specific Diameter vs Specific Speed for Single and Double Pitot Pumps	39
18. Pitot Pump-Preliminary Design	41
19. Pump Inlet Diameter as a Function of Pump Speed	42
20. Pump Specific Speed as a Function of Pump Speed	42
21. Pump Discharge Diameter as a Function of Pump Speed	45
22. Pump Efficiency vs Pressure Recover Coefficient	46
23. Barske Pump-Preliminary Design	49
24. Schematic of Tesla Pump	51
25. Specific Diameter of the Tesla Pump	52
26. Performance Potential of Tesla Pumps as a Function of Specific Speed	53
27. Calculated Efficiency of the Tesla Pump as a Function of Radius Ratio and Flow Factor	54
28. Local Reynolds Number as a Function of Vane Spacing and Fluid Viscosity	56

29. Vane Number as a Function of Spacing and Viscosity	58
30. Calculated Performance of the Tesla Pump With Rough Disks	60
31. Tesla Pump-Preliminary Design	62
32. Schematic of Drag Pump Rotor	64
33. Approximate N _s -D _s Diagram for the Drag Pump	66
34. Maximum Efficiency as Function of Specific Speed	67
35. Drag Pump-Preliminary Design	69
36. Inducer Blade Angles as a Function of Axial Distance From Leading Edge	78
37. Meridional Section of Impeller Flow Passage	80
38. Impeller Blade Angle Along Meridional Streamlines	81
39. Relative Fluid Velocities Along Meridional Streamlines	82
40. Pressures Along the Vane Surface in Meridional View	83
41. Estimated Performance of the Centrifugal Pump-Final Design	85
42. Centrifugal Pump Assembly	86
43. Centrifugal Pump Inlet and Volute Housing Sections	89
44. Initial Drive Concept Candidate	91
45. Mark 36 Pump Turbine Drive	92
46. Centrifugal Pump Impeller Stress Analysis	95
47. Centrifugal Pump Inducer Stress Analysis	96
48. Allowable Shaft Deflection vs Speed	97
49. Centrifugal Pump Shaft Stress Analysis	99
50. Centrifugal Pump Bearing Preload Washer Stress Analysis	100
51. Schematic of Drive Configuration	102
52. Critical Speed vs Pump Bearing Spring Rate	103
53. Normalized Mode Shape of Torquemeter/Turbine Drive System as a Function of Position Along Rotor Spring Rate for Both Pump Bearings = 10 ⁴ lb/in.	104
54. Relative Deflection of Torquemeter/Turbine Drive System as a Function of Position Along Rotor Spring Rate for Both Pump Bearings = 10 ⁵ lb/in.	105
55. Mark-36 Pump with Turbine Drive Critical Speeds	106
56. Mark-36 Pump With Turbine Drive, Critical Speed Mode Shapes	107

57. Mark-36 Turbine Coupled to Vortec A-20 Dynamometer, Critical Speeds	108
58. Mark-36 Turbine Coupled to Vortec A-29 Dynamometer, Critical Speed Mode Shapes	109
59. Moment Coefficients for Smooth Disks Rotating in an Enclosed Housing	111
60. Front Shroud Disk Friction for Liquid Cavity	113
61. Schematic of a Modified Mark 36, 12-gpm Centrifugal Pump Utilizing a Gas Cavity on Impeller Front Shroud and a Balance Piston	115
62. Schematic of a Modified Mark 36, 12-gpm Centrifugal Pump Utilizing an Open-Face Impeller and Balance Piston	116
63. Rotor Diameter as a Function of Axial Clearance	128
64. Clearance Effect on Gear Pump Efficiency	129
65. Gear Diameter as a Function of Speed	132
66. Gear Pump Loss Isolation	135
67. Preliminary Layout of Gear Pump	137
68. Vane Pump Rotor Diameter as a Function of Axial Clearance	140
69. Clearance Effect on Vane Pump Efficiency	141
70. Vane Pump Loss Isolation	143
71. Preliminary Layout of Vane Pump	144
72. Effects of Speed, Piston Clearance, and Piston Diameter on Axial Piston Pump Efficiency	147
73. Effect of Speed, Piston Clearance, and Piston Diameter on Radial Piston Pump Efficiency	148
74. Clearance Effect on Piston Pump Efficiency	149
75. Axial Piston Pump Loss Isolation	151
76. Radial Piston Pump Loss Isolation	152
77. Preliminary Layout of Axial Piston Pump	153
78. Preliminary Layout of Radial Piston Pump	154
79. Typical Helirotor Configurations	156
80. Effects of Speed, Rotor to Rotor Clearance, and Rotor Diameter in Helirotor Pump Efficiency	159
81. Calculated (Maximum) Loads on Helirotor Pump	160

82. Preliminary Layout of Diaphragm Pump	164
83. Effects of Speed on Axial Load for Various Piston Diameters and Strokes	169
84. Gear Pump Performance Map	170
85. 6000-rpm Gear Pump	171
86. 9000-rpm Gear Pump	173
87. Performance Map of the Gear Pump - Final Design	178
88. Final Gear Pump Design	181
89. Summary of Stresses and Factors of Safety at Thread Relief and at the Bearing Shoulder for the Driver Shaft	185
90. Gear Pump Pressure Distribution and Deflections	186
91. Summary of Gear Housing Stresses and Deflections	188
92. Gear Pump Critical Speed vs Bearing Stiffness	189

TABLES

I.	Rotating Pump Rating System	9
II.	Barske Pump Dimensions	48
III.	Pump Design Evaluation Summary	71
IV.	Pump Power Breakdown	72
V.	Rotating Pump Rating	73
VI.	Inducer Design Information	76
VII.	Impeller Design Information	77
VIII.	Critical Speeds for Various Modes and Estimated Bearing Spring Rates	103
IX.	Centrifugal Pump Power Breakdown	117
X.	Power Loss Values Due to Friction in Seals and Bearings	119
XI.	Positive Displacement Pump Rating Chart	122
XII.	Design Operating Conditions Positive Displacement Pumps	166
XIII.	Rating Matrix Positive Displacement Pumps	167
XIV.	Critical Speeds	170

~~PRECEDING PAGE BLANK NOT FILMED~~

ACKNOWLEDGMENTS

The overall guidance and technical assistance provided by Mr. Werner R. Britsch, the NASA Lewis Research Center Project Manager, is gratefully acknowledged.

Overall program direction was provided by Mr. H. G. Diem, the Rocketdyne Program Manager.

Dr. O. E. Balje provided valuable consultation, in the preliminary analysis of the pitot, drag, diaphragm and helirotor pump concepts.

The evaluation of various pump concepts, as well as selection, design and fabrication of the rotating and positive displacement pumps was accomplished under the technical direction of Mr. C. A. MacGregor.

Testing of the selected pump concepts and preparation of Volume II were accomplished under the technical direction of Mr. A. Csomor.

INTRODUCTION

Studies of future space missions show the requirement for relatively low thrust (1000 to 10,000 lb, 4448 to 44,480 N), high specific-impulse rocket engines in upper stages for orbital maneuvering and instrument package landers. For long-duration missions, or for vehicles having limited tankage volume, the use of high energy, space-storable propellant combinations such as methane-FLOX (fluorine-oxygen mixture) is desirable.

To realize the full potential of the high-energy propellants, it is necessary to achieve the lowest practicable values for engine size and weight and tank weight, thereby maximizing payload. A means for optimizing the performance, size and weight of the vehicle is the use of a high-pressure, pump-fed engine cycle.

At the thrust level of 1000 lb (4448 N) and a chamber pressure of 1000 psia (689.5 N/cm^2) the FLOX flowrate is 12 gpm ($7.57 \times 10^{-4} \text{ m}^3/\text{s}$) assuming an attainable specific impulse of 385 sec (3775 Ns/kg) at a mixture ratio of 5.75. A chamber pressure of 1000 psia will require a pump discharge pressure of approximately 1500 psia (1030 N/cm^2). Since the use of a separate low-speed inducer was not considered practical for these small engines, the maximum speed of the pump was limited primarily by cavitation requirements. The combination of flowrate, pressure rise, and fluid density together with the allowable range of speeds places the pump in the low specific speed regime where the predicted attainable efficiencies for several types of centrifugal pumps are below those of the positive displacement types.

The predicted efficiencies of centrifugal pumps available in the general literature are results obtained on pumps having flowrates in excess of 100 gpm ($6.31 \times 10^{-3} \text{ m}^3/\text{s}$). Extrapolation of these data to the flowrate required inherently assumes both geometric and hydrodynamic similarities are maintained. In these small size ranges, geometric similarity cannot be maintained. In contrast, the low viscosity of fluorine makes it possible to maintain a high Reynolds No.

despite the small size of the impeller. However, surface roughness and clearances that are practicably attainable become a significant percentage of the characteristic dimensions and can noticeably affect the efficiency. The inability to maintain geometric similarity can also make it difficult to attain the necessary cavitation performance. Because of these uncertainties in predicting the efficiencies and suction performance, test data were needed to establish the performance characteristics of rotating pumps operating under the hydrodynamic conditions imposed by these low-thrust rocket engines using high-energy propellants.

The capability of operating centrifugal pump impellers in fluorine mixtures was previously established (Ref. 1). In those tests, the impeller cavity and the bearing cavity were separated by a three-element seal to prevent mixing of the organic lubricant and the FLOX mixtures. The desire to alleviate critical speed problems in the 12-gpm ($7.57 \times 10^{-4} \text{ m}^3/\text{s}$) pump led to the decision to operate the bearings in liquid fluorine, thus eliminating one seal. Although bearings have been tested in fluorine, pump bearings have not previously been subjected to the fluorine. Tests to determine the feasibility of this design approach are necessary.

The scope of the program consisted of the following four areas of effort:

1. Evaluation of various concepts of small, lightweight, efficient rotating and positive displacement pumps, and on the basis of this evaluation select the best single design of positive displacement pump and the best single design of rotating pump. (Task I and Task V)
2. Design the two selected concepts. (Task II and Task VI)
3. Fabricate and assemble two rotating and positive displacement pumps. (Task III and Task VII)
4. Test the two pump designs in both Freon 12 and LF_2 to establish the mechanical integrity, and determine the pump performance and operating characteristics, and the fluorine compatibility of the drive elements (Task IV and VIII)

Volume I of this report describes the work accomplished in areas (1) and (2) above.
Volume II describes the effort of (3) and (4).

For purposes of identification, the centrifugal pump was designated as "Mark 36 Pump" and the gear pump as "Mark 37 Pump."

SUMMARY

Rotating and positive displacement pumps of various types were studied for pumping fluorine mixtures for low thrust, high specific impulse rocket engines, with the following specific requirements:

● Inlet Pressure	35 psia	(2.41×10^5 N/m ²)
● Inlet Temperature	159 R	(88.4 K)
● Discharge Pressure	1500 psia	(1.03×10^7 N/m ²)
● Flow	12 gpm	(7.57×10^{-4} m ³ /s)
● Fluid	Liquid Fluorine	

Analysis and preliminary layouts were made of the following rotating pump concepts: centrifugal pump, pitot, Barske, Tesla, and drag pumps. Comparison of the different concepts was made on the basis of performance, weight, reliability, cost and life. The centrifugal pump was selected as the rotating pump concept most suitable for this application. In a similar manner, positive displacement pumps consisting of gear, vane, axial piston, radial piston, diaphragm and heliotor types were evaluated. The evaluation criteria indicated that the gear pump and the vane pump were equally suitable candidates for this application. The gear pump was selected because the rubbing velocities at the points of contact were lower than those encountered in the vane pump.

Detailed analysis and design of the centrifugal and the gear pump were made and two sets of hardware were fabricated for each of these pump types.

During the initial test in Freon-12, the mechanical difficulties encountered with the gear pump precluded further test with it, and no further development of this pump was undertaken. The remainder of the contract effort was limited to the centrifugal pump.

The centrifugal pump was tested in Freon-12 for a total of 2.94 hours at speeds up to 80,000 rpm with a maximum discharge pressure and flow of 2000 psig and 14.5 gpm, respectively. Thirty start sequences were conducted during these tests. The overall efficiency at design flow was 52 percent. A maximum suction specific speed of 36,500 was achieved.

Subsequently, the centrifugal pump was tested in liquid fluorine for an accumulated time of 387 seconds under steady-state conditions at speeds up to 40,000 rpm. Some brief transient speed excursions to 104,000 rpm were encountered. During these fluorine tests, the ball bearings experienced excessive wear rates. These diametral wear rates were 0.004 in./hr (0.012 cm/hr) on the front bearing and 0.012 in./hr (0.0305 cm/hr) on the rear bearing. (This is in contrast to the Freon tests where no ball wear was experienced.) These wear rates are believed to be the cause of rotor instabilities which precluded tests above 40,000 rpm.

Funding limitations did not permit resolution of the bearing wear problems. No other deleterious effects due to the liquid fluorine were observed during these limited tests.

TASK I: ROTATING PUMP EVALUATION

Evaluations of several types of rotating pumps were conducted to determine the type best suited to the following requirements:

Pump Inlet Pressure, psig	35 (2.41×10^5 N/m ²)
Pump Inlet Temperature, R (LF ₂ Saturated at 20 psia, 1.38×10^5 N/m ²)	159 (88.5 K)
Pump Exit Pressure, psia	1500 (1.03×10^7 N/m ²)
Design Flowrate, gpm	12 (7.57×10^{-4} m ³ /s)
Pumped Fluid	LF ₂ (capability of FLOX operation)

A method was devised for comparing and rating the several types of rotating pumps on an equal basis so that a valid selection could be made. Since the evaluation must reflect the requirements of a deep space probe, primary emphasis in this comparison was placed on performance, life, reliability, and cost. Each of the first three categories is defined in terms of those design parameters (criteria) which have a material effect upon it. The criteria considered in each of the primary categories are as follows:

Performance Criteria

1. Hydraulic efficiency which is a measure of all the pump losses except bearings and seals.
2. Mechanical efficiency representing pump bearing and seal losses.
3. Overall efficiency which takes account of the turbine drive efficiency.
4. Size and weight.
5. Friction which is an estimate of the frictional losses expected of the different concepts.

Life Criteria

1. Seal load
2. Seal speed
3. Bearing load
4. Material compatibility

Reliability Criteria

1. Clearances and their effect on concept reliability
2. External leakage in terms of the number of external leakage paths
3. Rotating component stress and vibration

Cost was evaluated with respect to the following parameters:

1. Development cost which represents an estimate of the cost of developing each design. Estimate is based on component state of the art. Rocketdyne past experience and a review of current industry effort.
2. Unit cost is an estimate of the cost of fabrication of each design.

The rotating pump rating system is shown in Table I.

The selection of the pump concepts to be evaluated was based on specific speed and specific diameter limitations imposed by the available NPSH, required head and flow, and fabrication capability. Figure 1 shows the approximate N_s - D_s region which is applicable for the desired pump performance. Pumps selected to be evaluated were:

1. Centrifugal
2. Barske

TABLE I. ROTATING PUMP RATING SYSTEM

Performance (total points = 25)	
Hydraulic Efficiency	5
Mechanical Efficiency	5
Overall Turbopump η (turbine η x pump η)	5
Size and Weight	5
Friction	5
Life (total points = 20)	
Seal Loads	5
Seal Speeds	5
Bearing Loads	5
Material Compatibility	5
Reliability (total points = 30)	
Clearances	10
External Leakage	10
Rotating Component Stress and Vibration	5
Pump Discharge Pressure Oscillations	5
Costs (total points = 25)	
Development Costs	15
Unit Costs	10

R-8494-1

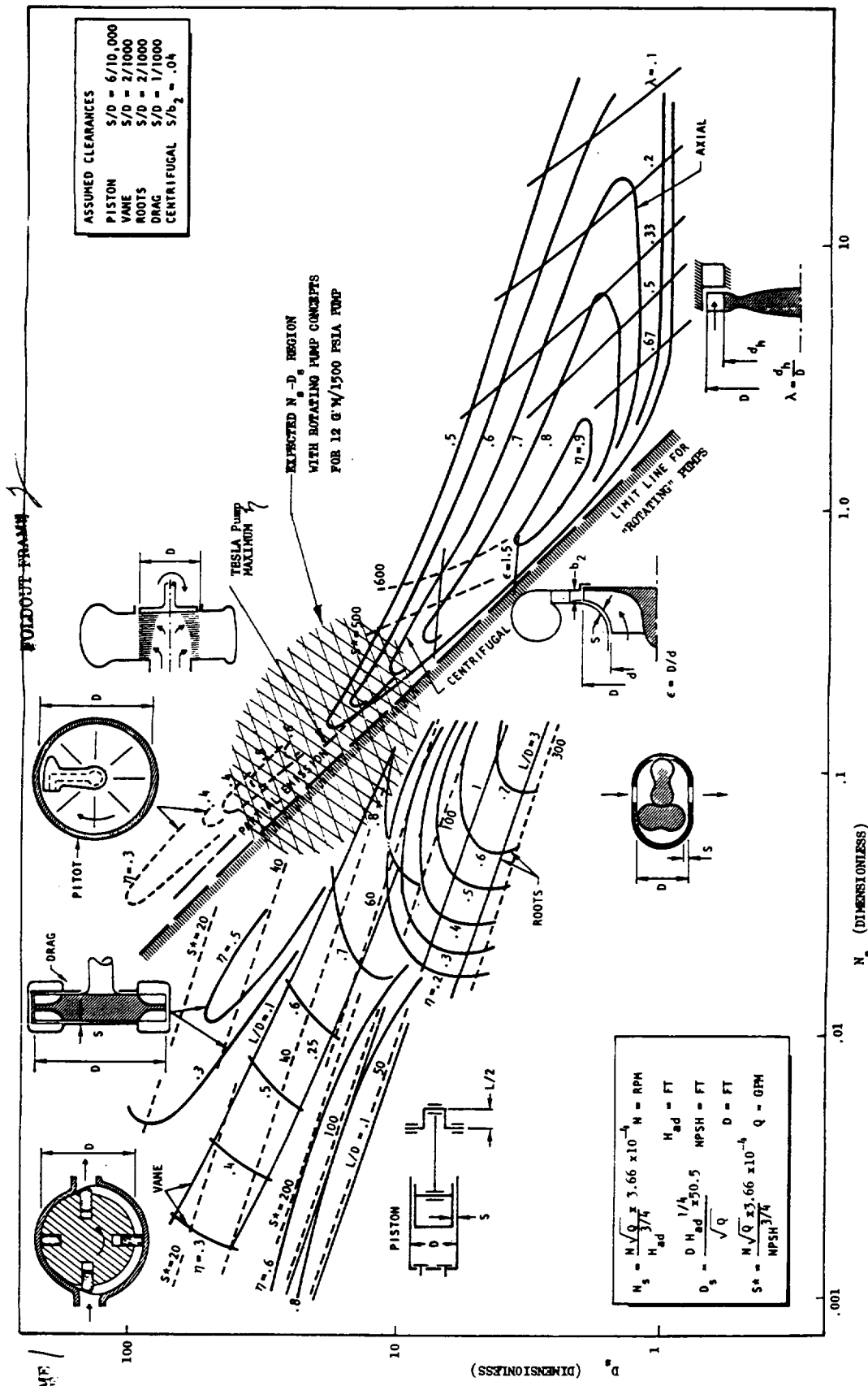


Figure 1. N_s -D_s Diagram for Pumps

-8494-1

3. Tesla

4. Drag

5. Pitot

A discussion of each of the concepts leading to a particular design to meet the specified operating requirements follows.

CENTRIFUGAL PUMP

The type of pump most commonly used in rocket engines is the centrifugal pump. It is ideally suited for the range of head rise and flowrate requirements of normal rocket engine thrust levels. For the low thrust levels being considered, the pump discharge pressures desired are of the same magnitude as those of the larger engines, but the mass flow is substantially reduced. The low flowrate relative to the pump head rise dictates the use of a high operating speed if the specific speed (N_s) is to be in a range that normally results in high pump efficiency. Cavitation performance, however, imposes an upper limit on pump speed. The speeds selected on the basis of cavitation performance are well below those for which efficient operation is indicated on the Specific Speed (N_s) - Specific Diameter (D_s) plot of Fig. 1. Specific speed is defined here in its dimensionless form by:

$$N_s = k_1 \frac{N Q^{1/2}}{H^{3/4}} \quad (1)$$

where N is the pump rotational speed (rpm), Q is the volumetric flowrate (gpm), and H is the pump head rise (ft). The constant k_1 , required to make the expression dimensionless, is derived as follows:

$$\begin{aligned} k_1 &= 2\pi \left(\frac{\text{rad}}{\text{rev}} \right) \frac{1}{60} \left(\frac{\text{min}}{\text{sec}} \right) \left[\frac{1}{7.48} \left(\frac{\text{ft}^3}{\text{gal}} \right) \frac{1}{60} \frac{\text{min}}{\text{sec}} \right]^{1/2} \left[\frac{1}{32.2} \frac{\text{sec}^2}{\text{ft}} \right]^{3/4} \\ &= 3.66 \times 10^{-4} \frac{(\text{ft})^{3/4}}{\left(\frac{\text{rev}}{\text{min}} \right) \left[\frac{\text{gal}}{\text{min}} \right]^{1/2}} \end{aligned} \quad (1a)$$

Equation 1 indicates that if the design flowrate is decreased while maintaining constant head, the pump speed must be increased to maintain constant specific speed.

The specific diameter is defined in terms of the impeller diameter by:

$$D_s = k_2 \frac{D H^{1/4}}{Q^{1/2}} \quad (2)$$

If the impeller diameter, D, is expressed in feet, the constant, k_2 , is obtained as follows:

$$\begin{aligned} k_2 &= \left[7.48 \left(\frac{\text{gal}}{\text{ft}^3} \right) \frac{1}{60} \frac{\text{sec}}{\text{min}} \right]^{1/2} \left[32.2 \left(\frac{\text{ft}}{\text{sec}^2} \right) \right]^{1/4} \\ &= 50.4 \frac{\left(\frac{\text{gal}}{\text{min}} \right)^{1/2}}{\left(\text{ft} \right) \left(\text{ft} \right)^{1/4}} \end{aligned} \quad (2a)$$

An important factor which must be considered when discussing specific speed is the speed limitations placed on the rotating assembly. The maximum speed of the pump is generally limited by the bearing DN capability expressed in bore diameter times rotative speed (mm·rpm). To date industry experience has been limited to a maximum DN value of 0.75×10^6 in fluorine. This value limits the centrifugal pump speed and therefore limits the pump specific speed at required flowrates. The required specific speed of the pump for this application is 0.286 based on a maximum pump speed of 75,000 rpm. With centrifugal pumps, as the specific speed decreases below approximately 0.586, the maximum obtainable pump efficiency also decreases.

The N_s - D_s diagrams are applicable only to larger size pumps. This is due to the fact that test data used in the development of the N_s - D_s diagram came from relatively large pumps. The relationships of pump size to pump efficiency has been

discussed by Kittredge (Ref. 2). He presents efficiency conversion formulas developed from many sources in an effort to predict prototype performance from model data. The pump size ranges presented are from impeller diameters of 400 mm (15.75 in.) to 100 mm (3.94 in.) which is larger than the pumps under study by a factor of three. Figure 2 presents the pump efficiency as a function of impeller diameter as developed by Rutschi and presented in the above reference. The data shown are for a pump specific speed range of 0.366 to 0.732. If the impeller eye diameter is used, the data show little dependence on specific speed. The impeller eye-to-tip diameter ratio for these pumps, however, is somewhat small compared to pumps for rocket engine applications requiring high suction performance.

The reduction in pump efficiency with the decrease in impeller size can be attributed to changes in relative roughness and the changes in leakage flows between high- and low-pressure regions. In scaling a large-diameter pump to a smaller diameter, the requirement for dynamic and geometric similarity holds. This cannot be attained by maintaining only the relationship:

$$\left[\frac{Q}{ND^3} \right]_{\text{full size}} = \left[\frac{Q}{ND^3} \right]_{\text{model}} \quad (3)$$

This relationship must be maintained, but all dimensions must be scaled as well. These dimensions include surface roughness and all internal pump clearances which, in some instances, cannot be scaled. An example of this is in oxidizer pump applications where wear ring clearances are set by the criteria of rubbing possibilities and material compatibility and cannot be scaled outside of these limits. Similarly, the surface roughness can be reduced only to a certain extent and, thereafter, the relative roughness will increase for smaller size pumps. These two effects cause considerable difficulty in the determination of performance levels of small pumps using information gained from pumps of larger dimension. At present, scale factors used to predict efficiencies of small pumps do not utilize relative roughness and wear ring clearance geometry relations as scale parameters. This makes them somewhat inadequate for use in this particular application.

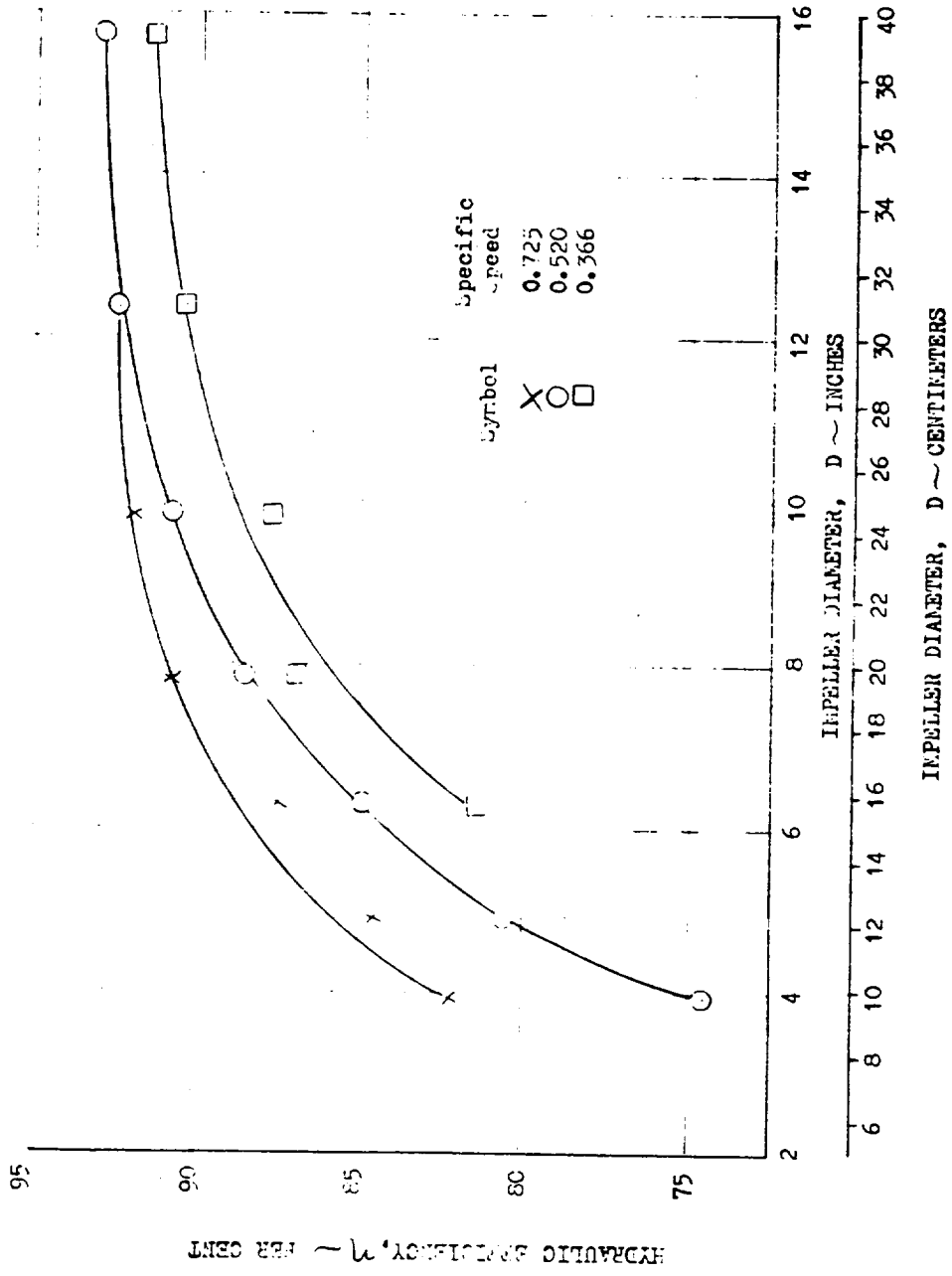


Figure 2. Hydraulic Efficiency as a Function of Impeller Diameter (Ref. 2)

R-8494-1

The best known available data for pumps within the size indicated for this application is shown in Fig. 3 . This curve, taken from Ref. 3 , is indicated as being based on available data for pumps up to 4.0 inches (10.16 cm) in diameter, and the source has considerable experience in pumps of the size indicated. As in all information presently available, it is not stated whether the pumps are scaleable from the standpoint of wear ring clearance and surface roughness.

Analytical Effort

Rocketdyne has developed a centrifugal pump loss isolation program for digital computers which is capable of predicting pump performance by calculation of specific pump losses. This program uses pump geometry and flow input to calculate internal loss mechanisms such as diffusion, skin friction and incidence and other loss effects such as wear ring leakage, disk friction, scroll friction and momentum, and diffuser losses. The use of this program provides a key to the effects of size on such losses as wear ring leakage and internal skin friction by utilizing geometry and relative roughness. The loss coefficients are based on all available data from studies found in literature surveys. Since internal clearances in small pumps are relatively larger than those in pumps of significantly larger diameter, friction coefficients are based on relative roughness and Reynolds Number thus accounting for the increased frictional effects in the smaller pumps. A breakdown of the loss components are presented in Fig. 4 for the centrifugal pump configuration considered for this application. As indicated, the efficiency is given as 58.7 percent at design flow. The same pump taken 10 times size shown an efficiency of 68.9 percent. In this calculation, the surface finish was maintained at 125 microinches (3.175 μm) for both pumps. The wear ring clearance of the full size pump 1.3 inch (3.3 cm) impeller OD, was 0.003 inch (0.076 mm) and that of the 10 times size pump 13.0 inch (33 cm) impeller OD, was 0.020 inch (0.508 mm). The impeller friction factor increased from 0.0146 in the large pump to 0.0251 in the small pump due to relative roughness. Thus, friction losses are increased by 72 percent.

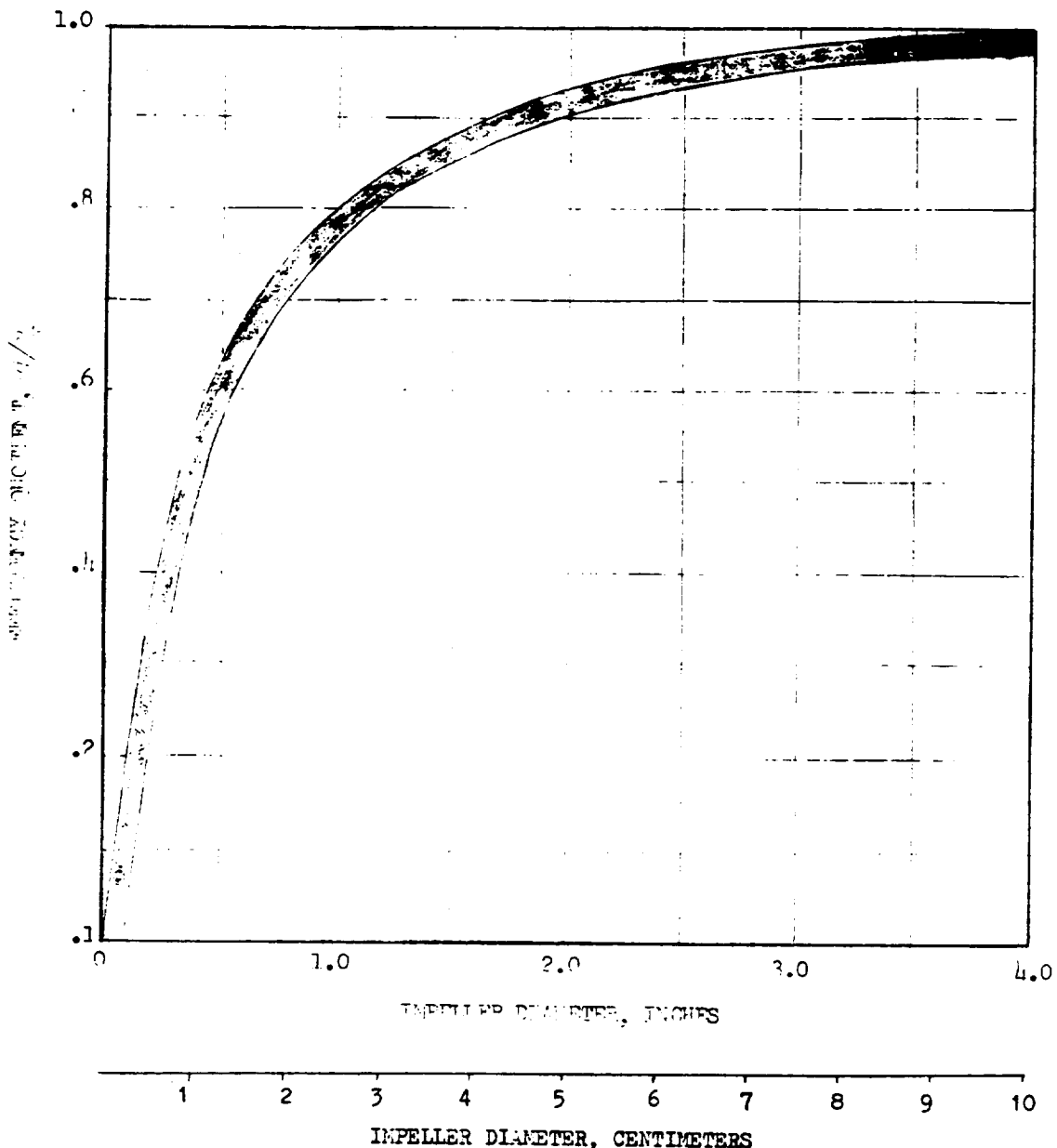


Figure 3. Effect of Impeller Size on Pump Efficiency

R-8494-1

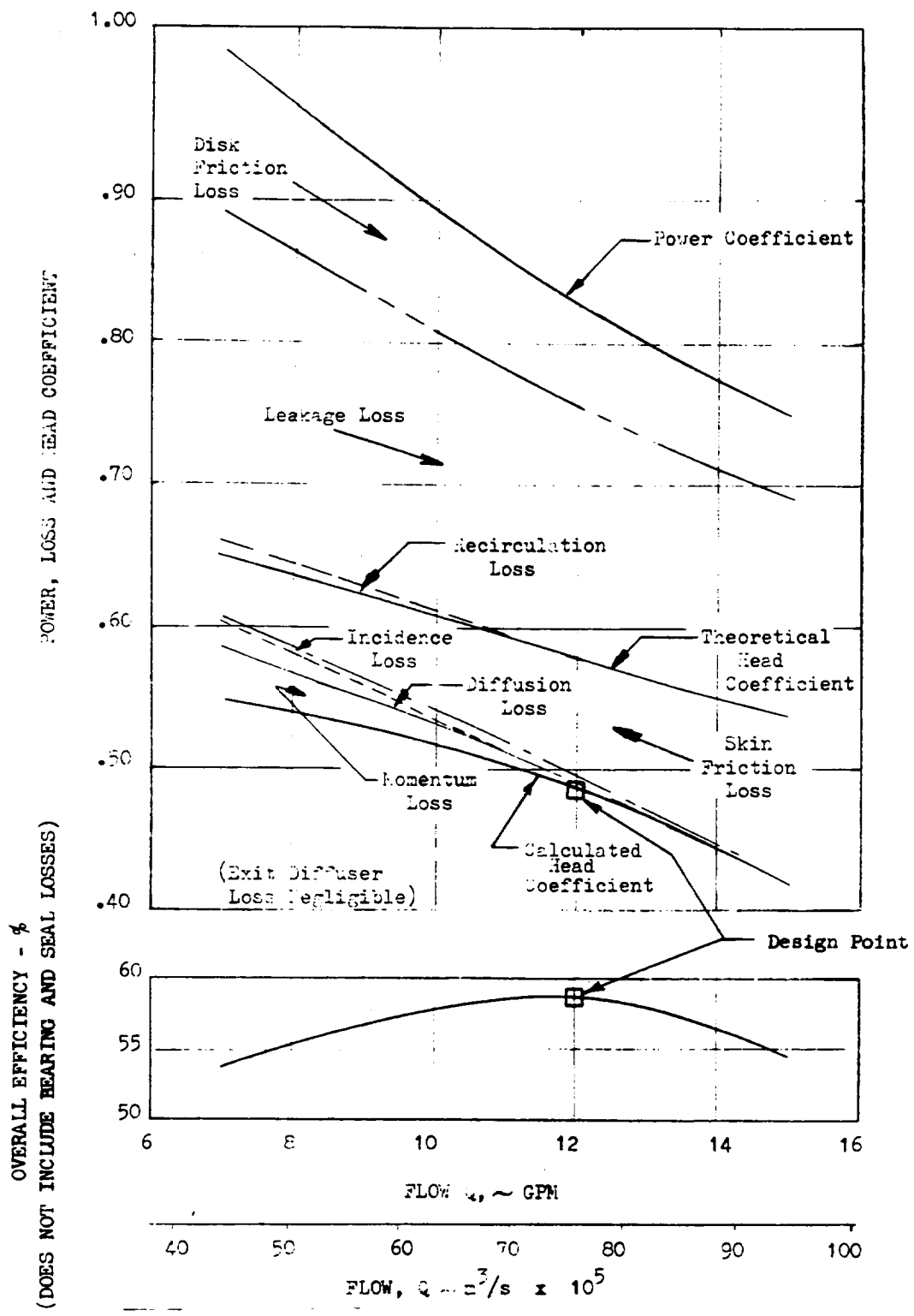


Figure 4. LF_2 Centrifugal Pump Loss Breakdown Preliminary Design

R-8494-1

Preliminary Design

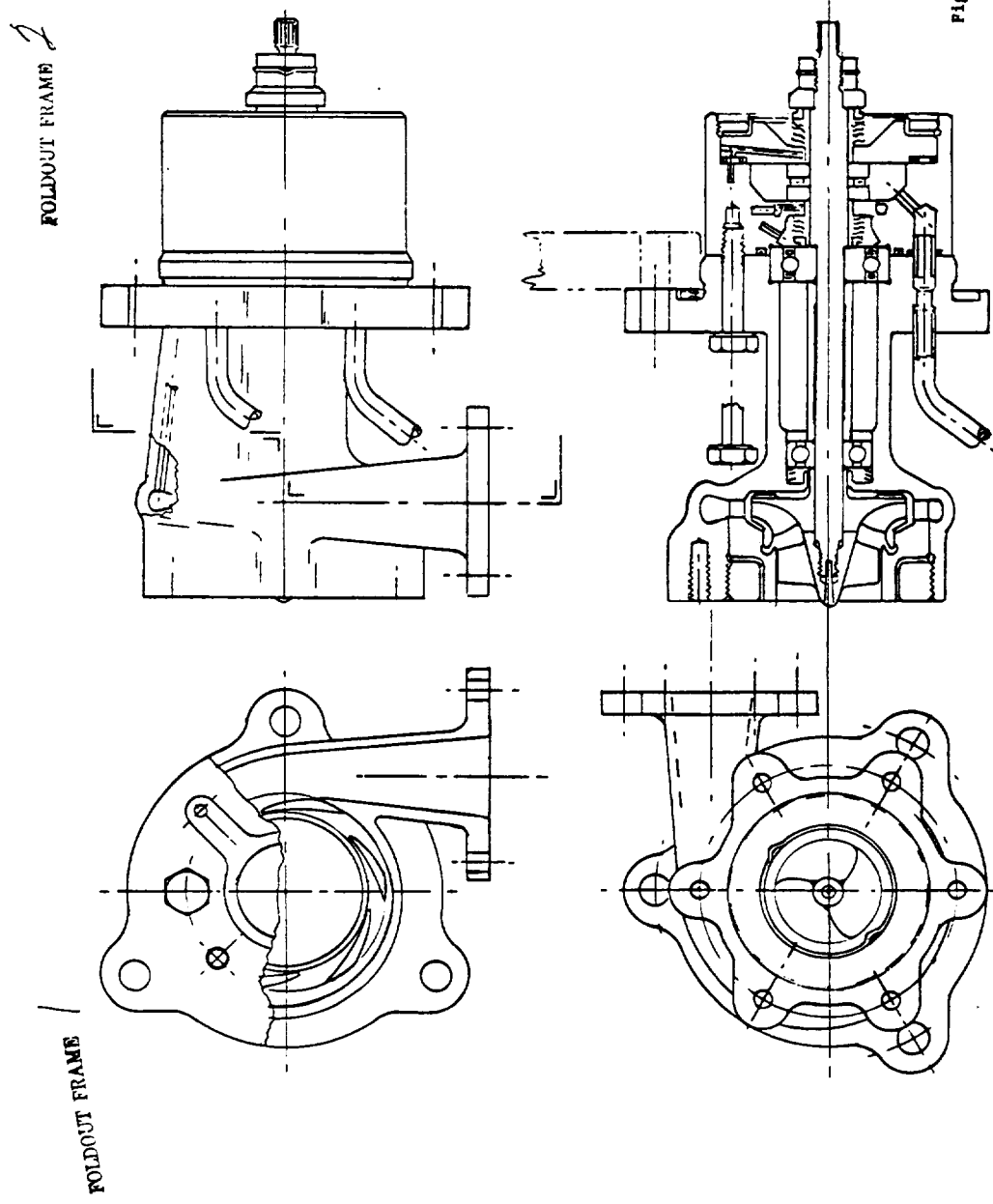
The most feasible centrifugal pump configuration found applicable to the requirements given is a design similar to that found in Fig. 5. This design consists of a shrouded centrifugal impeller preceded by a low head, high suction specific speed inducer. The impeller axial thrust is balanced by proper diameter wear rings on the front and rear impeller shrouds. The volute consists of a single discharge collector followed by a straight conical diffuser. This should provide acceptable design point and off-design radial loads on the bearings.

Because of size limitations and friction loss effects, double scrolls or the diffuser vanes shown in Fig. 5 did not prove practical.

The bearings will operate at a maximum DN of 0.75×10^6 and will be cooled with liquid fluorine. The seal package separating the bearings contains two face riding seals separated by a shaft seal with purged intermediate cavities. The seal diameters must be maintained as small as possible to minimize the friction losses.

Design Effort

Impeller Shrouds. A shrouded impeller was determined to be the best impeller configuration for use with fluorine. Axial clearances have a significant effect on the efficiency of an open face impeller. A clearance equal to 5 percent of the average impeller passage height will result in an efficiency loss of approximately 5 percent of the zero clearance design efficiency, according to Eckart (Ref. 4). The axial clearances of the pumps of this type must be large enough that rubbing will not occur while the low specific speeds require that impeller blade height be small. For this pump, the blade clearance to height ratio at impeller tip would be approximately 0.33 to eliminate rubbing. This makes the open impeller undesirable. The shrouded impeller can operate with large axial clearances and the leakage is controlled by radial clearances at the wear rings. Control of radial wear ring clearance can be achieved more reliably than close axial blade to housing clearances on open face impellers.



PRELIMINARY DESIGN

CENTRIFUGAL PUMP	
ROTATING SPEED, RPM	75,000
ROTOR TIP DIAMETER, IN.	1.30 (3.30 cm)
INLET DIAMETER, IN.	.674 (.161 cm)
SHAFT DIAMETER, IN.	.375 (0.94 cm)
REQUIRED NPSH, FT.	20 (6.1 m)
SUCTION SPECIFIC SPEED	10.05*
ROTOR TIP SPEED, FPS	426 (1.30 m/s)
BEARING DN, mm-RPM	750,000
SEAL RUBBING SPEED, FPS	125 (38 m/s)
WEAR RING SPEED, FPS	300 (92m/s)
ESTIMATED DRY WEIGHT, LB.	4.1 (1.9 kg)
MINIMUM ROTOR-HOUSING	NOT CRITICAL:SHROUDED
AXIAL CLEARANCE, IN.	
MINIMUM ROTOR HOUSING	
RADIAL CLEARANCE, IN.	
ESTIMATED EFFICIENCY, %	
(NOT INCLUDING SEAL &	
HEARING LOSSES	
HEARING AXIAL LOAD, L_{BF}	25 (111 N)
HEARING RADIAL LOAD, L_{BR}	10 (45.5 N)
OVERALL EFFICIENCY, %	53
GAS POWER REQUIRED, HP	54.5 (40.6 kW)
	.003 (0.076 mm)
	58

$$* \quad \eta_{\text{eff}} = \frac{\pi Q}{(NPSH)} \cdot \frac{1/2}{3/4} \times 3.66 \times 10^{-4}, \text{ in dimensionless form}$$

Figure 5. Centrifugal Pump-Preliminary Design

Diffusion System. The use of a single volute followed by a straight conical diffuser has many advantages from the basis of cost and ease of manufacture. However, in this system the friction losses are high due to the high velocities in the collector or scroll. A method of reducing these losses in some cases is the use of a vaned diffuser directly after the impeller discharge. With a vaned diffuser the velocity is reduced efficiently before being collected with a resultant savings by the reduction in scroll friction loss. Experience indicates that vaned diffusers are desirable for specific speeds below 0.366 or when the head coefficient is greater than 0.6. For small pumps due to other loss penalties this head coefficient limitation could be reduced to 0.5 or less.

However, calculations indicate that for this pump specifically, a vaned diffuser will not improve efficiency since friction losses are also large in a vaned diffuser due to relative roughness limitations. The use of a vaneless space for diffusion purposes before collection by the scroll results in increased losses since friction losses are high also due to relative roughness and increased flow path length. As a result it was decided not to use the diffuser vanes which are shown in the preliminary sketch in Fig. 5, but adopt a single discharge volute.

The single discharge volute has the disadvantage that bearing radial loads occur at off design conditions. The radial load at off design conditions of this pump is small due to the small impeller area exposed to the unbalanced pressure. There is an optimum design of the scroll based on a tradeoff between the side-wall friction loss on the collector and the momentum loss between the impeller discharge and the entrance to the straight conical diffuser. This tradeoff requires that the scroll be oversized from 120 to 180 percent over the area based on zero scroll momentum loss. Figure 6 shows typical curves of volute friction loss and scroll momentum loss as a function of pump flow. The curve indicates an oversized volute gives more scroll momentum loss but less volute friction loss and the total loss can be optimized at a given design flow point.

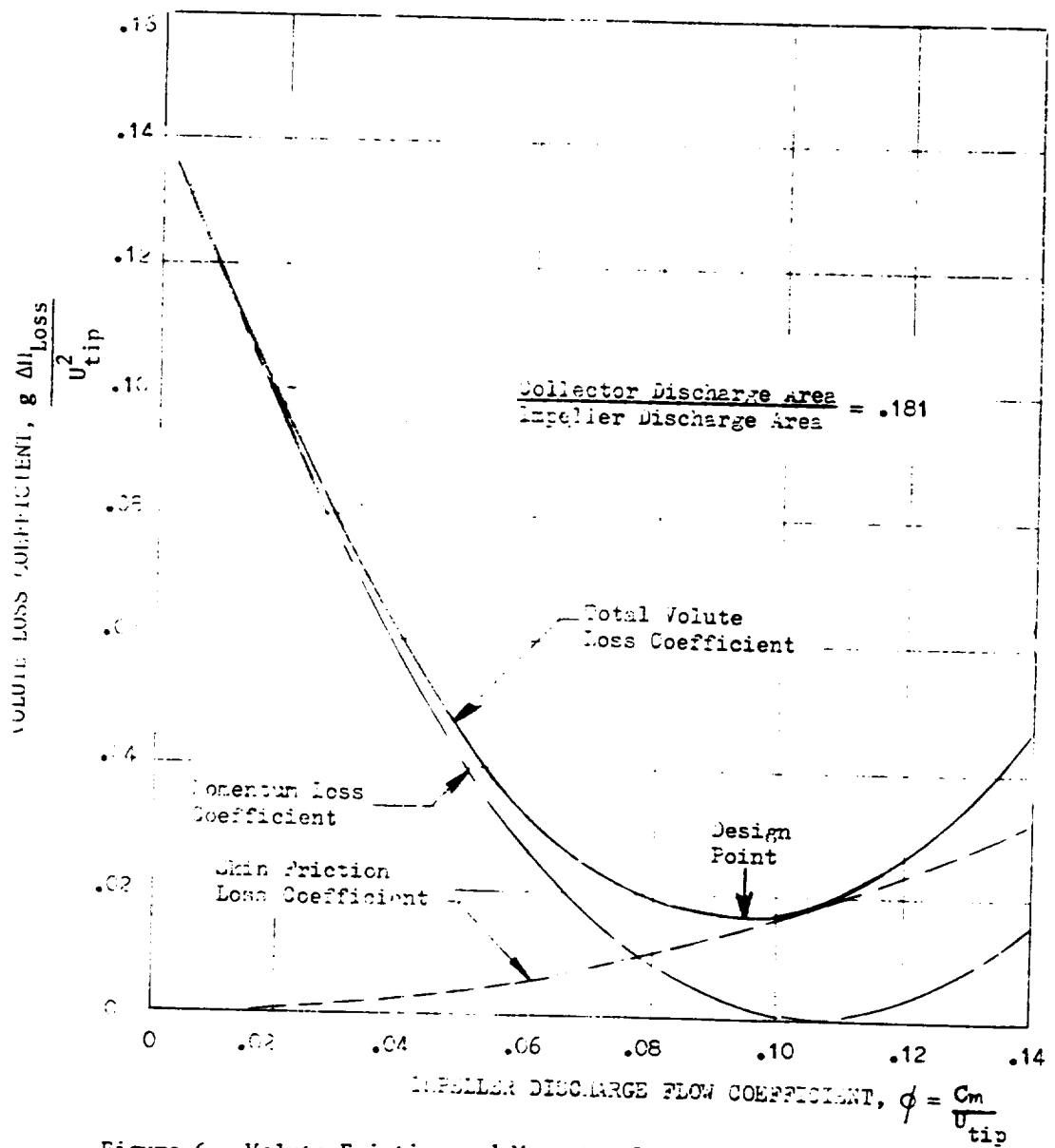


Figure 6. Volute Friction and Momentum Loss as a Function of Flow Coefficient

R-8494-1

PITOT PUMP

Introduction

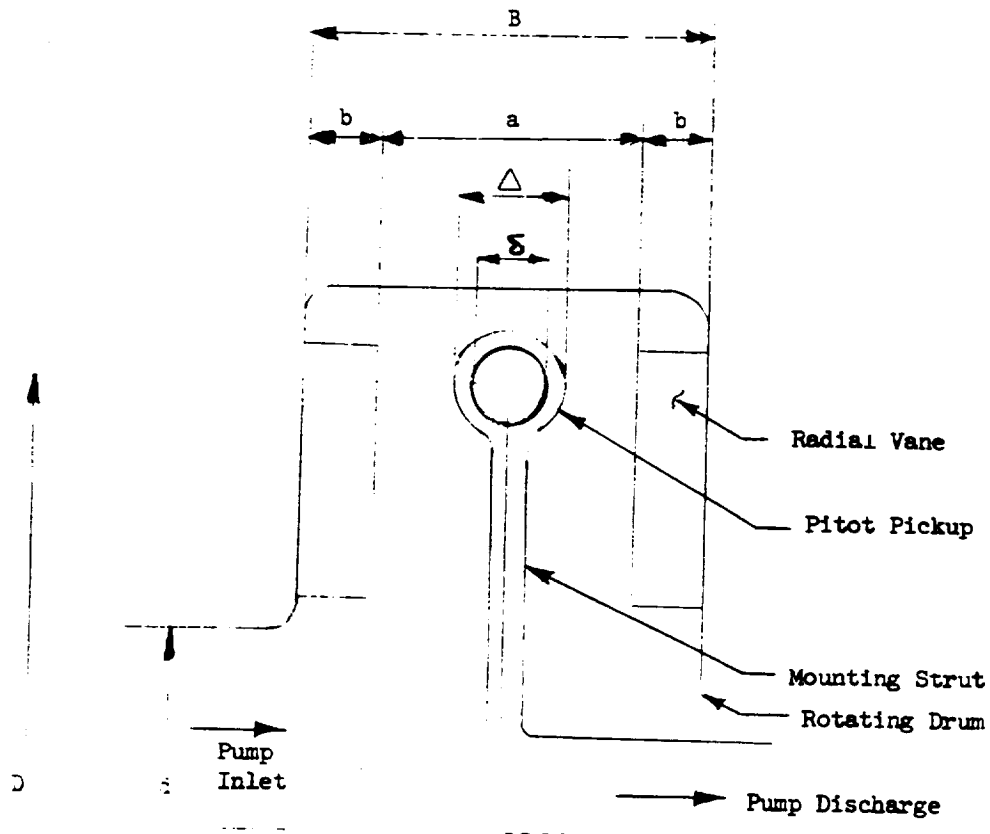
Pitot pumps are typical low specific speed pumps and are expected to give higher efficiencies in the low specific speed regime than conventional (full emission or partial emission) pumps. This is due to the design features of the Pitot pump which tend to minimize the parasitic losses usually occurring between the back of the rotor disk and the stationary housing in conventional pumps. This loss is minimized by employing an "unconventional" pumping principle. A rotating liquid ring is created inside a rotating drum and pressurized fluid is scooped from this ring by stationary Pitot heads and ducted to the outside. This mode of operation minimizes the internal losses within the rotating drum but does, however, provide a large frictional area at the outside of the drum. This would create extremely high windage losses if the drum rotates within a fluid which has the same density as the pumped liquid. In cases, however, where the density of the surrounding medium is significantly lower than that of the pumped liquid, the outside windage losses becomes small. It is only under these conditions that the Pitot pump can exhibit higher efficiencies than conventional pumps in the low specific speed regime.

Analysis

A principal cross section through a Pitot pump is presented in Fig. 7 which shows a pitot pickup mounted on a stationary strut, operating within the rotating drum which is filled with liquid. Radial vanes are protruding from the inner walls of the rotating drum to create a rotating liquid ring.

For the purpose of this analysis it is assumed that the fluid rotates with the impeller as a solid body. The static pressure within the rotating liquid ring increases with the square of the peripheral speed:

$$H_{\text{static}} = \frac{U^2}{2 g m} \quad (4)$$



$$X = \frac{\Delta}{\delta}$$

$$K = \frac{d}{\Delta}$$

$$Y = \frac{a}{\delta}$$

$$D^* = \frac{D}{\delta}$$

$$L = \frac{3}{\delta}$$

Figure 7. Schematic of Pitot Pump

R-8494-1

where U_2 denotes the peripheral speed of the radial vane trailing edges, and m denotes a slip factor which depends mainly on the number of vanes and the diameter ratio D/d where D = outside diameter of the vanes and d is the inlet diameter. The slip factor can be expressed by the approximate relation:

$$m = 1 + \frac{\pi}{2Z(1 - \frac{d}{D})} \quad (5)$$

This expression shows good accuracy for the straight radial vanes used in pitot pumps.

If no fluid is extracted from the Pitot pickup, a high percentage of the velocity head can be converted into pressure rise. In the ideal case, i.e., complete conversion of velocity head into pressure, the total pressure will be twice the static pressure:

$$H_{th} = \frac{U^2}{2g} \quad (6)$$

The actually recovered velocity head will decrease with increasing flowrates due to the residual velocity head and due to the frictional losses so that the total head will tend to decrease with increasing flow coefficient if the flow coefficient is defined by:

$$\phi = \frac{C_p}{U^2} \quad (7)$$

C_p denoting the velocity in the Pitot pickup.

The frictional losses can be determined by a loss analysis. Several loss sources have to be accounted for: (1) the frictional losses within the drum and within the Pitot tube and strut, (2) drag losses of the Pitot head and strut, and (3) the windage losses on the outside of the drum. For this analysis, several geometric parameters have to be considered.

These parameters are as follows:

D = diameter at which the Pitot pickup is located
d = inlet diameter of the housing
 δ = diameter of the Pitot pickup
 Δ = diameter of the Pitot body
B = axial extension of the rotating drum
b = axial extension of the radial vanes
a = spacing between the vanes

These parameters may be grouped into proportionality factors such as:

$$\begin{aligned}X &= \Delta/\delta \\Y &= a/\delta \\N &= B/\delta \\K &= d/\Delta\end{aligned}$$

The loss analysis may be done by using dimensionless coefficients, i.e., by relating every individual head loss to a fictitious head. Thus, the head loss coefficient, expressing the head loss experienced by the flow in going through the bladed portion of the drum, is given by:

$$q_L = \frac{H_{lost}}{U_2^2/g} = \frac{\emptyset^2}{2} \left[\frac{1 - d/D}{2} \right] \left[\frac{D}{b} + \frac{Z}{\pi} \right] \zeta_R \quad (8)$$

where ζ_R denotes a loss factor (which depends on the Reynolds Number) and Z the blade number. Another loss is experienced in the channel within the Pitot tube,

strut, and exit duct where two right-angular bends are encountered. These losses may be expressed by the relation:

$$q_p = \frac{\phi^2}{2} \zeta_p \quad (9)$$

where ζ_p denotes a loss coefficient for the internal ducting. The actually developed head, expressed in terms of a head coefficient, can thus be expressed by:

$$q_d = \frac{H_{ad}}{U_2^2/g} = q_{th} - \frac{\phi^2}{2} \left[\zeta_R \left(\frac{1-d/D}{2} \right) \left(\frac{D}{b} + \frac{Z}{\pi} \right) + \zeta_p \right] \quad (10)$$

where q_{th} denotes the theoretical head coefficient which, from Eq. 8, is

$$q_{th} = \frac{1}{m} \quad (11)$$

Other losses which have to be considered are the drag of the Pitot pickup and of the supporting strut, the losses occurring in the energy transfer from the fluid within the vanes to the fluid surrounding the probe, and the wheel disk friction on the external surfaces of the rotating pump casing. Of these losses, only the external disk friction on the rotating casing has no effect on the pressure rise produced by the pump, but it affects the power input to the pump required to generate the output head. The remaining losses mentioned above can reduce the fluid velocity and the relative total head at the Pitot probe, thus requiring a higher rotating speed to effect the desired pressure rise. One of the most important criteria for the performance of the Pitot pump is the resistance coefficient for the Pitot pickup and strut. Tentative values for this parameter can be found in the literature (Ref. 5). These data indicate that the drag coefficient depends on the body shape, varying from values of $\zeta_D = 1.17$ for a flat disk and $\zeta_D = 0.1$ for streamlined bodies. These values can claim validity only if it can be assumed that the body is in a free stream. The Pitot pickup as well as the strut, however, are located between rotating vanes. Thus, the distance between Pitot body and strut would be expected to become an influential parameter. For close distances, an interference drag will increase the overall drag loss. Guidelines for

the total drag loss and its interrelation with distance can also be found in Ref. 5, which shows (Fig. 8) that compared to the free stream condition, the drag coefficient approximately doubles when the distance between the struts is equal to the width of the strut, and that the drag coefficient quadruples when the distance is about 0.4 of the strut width.

The effect of the Pitot probe can be better understood from the following discussion. First, assume that the pitot pickup is removed from the pump. If the impeller is now filled with liquid and rotated, the whole fluid body within the impeller can be assumed to rotate as a forced vortex due to the combined action of the vanes and the viscous forces. However, when the stationary Pitot probe is introduced, the central ring of fluid, which is not contained within the vanes but flows between the strut and the vanes, will experience a viscous shear force due to the presence of the probe and wake region behind the probe. This shear force introduces an axial gradient in the tangential velocity, which increases with radius out to the maximum radius of the strut, and a corresponding static pressure gradient. The presence of this static pressure gradient causes a secondary flow phenomenon which results in an outward flow of the fluid within the impeller vanes and an inward flow of the fluid in the central ring (Fig. 9). If no other flow phenomena were involved with the presence of the secondary flow, these secondary flows would not affect the pump pressure rise, but would serve only to increase the power requirements. However, because of viscous forces acting on the Pitot probe, a wake consisting of low-energy fluid is created behind the probe. The pressure difference between the fluid in the central core and this wake region introduces a mixing of these two fluid regimes which results in a relative total pressure deficit in the plane of the Pitot head necessitating an increase in the wheel speed.

The increase in the power required to sustain the secondary flow in the central core can be obtained by merely increasing the drag coefficient by a factor which depends on the spacing between the strut and vane and on the depth of the vaned portion of the impeller. With these assumptions, the loss associated with the probe drag may be expressed by the coefficient:

$$q_d = \frac{x^2 \zeta_D A}{2 m^3 \phi} \quad (12)$$

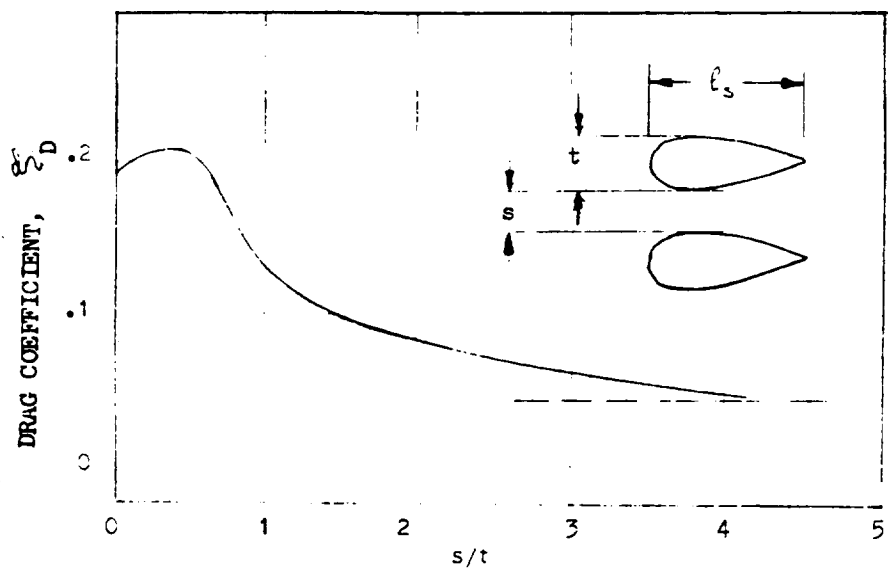


Figure 8. Typical Values for Drag Coefficient

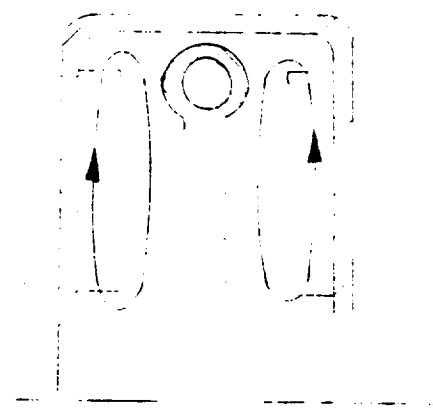


Figure 9. Relative Eddy Within the Pitot Pump

where ζ_D denotes the original strut drag coefficient and A the amplification factor which is the inverse of the Pitot pump vane efficiency ($A = 1/\eta_B$)

The wheel disk friction power loss at the outer part of the rotating drum is determined by using the relation derived in Ref. 6 :

$$P_w = U_2^3 D(D+5B) \beta_w \gamma_g \frac{1}{g} \quad (13)$$

where γ_g denotes the specific weight of the gas surrounding the rotating drum.

To convert the above expression into the form of a head loss coefficient, the terms which define the head and flow coefficients are substituted into the equation $HP = QH\gamma_f$, resulting in the expression:

$$HP = \left[\frac{\pi \delta^2}{4} U_2^2 \right] \left[\frac{\gamma_w U_2^2}{g} \right] \gamma_f \quad (14)$$

Then, substituting the terms of Eq. 14 for P_w in Eq. 13, and rearranging and clearing terms results in the following expression for head loss coefficient due to wheel disk friction:

$$q_w = \frac{4 (1+\zeta_B)}{\phi \pi} \left[\frac{D}{\delta} \right]^2 \frac{\gamma_g}{\gamma_f} \quad (15)$$

where β_w denotes the friction coefficient, γ_g the specific weight of the gas medium surrounding the housing, and γ_f the specific weight of the flow inside the Pitot pump. Thus, the power input can be expressed by an input head coefficient of the form:

$$P_c = q_{th} + q_D + q_w \quad (16)$$

and, consequently, the efficiency by:

$$\eta = \frac{q_{ad}}{P_c} \quad (17)$$

Pitot Pump Calculated Performance Data

Single Pitot Head. The relations just presented may now be used to calculate the maximum obtainable efficiency as function of specific speed and specific diameter by calculating the head coefficient and efficiency as function of flow coefficient for different values of the geometrical parameters. The relations:

$$N_s = \frac{\sqrt{\phi}}{q_{ad}^{3/4} (D/\delta)} \quad (18)$$

$$\text{and } D_s = \frac{(D/\delta) q_{ad}^{1/4}}{\sqrt{\phi}} \quad (19)$$

convert the flow coefficient and head coefficient data into specific speed and specific diameter for single-headed Pitot pumps.

Analysis of available Pitot performance data shows that conventional designs can be identified by loss and drag coefficients (Ref. 7). With these data, an N_s - D_s diagram as shown in Fig. 10 is calculated which shows a maximum efficiency potential of about 37 percent occurring at specific speeds of about 0.116, desiring a geometry factor of $D/\delta = 12$. Additionally, lines of constant Thoma cavitation parameter are shown defined as:

$$\sigma = \frac{NPSH}{H_{ad}} \quad (20)$$

This parameter is calculated on the basis of a drag wake coefficient (Ref. 5) assuming a width-to-length ratio (t/l_s , Fig. 8) of the strut of 0.10. Lines of constant cavitation parameter shown in Fig. 10 indicate that the σ values increase with increasing specific speed, and that a value of $\sigma = 0.008$ would be required for specific speeds which give the highest efficiency. Assuming a rotational speed of 30,000 rpm, this value would correspond to suction specific speed of less than 12,000, which appears reasonable for a first approximation.

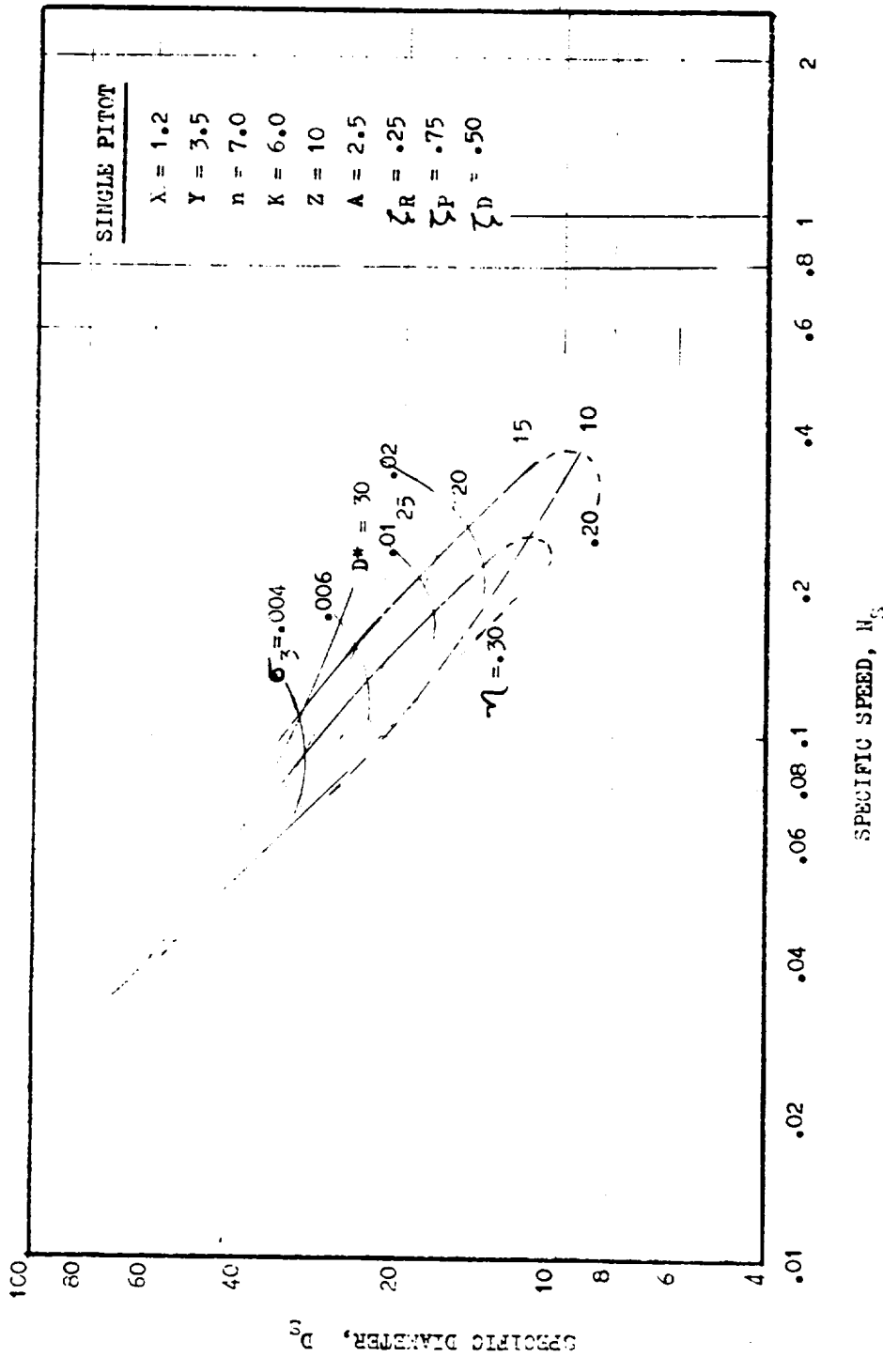


Figure 10. N_s - D_s Diagram for the Pitot Pump With a Single Pitot

Double Pitot Head. A disadvantage of the geometry considered so far is that only one Pitot pickup is provided within the rotating liquid. Thus, a comparatively high radial load may be generated. This radial load can be eliminated by providing two Pitot pickups. This increases the drag, thus increasing the required power input. Using the same characteristic data (loss coefficients and drag coefficients) as used for the single pickup type, the N_s - D_s diagram for a double Pitot pickup is calculated and shown in Fig. 11. Comparing these two diagrams, it becomes apparent that the efficiency potential for the double Pitot pickup is decreased by about 6 to 8 points, but that the suction specific speed and optimum geometry factors are hardly affected. The optimum specific speed is increased somewhat as would be expected.

Comparatively little research on Pitot pumps has been published in the available literature. Thus, it is not obvious that the loss factors used for the analysis are the minimum obtainable values. Actually, it can be speculated that the Pitot drag coefficient may be decreased with further research. Assuming, for example, that the drag coefficient (ζ_D) can be reduced by a factor of 2, Fig. 12 results, which shows a maximum efficiency potential of 42 percent (as compared to 28 percent quoted in Fig. 11). An even higher increase in efficiency, namely up to $n = 50$ percent, appears possible if the drag coefficient can be reduced to the ideal value of 0.16 and still retain an amplification factor of 2.5 (Fig. 13). If the amplification factor can be reduced to 1.4, a maximum efficiency of 60 percent is calculated as shown in Fig. 14. The corresponding N_s - D_s diagram is given in Fig. 15 showing that the optimum specific speed is still between 0.078 and 0.116, and that the values for the Thoma cavitation parameter are identical to those reported for the higher drag coefficients.

The calculated data are summarized in Fig. 16 and 17 by showing the optimum specific diameter (defined as that specific diameter at which the highest efficiency is obtained) as function of specific speed for the different loss assumptions together with the required values for the cavitation parameter. It is evident that the optimum specific diameter changes little with the loss assumptions and that the cavitation value is affected only to a minor degree. The associated efficiency, however, changes quite drastically as shown in Fig. 16.

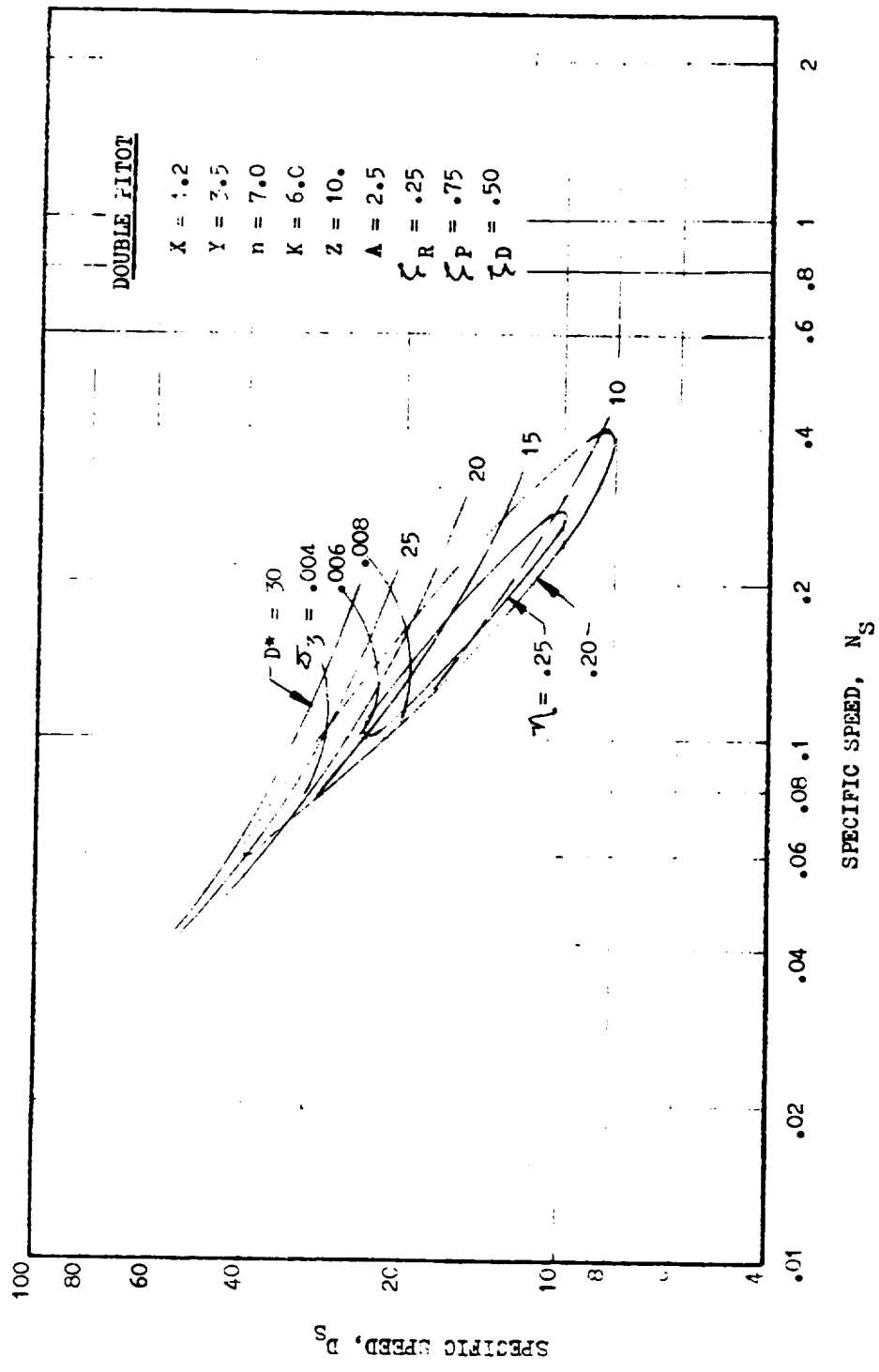


Figure 11. N_s - D_s Diagram for the Pitot Pump With a Double Pitot

R-8494-1

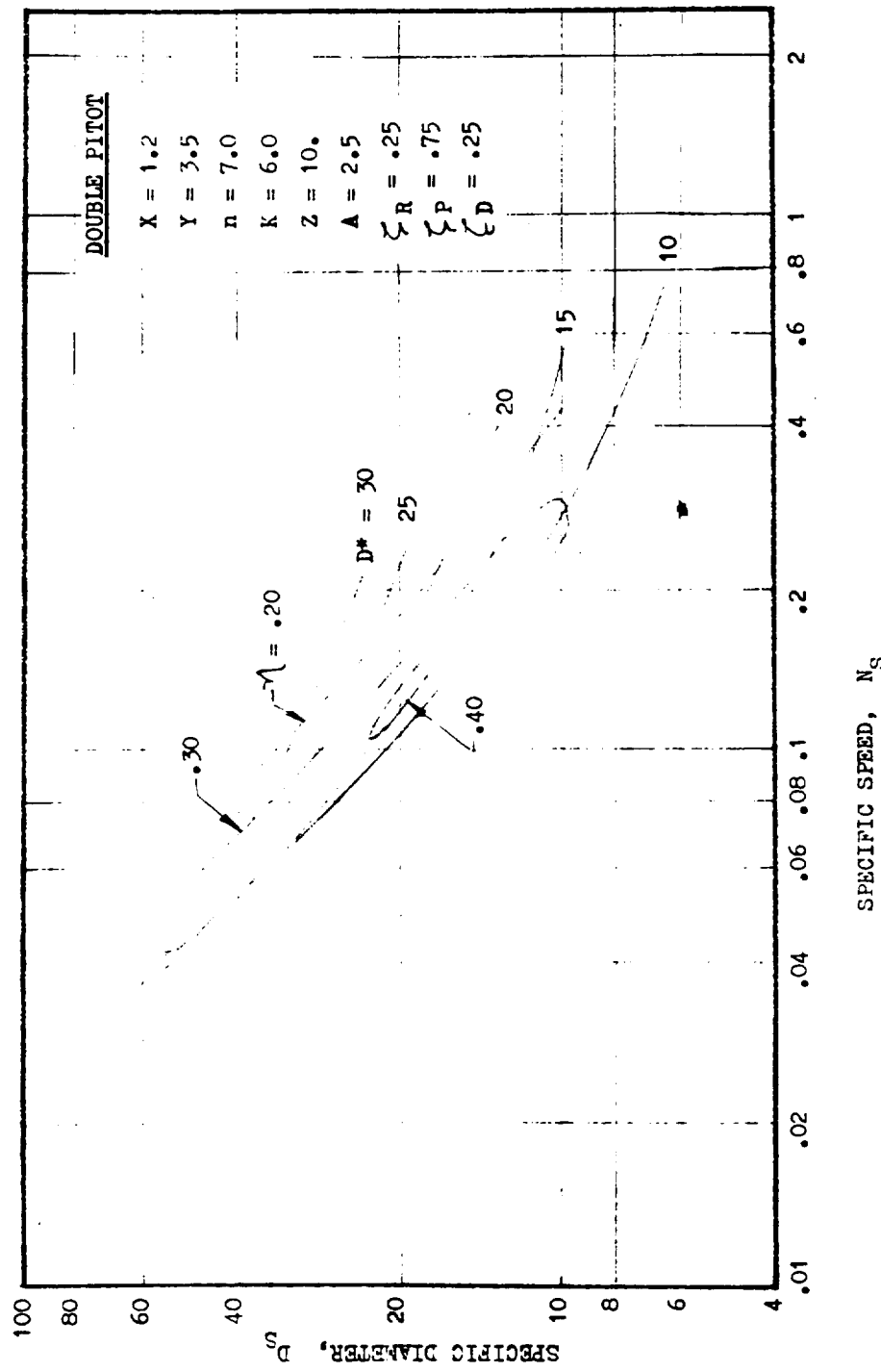


Figure 12. N_s - D_s Diagram for the Pitot Pump With a Double Pitot

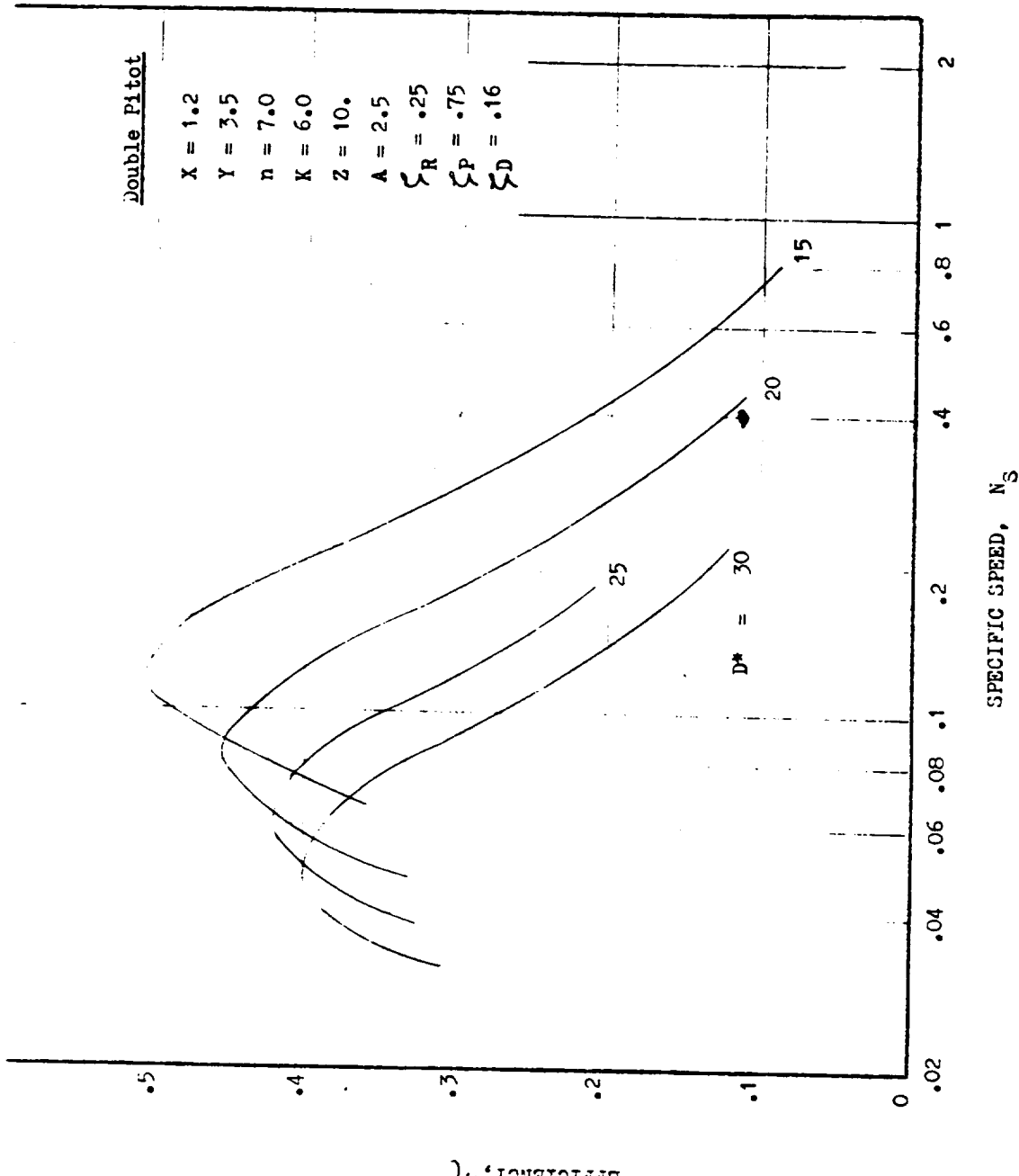


Figure 13. Efficiency vs Specific Speed for Pump With Double Pitot

R-8494-1

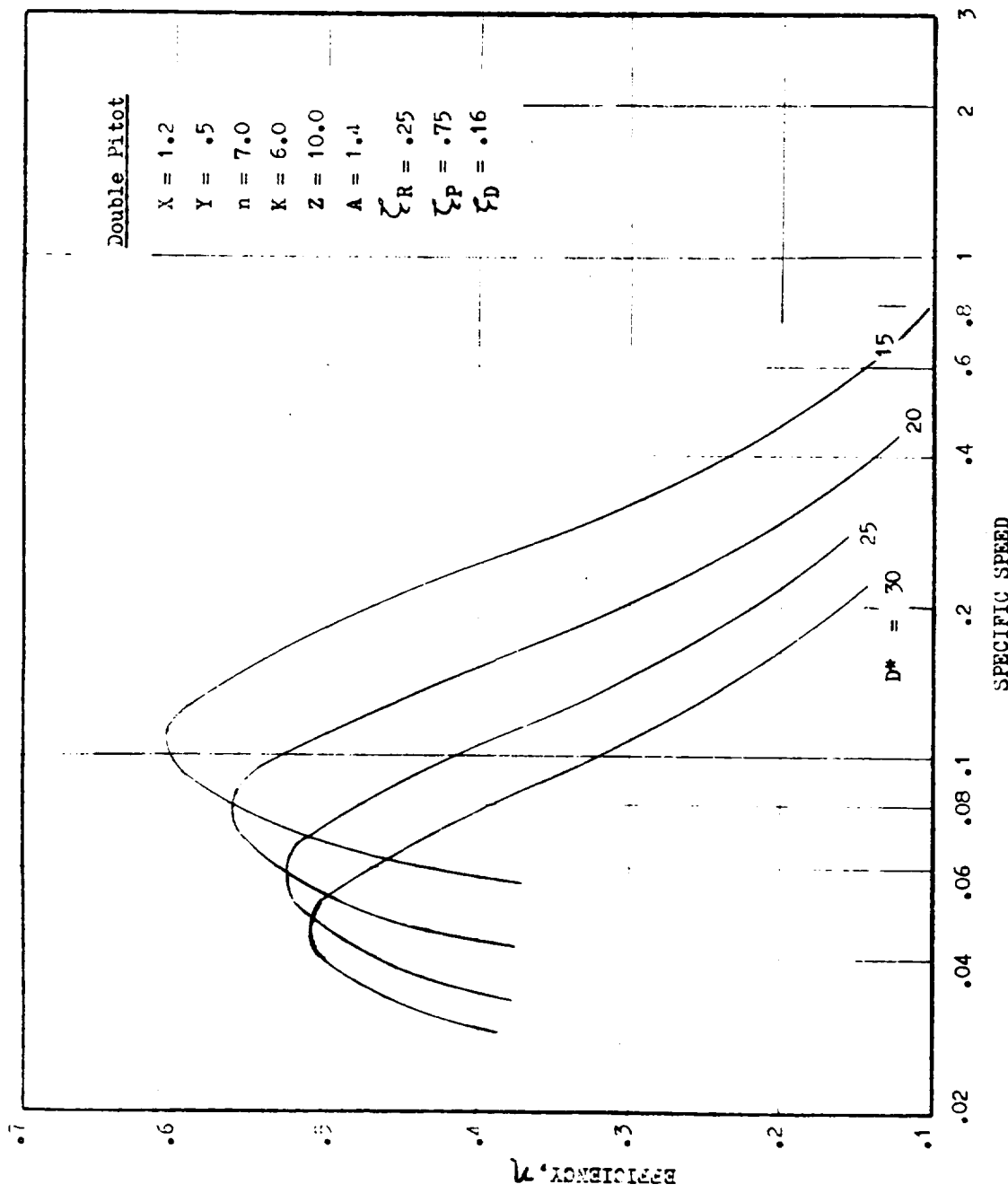


Figure 14. Efficiency vs Specific Speed for Pitot Pump With a Double Pitot

R-8494-1

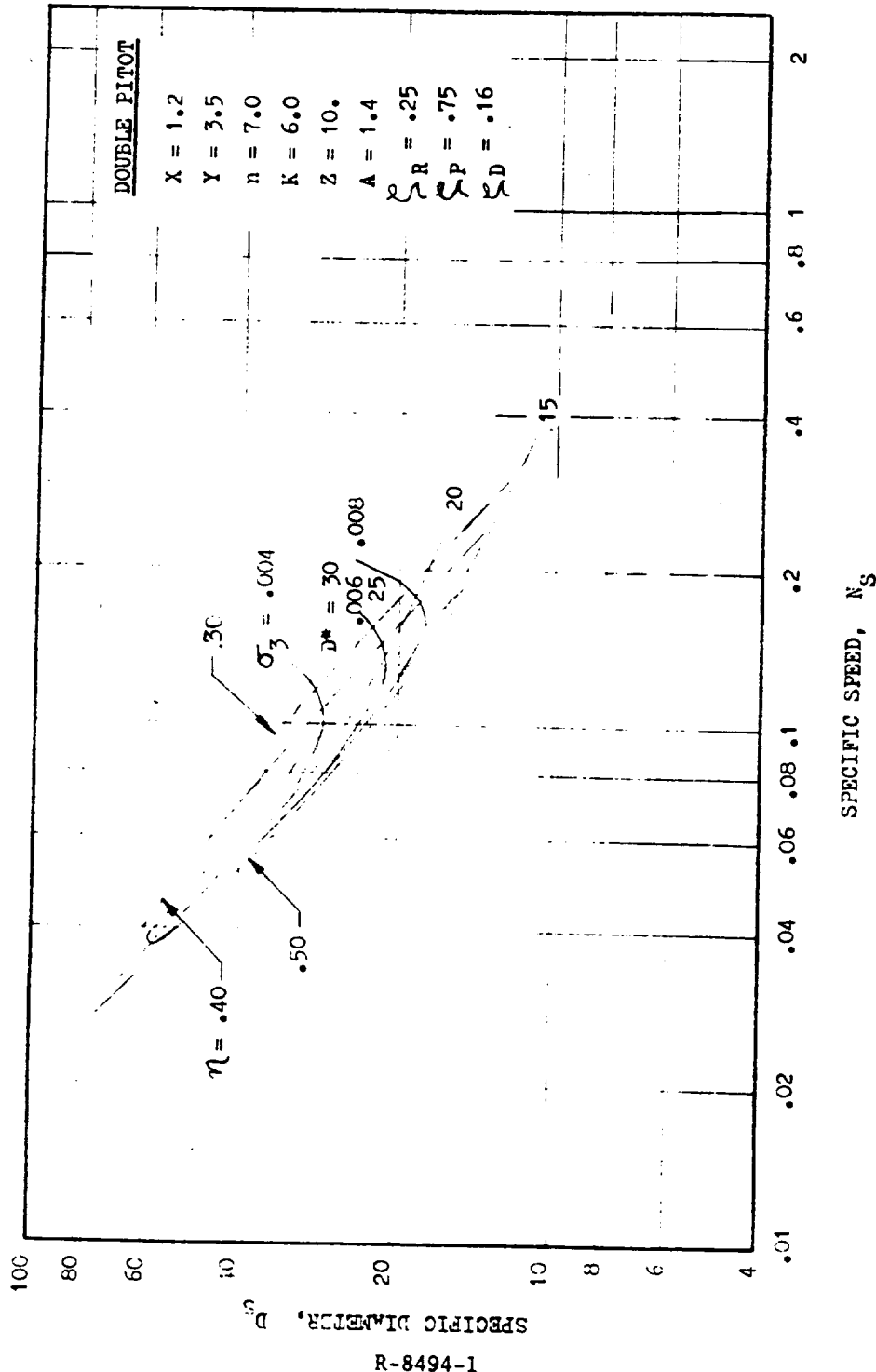


Figure 15. N_s - D_s Diagram for the Pitot Pump With a Double Pitot

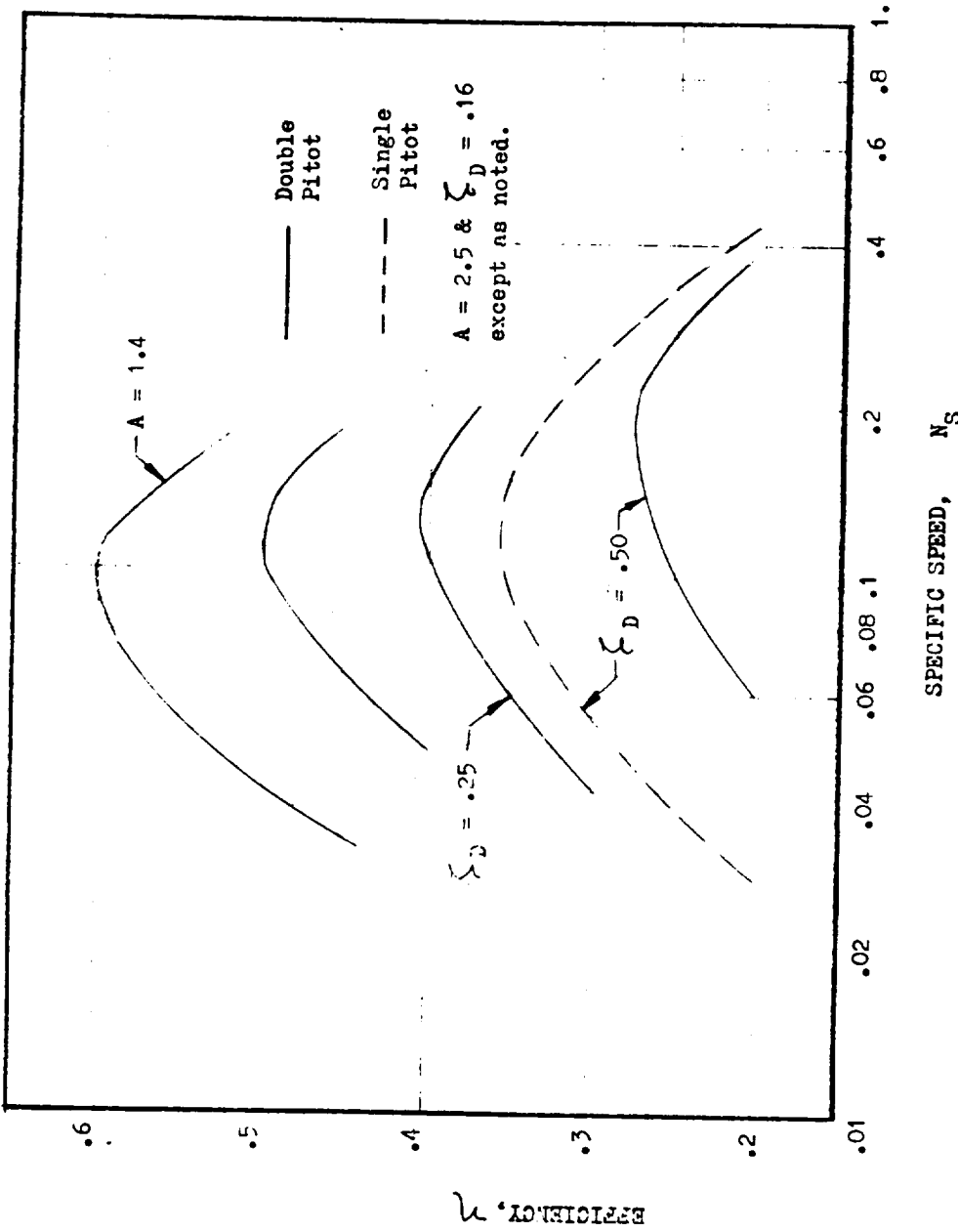


Figure 16. Efficiency vs Specific Speed - Comparison of the Single and Double Pitot Pumps

R-8494-1

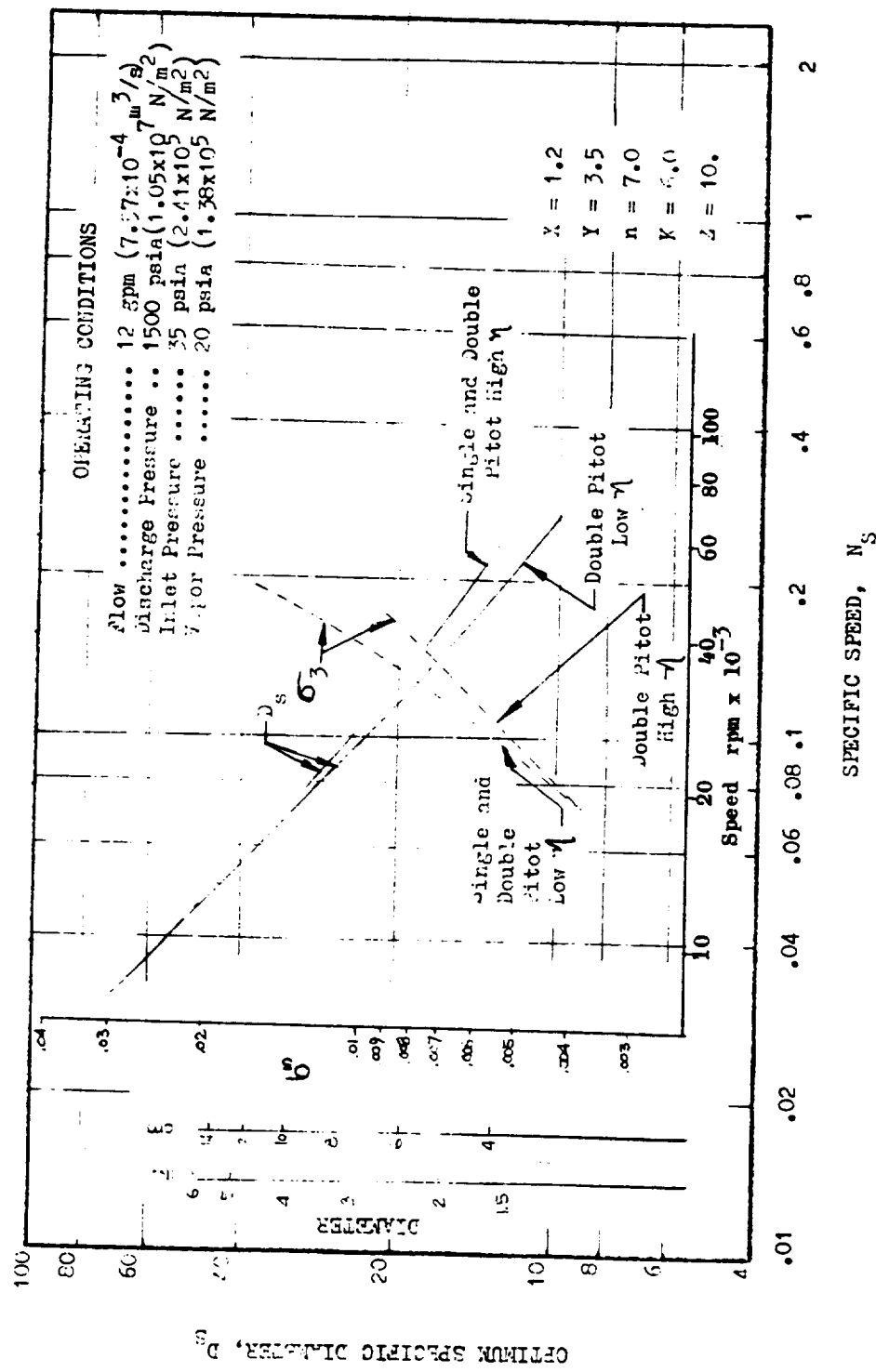


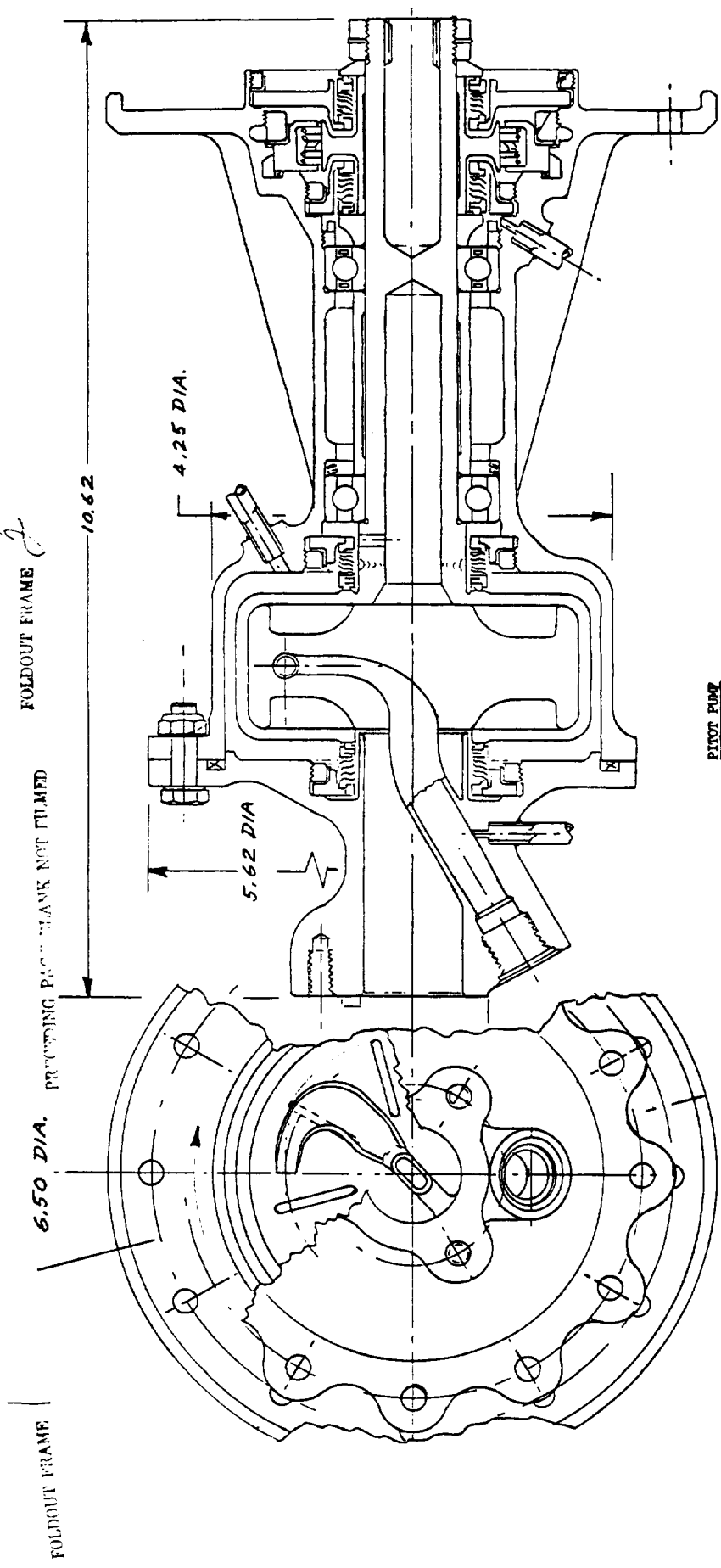
Figure 17. Optimum Specific Diameter vs Specific Speed for Single and Double Pitot Pumps

Design Considerations. The approximate dimensions and the approximate efficiency potential for the pump design requirements are found when it is considered that the specific speed is directly proportional to the rotative speed (while holding $Q^{1/2}/H^{3/4}$ constant), and that the specific diameter is proportional to the diameter of the pump. Thus, rotative speed scales and diameter scales can be superimposed on the specific speed and specific diameter scales of Fig. 17. Assuming that the maximum allowable value for the cavitation parameter is $\sigma = 0.01$, it results from Fig. 17 that the maximum allowable speed is 40,000 rpm and that for this condition a pitch line diameter of $D = 2$ inches (5.08 cm) will be required. The associated specific speed in $N_s = 0.155$. Thus, an efficiency potential of $\eta = 0.275$ is obtained for a double-headed Pitot pump and $\eta = 0.35$ for a single-headed Pitot pump if high drag coefficients ($\zeta_D = 0.5$) are encountered (Fig. 16). When a design configuration can be developed where the drag coefficient is reduced to $\zeta_D = 0.16$, a specific speed of $N_s = 0.116$ (i.e., rotative speed of 30,000 rpm and a pitch line diameter of 2.5 inches (6.4 cm) would be preferable because then an efficiency potential of 50 percent is calculated for double-headed pumps and even higher values ($\eta = 0.64$) when the amplification factor can be reduced. A sketch of a proposed pump configuration is presented in Fig. 18.

BARSKE PUMP

The Barske pump is a low specific speed pump having an open-face impeller and radial vanes. Its relatively high efficiency at low specific speed make this type of pump eligible for consideration in this study.

The primary variables investigated for selection of pump size were the speed and the flow coefficient. The pump speeds considered were $N = 25,000$, $50,000$, and $74,000$ rpm. Although a flow coefficient of 0.07 is a typical design value for inducers, values of 0.09 and 0.11 were also investigated. For the specified flow-rate and a given value of flow coefficient, the pump inlet diameter will vary so that the product of speed (N) and inlet diameter (D_1) remains a constant. The variation of inlet diameter with speed for three values of design flow coefficient is shown in Fig. 19. Equation 1 shows that because both design flow and head are fixed and, therefore, are constant for this analysis, the pump specific speed will vary linearly with speed, as shown in Fig. 20.



ROTATING SPEED, RPM	30,000	MINIMUM ROTOR-HOUSING AXIAL CLEARANCE, IN.	.195 (.495 cm)	NOT CRITICAL
ROTOR TIP DIAMETER, IN.	3.75 (9.53 cm)	MINIMUM ROTOR-HOUSING RADIAL CLEARANCE, IN.	1.00 (2.54 cm)	NOT CRITICAL
INLET DIAMETER, IN.	.195 (0.495 cm)	ESTIMATED EFFICIENCY, %	43.4	
SHAFT DIAMETER, IN.	1.00 (2.54 cm)	(NOT INCLUDING SEAL & BEARING LOSSES)		
REQUIRED NPSH, FT.	20 (6.1 m)	BEARING AXIAL LOAD, LB.	50 (222 N)	
SUCTION SPECIFIC SPEED	4.03	BEARING RADIAL LOAD, LB.	25 (111 N)	
ROTOR TIP SPEED, FPS	1,911 (150 m/s)	OVERALL EFFICIENCY, %	27.8	
BEARING IN, MM-RPM	750,000	GAS POWER REQUIRED, HP	117.1 (87.5 kW)	
SEAL RUBBING SPEED, FPS	195 (159.5 m/s)			
WEAR RING SPEED, FPS	--			
ESTIMATED DRY WEIGHT, LB.	16.5 (7.5 kg)			

Figure 18. Pilot Pump-Preliminary Design

R-8494-1
41

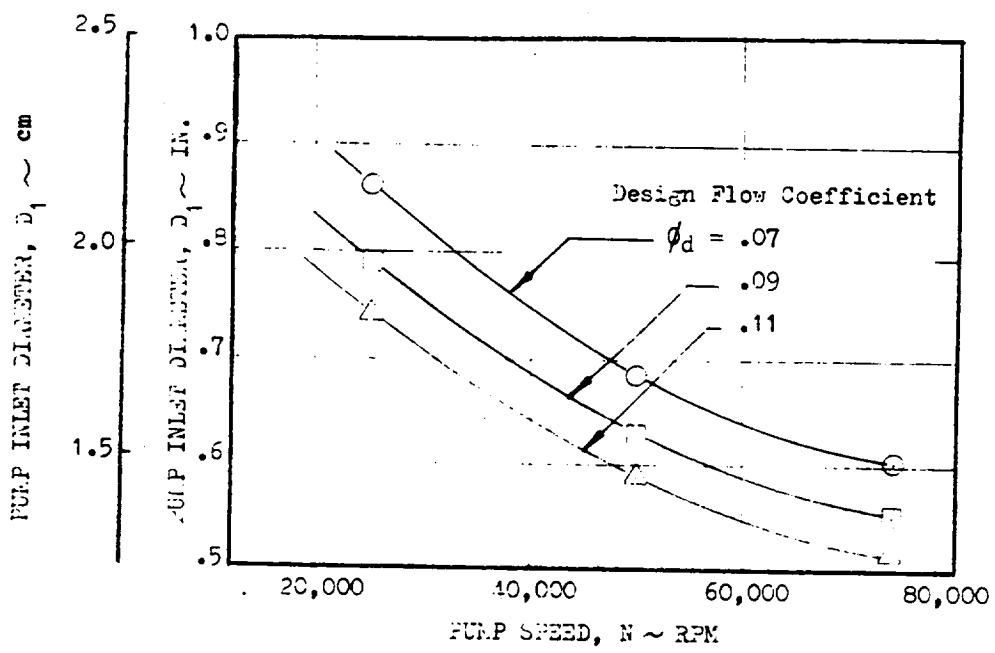


Figure 19. Pump Inlet Diameter as a Function of Pump Speed

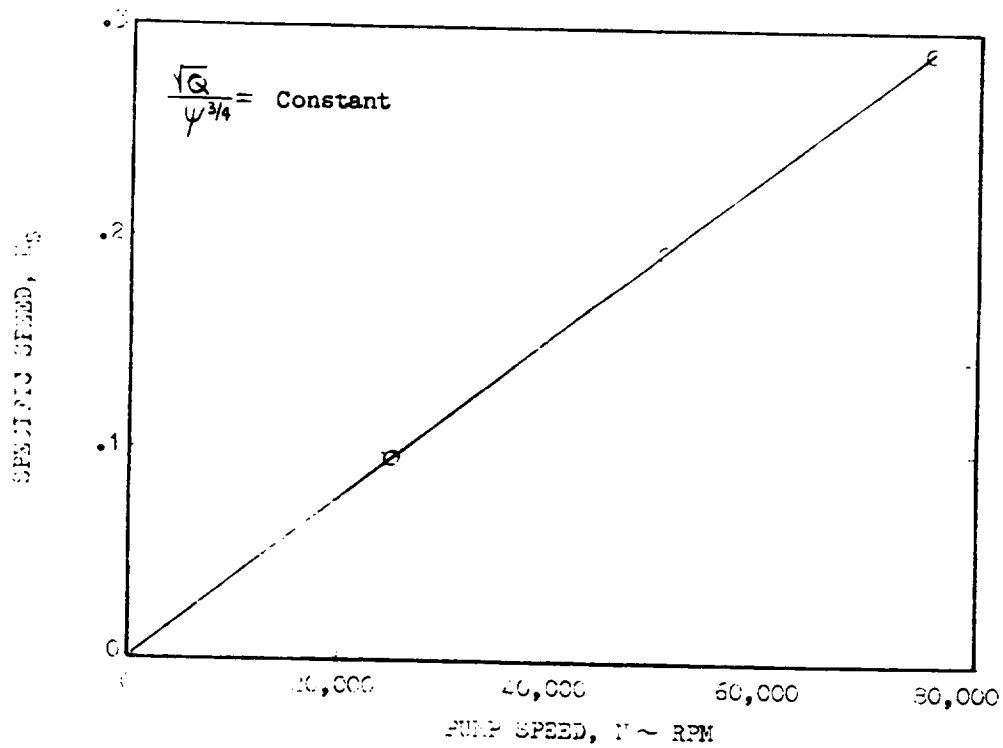


Figure 20. Pump Specific Speed as a Function of Pump Speed

R-8494-1

In the Barske pump with a small emission angle, the flow in the pump is very closely approximated by a forced vortex flow. Thus, the pump head can be determined by a relation of the form:

$$H = (U_2^2 - U_1^2)/2g + \zeta_R U_2^2/2g \quad (21)$$

The first term represents the increase in static pressure in a forced vortex. The second term represents the portion of the velocity head which can be recovered. The theoretical head of the pump is found assuming full recovery, i.e., $\zeta_R = 1.0$. The correct value of ζ_R will depend primarily on the losses encountered in entering and passing through the diffusion system downstream of the pump. Barske (Ref. 8) quotes values of ζ_R from 0.2 to 0.6, the higher values being obtainable only under favorable conditions of good surface finish, low liquid viscosity, and optimum diffuser design.

From Eq. 21 and the familiar relationships between pump diameter, speed, and blade velocity, an expression for the impeller discharge diameter can be derived:

$$H = \frac{(U_2^2 - U_1^2)}{2g} + \frac{\zeta_R U_2^2}{2g}$$

$$2gH = (U_2^2 - U_1^2) + \zeta_R U_2^2$$

$$U = \frac{\omega D}{2}$$

$$2gH = \frac{\omega^2 D_2^2}{4} - \frac{\omega^2 D_1^2}{4} + \zeta_R \frac{\omega^2 D_2^2}{4}$$

$$gH = D_2^2 \left(\frac{\omega^2}{2} + \zeta_R \frac{\omega^2}{R^2} \right) - \frac{\omega^2 D_1^2}{2}$$

$$gH = \frac{\omega^2}{2} D_2^2 (1 + \zeta_R) - \frac{\omega^2}{2} D_1^2$$

$$\frac{gH}{\frac{\omega^2}{2}} = D_2^2 (1 + \zeta_R) - D_1^2$$

$$\frac{2gH}{\omega^2} = D_2^2 (1 + \zeta_R) - D_1^2$$

$$D_2^2 (1 + \zeta_R) = \frac{2gH}{\omega^2} + D_1^2 \quad (22)$$

The dependence of the diameter D_2 on the flow coefficient ϕ , as occurs through the parameter D_1 , is actually small; and considering the lack of adequate information on the value of ζ_R , there is no need to investigate D_2 as a function of ϕ . Therefore, the values of D_1 corresponding to $\phi = 0.07$ are here used to study D_2 . The resulting values of D_2 are shown in Fig. 21 as a function of pump speed and and the pressure recovery coefficient, ζ_R .

The power output of the pump is given by

$$P = \dot{W}H \quad (23)$$

where \dot{W} is the weight flowrate. The theoretical power (P_{th}) is found by using the theoretical head in Eq. 23. The hydraulic efficiency can then be expressed as:

$$\eta = \frac{P}{P_{th} + P_L} \quad (24)$$

where P_L is the power loss due to fluid friction in the pump itself. This power loss consists primarily of disk friction losses and is given by Barske (Ref. 8) as:

$$P_L = 75(10^{-6}) \left[\frac{\gamma}{62.4} \right] v^{0.2} \left[\frac{N}{1000} \right]^{2.8} (D_2^{4.6} + 1.28 D_1^{4.6}) \quad (25)$$

where γ is the specific weight of the fluid and v is the kinematic viscosity. Using the properties of fluorine, the efficiency was determined for various values of pump speed and pressure recovery coefficient. The results are plotted in Fig. 22. It must be kept in mind that ζ_R is not a parameter which can be arbitrarily chosen, rather, it is determined by the design, particularly that of the diffusion system. With the high pump speeds and fluid velocities of the pump under consideration here, the value of ζ_R obtained can be expected to be no greater than 0.4.

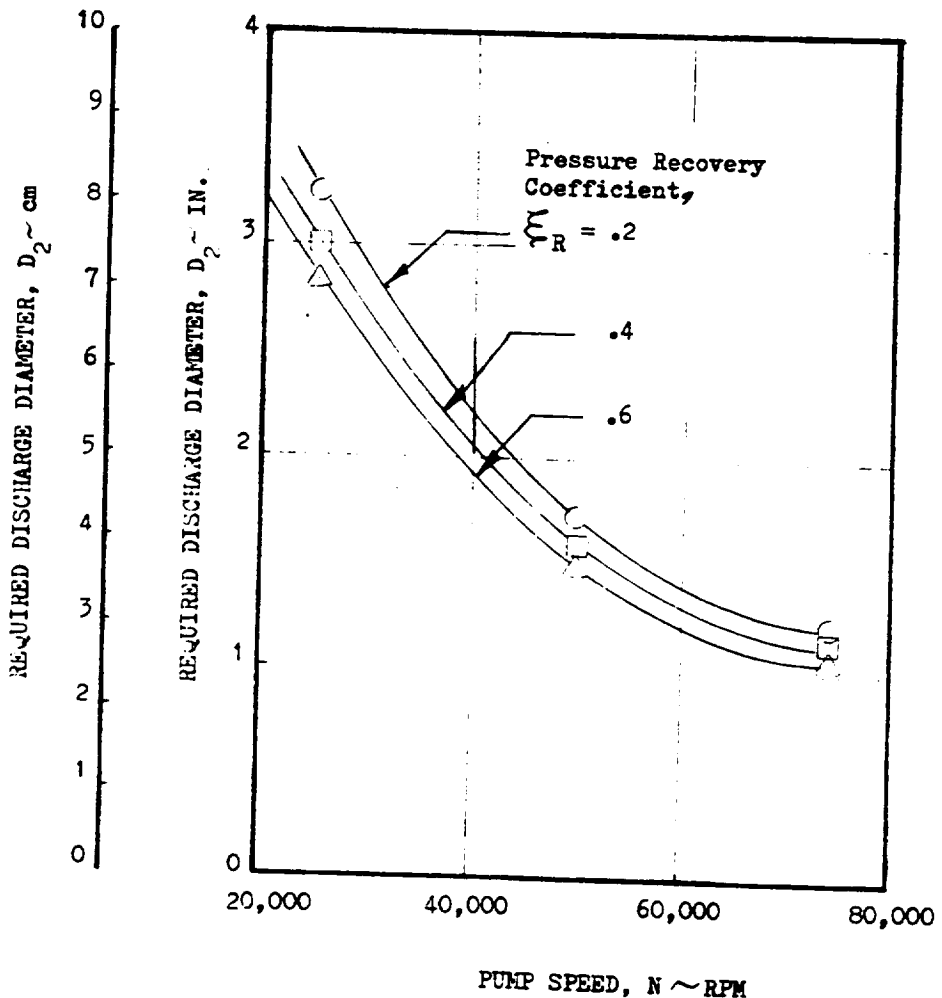


Figure 21. Pump Discharge Diameter as a Function of Pump Speed

R-8494-1

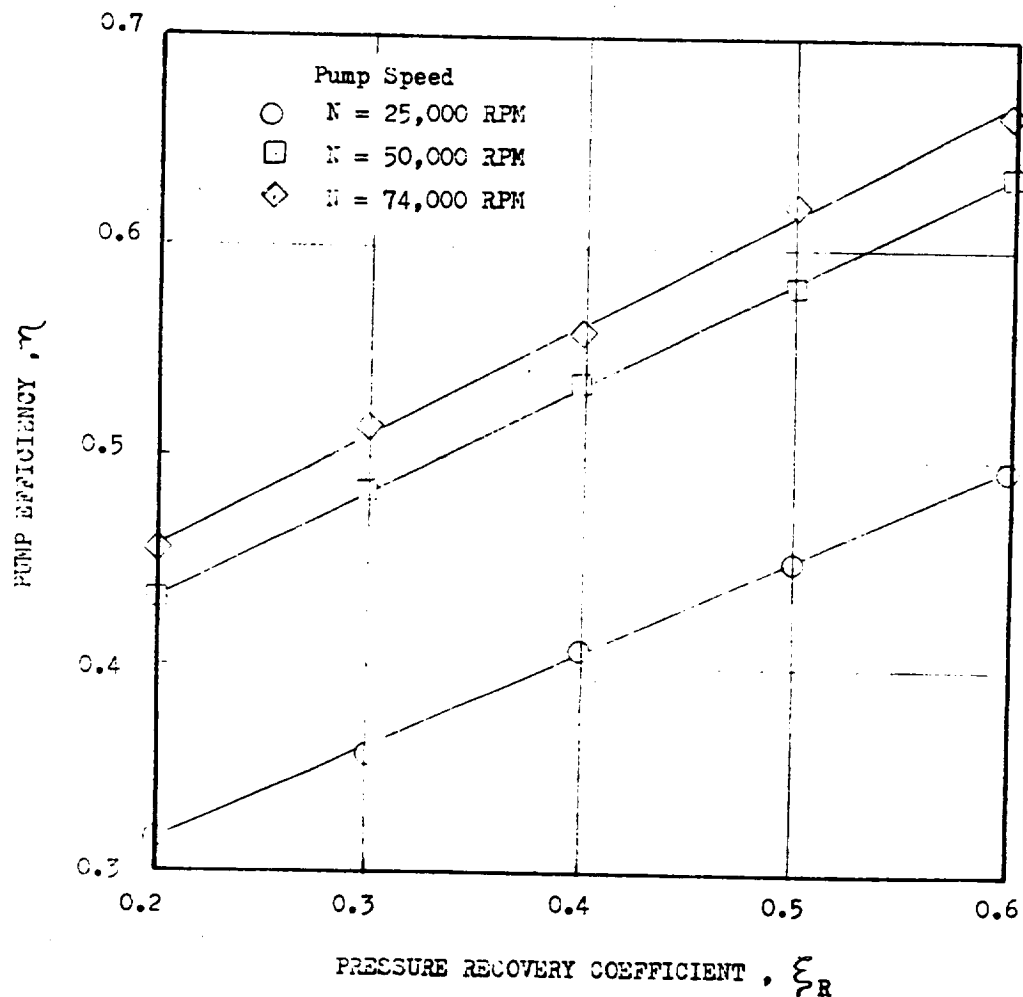


Figure 22. Pump Efficiency vs Pressure Recovery Coefficient

R-8494-1

The basic principle observed in designing the blade heights is to attempt to maintain a uniform velocity in the direction of through flow. Thus, if D_1 is the inlet diameter, then

$$D_1 b_1 r = (\pi/4) D_1^2 \quad (26)$$

where b_1 is the inlet blade height and r the assumed ratio of free area to total area due to boundary layers. A free-area ratio of 0.8 is a commonly used value for such calculations. For the discharge:

$$\pi b_2 D_2 \geq \pi b_1 D_1 \quad (27)$$

Therefore,

$$b_2 \geq b_1 \frac{D_1}{D_2} \quad (28)$$

Since the efficiency of the pump is strongly affected by the losses in the discharge diffuser system, it is desirable to design this part of the pump to minimize these losses. The most desirable diffuser would be a cone with an 8.0-degree (0.140 rad) included angle (Ref. 9). The diffuser inlet area should be sufficient to handle the required flowrate at a velocity of approximately U_2 , the impeller tip speed. The length of the diffuser is chosen to give the desired velocity at the diffuser discharge but must not be excessive in length to avoid boundary layer buildup.

One question which has not been adequately answered and which appears to be beyond the present capabilities is the effect on the efficiency of the emission angle of the pump, i.e., the arc over which the fluid is allowed to be diffused, before it is discharged. Barske's basic design (Ref. 8) had the diffuser inlet tapped directly off the toroidal scroll with no volute section to collect the flow before its entrance into the diffuser. Rocketdyne felt that a volute section was required to help minimize the losses. To calculate the percent of emission of the circumferential perimeter to be used for the volute, the desired throughflow velocity (C_m) at the impeller discharge was chosen and substituted into the following equation:

$$\frac{Q}{C_m} = \pi D_2 b_1 S \quad (29)$$

R-8494-1

Using the basic design principles discussed above, the operating parameters shown in Table II were selected for the Barske pump. A sketch of the pump configuration is shown in Fig. 23.

TABLE II. BARSKE PUMP DIMENSIONS

Pump Speed	N = 50,000 rpm
Inlet Diameter	$D_1 = 0.686$ in. (1.741 cm)
Discharge Diameter	$D_2 = 1.64$ in. (4.17 cm)
Shaft Diameter	$D_s = 0.375$ in. (0.952 cm)
Inlet Blade Height	$b_1 = 0.218$ in. (0.554 cm)
Discharge Blade Height	$b_2 = 0.102$ in. (0.259 cm)
Diffuser Inlet Diameter	= 0.1175 in. (0.2980 cm)
Diffuser Length	= 0.75 in. (1.90 cm)
Diffuser Discharge Diameter	= 0.234 in. (0.594 cm)

FOLDOUT FRAME / PRECEDING PAGE BLANK NOT FILMED
BARRETT PUMP

ROTATING SPEED, RPM
ROTOR TIP DIAMETER, IN.
INLET DIAMETER, IN.
SHAFT DIAMETER, IN.
REQUIRED NPSH, FT.
SUCTION SPECIFIC SPEED
ROTOR TIP SPEED, FPS
BEARING DN, MM-PFM
SEAL RUBBING SPEED, FPS
WEAR RING SPEED, FPS
MINIMUM ROTOR-HOUSING
AXIAL CLEARANCE, IN.
MINIMUM ROTOR-HOUSING
RADIAL CLEARANCE, IN.
ESTIMATED EFFICIENCY, %
(NOT INCLUDING SEAL AND
BEARING LOSSES)
BEARING AXIAL LOAD, LB_F
BEARING RADIAL LOAD, LB_F
OVERALL EFFICIENCY, %
GAS POWER REQUIRED, HP
ESTIMATED DRY WEIGHT, LB

50,000
1.63 (4.14 cm)
.686 (1.742 cm)
.375 (0.953 cm)
20 (6.1 m)
6.70
356 (108 m/s)
500,000
82 (25 m/s)
**
.011 (0.28 mm)
.020 (0.508 mm)
48

50 (222 N)
25 (111 N)
45.5
71.4 (53.3 KW)
4.8 (2.19 KG)

FOLDOUT FRAME 2

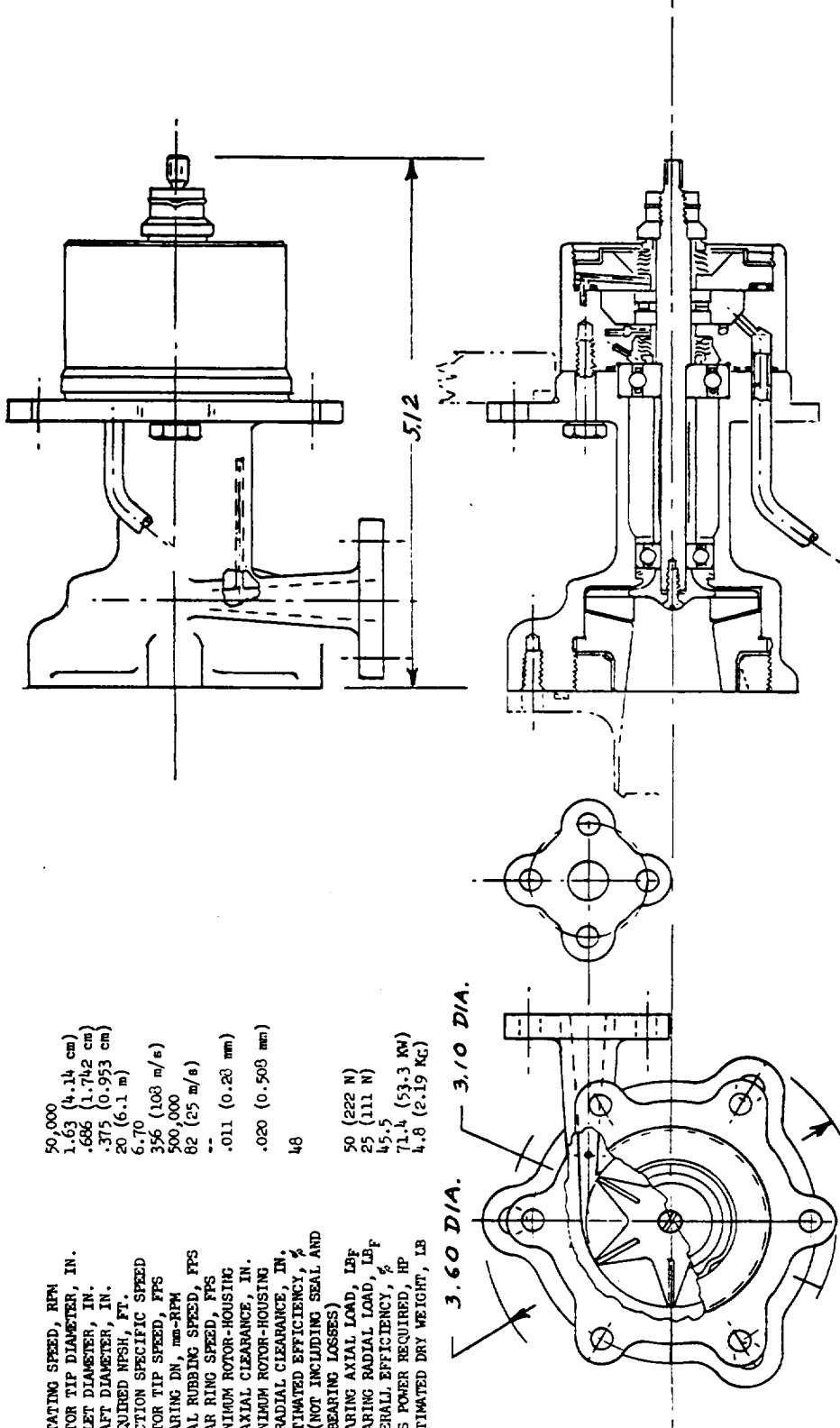


Figure 23. Barrett Pump-Preliminary Design

TESLA PUMP

The Tesla pump, an unconventional low specific speed pumping device, is similar to the centrifugal pump with the exception of the rotor configuration. The Tesla pump rotor consists of many closely spaced disks as shown schematically in Fig. 24. The flow enters axially, flows through the narrow spaces between rotor disks, and discharges radially into a collector with a low radial flow component.

The pumping action in a Tesla pump is due to shear forces that produce peripheral flow velocities which approach that of the disk velocity at the rotor tip. As a consequence, the highest obtainable head coefficient is unity (Ref. 10).

$$\varphi = \frac{gH}{U_{tip}^2} \quad (30)$$

The Tesla pump operates at maximum efficiency in a specific speed regime of 7.75×10^{-5} to 9.31×10^{-2} . This relatively low specific speed is realized from the fact that the rotor flow channels are extremely narrow and that the radial flow component in the rotor channel is low.

The range of specific diameter corresponding to the maximum efficiency operation is 24 to 24,000. The N_s - D_s relation for maximum efficiency is shown graphically in Fig. 25.

The N_s - D_s diagram reveals a pertinent characteristic of the Tesla pump. This characteristic is that for high pressure ratios or high head requirements at low rotational speeds, an extremely large rotor diameter is required for maximum efficiency.

Figure 26, in conjunction with Fig. 27, presents the efficiency characteristics as a function of geometry, flow range, and rotational speed requirements. Theoretically, the rotor efficiency may be as high as 50 to 70 percent at any specific speed, limited only by the parameter β as defined on the figures.

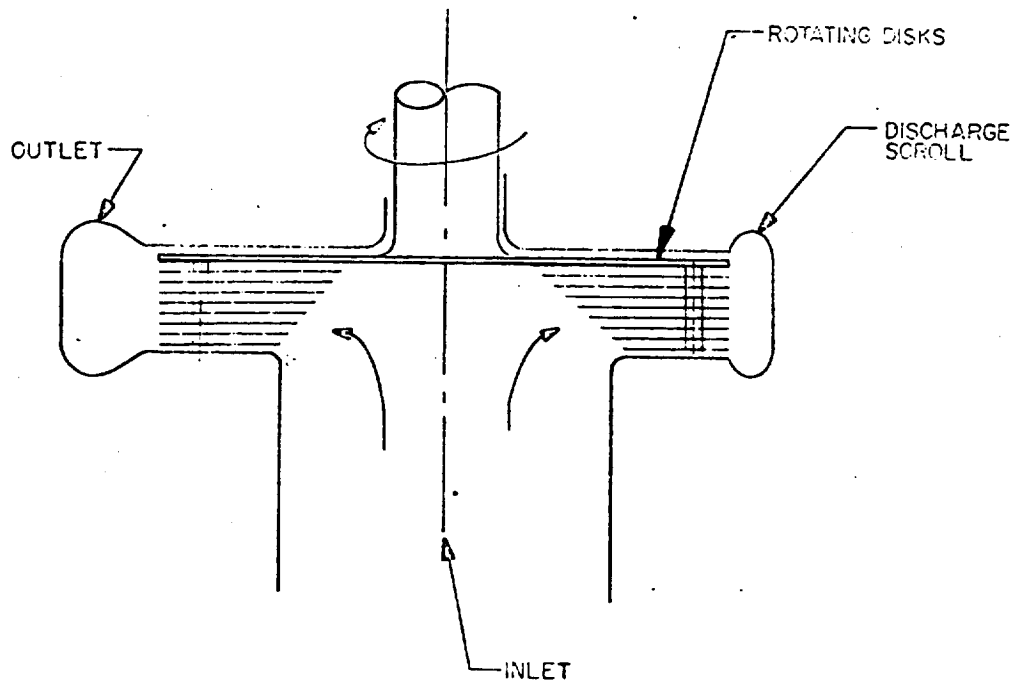


Figure 24. Schematic of Tesla Pump

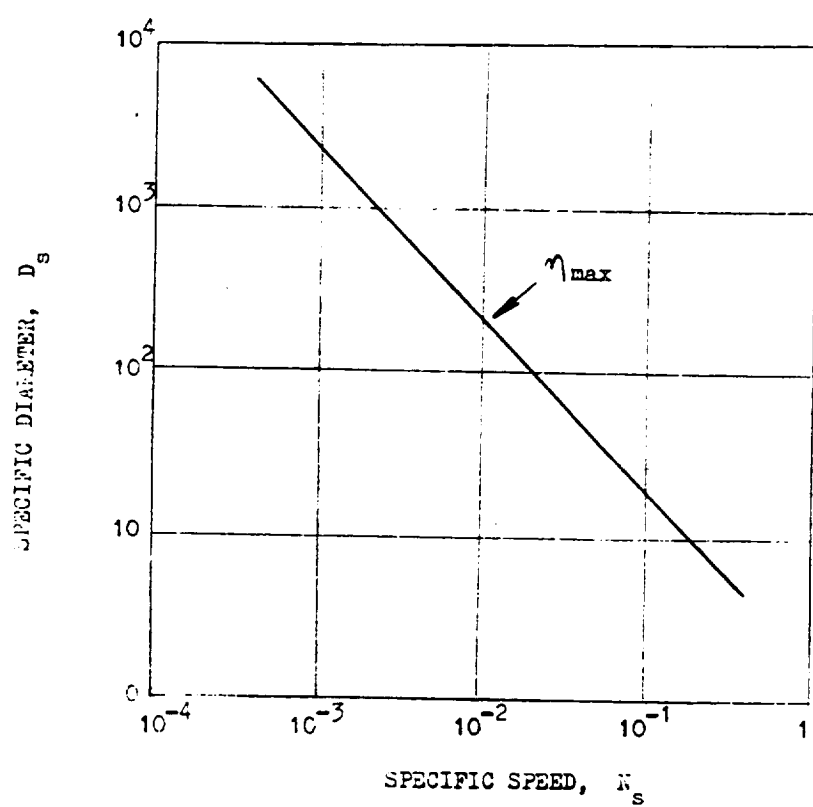


Figure 25. Specific Diameter of the Tesla Pump

R-8494-1

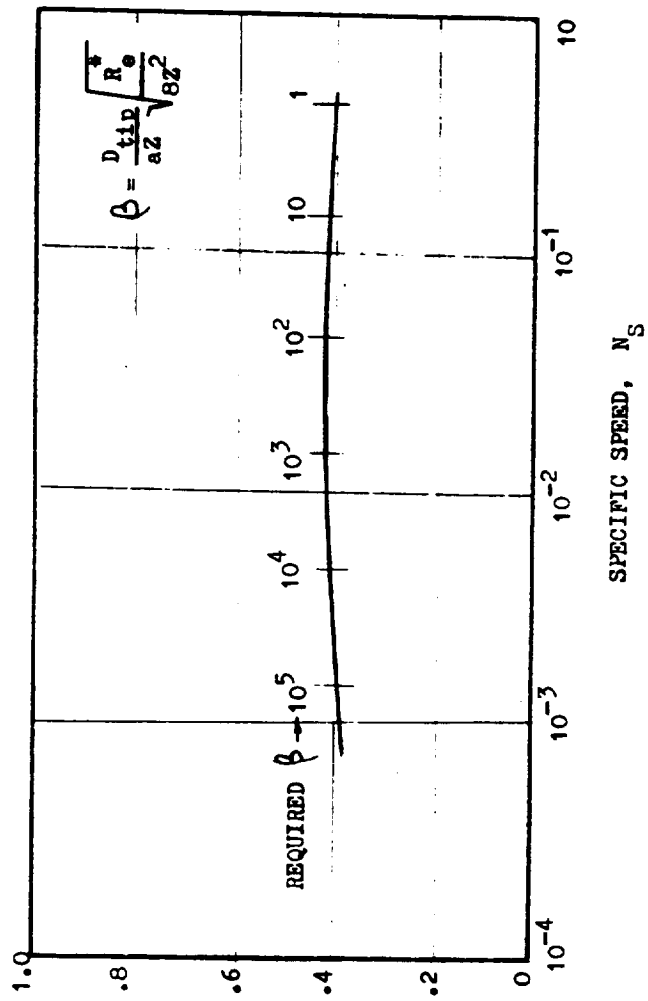
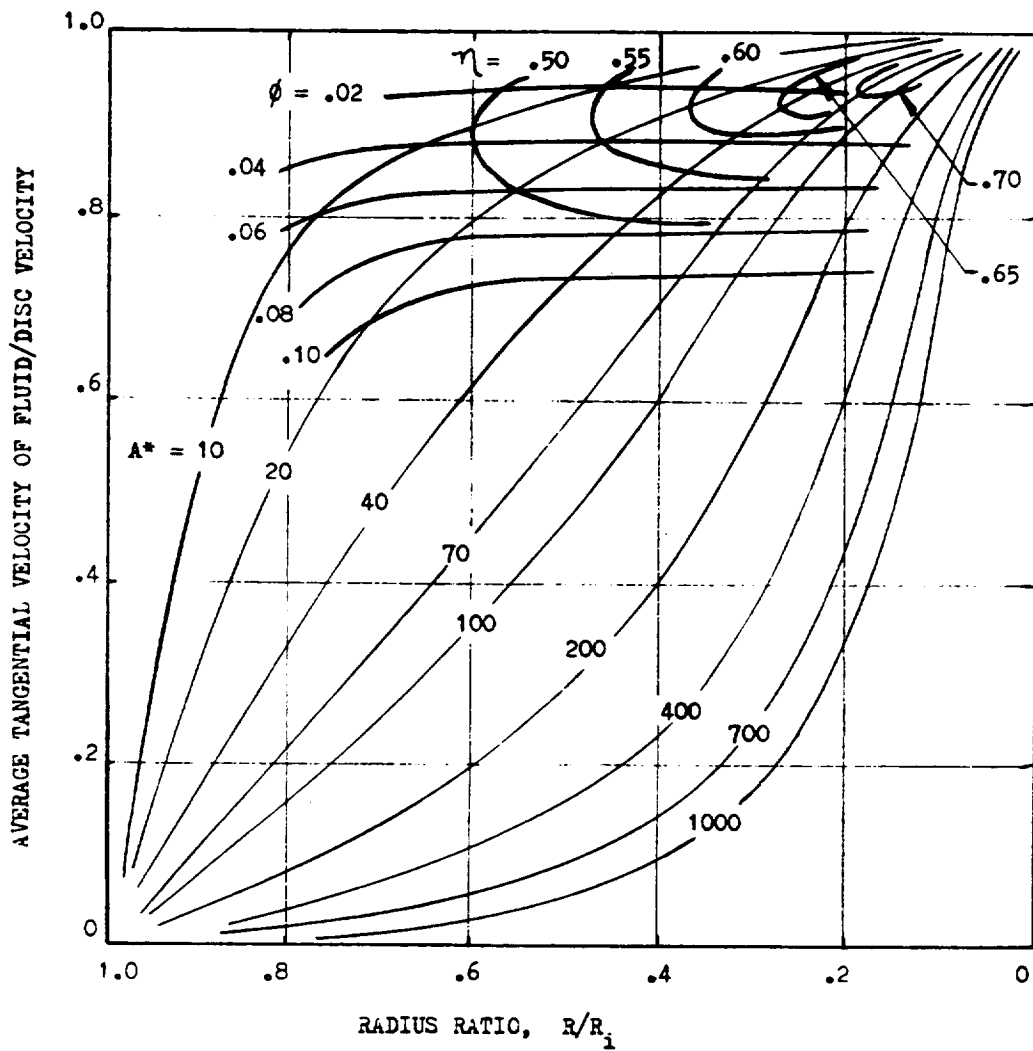


Figure 26. Performance Potential of Tesla Pumps as a Function of Specific Speed

MAXIMUM PUMP EFFICIENCY, η_{max}

R-8494-1



η = ROTOR EFFICIENCY

$$A^* = 8\pi\phi(R/R_i)^2 P_T^2$$

$$\beta = (D/aZ)\sqrt{R_e^*/8Z^2}$$

$$P_T = (a/2)\sqrt{\omega/\beta}$$

$$R_e^* = UD/v$$

Figure 27. Calculated Efficiency of the Tesla Pump as a Function of Radius Ratio and Flow Factor (According to Ref. 10)

Due to the unconventional design concept and limited literature available, an analytical effort was performed to determine the effects of viscosity, Reynolds number, rotational speed, blade number, etc., on the efficiency and operating characteristics of the Tesla pump.

A critical dimension for this type of pump is the spacing of the rotor blades. The blade spacing parameter, a , is derived in Ref. 11 and 12 and can be expressed as:

$$a \sqrt{\frac{\omega}{v}} = K \quad (31)$$

where $K = 4$ for laminar flow. It can be seen that blade spacing is only a function of viscosity and rotational speed. The optimum blade spacing for a laminar flow regime then becomes:

$$a = 4 \sqrt{\frac{v}{\omega}} \quad (32)$$

This equation suggests that the Reynolds number becomes a significant criterion for pump performance, since $\sqrt{\frac{v}{\omega}}$ is proportional to the Reynolds number. Laminar flow requires a low local Reynolds number within the rotor passages. The local Reynolds number may be expressed as:

$$Re_{local} = \frac{[U(r)_{disk} - \bar{C}_u(r)]2a}{v} \quad (33)$$

where:

$U(r)_{disk}$ = local tangential velocity of the disk at any given radius
 $\bar{C}_u(r)$ = average tangential velocity in the gap as defined by:

$$\bar{C}_u(r) = \frac{1}{a} \int_0^a C_u(r, n) dn \quad (33a)$$

Then, for low Reynolds number, high viscosity and low blade spacing is required. These effects are presented in Fig. 28.

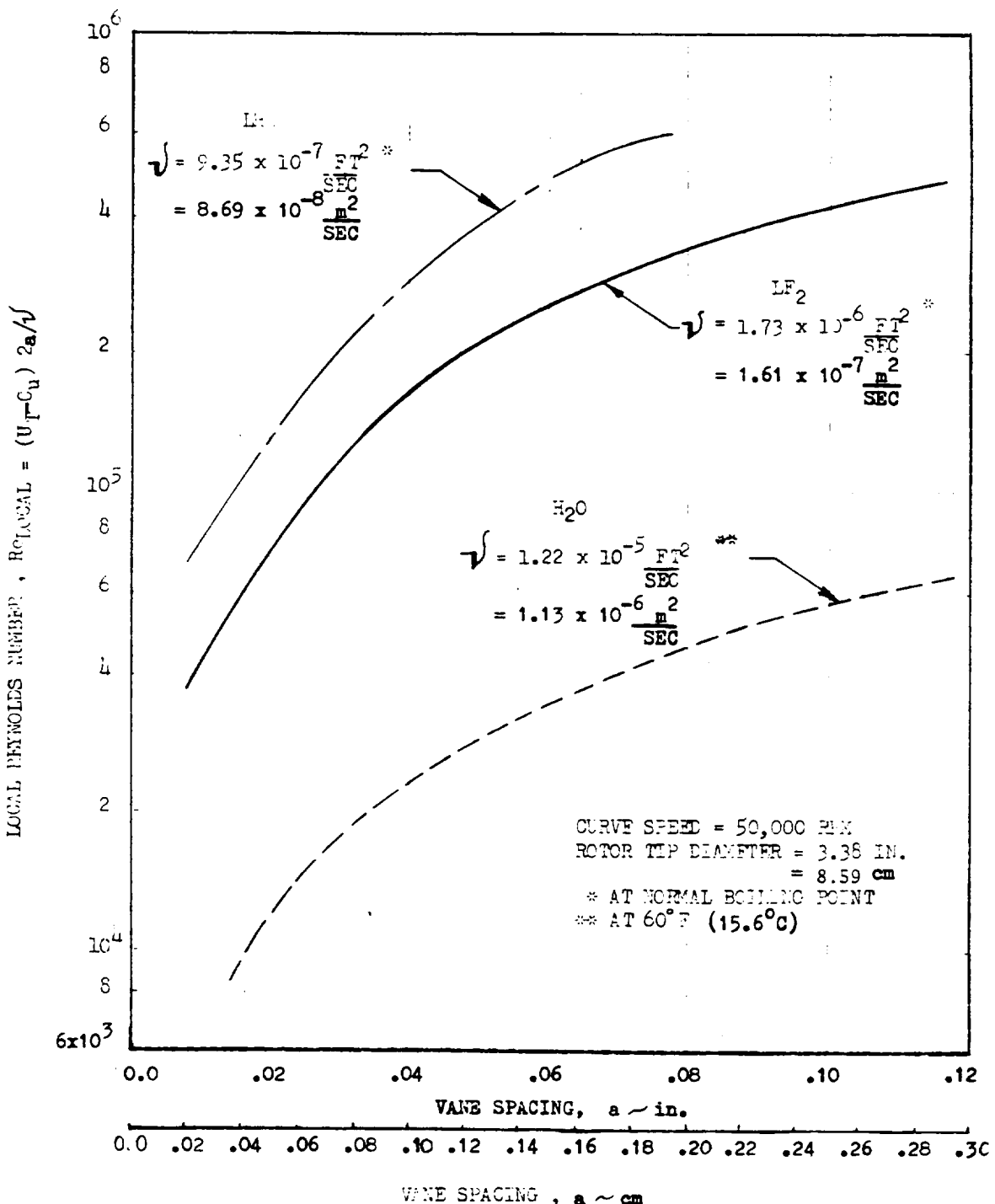


Figure 28. Local Reynolds Number as a Function of Vane Spacing and Fluid Viscosity

R-8494-1

Optimum blade number for the Tesla pump must be considered. Reference 10 indicates that specific speed and specific diameter are related to the blade number as follows:

$$N_s = \frac{K_1 \phi^{1/2} m^{3/4}}{\left[\left(\frac{D_{tip}}{az} \right) \left(\frac{R_e^*}{8Z^2} \right)^{1/2} \right]^{1/2}} \quad (34)$$

and

$$D_s = \frac{K_2 \left[\frac{D_{tip}}{2Z} \left(\frac{R_e^*}{8Z^2} \right)^{1/2} \right]}{\phi^{1/2} m^{1/4}} \quad (35)$$

where ϕ = discharge flow coefficient.

$$m = \frac{U_{tip}}{(C_u)_{fluid}} \quad (36)$$

D_{tip} = rotor tip diameter

Re^* = peripheral Reynolds number, $\frac{U_{tip} D_{tip}}{\nu}$

K_1, K_2 = constants

These equations can be solved for Z :

$$z = \frac{K_3 N_s D_{tip} R_e^{*1/4}}{m^{3/4} \phi^{1/2} a^{1/2}} \quad (37)$$

Figure 29 indicates the effect of vane spacing (a), and viscosity (ν), on vane number (Z).

Reasonable rotor axial length necessitates a reasonable number of blades, since the spacing, a , and blade thickness are set by fabrication capabilities. Axial length must not be excessive because of bearing overhang, maintenance of axial clearances, and structural limitations.

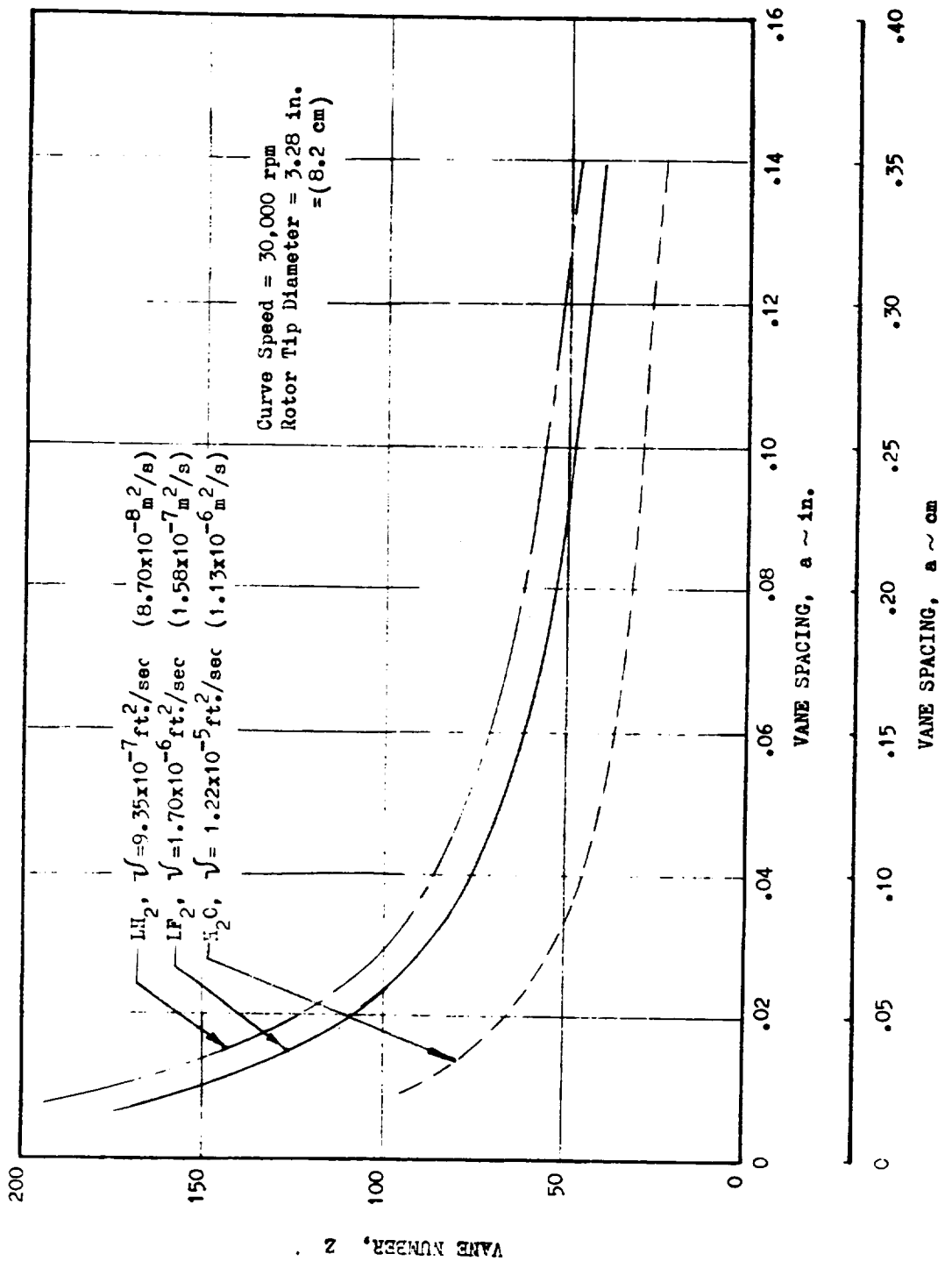


Figure 29. Vane Number as a Function of Spacing and Viscosity

2.

R-8494-1

Equation 51 may be simplified by substitution:

$$N_s = \frac{NQ^{1/2}}{H^{3/4}}$$

$$R_e^{1/4} = \left[\frac{U_{tip} D_{tip}}{\nu} \right]^{1/4} = \left[\frac{ND_{tip}^2}{229\nu} \right]^{1/4} = K' \frac{N^{1/4} D_{tip}^{1/2}}{\nu^{1/4}}$$

$$\phi^{1/2} = \left[\frac{Q}{AU_{tip}} \right]^{1/2} = \left[\frac{(Q)(229)(144)}{(Z\pi D_{tip}^a)(ND_{tip})(448)} \right]^{1/2} = K'' \frac{Q^{1/2}}{z^{1/2} D_{tip}^{a/2} N^{1/2}}$$

$$z = \frac{K''' N Q^{1/2} D_{tip}^{1/2} N^{1/4} D_{tip}^{1/2} z^{1/2} D_{tip} a^{1/2} N^{1/2}}{H^{3/4} \nu^{1/4} m^{3/4} Q^{1/2} a^{1/2}}$$

$$z = \frac{K'''' N^{7/4} D_{tip}^2}{H^{3/4} \nu^{1/4} m^{3/4}}$$

$$z = \frac{K_4 N^{7/2} D_{tip}^4}{H^{3/2} \nu^{1/2} m^{3/2}} \quad (38)$$

where K_3 , K' , K'' , K''' and K_4 are all constants, which implies that small blade numbers derive from low rotational speeds, small tip diameters, high heads, and high viscosity fluids. However, the $N_s - D_s$ relation has limited low speeds to extremely large rotor diameters. For the application being considered, liquid fluorine is specified as the pump fluid, which because of its low viscosity, forces the blade number to be excessive. It appears that the Tesla pump is more applicable to pumping more viscous fluids, at very low speeds and large tip diameters.

Figure 30 compares the calculated performance of the Tesla to that of the conventional centrifugal pump. The ψ and η vs ϕ curve indicates that the Tesla pump has efficiencies that approach centrifugal pump efficiencies at very low flow coefficients. At flow coefficients normally encountered the Tesla is much less efficient than centrifugal pumps (Ref. 13).

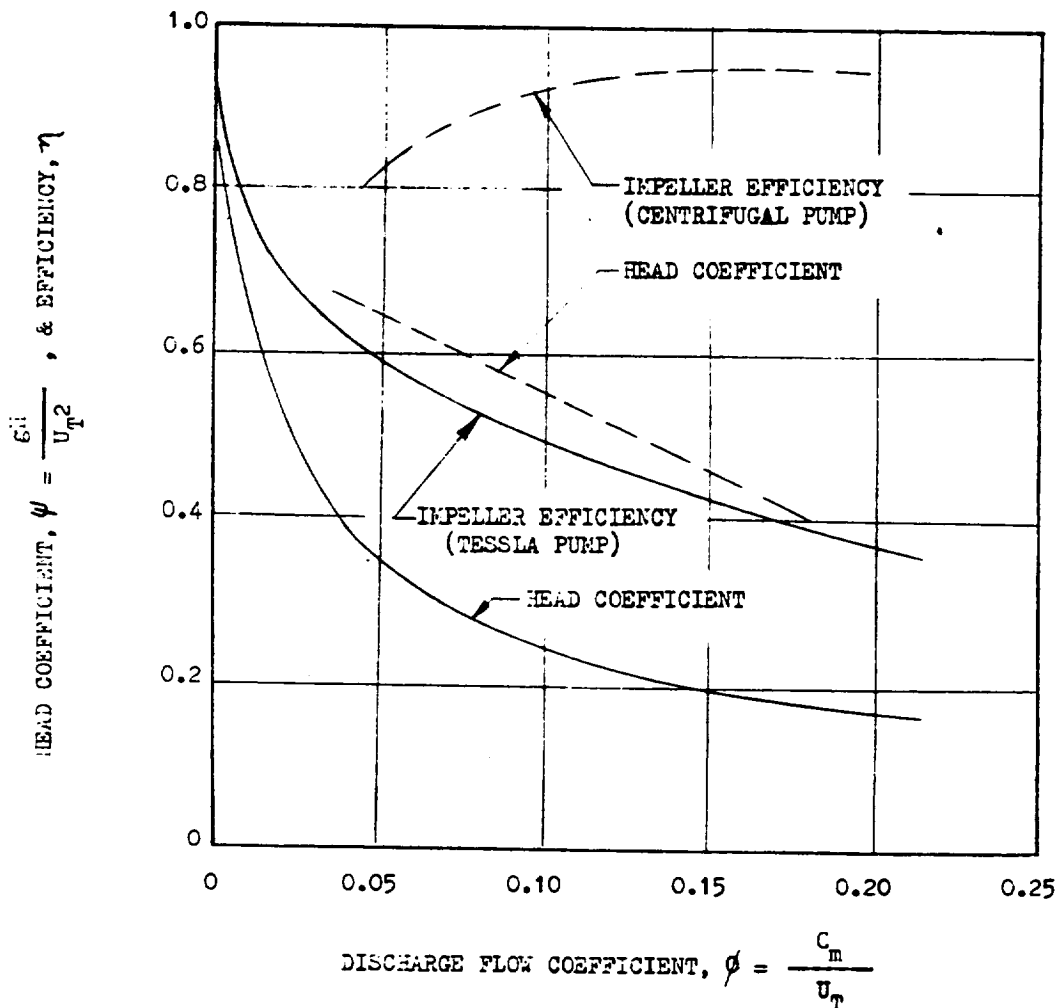


Figure 30. Calculated Performance of the Tesla Pump With Rough Disks
(5X Roughness of a Smooth Disk)

R-8494-1

Preliminary Design

After the analytical effort was made to determine the Tesla pump performance characteristics, a preliminary design was conceived. A sketch of this design is found on Fig. 31.

Design information and test data on the Tesla pump performance are very limited and, as a result, theory was heavily relied on to produce the preliminary design. A reasonable operating point (ψ and ϕ) was chosen after giving consideration to Fig. 30. Radius ratio and ψ_{ad} were obtained from Fig. 27, and rotational speed chosen. Blade spacing and thickness are set by fabrication capabilities and are about 0.020 inch (0.508 mm) and 0.040 inch (1.016 mm), respectively, which allowed a choice of the required blade number. High speeds (60,000 to 100,000 rpm) resulted in very small rotor diameters but an excessive axial length. A speed of 30,000 rpm was chosen which resulted in a more reasonable rotor diameter and axial length.

The tapered inlet passage was designed to give a constant axial velocity just prior to entering each blade passage. Axial and radial loads were calculated and found to be small and no problem could be foreseen in thrust balance and bearing loads. Due to the relatively long axial length, the collector design presented a problem but a scroll collector with a single discharge seemed feasible. The diffusion efficiency will be adversely effected by the required length of the collector and conical diffuser.

Problems and Possible Solutions

Study of the present technology, design parameters, characteristics, and unusual configuration has revealed several problem areas. These areas include performance limitations, present fabrication capabilities, structural limitations, and seal and bearing development.

The N_s - D_s diagram indicates a large rotor diameter is required for low speeds at maximum efficiency in order to generate high pressure differentials. This, however, forces the axial length to be excessive, as can be seen in Eq. 38. The

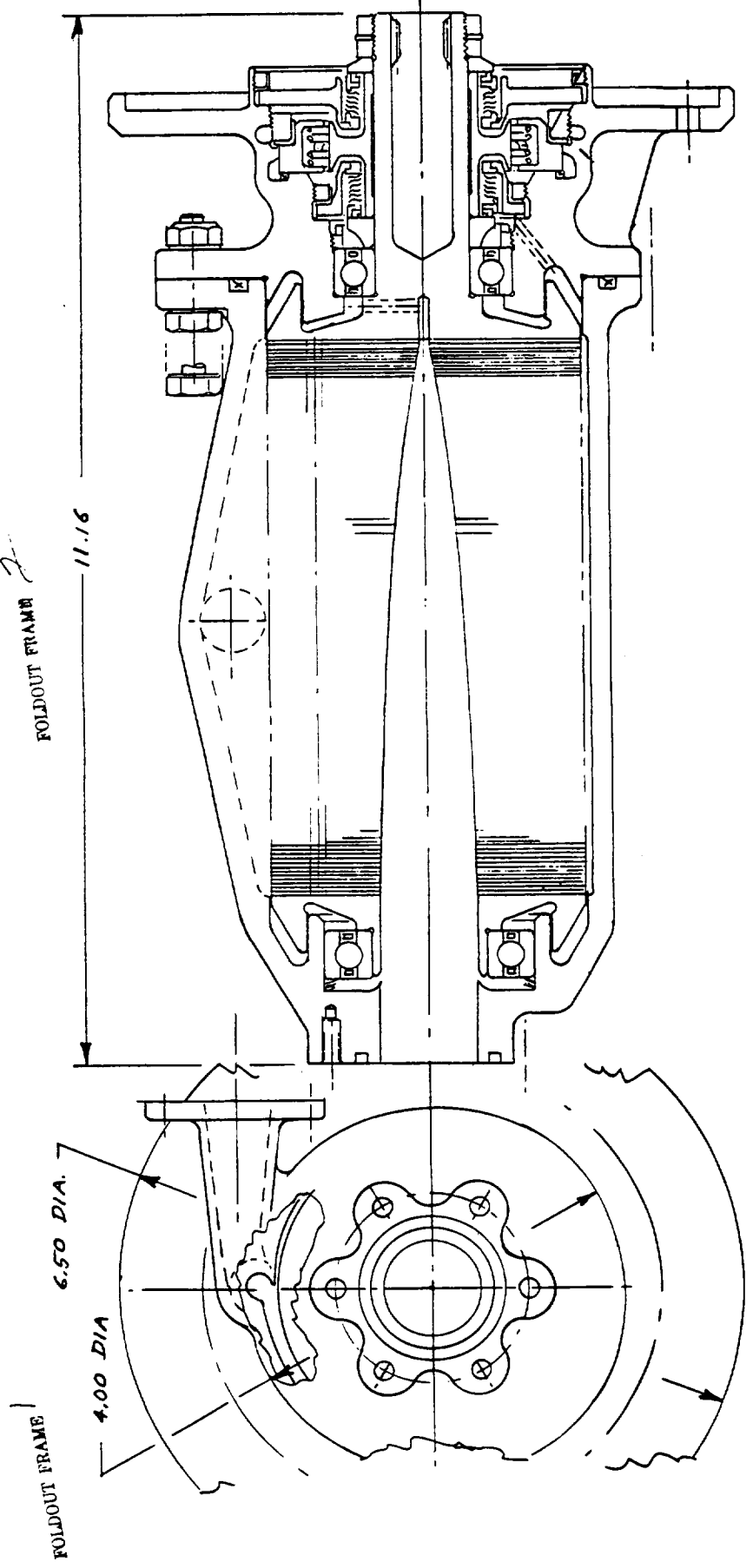


Figure 31. Tesla Pump-Preliminary Design

R-8494-1
62

blade number required increases with the fourth power of blade diameter. The low viscosity of LF_2 further increases the axial length. As a result, the Tesla pump is characterized by its long rotor required for this application. The Tesla pump therefore, is more applicable to pumping very viscous fluids at low speeds.

The Tesla pump is capable of high rotor efficiencies but at extremely low flow coefficients. At flow coefficients expected for this application, the Tesla pump does not offer outstanding efficiencies or head coefficients. Suction performance is good and there is no apparent cavitation problem in the Tesla pump.

The blades of the rotor must be spaced very closely to obtain satisfactory performance when pumping low viscosity LF_2 . Fabrication capabilities limit this spacing to 0.020 inch (0.508 mm) which is not sufficient to decrease the axial length to any degree.

The rather long axial length over which the flow leaving the blades must be collected imposes collector design problems, among which are diffusion and momentum losses. A scroll collector with a single discharge appears to be a feasible solution to some of these problems as shown in Fig. 31.

Information concerning the design, performance, and test data is extremely limited, and additional development effort would definitely be required.

DRAG PUMP

The drag pump, a low specific speed pumping device, is of the regenerative type and derives its name from the pumping action. The drag pump rotor consists of a disk with many short radial blades as shown schematically in Fig. 32. The flow enters radially and is carried within the blade passages around the disk and discharged radially through a port.

There are two conflicting theories of drag pump principle. One theory is that the pumping of the fluid is due to purely centrifugal action. The other concerns a

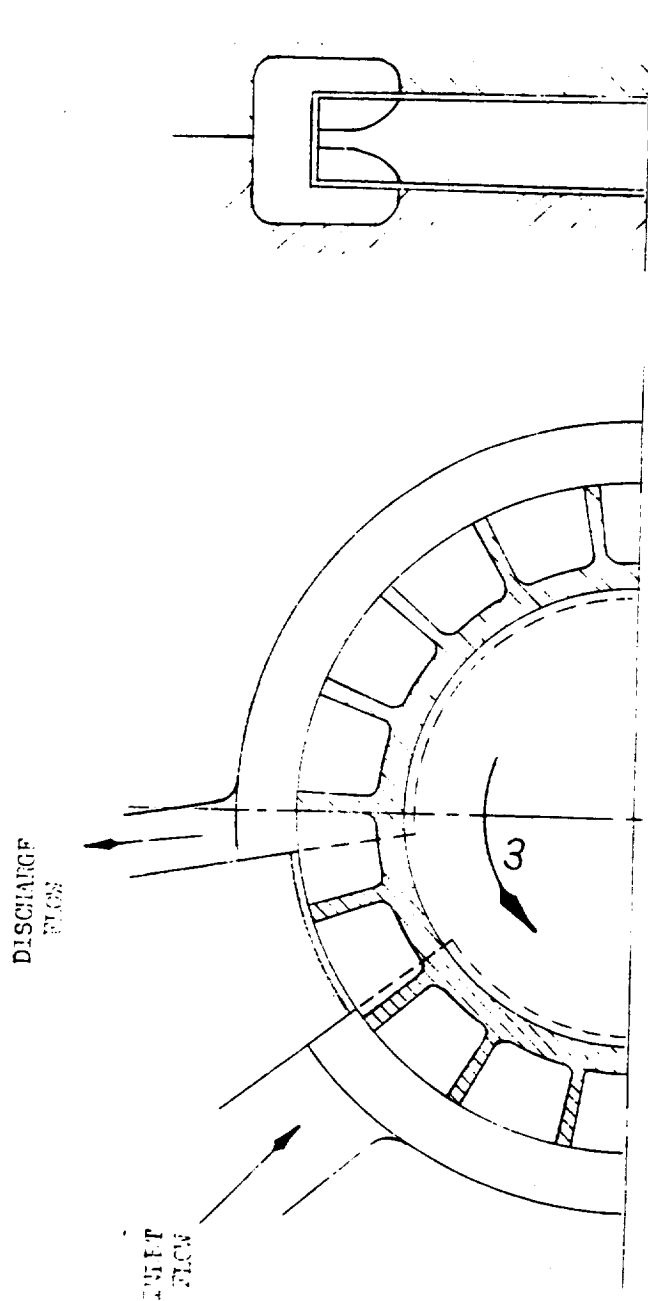


Figure 32. Schematic of Drag Pump Rotor

complex friction drag action. The flow pattern is a combination of a peripheral component and a circulatory component extending from the rotor hub to the rotor tip within the rotor and returning from the tip to the hub in the channel. In either case, the pumping action is regenerative and head coefficients greater than one can be expected (Ref. 14).

The drag pump operates at maximum efficiency in a specific speed regime of 9×10^{-2} to 23.3×10^{-2} . The range of specific diameter corresponding to the maximum efficiency operation is 2.38 to 23.8. The N_s - D_s relation of the drag pump is presented in Fig. 33 and 34. Note that the drag pump operating range closely resembles that for the Pitot pump.

The efficiency may be expressed as a function of head, fluid viscosity, and rotational speed as (Ref. 15):

$$\eta = \frac{1-K_1 \left(\frac{H}{\nu \omega} \right)}{1+K_2 \left(\frac{\nu \omega}{H} \right)} \quad (39)$$

where $K_1 K_2 > 1/3$, or the efficiency may be expressed as (Ref. 14):

$$\eta = \frac{1}{\chi} \left[1 - \frac{\lambda}{(\chi-1)^2} \right] \quad (40)$$

where

$$\chi = 1/\$$$

$$\lambda = \frac{\text{casing drag}}{\text{rotor drag}}$$

Reference 14 states that optimum performance occurs at $\chi = 2$ and $\lambda = .1$, i.e., $\eta_{\text{max.}} = 45\%$. It is evident that λ must be small (large rotor drag) and χ , large (low tip speeds).

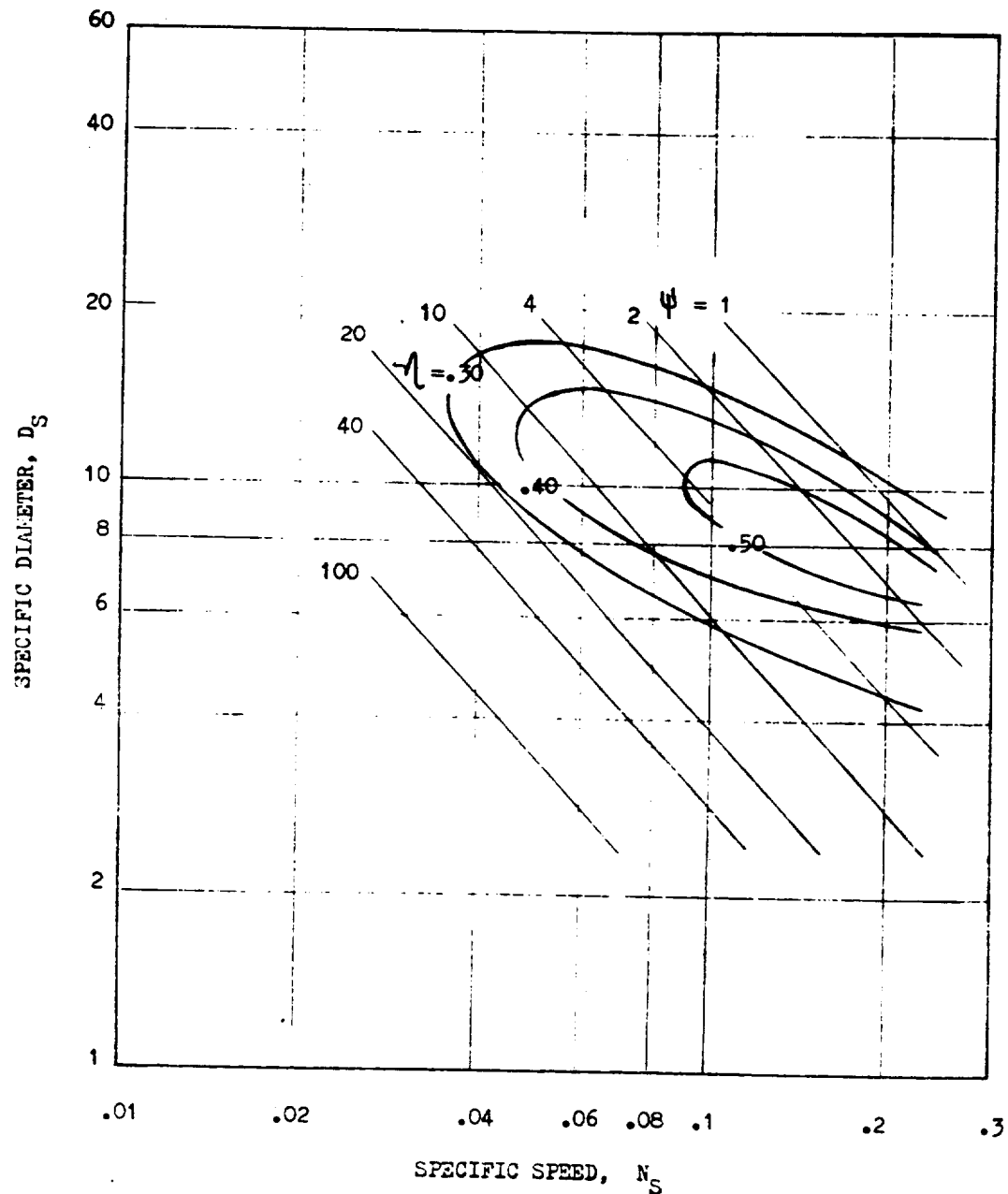


Figure 33. Approximate N_s - D_s Diagram for the Drag Pump

R-8494-1

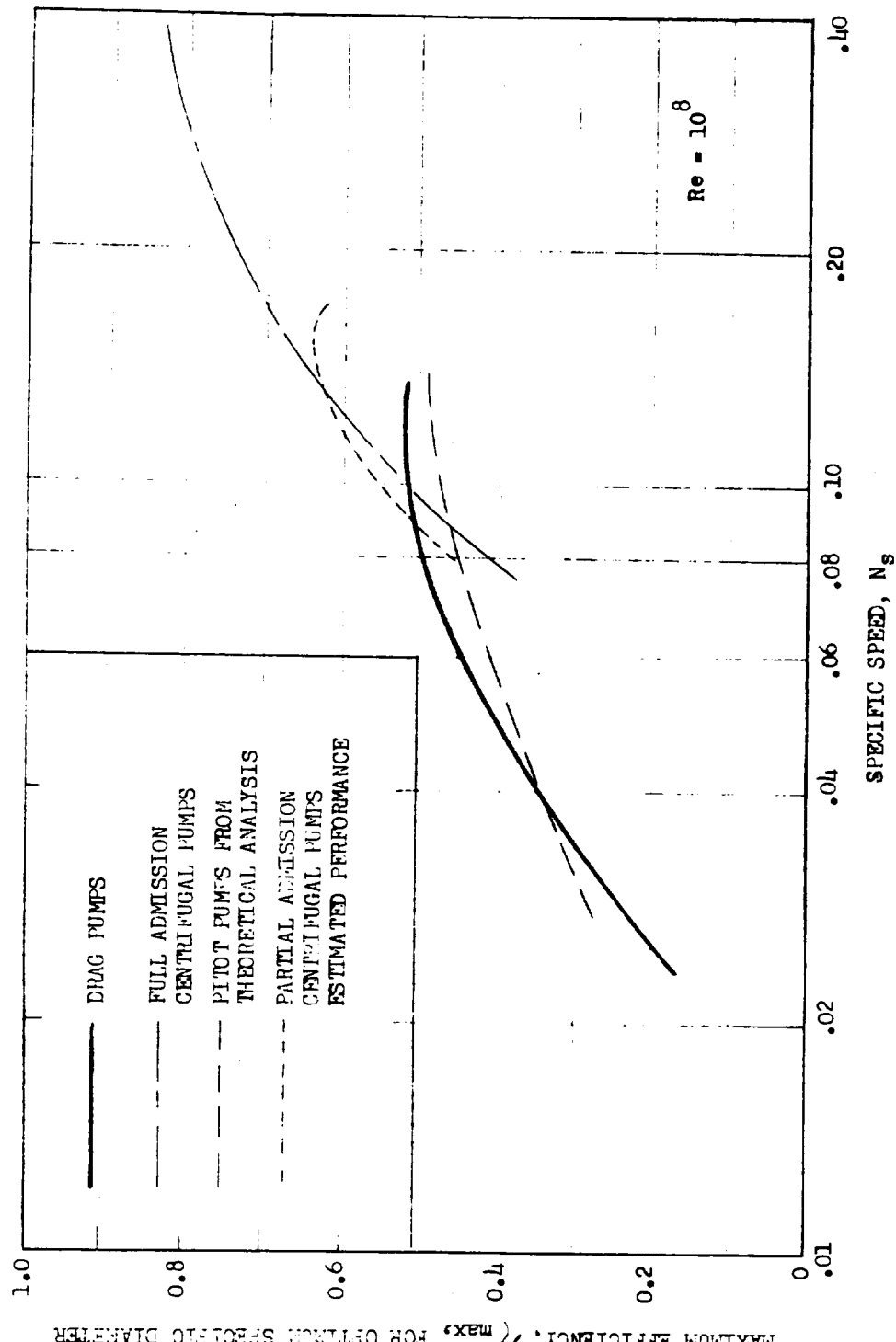


Figure 34. Maximum Efficiency as Function of Specific Speed

For a specific speed less than 0.09, the drag pump yields higher efficiencies than the conventional centrifugal pump (including both the full and partial admission) for $\chi = 2$ and $\psi = 2$ to 2.5 (Fig. 34).

Equation 39 above indicates the effect of viscosity on efficiency. Drag pumps, evidently, are more efficient pumping highly viscous fluids at low speeds. As stated before, LF_2 is of relatively low viscosity. High viscosity increases rotor drag which would reduce λ and further improve the efficiency according to Eq. 40. For a given flow the rotor drag is a function of blade number and, in general, efficiency and head increase with the blade number (Ref. 14).

High pressure ratios require a large ratio of rotor drag area to through flow area so that U_{tip}/C_m is comparatively small, according to Ref. 14. This, of course, limits the rotor to low tip speeds.

There is only limited information available on the design of the drag pump and even less test data available for verification of the present theories. For this reason, the preliminary design of the drag pump involved scaling a commercial pump of known performance. N_s and D_s were maintained and the efficiency was adjusted to include sizing effects according to Ref. 2. Figure 35 is the preliminary design sketch.

The calculated axial load was negligible but the radial load on the bearings proved to be quite considerable because of the inlet and discharge configuration. To help reduce these loads, staging was considered. Two stages proved adequate and were capable of balancing the radial loads to within a tolerable level. Also, the two stages allowed a decrease in shaft speed and tip diameter which increased the predicted efficiency slightly.

Problems

The drag pump presents several problems concerning its low efficiency, high radial loads, complexity of multistaging, sensitivity to axial clearances, high rubbing speeds, and suction performance.

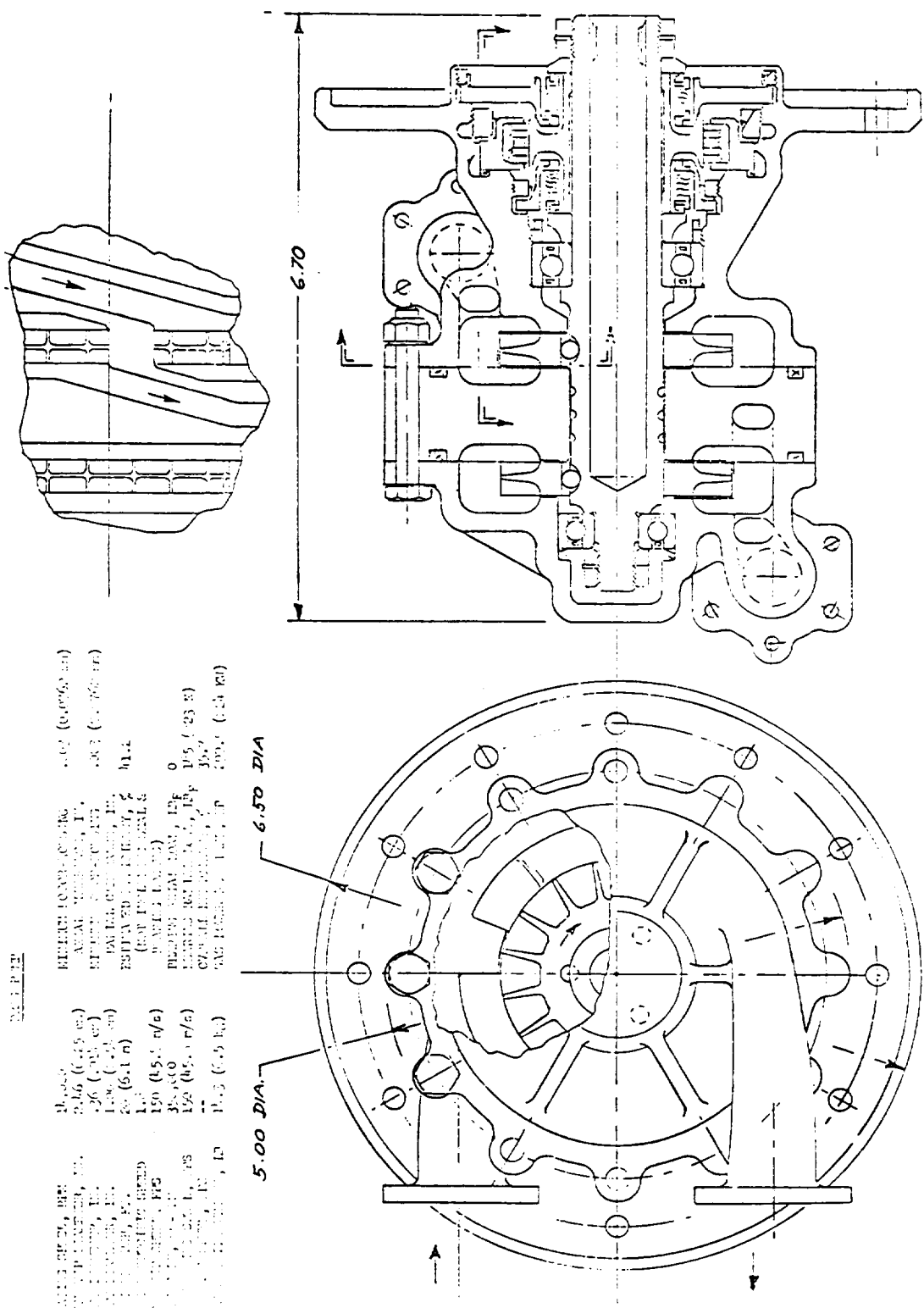


Figure 35. Drag Pump-Preliminary Design

R-8494-1

Even though the drag pump has low efficiency, it is of quite simple design and inexpensive to fabricate. However, minimum axial clearances are required to reduce the leakage which includes leakage between the inlet and exit port, between the rotor hub and casing, and shaft leakage. This total leakage may be as great as 15 to 20% of the delivered flow. The leakage is extremely sensitive to axial clearance.

Reference 14 states that optimum axial clearance to blade width ratio should be 0.01 to 0.02. Then, for the preliminary design (blade width of 0.18 inch, 0.46 cm) the axial clearance becomes approximately 0.002 inch (0.0508 mm). This tight clearance introduces possibilities of rubbing at speeds approaching the rotor tip velocity.

The high relative velocity between the incoming fluid and the rotor will result in poor suction performance. No data concerning suction performance are presently available.

The preliminary analysis and design has revealed that the drag pump suffers from low efficiencies and poor suction performance. Even though it appears to be of simple design and inexpensive to fabricate, the drag pump seems to be more suitable for pumping quite viscous, nonreactive fluids at low tip speeds and lower specific speed requirements.

PUMP EVALUATION (ROTATING)

The data generated for the various pump concepts are summarized in Tables III and IV.

Utilizing the design data, an evaluation of the technology level of each design to establish development costs and a cost analysis based on the layout drawings, the rating matrix of Table V was completed.

On the basis of the rating matrix of Table V, the centrifugal pump was selected as the best rotating pump concept for this application.

TABLE III. PUMP DESIGN EVALUATION SUMMARY

	Pitot	Tesla	Darske	Drag (Two Stage)	Shrouded Centrifugal
Rotating Speed, rpm	30,000	30,000	50,000	14,000	75,000
Rotor Tip Diameter, inches	3.75 (9.53 cm)	3.28 (8.34 cm)	1.63 (4.14 cm)	2.46 (6.25 cm)	1.30 (3.30 cm)
Inlet Diameter, inches	0.195 (0.495 cm)	0.085 (2.50 cm)	0.686 (1.742 cm)	0.36 (0.914 cm)	0.674 (1.71 cm)
Shaft Diameter, inches	1.00 (2.54 cm)	1.00 (2.54 cm)	0.375 (0.953 cm)	1.00 (2.54 cm)	0.375 (0.954 cm)
Required NPSH, feet	20 (6.1 m)				
Suction Specific Speed	4.03	4.03	6.70	1.8	10.05
Rotor Tip Speed, ft/sec	491 (150 m/s)	430 (131 m/s)	356 (108 m/s)	150 (46 m/s)	426 (130 m/s)
Bearing DN, mm-rpm	750,000	900,000	500,000	350,000	750,000
Seal Rubbing Speed, ft/sec	195 (59.5 m/s)	195 (59.5 m/s)	82 (25 m/s)	150 (46 m/s)	125 (38 m/s)
Near Ring Speed, ft/sec	--	328 (100 m/s)	--	--	300 (92 m/s)
Minimum Rotor-Housing Axial Clearance, inch	Not Critical	Not Critical	0.011 (0.28 mm)	0.003 (0.076 mm)	Not Critical
Minimum Rotor-Housing Radial Clearance, inch	Not Critical	0.003 (0.076 mm)	0.020 (0.51 mm)	0.003 (0.076 mm)	0.003 (0.076 mm)
Estimated Efficiency (not including seal and bearing losses), percent	43.2	40	48	41.2	58
Bearing Axial Load, lbf	50 (222 N)	80 (356 N)	50 (222 N)	0	25 (111 N)
Bearing Radial Load, lbf	25 (111 N)	25 (111 N)	25 (111 N)	185 (823 N)	10 (45 N)
Overall Efficiency, percent	27.8	28.8	45.5	35.7	53.0
Gas Power Required, hp	117.1 (87.5 kw)	113.0 (84.5 kw)	71.4 (53.3 kw)	299.5 (224 kw)	54.5 (40.6 kw)

R-8494-1

TABLE IV. PUMP POWER BREAKDOWN

	Pitot hp	Tesla hp	Barske hp	Drag (two stage) hp	Shrouded Centrifugal hp
Hydraulic Power	24.06 (17.95)	26.00 (19.40)	21.65 (16.15)	25.30 (18.87)	17.95 (13.39)
Friction Power					
Face Seals	6.68 (4.98)	3.34 (2.49)	0.62 (0.46)	1.56 (1.16)	0.93 (0.69)
One Shaft Seal	6.55 (4.89)	6.55 (4.89)	0.44 (0.33)	3.06 (2.28)	0.66 (0.49)
Two Bearings	0.19 (0.14)	0.30 (0.22)	0.14 (0.10)	0.03 (0.02)	0.08 (0.06)
Net Required Pump Power	37.48 (27.96)	36.19 (27.00)	22.85 (17.05)	29.95 (22.34)	19.62 (14.64)
Pump Delivered Fluid Power	10.40 (7.76)	10.40 (7.76)	10.40 (7.76)	10.40 (7.76)	10.40 (7.76)
Efficiency (Pump and Seal Package), percent	27.8	28.8	45.5	35.7	53.0
Turbine Gas Power Required (Fluorine-Methane Pressure = 10.0)	117.1 (87.5)	113.0 (84.3)	71.4 (53.27)	299.5 (223.4)	54.5 (40.7)

R-8494-1

TABLE V. ROTATING PUMP RATING

	Points Allowed	Pitot	Tesla	Barstke	Drag (two stage)	Centrifugal Shrouded
Performance (total points = 25)						
Hydraulic Efficiency	5	3	3	4	3	5
Mechanical Efficiency	5	3	3	5	5	4
Overall Turbopump η (turb. η x pump η)	5	2	3	4	1	5
Size and Weight	5	3	3	4	1	5
Friction	5	2	2	5	3	4
Life (total points = 20)						
Seal Loads	5	5	5	5	3	5
Seal Speeds	5	2	2	5	3	4
Bearing Loads	5	5	4	4	2	5
Material Compatibility	5	5	5	5	5	5
Reliability (total points = 30)						
Clearances	10	10	8	6	1	8
External Leakage	10	9	10	10	10	10
Rotating Component Stress and Vibration	5	3	3	4	4	4
Pump Discharge Pressure Oscillations	5	4	5	4	4	4
Costs (total points = 25)						
Development Costs	15	12	10	13	5	14
Unit Costs	10	8	2	10	6	10
Overall	100	76	68	88	56	92

TASK II: ROTATING PUMP DESIGN

The final design effort consisted of finalizing the hydrodynamic design of the inducer, impeller, and related flow passages and finalizing the mechanical design of the pump assembly including bearing and seal packages. A discussion of this effort follows.

HYDRODYNAMIC DESIGN

Several unique problems were influencing factors in the hydrodynamic design of the pump. The leakage flow in a pump of this size is a major problem since the leakage paths return the fluid to the impeller eye. Provisions must be made for this effect on the impeller inlet fluid angle to maintain adequate incidence angles. The leakage flow was calculated as being 60 percent of the delivered flow (7.2 gpm, $4.55 \times 10^{-4} \text{ m}^3/\text{s}$) or 37.5 percent of the total flow pumped by the impeller. The inducer preceding the impeller will not be affected by this additional flow and, therefore, will be of correspondingly smaller diameter than the impeller eye diameter. The inducer design information is presented in Table VI. The inducer is a low head coefficient, high suction performance inducer developing 137 feet (42 m) of head with a suction specific speed of 11.9 based on dimensionless units at 75,000 rpm. The inducer is a helical design with variable lead, having an inlet tip blade angle of 7 degrees (0.122 rad) and discharge tip blade angle of 9 degrees (0.157 rad). The blade angle versus axial distance from leading edge is presented in Fig. 36. Based on the minimum required NPSH to the inducer of 16 feet (4.88 m), plus the expected inducer head rise, the impeller suction specific speed needs to be 2.75 in dimensionless units. This is well within current practice.

The impeller selected is a six-vane, shrouded, centrifugal impeller. The impeller discharge blade angle is 25 degrees (0.436 rad) measured from the tangential direction. A steeper blade angle at discharge would produce a positive head versus flow curve slope at the low flowrates resulting in possible instabilities. The impeller design information is presented on Table VII. The impeller tip speed is 426 ft/sec (130 m/s) which is not exceedingly high for pumps of this type. The

TABLE VI. INDUCER DESIGN INFORMATION

Type	Variable lead helix
Speed	75,000 rpm
Flow	12 gpm ($7.57 \times 10^{-4} \text{ m}^3/\text{s}$)
Developed Head	137 feet (41.76 m)
NPSH, minimum	16 feet (4.88 m)
Required Suction Specific Speed	11.9
Blade Angle, Inlet Tip	7.0 (0.12 rad)
Blade Angle, Discharge Tip	9.0 (0.16 rad)
Solidity	≈ 2.5
Inlet Flow Coefficient	0.07
Number of Vanes	3
Inlet Tip Diameter	0.64 inch (1.626 cm)
Inlet Hub Diameter	0.27 inch (0.686 cm)
Discharge Tip Diameter	0.64 inch (1.626 cm)
Discharge Hub Diameter (blading)	0.404 inch (1.026 cm)
Vane Thickness, Tip	0.010 inch (0.254 mm)
Vane Thickness (0.27-inch diameter)	0.020 inch (0.508 mm)
Cant Angle	15 degrees (0.262 rad)

TABLE VII. IMPELLER DESIGN INFORMATION

Type of Impeller	Shrouded radial
Speed	75,000 rpm
Through Flow	12.0 gpm ($7.57 \times 10^{-4} \text{ m}^3/\text{s}$)
Leakage Flow	7.2 gpm ($4.54 \times 10^{-4} \text{ m}^3/\text{s}$)
Pump Head	2265 feet (690.4 m)
Specific Speed	0.364 (total flow)
Required Suction Specific Speed	2.78
Blade Angle, Discharge	25 degrees (0.44 rad)
Blade Angle, Inlet Tip	19 degrees (0.33 rad)
Blade Angle, Inlet Hub	27 degrees (0.47 rad)
Discharge Fluid Angle	12.8 degrees (0.22 rad)
Inlet Flow Coefficient	0.1023
Discharge Flow Coefficient	0.052 (negligible blockage)
Number of Vanes	6
Impeller Eye Diameter	0.75 inch (1.905 cm)
Impeller Discharge Diameter	1.30 inches (3.302 cm)
Discharge Tip Width	0.044 inch (0.112 cm)

R-8494-1

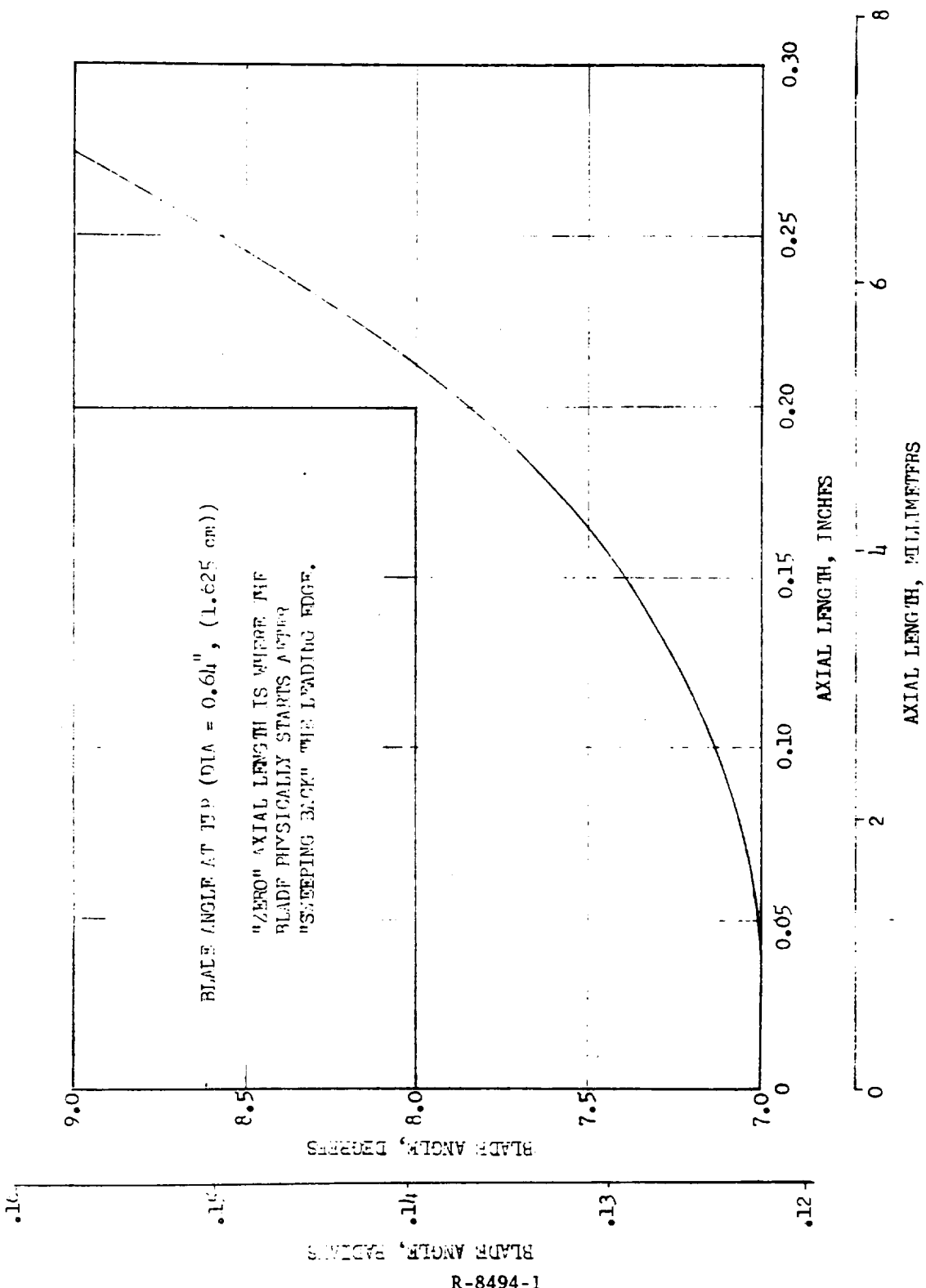


Figure 36. Inducer Blade Angle as a Function of Axial Distance
From Leading Edge

60-percent leakage flow (37.5 percent of total flow) mentioned previously enters the impeller eye from the front wear ring and also from bleed holes in the impeller hub which set the balance cavity pressure. This flow at inlet was assumed to have a tangential velocity C_u of one-half the rotor velocity. The impeller inlet blade angle requirement was determined utilizing this assumption in conjunction with the inducer discharge flow pattern and blade blockage. It was assumed that the impeller inlet blade angle would be set at zero incident angle.

Figure 37 presents the meridional cross section of the impeller scaled 20 times size. The horizontal reference line is parallel to the shaft centerline, but is located 4 inches (10.1 cm) above it on this 20 times size drawing. The streamlines 1 through 4 are also indicated.

Figure 38 is the blade angle distribution for the four streamlines shown in Fig. 37. On streamline No. 4, the angle goes above 27 degrees (0.471 rad) because a slight S-shape is necessary. To eliminate the S-shape would require a lengthening of the streamline to such an extent that the difference in wrap between streamlines No. 1 and No. 4 would be too great. This lengthening of the theoretical streamline (or blade wrap) would result in an excessive vane leading edge forward sweep with a proportional increase in flow area reduction or blockage. It would also require a large deviation of the blades from being normal to the shrouds, which is undesirable from an efficiency standpoint due to the increased flow passage surface area. All vanes are 0.020 inch (0.51 mm) thick starting at the inlet, increasing to 0.028 inch (0.71 mm), and then decreasing to 0.020 inch (0.51 mm) again at the discharge. This will provide adequate structural rigidity of the vanes.

The relative velocities in the impeller were calculated using a computer program described in Ref. 16. The average relative velocities of the flow in the three stream tubes between the four streamlines previously described is presented in Fig. 39. The flow is from right to left in the figure. The relative velocity distribution is within limits considered by Rocketdyne to be good practice. The vane pressure distribution is given in Fig. 40. The impeller blade loading program of

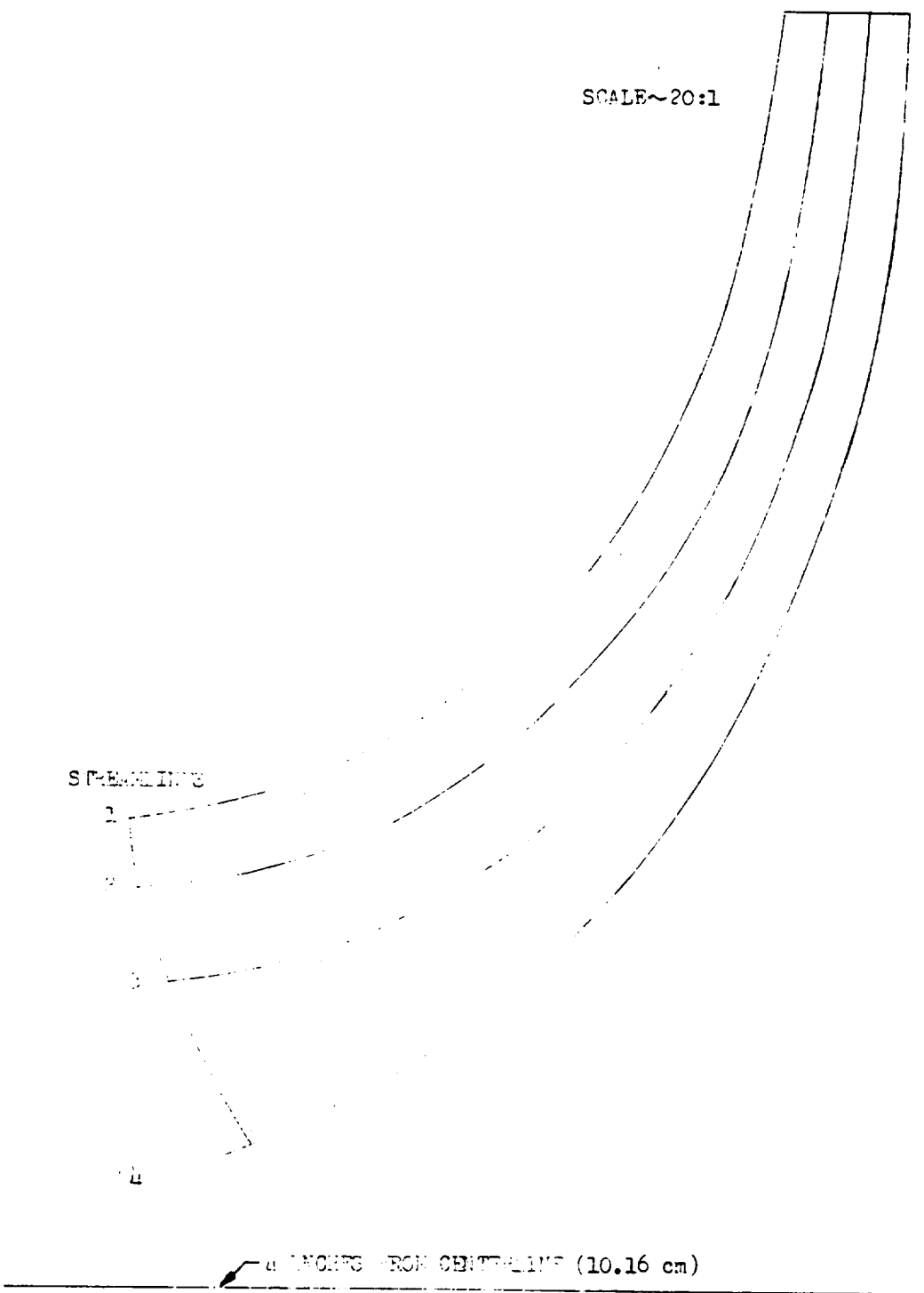


Figure 37. Meridional Section of Impeller Flow Passage

R-8494-1

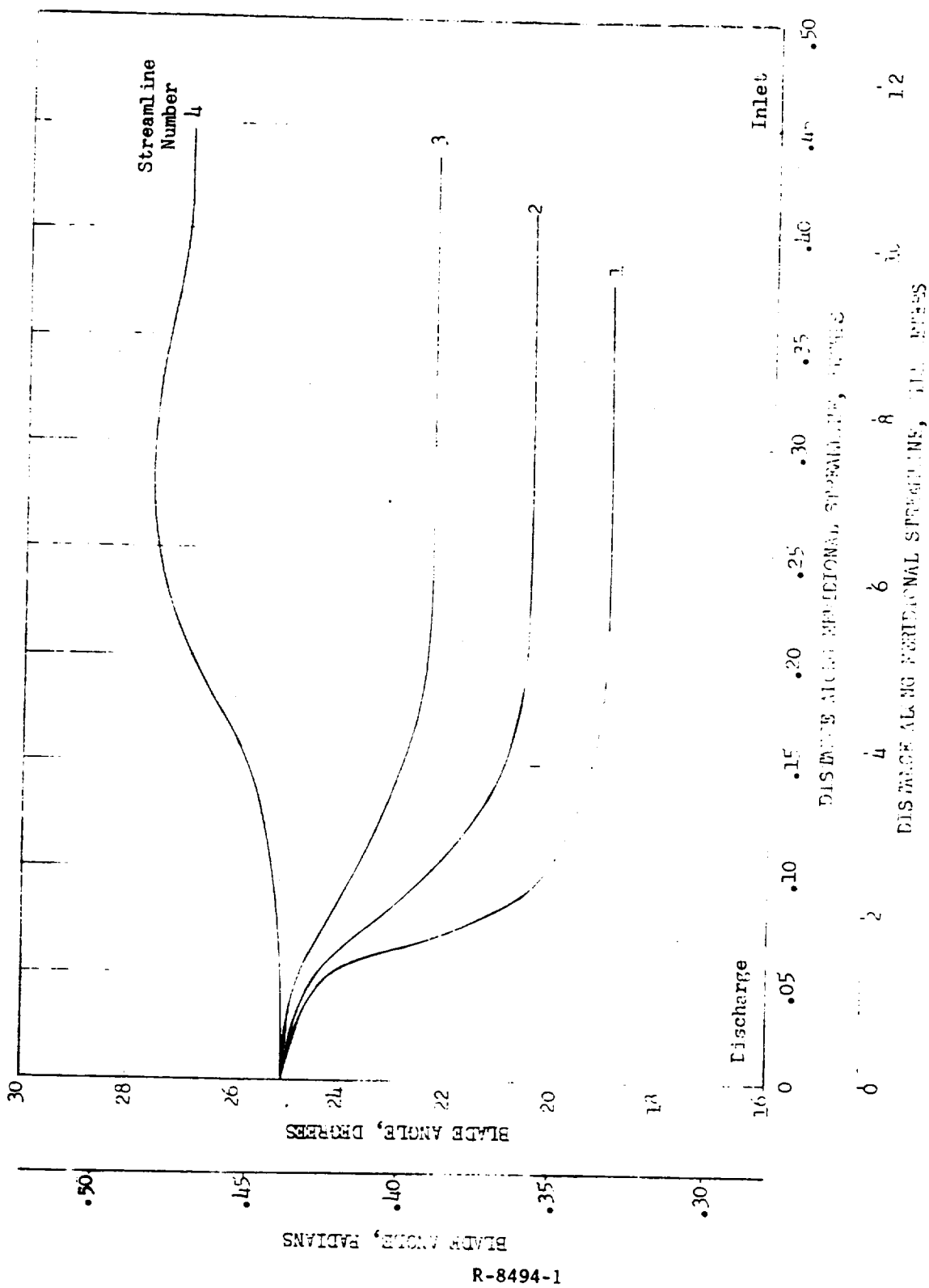


Figure 38. Impeller Blade Angle Along Meridional Streamlines

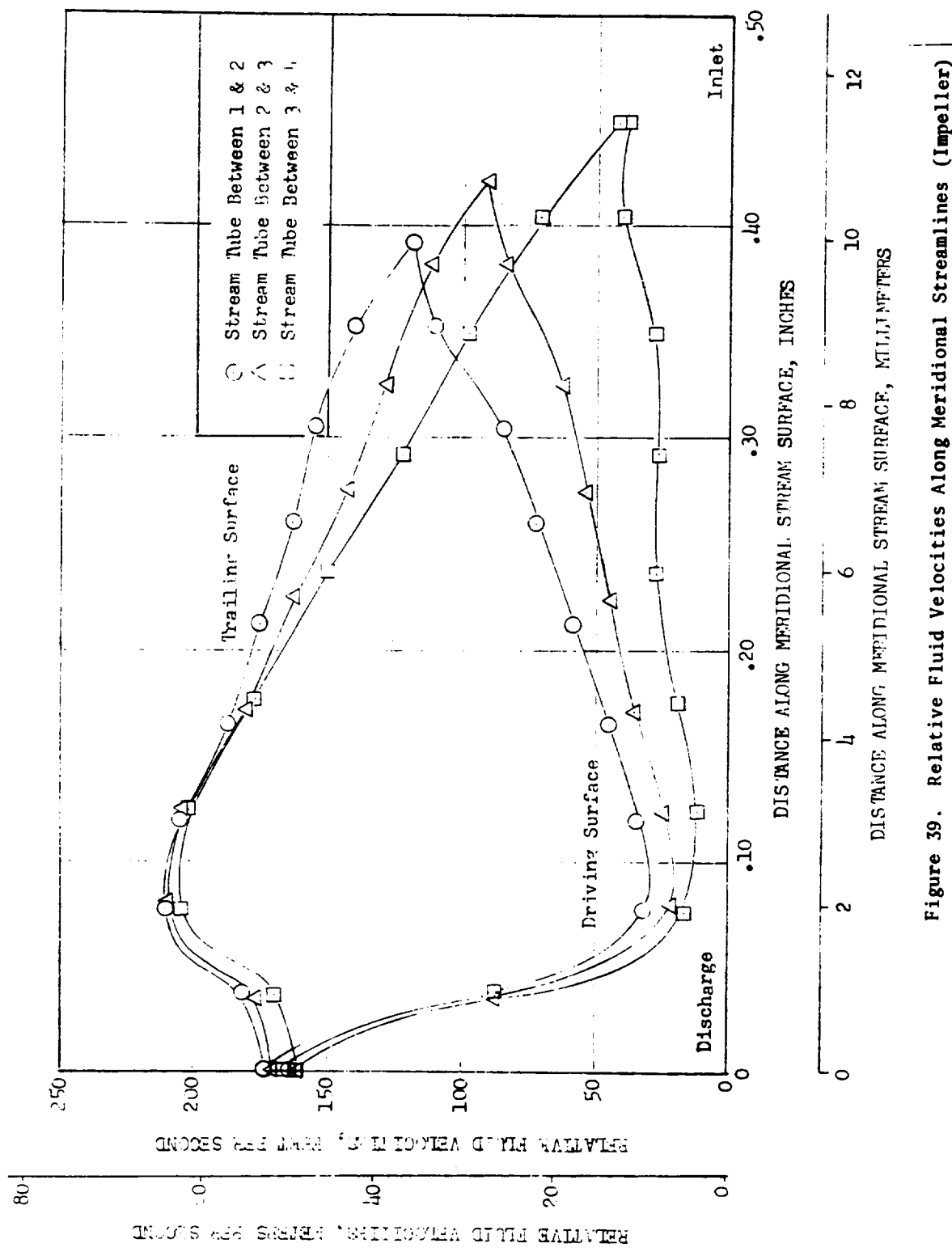


Figure 39. Relative Fluid Velocities Along Meridional Streamlines (Impeller)

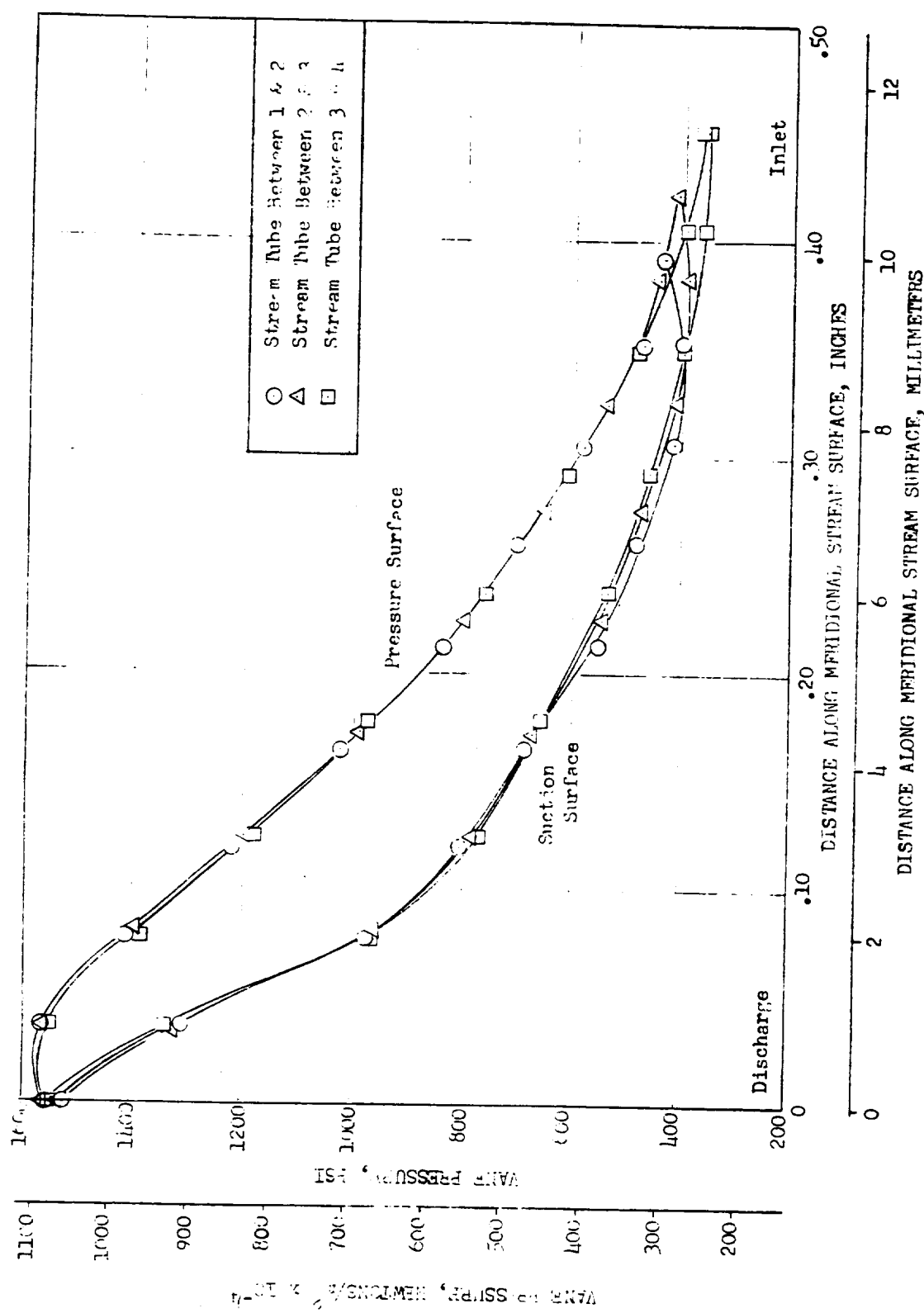


Figure 40. Pressures Along the Vane Surface in Meridional View (Impeller)

Ref. 16 indicates the slip would result in a discharge fluid angle of 12.8 degrees (0.223 rad) for a zero pressure difference from suction to pressure side at the discharge. This is the value which was used in the blading analysis. According to R. B. Furst (Ref. 17), Pfleiderer, and Stodola, the discharge fluid angle is between 10.9 and 11.7 degrees (0.191 and 0.205 rad) if the pressure differential across the vane at the discharge is not held at zero. These values show slightly less slip than if the zero pressure differential criterion is maintained.

Wear rings are used on the front and back impeller shrouds to restrict leakage and to obtain a net axial thrust of zero for the pump. The wear ring diametral clearances are set at 0.003 to 0.004 inch (0.076 to 0.102 mm) to avoid contact of the impeller with the wear ring. The axial thrust calculations indicate for a front wear ring diameter of 0.830 inch (2.110 cm) the wear ring must be at 0.880 inch (2.240 cm) in diameter to obtain zero axial thrust. The balance cavity pressure is controlled by a set of bleed holes drilled axially through the impeller hub connecting the impeller eye to the back casing.

To minimize the radial loads on the pump bearings, the volute around the periphery of the impeller discharge was designed to provide constant radial pressure. The volute flow area increases with length slightly faster than that required for constant fluid velocity. This causes a slight amount of diffusion and pressure rise. This pressure rise is calculated to be equal to the pressure losses experienced by the fluid due to friction on the collector sidewalls. With this method, a constant pressure is developed within the periphery of the collector eliminating radial loads. The collector is connected to a single discharge conical diffuser with an 8-degree (0.140 rad) included angle for efficient diffusion. Estimated performance of final design is shown in Fig. 41.

MECHANICAL DESIGN

The pump consists of an inducer, impeller, volute and a discharge diffusion cone. The final rotating pump configuration is shown in Fig. 42. It has a single shaft mounted on two ball bearings. The bearings are separated by a bearing spacer on the shaft. The inducer and impeller are overhung on one end of the shaft and the



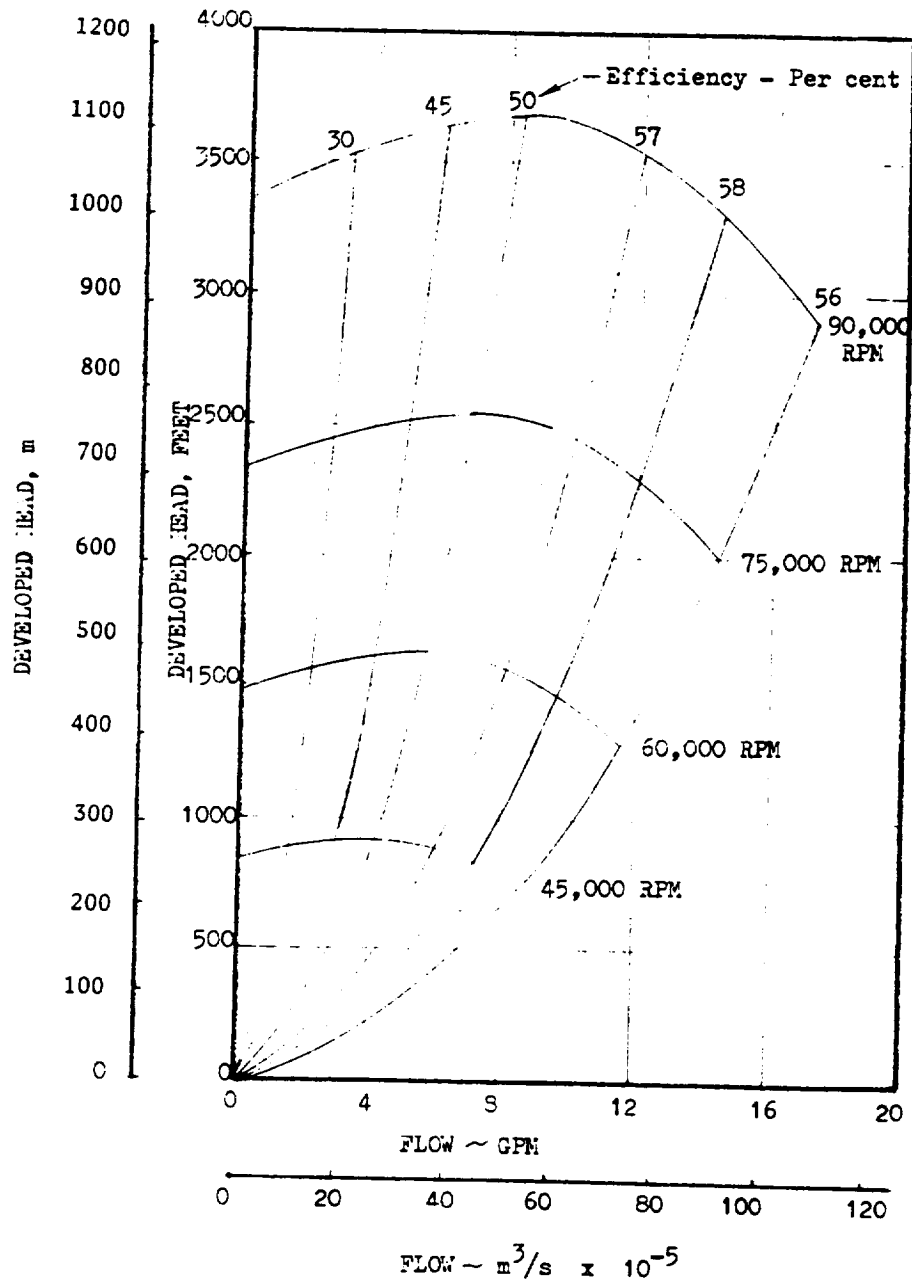


Figure 41. Estimated Performance of the Centrifugal Pump-Final Design

R-8494-1

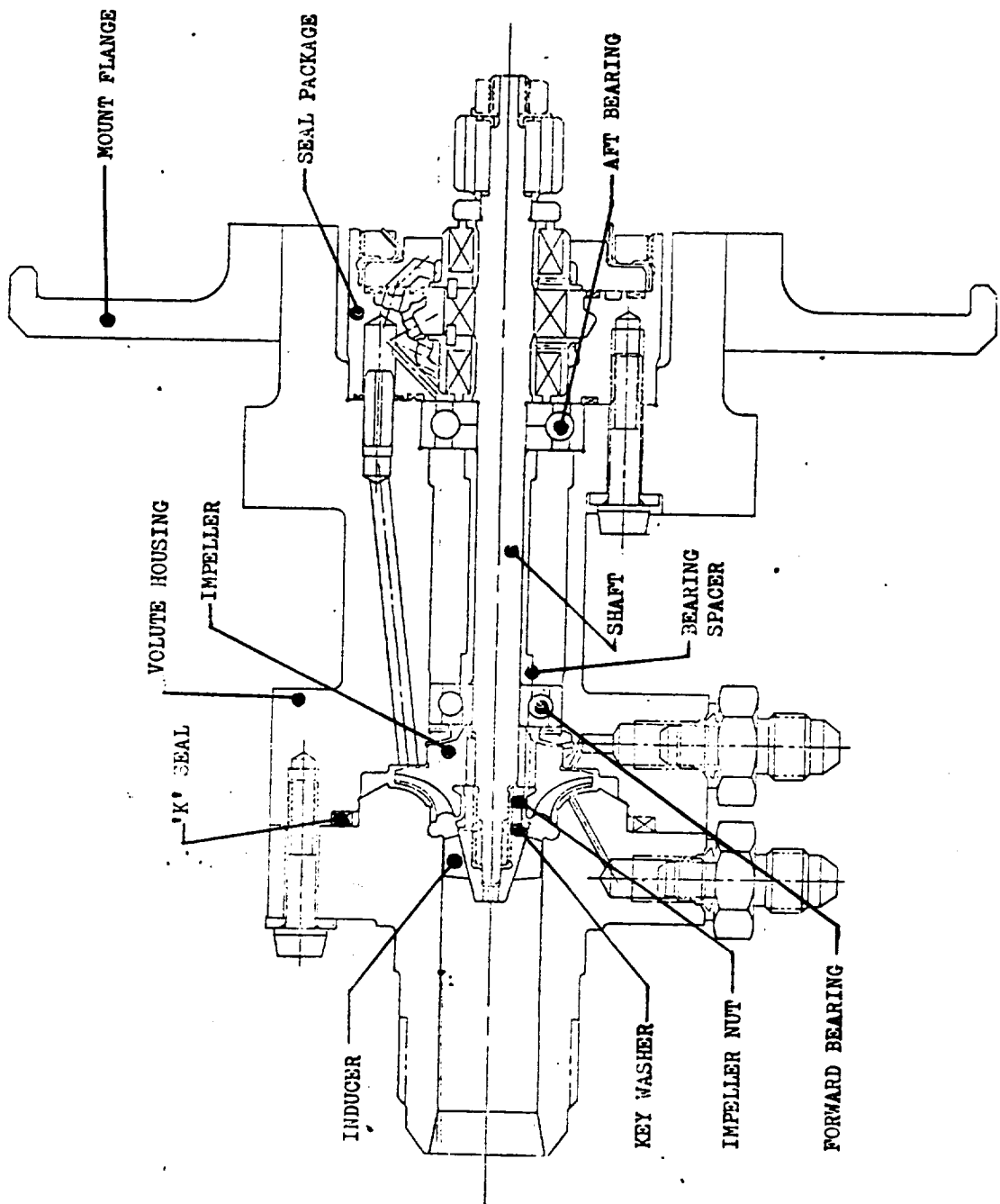


Figure 42. Centrifugal Pump Assembly

dynamic seals are outboard of the bearing on the other end of the shaft. The bearings are lubricated by the pumped fluid. The seal package is of the conventional design, a primary face riding seal, an intermediate purged shaft riding seal and a secondary face riding seal. Due to the small pump size, an unconventional method of volute construction was required.

Casting was chosen as the method of fabrication for the impeller because of its small size. The physical properties of INCO 718 best met the impeller requirements; therefore, all other parts except the bearings and seals were made of INCO 718 to eliminate the problems of thermal contraction associated with the usage of different materials at cryogenic temperatures. The bearing inner race, outer race, and ball material is AISI 440-C. This material has shown in past usage to be the best bearing material for cryogenic applications. The bearing ball cage material is K Monel. The primary seal nose material is an aluminum oxide (Al_2O_3) plasma-sprayed coating on a nickel-chrome mixture base running against the bearing inner race coated with Al_2O_3 . It has INCO 718 bellows. The intermediate seal is two BaF_2 - CaF_2 composite (sintered Inconel 600 with a BaF_2 - CaF_2 filler) floating gap, solid rings, purged, running on a BaF_2 - CaF_2 coated surface of the INCO 718 shaft. The secondary seal is a carbon PSN nose insert, INCO 718 bellows face type seal running on a chrome-plated INCO 718 mating ring.

The shaft is made from an INCO 718 bar heat treated to a tensile strength of 180,000 to 200,000 psi (1240×10^6 to $1380 \times 10^6 N/m^2$). It incorporates the mating surface for the intermediate seal. The bearings, bearing spacer, and impeller are installed on the shaft with a press fit. This type of assembly results in a stiffer shaft raising the critical speed.

The impeller is an INCO 718 investment casting. The selection of a casting for this part resulted from a study of several methods of manufacturing and was dictated by the part size and the requirement of shrouding the vanes. The part cannot be machined from a forging because of the large wrap angle of the vanes. Machining an open face impeller was quite feasible but any method of bonding or attaching the shroud to the thin vanes was impractical. The impeller is keyed to the shaft and retained by the impeller nut. The impeller nut also maintains the preload in the shaft.

The inducer is machined from an INCO 718 forging and threaded to the shaft as a nut. It pilots to the shaft on a machined internal pilot diameter. A washer which is keyed to the shaft is sandwiched between the inducer hub and the impeller nut. This washer is deformed into slots in both the inducer hub and the impeller nut locking both into place.

The volute or scroll is machined in two halves--one half in the inlet and the other half in the volute housing. The inlet half contains the pump inlet, the front impeller seal land and the front half of the discharge scroll. The volute housing contains the rear impeller seal land, the rear half of the discharge scroll, and the discharge diffuser cone. Other parts contained in the volute housing are described later. The inlet and volute housing are machined from INCO 718 bar and plate stock, heat treated to a tensile strength of 180,000 to 200,000 psi (1240×10^6 to 1380×10^6 N/m²). The scroll portions of the inlet are machined as concentric surfaces (Fig. 43). The scroll is obtained by machining the volute outer periphery on the volute housing as a spiral. The discharge cone was offset by 9 degrees (0.157 rad) so a continuous flat split line could be obtained for a proper sealing surface. The two halves are bolted together and a standard K seal is used at the split line to prevent fluorine leakage.

The front bearing is an 8-mm bore angular contact ball bearing equipped with an outer land riding cage. This bearing is a separable assembly with no ball retaining lip on the low shoulder of the inner race. The second or rear bearing has an 8-mm bore with a larger, nonstandard OD of 1.0700 inches (2.7178 cm). It is a split inner race bearing equipped with an outer land riding cage. The reason for this nonstandard bearing was to reduce the shaft overhang by incorporating the primary seal mating ring as the inner race of the bearing. The rear half of the split inner race will have an Al_2O_3 coating on the primary seal side. It will be lapped and polished and serve as the mating ring. The bearings are housed in the volute housing. The rear bearing is held in the axial direction and the preload is obtained by spring loading the outer race of the front bearing in the aft direction. The bearings are submerged in and cooled by the pumped fluid. A passageway is drilled in the volute housing which allows a metered amount of

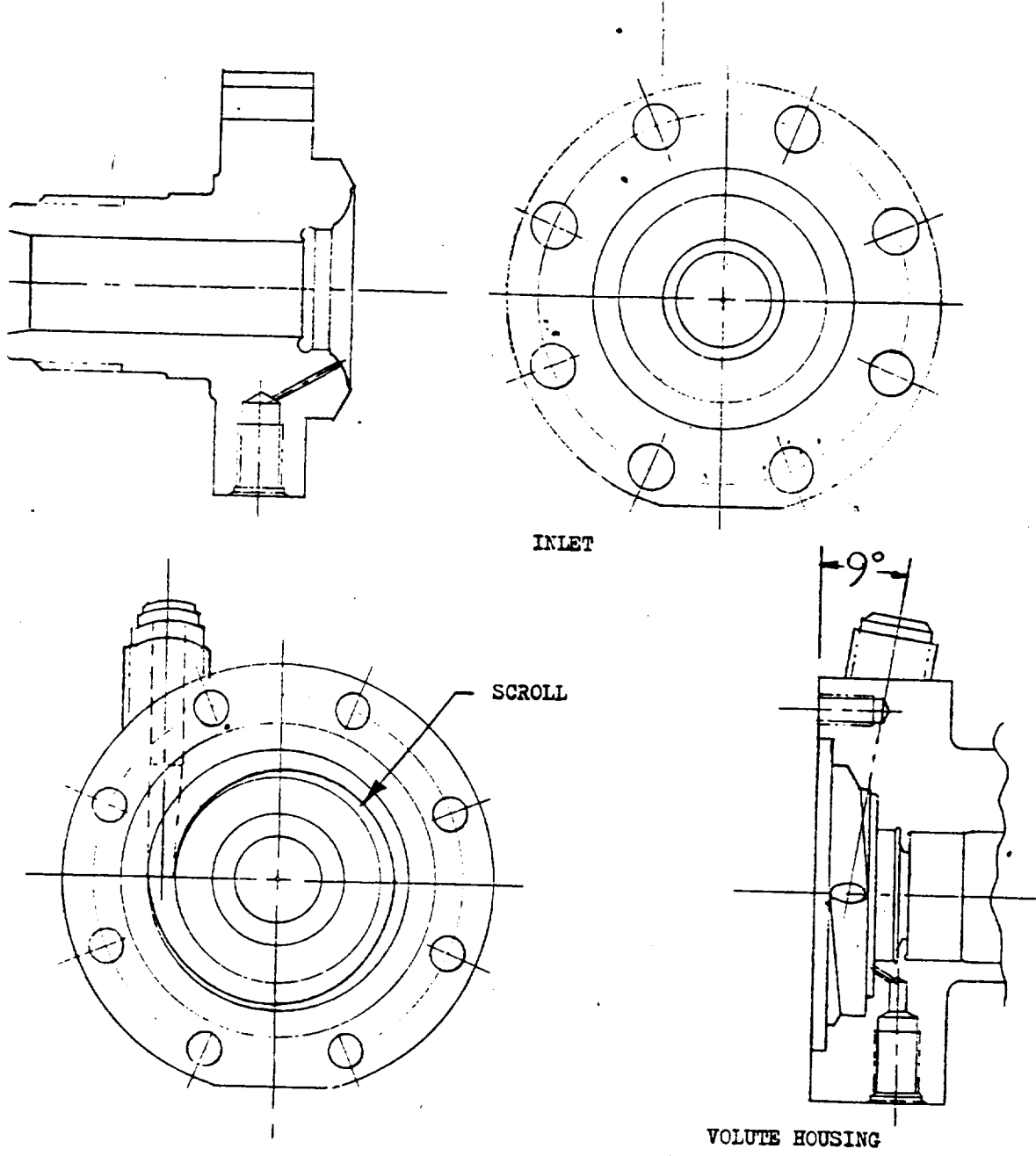


Figure 43. Centrifugal Pump Inlet and Volute Housing Sections

R-8494-1

coolant to flow from the impeller back face to the primary seal side of the aft bearing. This coolant fluid flows through both bearings and is discharged behind the inducer through holes drilled in the impeller hub.

The seal package is mounted to the volute housing. It is composed of a primary face seal, a purged intermediate shaft seal, and a secondary face seal. The purge gas enters the intermediate seal and flows in both directions, forward and aft, along the shaft. This purge gas scavenges the seal leakage of the primary and secondary seal overboard through separate seal drains.

The pump is mounted by a flange welded to the volute housing and sized to fit the facility hardware.

DRIVE DESIGN

The drive system originally intended for the centrifugal pump (Fig. 44) consisted of a commercial gas turbine coupled with a splined quill shaft to a torquemeter, which in turn was coupled to the pump shaft with another quill shaft. The turbine selected was an AiResearch Model T04 turbocharger turbine. The torquemeter was manufactured by Himmelstein and Company (Model 3S-08T, 16-1).

This same basic drive train was subsequently used to drive a bearing and seal tester shaft on the AMPS program (Ref. 28). During this test program, severe rotordynamic problems were encountered with the drive train, which eventually resulted in structural damage to the torquemeter. In view of the above experience, it was decided to fabricate a low-cost aluminum breadboard turbine to drive the centrifugal pump. The configuration of the breadboard turbine drive is presented in Fig. 45. The aluminum turbine disk is mounted directly on the pump shaft in place of the original drive spline. It incorporates six straight radial vanes for gas path elements. The manifold is of welded aluminum breadboard construction, with four equally spaced drilled holes serving as the nozzle. Ambient gaseous nitrogen is used as the driving fluid.

12 GPM CENTRIFUGAL PUMP TEST ASSEMBLY

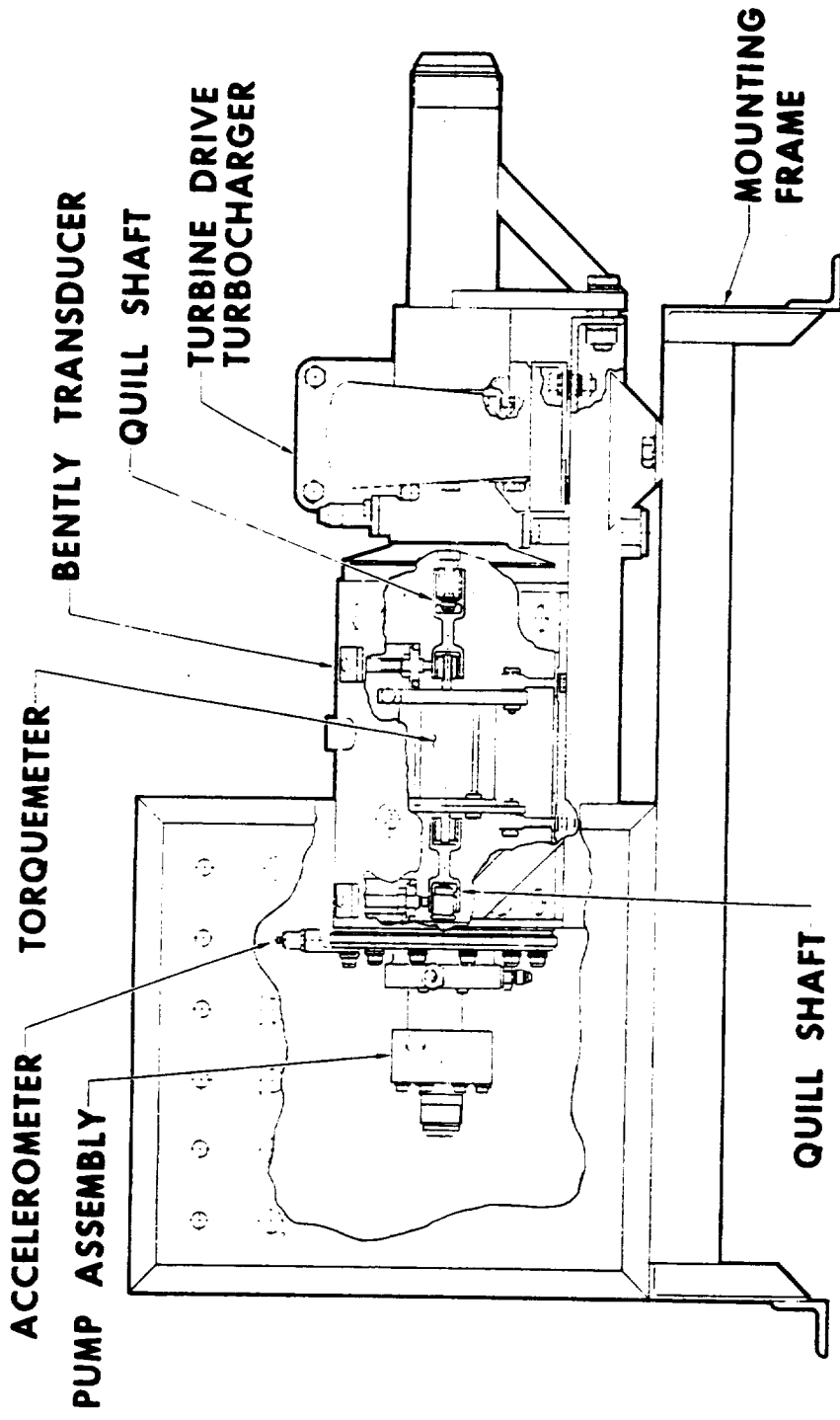
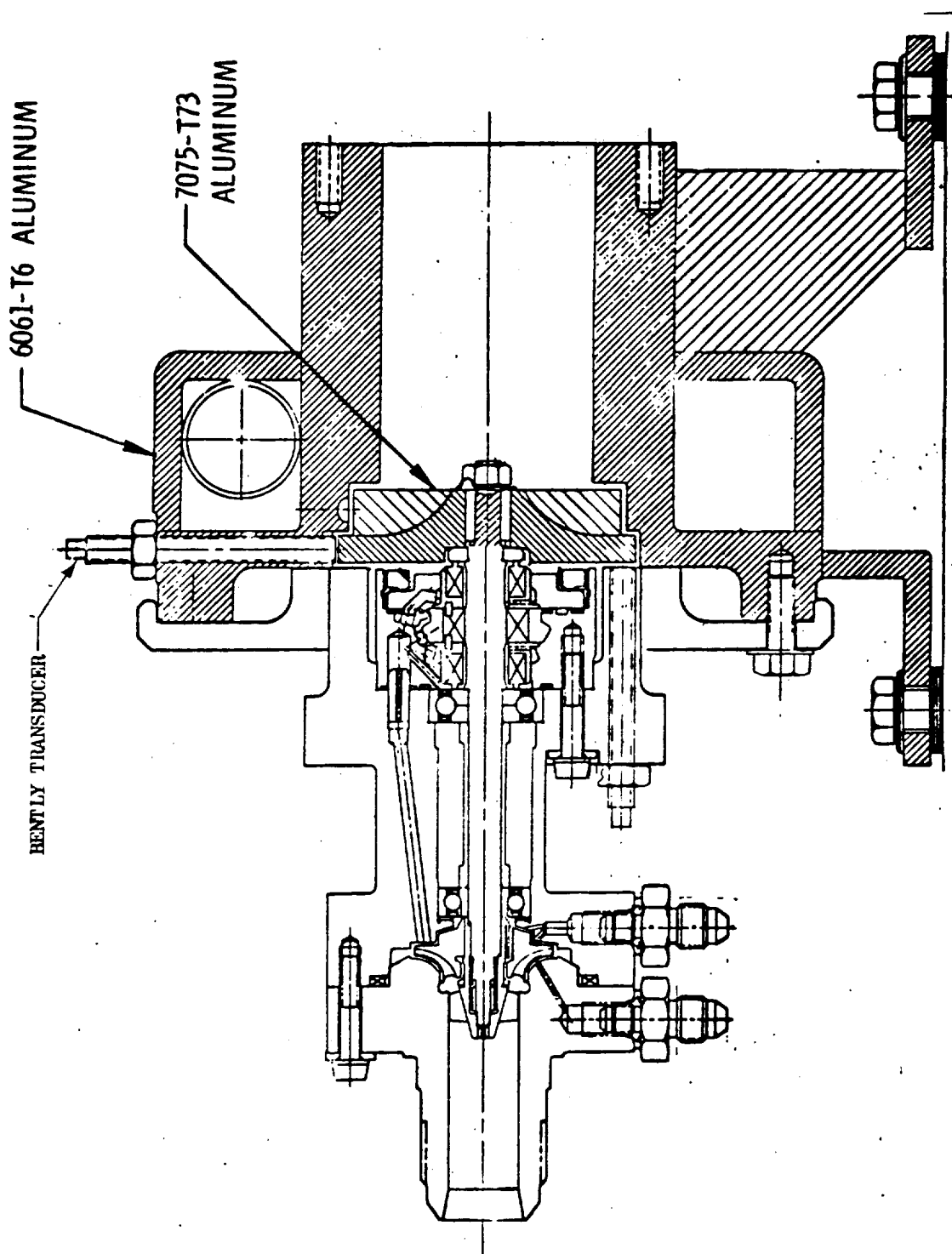


Figure 44. Initial Drive Concept Candidate



R-8494-1

92

Figure 45. Mark 36 Pump Turbine Drive

In addition to simplifying the rotordynamics of the drive system, the integrally mounted turbine drive has the advantage of simulating the concept of an overhung turbine, which would be used in an actual engine application..

STRESS AND DYNAMIC ANALYSIS

The structural analysis of the centrifugal pump was based on the following parameters:

<u>Parameter</u>	<u>Nominal</u>	<u>Maximum</u>
Speed, rpm	75,000	82,500
Power, hp	18.5 (13.8 kw)	26.4 (19.7 kw)
Torque, in.-lb	15.5 (1.75 Nm)	20.2 (2.28 Nm)
Discharge Pressure, psi	1500 (1.034×10^7 N/m ²)	1800 (1.241×10^7 N/m ²)

All parts are structurally adequate for the imposed operating conditions. The stresses reported herein are limit stresses, which are 20 percent greater than the predicted maximum operating values. In many areas, material selection and section thicknesses were based on thermal compatibility, or functional and manufacturing requirements, rather than structural need.

Impeller

The impeller is made of cast INCO 718. The impeller backplate burst speed is 184,900 rpm, resulting in a safe operating speed of 138,700 rpm for the backplate only. The vanes are adequate for the maximum speed of 82,500 rpm. The inlet

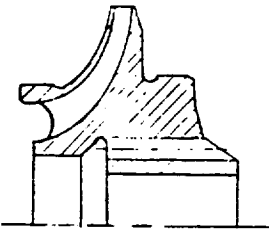
edge of the impeller vanes is the most highly stressed portion of the vanes. This is due mainly to the relatively large overhanging inlet portion of the shroud which serves as the impeller seal ring. The vane limit stress at the impeller inlet is 93,900 psi (6.47×10^8 N/m²), which includes 16,900 psi (1.16×10^8 N/m²) direct centrifugal stress and 77,000 psi (5.31×10^8 N/m²) centrifugal bending stress. The vane shear stresses and shroud bending stresses are low. A summary of the stresses and safety factors is presented in Fig. 46.

Inducer

The inducer is machined from wrought INCO 718 and is structurally adequate for the imposed operating conditions. The hub stresses are low. The vane limit mean stress is 50,000 psi (3.45×10^8 N/m²) at the critical point on the vane. The corresponding limit alternating stress is 13,300 psi (9.17×10^7 N/m²). A summary of the inducer stresses and factors of safety is presented in Fig. 47.

Shaft

The dynamic response of the shaft was predicted as part of the rotordynamic analysis. The results of this study indicated that the relationship between deflection at the coupling and moment at the critical section of the shaft varied with speed, with a smaller moment for a given deflection resulting as the speed increased. The shaft deflection limitations presented in Fig. 48 were generated utilizing this information. The pump shaft, machined from wrought INCO 718, is adequate for the imposed operating conditions providing the shaft deflections, measured at the pump coupling, remain within the limits presented in Fig. 48. The limit torsional stress in the shaft is 6100 psi (4.21×10^7 N/m²), and the axial stress due to nut preload is 41,300 psi (2.85×10^8 N/m²). The shaft deflection limit is based on a combined bending and axial preload stress of 77,700 psi (5.36×10^8 N/m²). The deflection will be monitored during testing with a Bently proximity transducer.



P/N RL001403E

Material: Heat-treated, cast INCO 718

Material Properties:

<u>Property</u>	<u>Room Temperature</u>	<u>-300 F (88.7 K)</u>
F_{tu} , ksi	140 (9.65×10^8 N/m 2)	150 (1.03×10^3 N/m 2)
F_{ty} , ksi	100 (6.90×10^8 N/m 2)	112 (7.72×10^8 N/m 2)
Elongation, percent	12	7

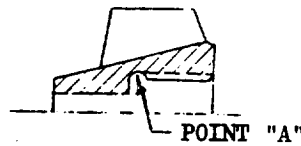
Impeller Backplate Stress and Burst Speed:

Average Tangential Stress at 82,500 rpm	$12,150$ psi (8.38×10^7 N/m 2)
Maximum Tangential Stress	$22,320$ psi (1.54×10^8 N/m 2)
Burst Speed	184,900 rpm
Yield Speed (gross yielding)	214,300 rpm
Backplate Safe Operating Speed	138,700 rpm
Maximum Radial Stress (Compressive stress due to impeller fit on shaft; this occurs at 0 rpm)	$-24,400$ psi (-1.68×10^8 N/m 2)

<u>Limit Vane Stress:</u>	<u>Direct</u>	<u>Centrifugal</u>	<u>Total</u>	<u>Factor</u>
<u>Wrap Angle, degrees (OD is zero degrees)</u>	<u>Centrifugal Stress, ksi (10^7 N/m2)</u>	<u>Bending Stress, ksi (10^7 N/m2)</u>	<u>Centrifugal Stress, ksi (10^7 N/m2)</u>	<u>of Safety on Ultimate</u>
10	0	78.5 (54.12)	78.5 (54.12)	1.9
40	5.6 (3.86)	42.8 (29.51)	48.4 (33.37)	3.1
80	6.1 (4.21)	60.7 (41.85)	66.8 (46.06)	2.2
114	16.9 (11.65)	77.0 (53.09)	93.9 (64.74)	1.6

Fluid bending stresses are less than 2700 psi (1.86×10^7 N/m 2) (limit), and they subtract from the centrifugal stresses. Shroud Bending Stress, 12,200-psi limit (8.41×10^7 N/m 2)

Figure 46. Centrifugal Pump Impeller Stress Analysis



P/N RL001402E

Material: Heat-Treated, Wrought INCO 718.

Material Properties:

<u>Property</u>	<u>Room Temperature</u>	<u>-300 F (88.7 K)</u>
F_{tu} , ksi	$175 (1.21 \times 10^9 \text{ N/m}^2)$	$213 (1.47 \times 10^9 \text{ N/m}^2)$
F_{ty} , ksi	$145 (1.0 \times 10^9 \text{ N/m}^2)$	$162 (1.12 \times 10^9 \text{ N/m}^2)$
F_{te} , ksi	$42 (2.9 \times 10^8 \text{ N/m}^2)$	$55 (3.79 \times 10^8 \text{ N/m}^2)$
Elongation, percent	10	12

Limit Hub Stress:

Tangential Centrifugal Stress at Worst Section, Point "A":

Due to Blade Weight	$2660 \text{ psi } (1.83 \times 10^7 \text{ N/m}^2)$
Due to Hub Weight	$2310 \text{ psi } (1.59 \times 10^7 \text{ N/m}^2)$
Total	$4970 \text{ psi } (3.43 \times 10^7 \text{ N/m}^2)$

Tangential Stress due to Pretorque of 15 in.-lb (1.70Nm):

$$= 10,700 \text{ psi } (7.38 \times 10^7 \text{ N/m}^2)$$

Limit Blade Stress:

Stress at Worst Stress Point	130 degree (2.27 rad) wrap
Direct Centrifugal Stress	$3.0 \text{ ksi } (2.07 \times 10^7 \text{ N/m}^2)$
Centrifugal Bending Stress	$-19.5 \text{ ksi } (-1.34 \times 10^8 \text{ N/m}^2)$
Fluid Bending Stress	$66.5 \text{ ksi } (4.59 \times 10^8 \text{ N/m}^2)$
Mean Stress	$50.0 \text{ ksi } (3.45 \times 10^8 \text{ N/m}^2)$
Alternating Stress	$13.3 \text{ ksi } (9.17 \times 10^7 \text{ N/m}^2)$
Combined Steady-Fatigue Failure Factor of Safety	2.0

Figure 47. Centrifugal Pump Inducer Stress Analysis

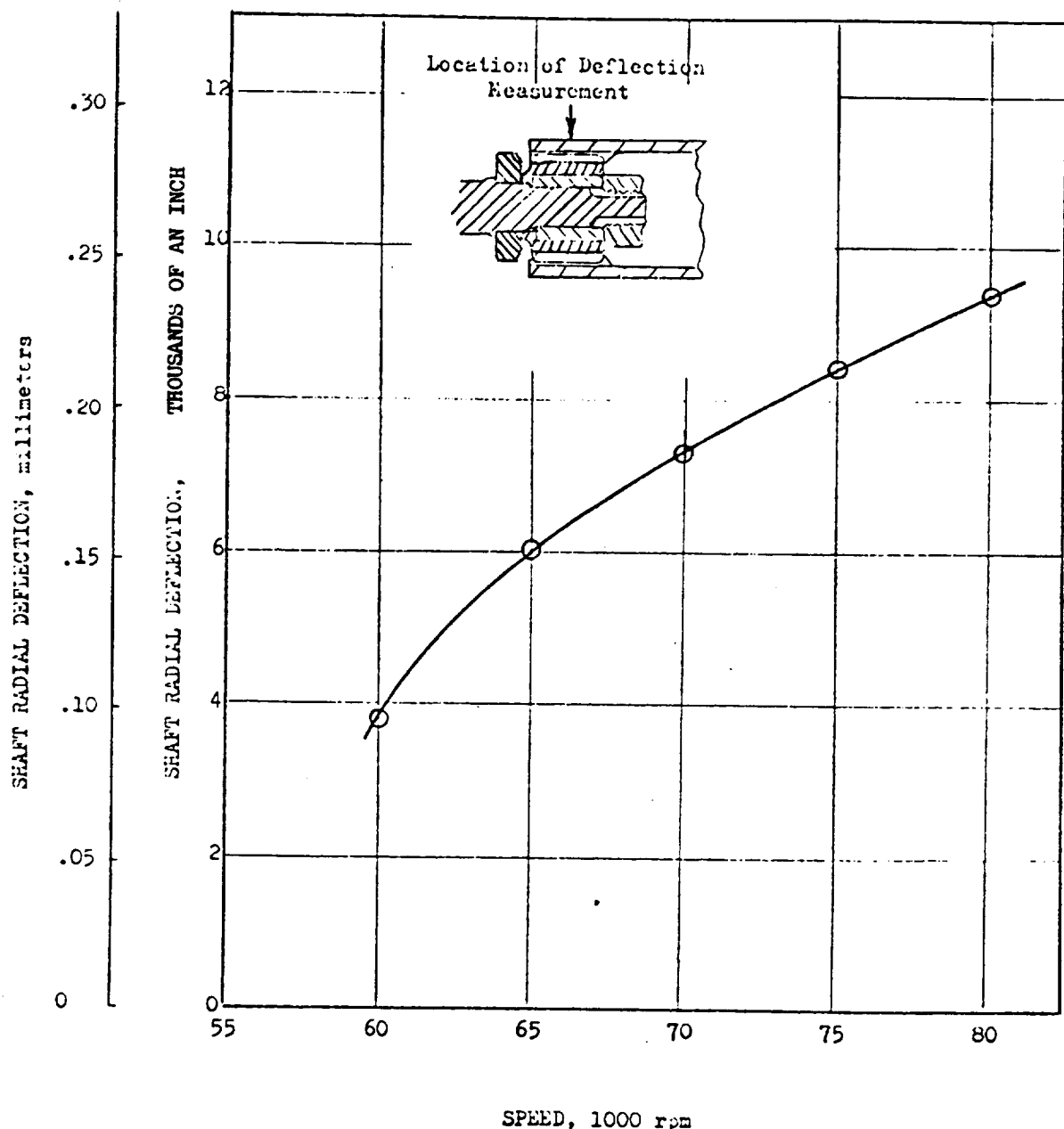


Figure 48. Allowable Shaft Deflection vs Speed

R-8494-1

The shaft limit stresses are summarized in Fig. 49. The safety factors are based on room temperature properties. At operating temperature the shaft will be colder and the actual safety factors will be higher; since the safety factors were satisfactory even for a conservative assumption of room temperature level, a detailed heat transfer study to establish the actual levels was not required.

Volute and Inlet Housing

The volute and inlet housings are made of wrought INCO 718. The stresses in both are low, and present no structural problem.

Bearing Preload Washer

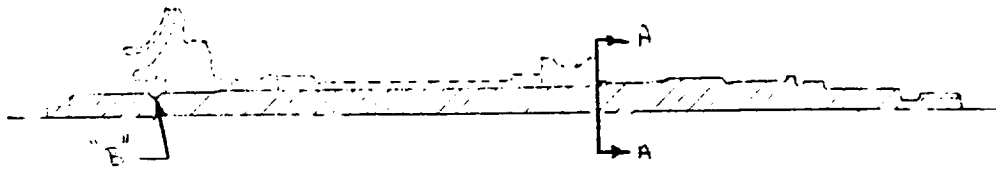
The bearing preload washer is made of wrought INCO 718. The washer dimensions were selected to provide an axial load of 60 pounds (266.9 N) with an axial deflection of approximately 0.010 inch (0.254 mm). At the 60-pounds (266.9 N) load, the maximum stress is below the allowable yield stress. The stresses are summarized in Fig. 50.

Miscellaneous Components

All of the fasteners and other miscellaneous components have been selected to provide adequate factors of safety for both the preload conditions and maximum operating conditions.

ROTORDYNAMIC ANALYSIS

The critical speeds of the rotating assemblies were calculated by a finite element method. A series of concentrated masses and inertias (which include the gyroscopic effect) connected by beam elements were used to model the rotor. Bending and shear effects were included in the beam element formulation. The radial stiffness of the bearings was treated as linear springs to ground. Critical speeds predicted by this method have been verified on other programs



P/N RL001406E

Material: Heat-treated, wrought INCO 718.

Material Properties at Room Temperature:

F_{tu} , ksi	180 (1.24×10^9 N/m 2)
F_{ty} , ksi	150 (1.03×10^9 N/m 2)
F_{te} , ksi	42 (2.90×10^8 N/m 2)

Limit Shaft Stress at Critical Section, Section A:

Steady Torsional Stress	6100 psi (4.21×10^7 N/m 2)
Alternating Torsional Stress	300 psi (2.07×10^6 N/m 2)
Axial Preload Stress	41,300 psi (2.85×10^8 N/m 2)

Bending Stress

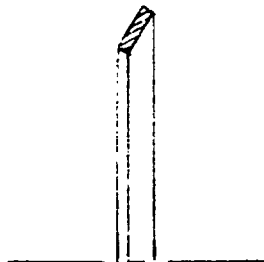
The shaft deflection is limited as indicated in Fig. 49; the combined bending and axial preload stress corresponding to this limitation is 77,700 psi (5.36×10^8 N/m 2).

Factor of Safety on Combined Steady and Fatigue Stress: 1.5

Limit Combined Tension-Torsion Stress at Point "B" due to Impeller Retaining Nut Load, 120,000 psi (8.27×10^8 N/m 2).

Factor of Safety on Combined Tension-Torsion Stress: 1.5

Figure 49. Centrifugal Pump Shaft Stress Analysis



P/N R1001409E

Material: Heat-treated, wrought INCO 718

Material Properties:

<u>Property</u>	<u>Room Temperature</u>
F_{tu} , ksi	175 (1.21×10^9 N/m 2)
F_{ty} , ksi	145 (1.00×10^9 N/m 2)

Stress and Deflection for 60 Pounds (266.9 N) Load:

Deflection

$$\delta = 0.086 \text{ inch (} 0.218 \text{ mm) to } 0.0106 \text{ inch (} 0.269 \text{ mm)}$$

Stress

$$\sigma_{\min} = -140,000 \text{ psi } (-9.65 \times 10^8 \text{ N/m}^2)$$

$$\sigma_{\max} = 93,000 \text{ psi } (6.41 \times 10^8 \text{ N/m}^2)$$

These stresses are less than yield strength.

Figure 50. Centrifugal Pump Bearing Preload Washer Stress Analysis

by rotor displacement measurements and by accelerometer measurements. Resonant amplification of rotor unbalance response can be limited by avoiding steady-state operation within ± 20 percent of any synchronous critical mode. This criterion reduces the dependency on damping and makes rotor response primarily a function of unbalance which can be controlled. The bearing radial stiffness values were calculated as a function of axial preload. The axial load will be set during assembly by preloading the bearings against each other with a shimmed Belleville spring.

The rotordynamic behavior of two candidate drive configurations were examined. The initial configuration evaluated included a separate drive turbine connected to the pump through two quill shafts and a torquemeter, as shown in Fig. 51. The critical speeds for the various modes are shown in Table VIII and the critical speed versus pump bearing spring rate is shown in Fig. 52. The mode shapes at the calculated critical speeds are shown in Fig. 53 and Fig. 54 for pump bearing spring rates of 10^4 lb/in. (1.75×10^6 N/m) and 10^5 lb/in. (17.5×10^6 N/M), respectively. In these figures, the maximum deflections are assigned a value of unity and deflections at other points of the rotor are indicated as fractions of the maximum deflection.

The presence of four critical speeds below the operating range indicated potential problems during speed buildup or at low-speed operation. Furthermore, subsequent experience with a similar drive system showed that it would be difficult to maintain a long drive train of this type stable at high operating speeds. As a result, the integral drive turbine concept shown in Fig. 45 was adopted. The results of the critical speed analyses conducted for the integral turbine rotor configuration are included in Fig. 55 through 58. For the predicted bearing spring rates of 10^5 lb/in. (17.5×10^6 N/m), only one critical speed, at 27,900 rpm, was calculated below the operating speed of the pump.

REDUCTION IN POWER LOSSES USING GAS CAVITIES

In centrifugal pumps, a considerable amount of power can be absorbed in the rotor housing space due to fluid friction and from leakage of high-pressure fluid back to the pump inlet. In pumps of low specific speed and small dimension the leakage

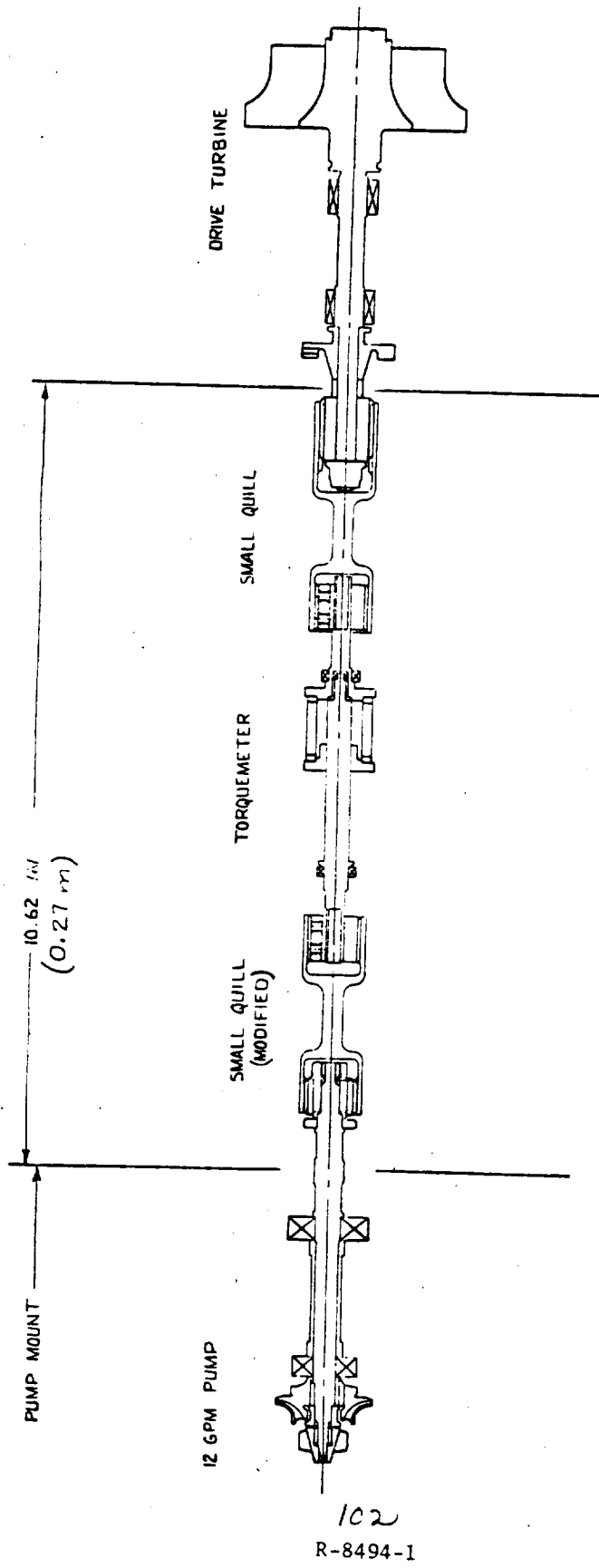


Figure 51. Schematic of Drive Configuration

TABLE VIII. CRITICAL SPEEDS FOR VARIOUS MODES AND ESTIMATED BEARING SPRING RATES

Mode No.	Critical Speed	
	$K = 10^4$ lb/in.	$K = 10^5$ lb/in.
1	22,700 rpm	26,600 rpm
2	26,600	40,700
3	40,700	53,000
4	44,400	53,800
5	53,800	113,600
6	117,600	121,800

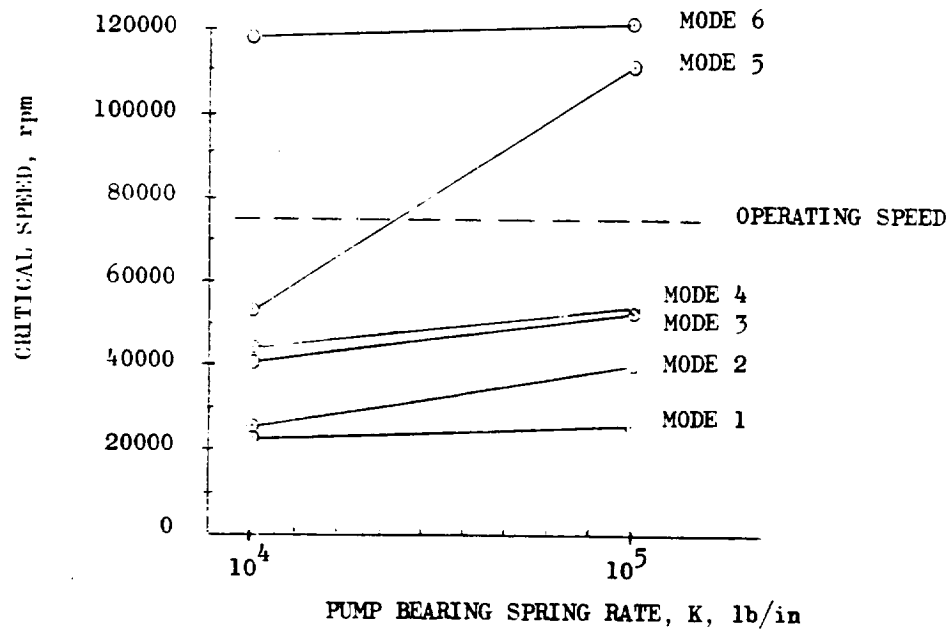


Figure 52. Critical Speed vs Pump Bearing Spring Rate

R-8494-1

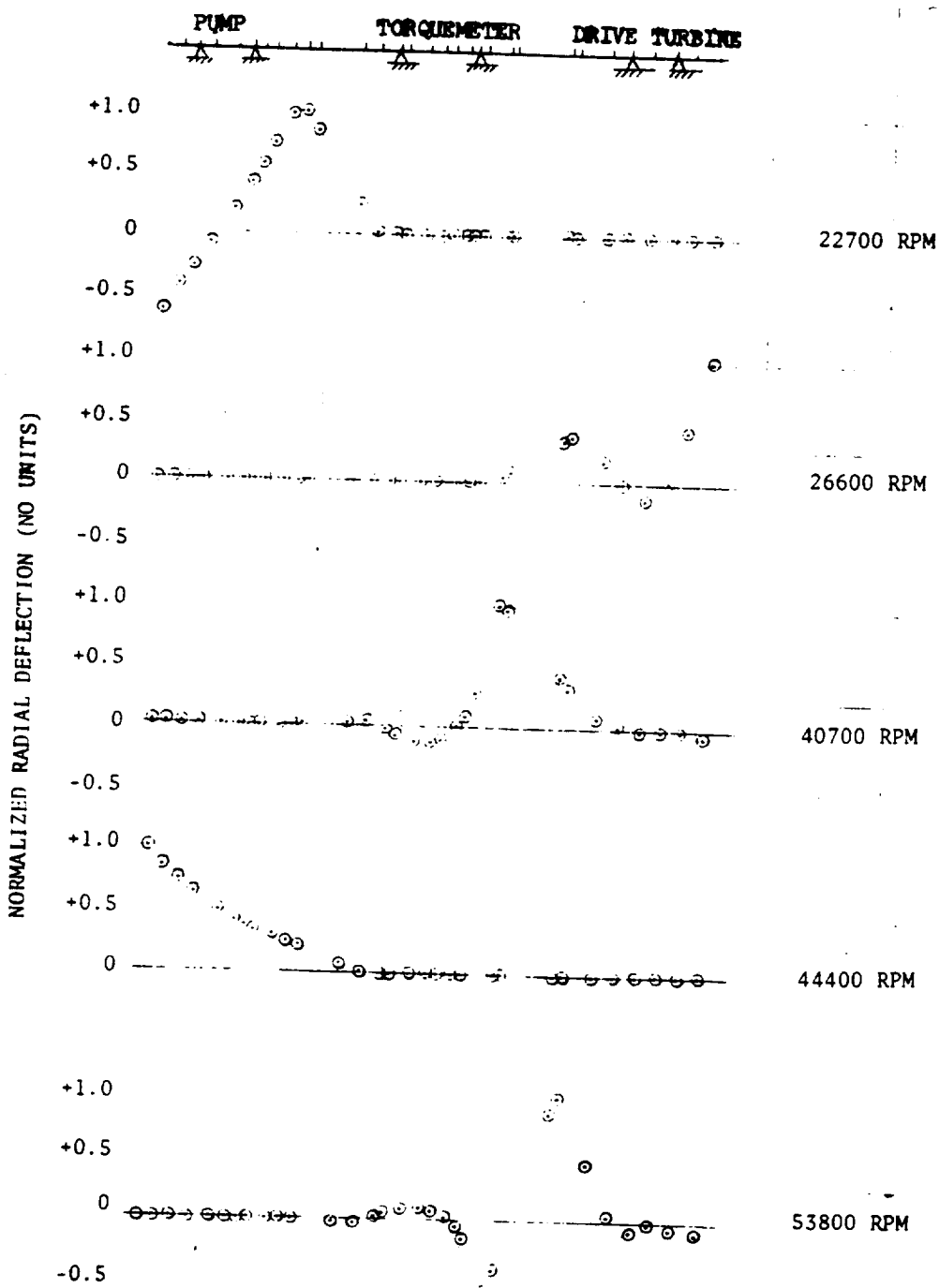


Figure 53. Normalized Mode Shape of Torquemeter/Turbine Drive System as a Function of Position Along Rotor Spring Rate for Both Pump Bearings = 10^4 lb/in.

R-8494-1

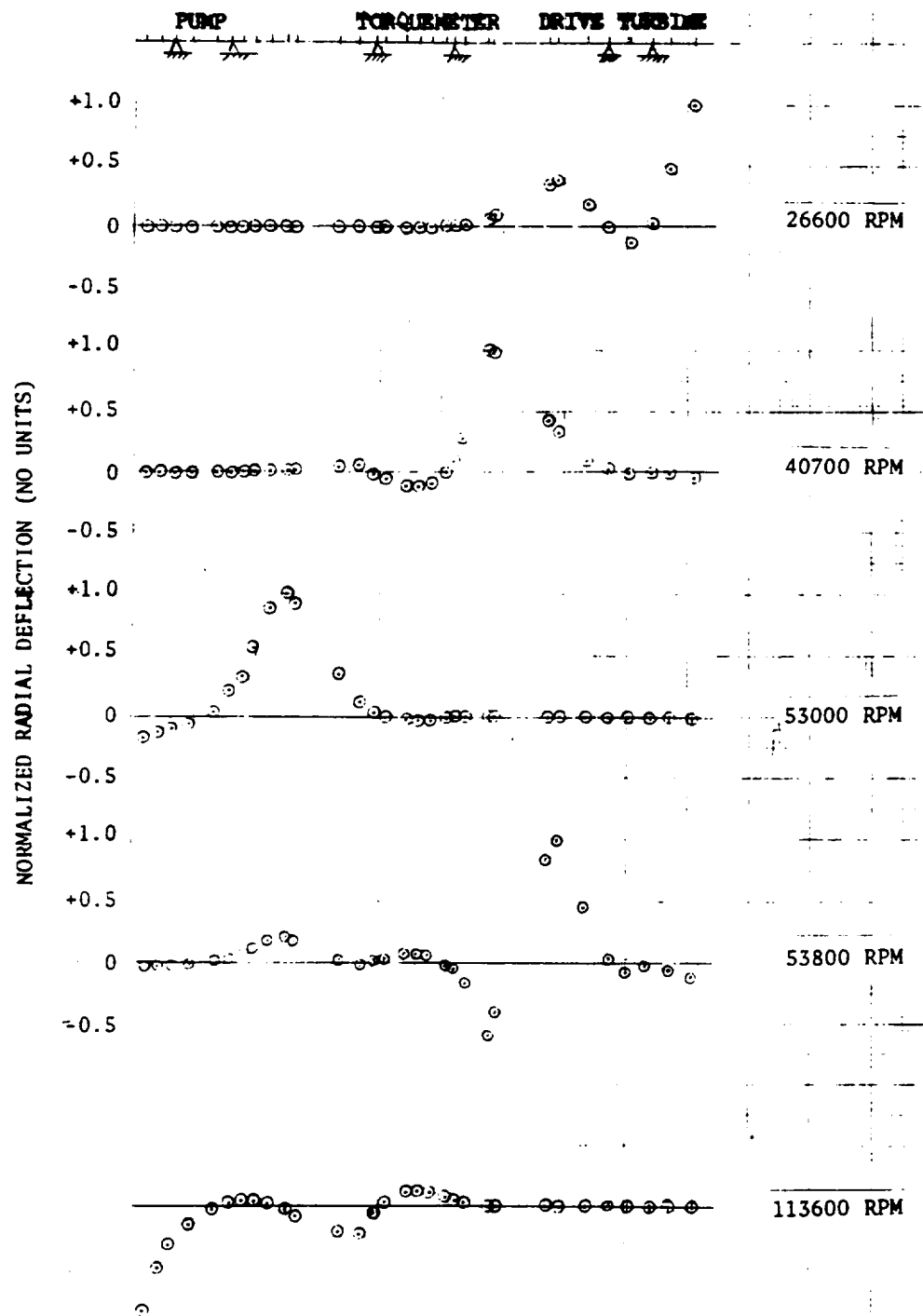


Figure 54. Relative Deflection of Torquemeter/Turbine Drive System as a Function of Position Along Rotor Spring Rate for Both Pump Bearings = 10^5 lb/in.

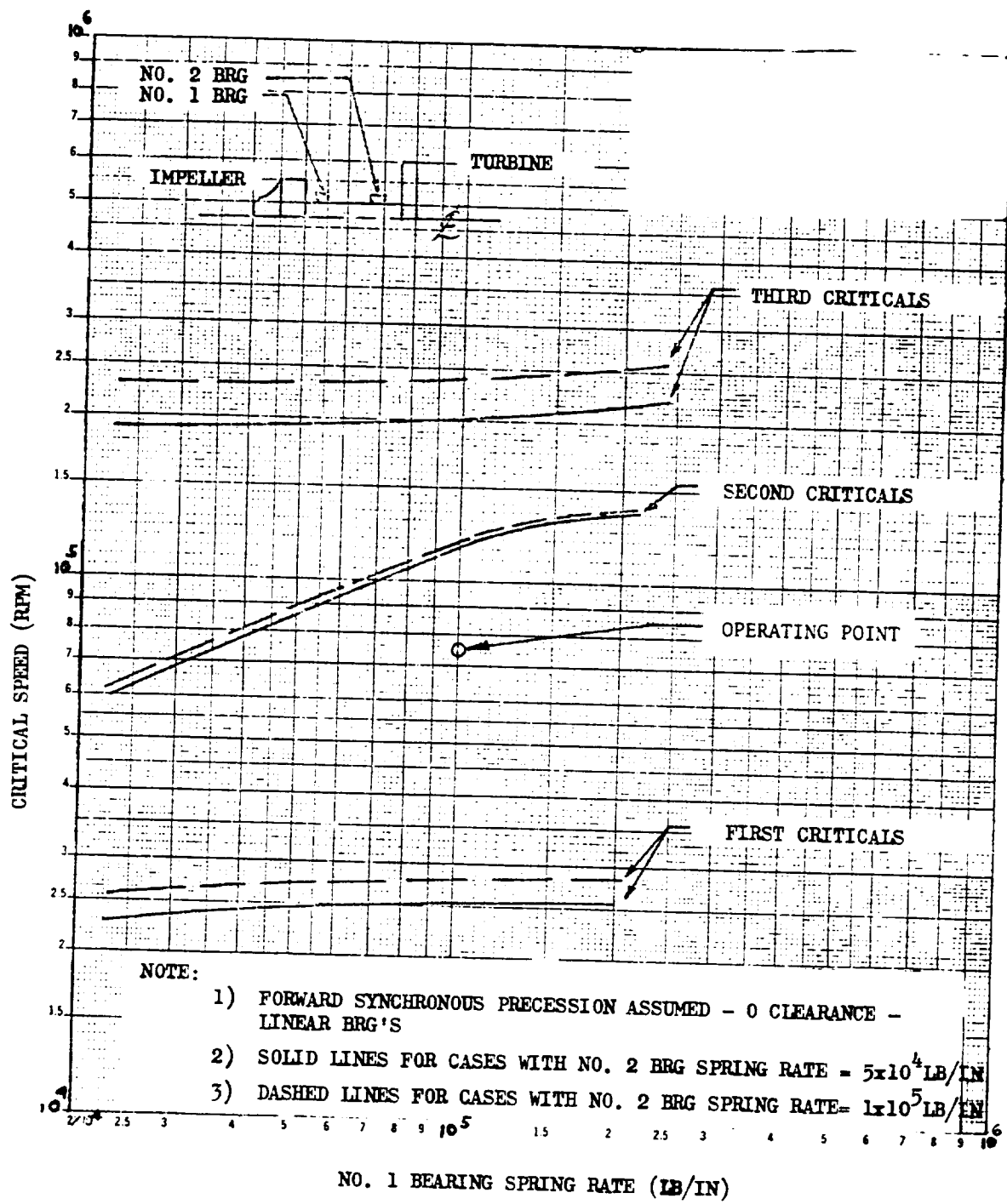


Figure 55. Mark-36 Pump With Turbine Drive Critical Speeds

R-8494-1

NOTE:

- 1) FORWARD SYNCHRONOUS PRECESSION ASSUMED
- 2) ALL BEARING SPRING RATES = 1×10^5 LB/IN
- 3) • JOINT
- 4) o BEARING

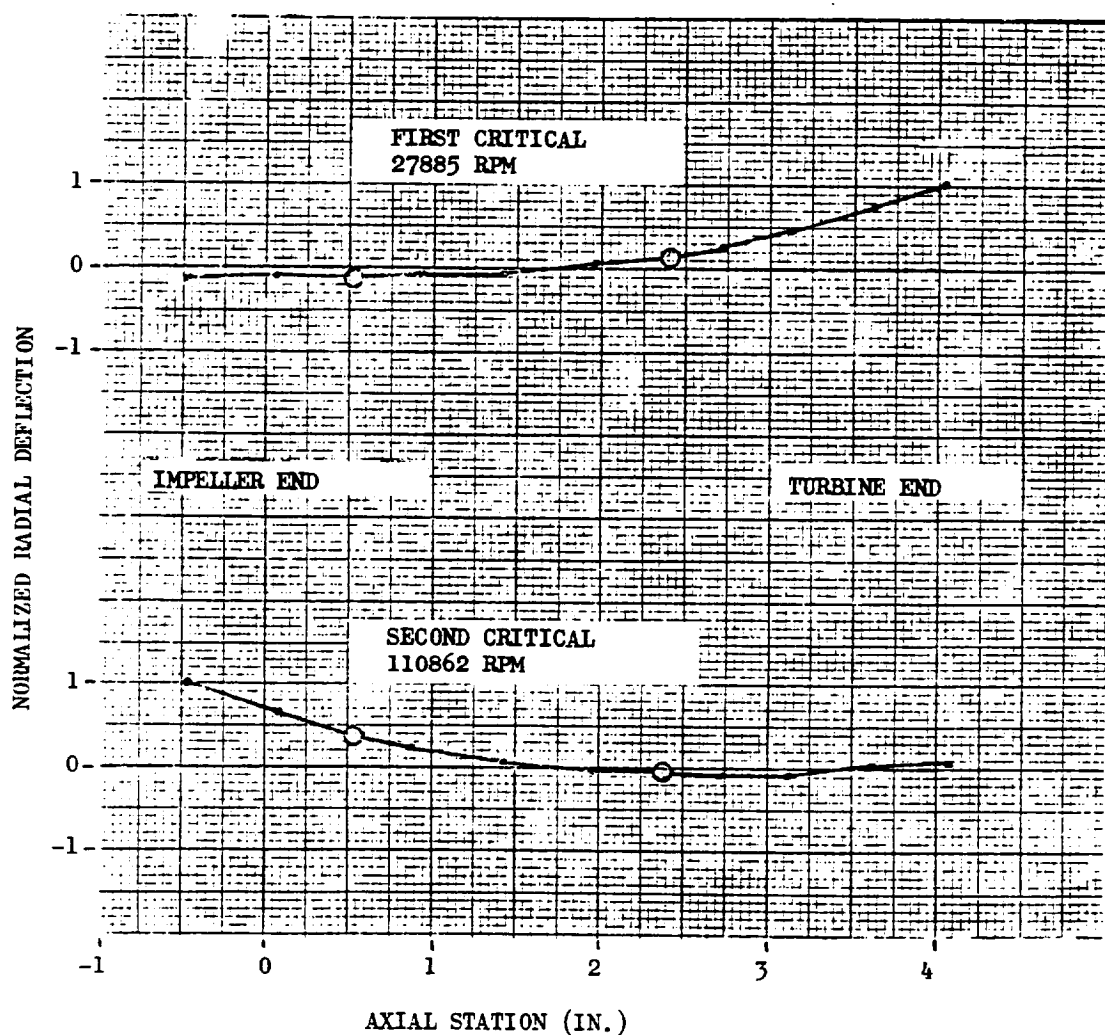
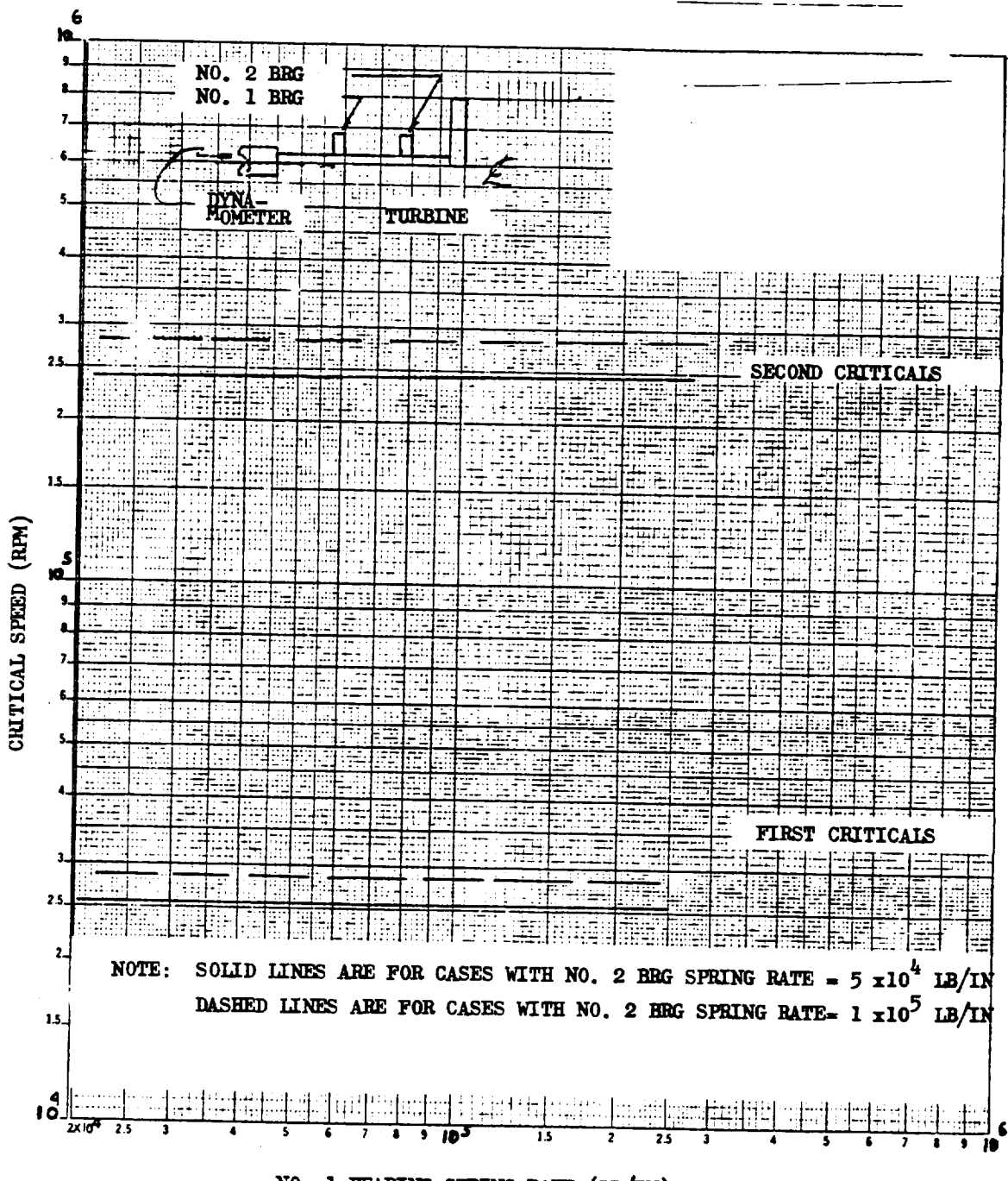


Figure 56. Mark-36 Pump With Turbine Drive, Critical Speed Mode Shapes



NO. 1 BEARING SPRING RATE (LB/IN)

Figure 57. Mark-36 Turbine Coupled to Vortec A-20 Dynamometer,
 Critical Speeds

R-8494-1

NOTE:

- 1) FORWARD SYNCHRONOUS PRECESSION ASSUMED
- 2) ALL BEARING SPRING RATES EQUAL 5×10^4 LB/IN
- 3) COUPLING AT DYNAMOMETER TREATED AS CONTINUOUS ELASTIC ELEMENT
- 4) SECOND CRITICAL = 241049 RPM

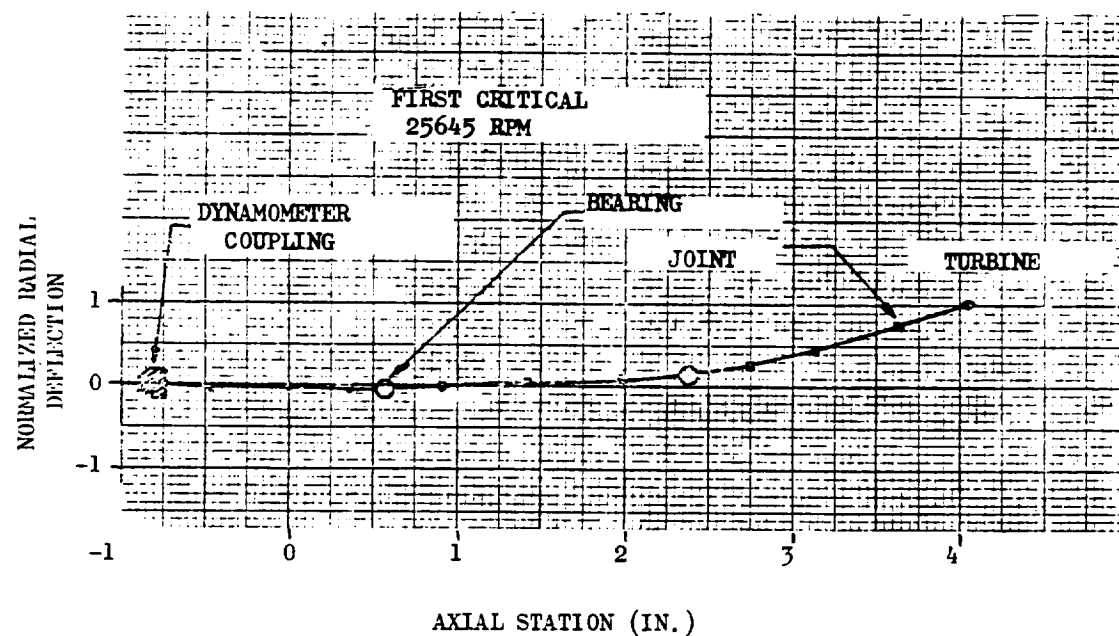


Figure 58. Mark-36 Turbine Coupled to Vortec A-29 Dynamometer,
Critical Speed Mode Shapes

loss can be very high. A study has been made in an attempt to minimize the power loss from these effects.

A close examination of the loss mechanisms would provide a clue as to a method by which they may be reduced. Disk friction in a centrifugal pump requires that power be used to rotate the fluid adjacent to the impeller shrouds. The average velocity of this fluid is in the order of 50 percent of the angular velocity of the shroud since the configuration of a centrifugal pump shroud approximates very nearly a rotating disk surrounded by fluid and enclosed in a housing. The moment due to frictional resistance on an enclosed rotating disk can be expressed by the equation

$$T = \frac{1}{2} \zeta_M \rho \omega^2 R^5 \quad (41)$$

where

ρ = mass density of the fluid, slugs/ft³

R = disk radius, ft

ζ_M = moment coefficient

The moment coefficient is a function of disk-housing clearance, disk roughness and Reynolds number. The Reynolds number (R_e) is defined as:

$$R_e = \frac{\omega R^2}{v} \quad (42)$$

The moment coefficient has been obtained experimentally by Daily and Nece (Ref. 18) and others (Ref. 19 and 20). Data from these sources for smooth disks are presented in Fig. 59. Agreement among these sources is very good.

As is evident from Eq. 41, the disk friction is greatly influenced by the angular velocity and size of the pump. It would, therefore, be advantageous to reduce these values in order to reduce the disk friction. For a given pump, the required head and flow restrict the speed and diameter. In rocket propellant pumps high speed and small diameters are more desirable. The size and speed fixes the power loss due to disk friction for a given density and viscosity of the fluid acting on

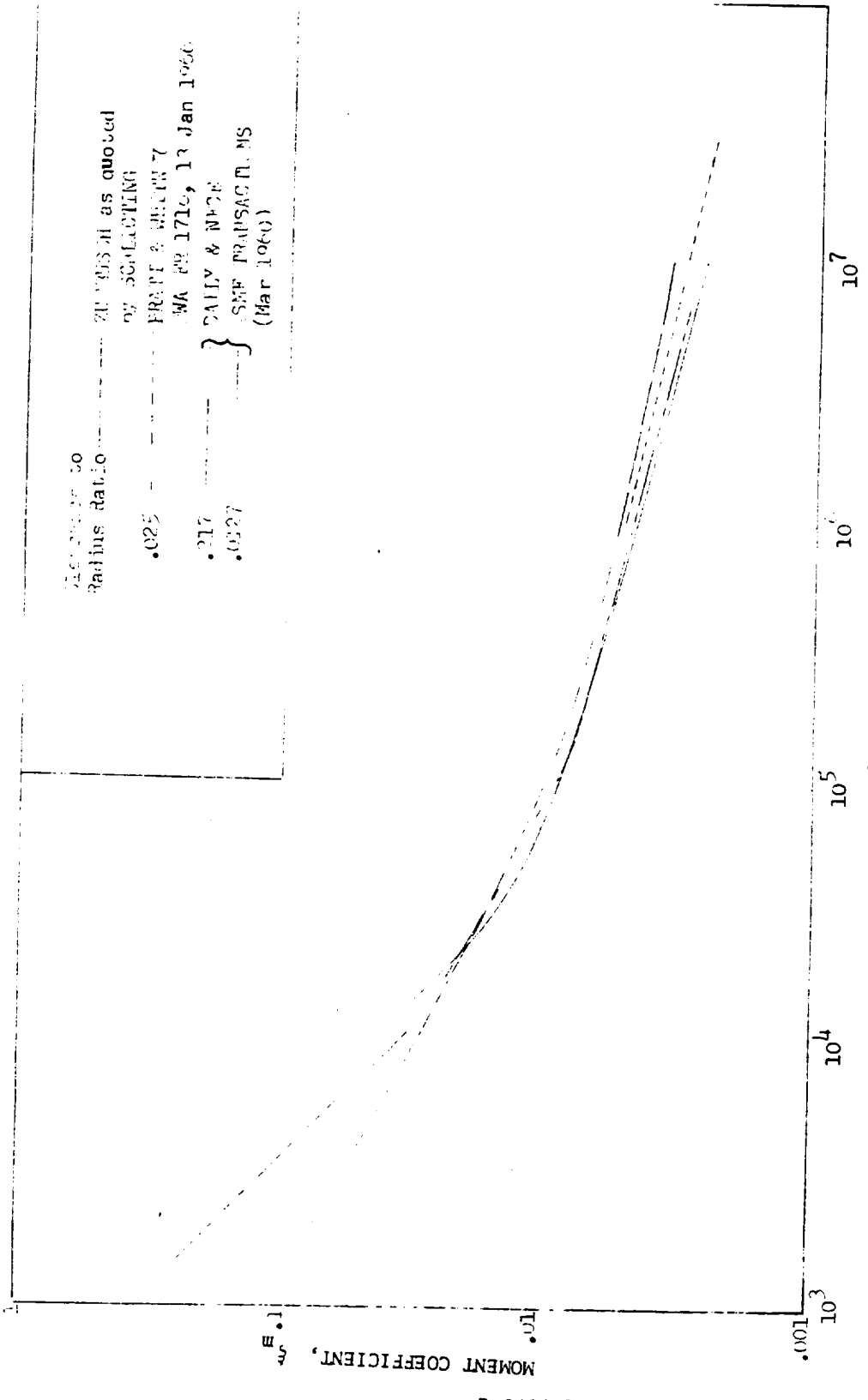


Figure 59. Moment Coefficients for Smooth Disks Rotating in an Enclosed Housing

the shrouds. The operation of a gaseous cavity acting over the shrouds of an impeller could reduce friction loss considerably. Figure 60 presents disk friction power loss on an impeller front shroud acting in fluorine as a function of temperature. The static front shroud pressure is 1500 psia (1.03×10^7 N/m²) (well above the critical point pressure). As the temperature increases the density decreases resulting in a decreased power loss.

The maintenance of a stable gas cavity is a difficult problem. Calculations indicate that seals would be necessary to entrap or maintain a gas cavity with the requisite qualities of low density and high pressure. The low density is required to minimize friction but the high pressure is necessary to maintain positive leakage from the cavity for stability. Both requirements could be satisfied by tapping high pressure fluid from the pump discharge and passing it through a heat exchanger to reduce its density. Assuming the gas cavity inner seal has a clearance of 0.0005 inch (0.0127 mm), the impeller eye leakage flow would be 0.0706 lb/sec (0.0325 Kg/s) at 760 R (422 K) or 8.5 percent by volume of the pump delivered flow for a 12 gpm (7.57×10^{-4} m³/s) fluorine pump. This leakage would be injected into the impeller inlet and could cause severe cavitation problems. An energy balance indicates the mean inlet fluid temperature if completely mixed would be increased from 159 R to 165 R (88 R to 92 K). This, in turn, would cause a minimum increase in required inlet NPSH of 14.3 feet (4.4m) at the impeller eye.

Of prime importance to the study is the fact that the pump axial thrust balance must be maintained. This requires that the pressure distribution and acting areas on the front and rear impeller shrouds must be manipulated simultaneously to maintain this balance. Thrust balance limits the location of wear ring placement for minimum power loss. A method designed to eliminate this restriction is the use of a gas operated balance piston in the vicinity of the seal package which would control axial thrust. This would allow the pump to be designed for optimum efficiency since the gas cavity on the impeller shrouds is severely handicapped by axial thrust control problems. The use of helium is ideal for the gas operated balance piston pressurization due to its low density and inert qualities. This

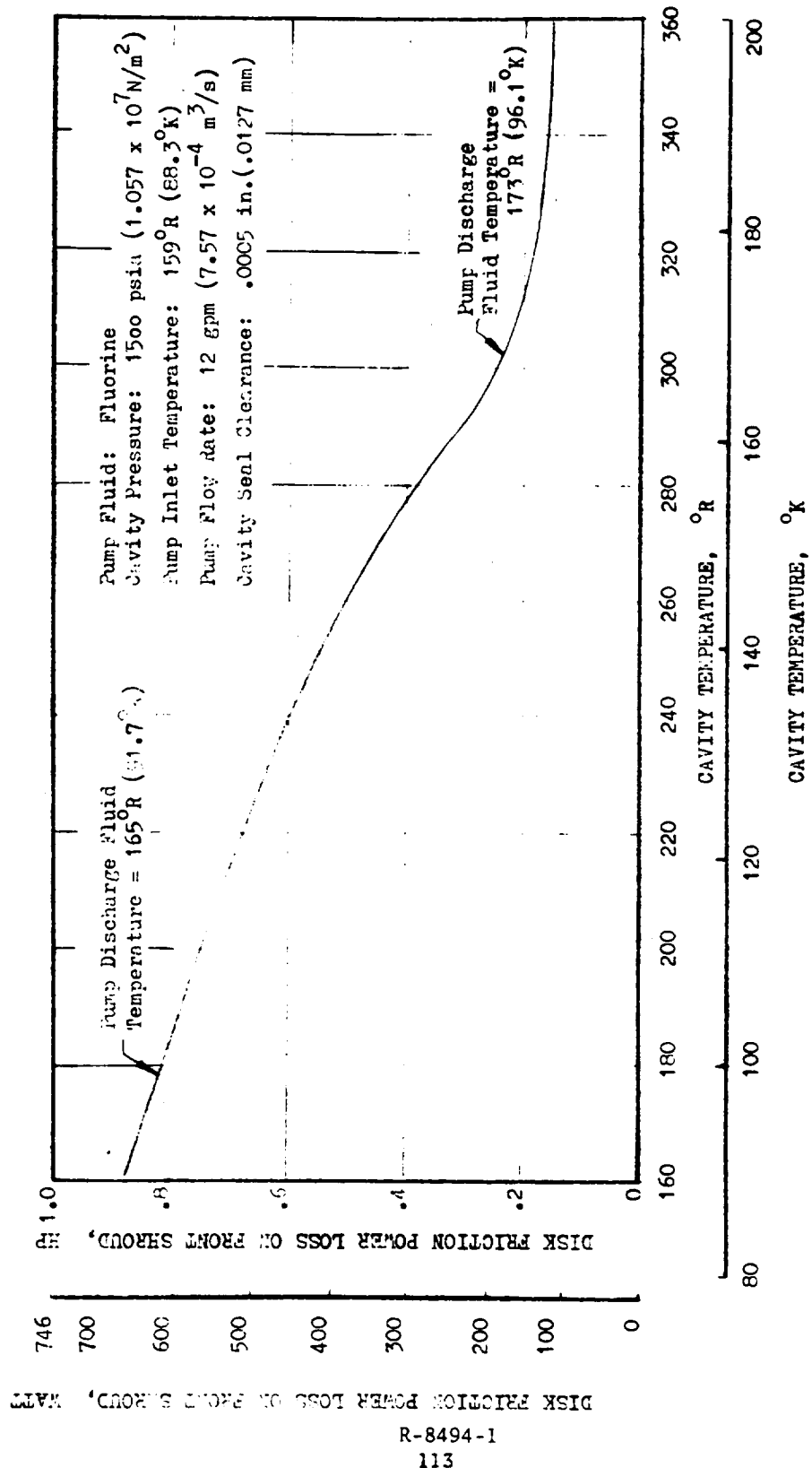


Figure 60. Front Shroud Disk Friction for Liquid Cavity

concept of a gas operated piston balanced pump is presented in Fig. 61. The piston is located between the primary fluorine face seal and the turbine gas seal with an intermediate floating gas seal on the piston outer diameter. Friction losses of the seal and piston are small.

Figure 61 presents the impeller front shroud gas cavity used in conjunction with a smooth rear shroud without a rear wear ring. The axial thrust imbalance is taken up by the balance piston.

Data indicate that the disk friction is reduced when an open face impeller is used in place of a shrouded impeller. This would result in a simpler design than the gas cavity front shroud configuration, eliminate the heat exchanger requirement; however, close axial clearances would be required to attain acceptable efficiency. This design is shown in Fig. 62. The gas operated balance piston is still used to provide axial thrust balance and eliminate the rear wear ring leakage.

A breakdown of the power losses is shown in Table IX to indicate the changes in loss values calculated for the several pump configurations shown. The advantages presented are the low pressure differentials across the face seals and the small friction power loss achieved while still obtaining an axial thrust balance. This combined with improvements in hydraulic efficiency show fairly large overall efficiency increases. These concepts although considered feasible, would require additional development to achieve a reliable working system and are, therefore, considered to be outside the scope of this contract.

BEARING AND SEAL POWER LOSSES

High relative power loss due to the pump bearing and seal package must be expected in small pump systems of this type. The power absorption due to rubbing contact at the seal face is proportional to the diameter and relative speed of the seal face which is a function of seal cavity pressure. The loss relationship can be expressed for a seal as:

$$P_{\text{loss}} \propto D_p N \quad (43)$$

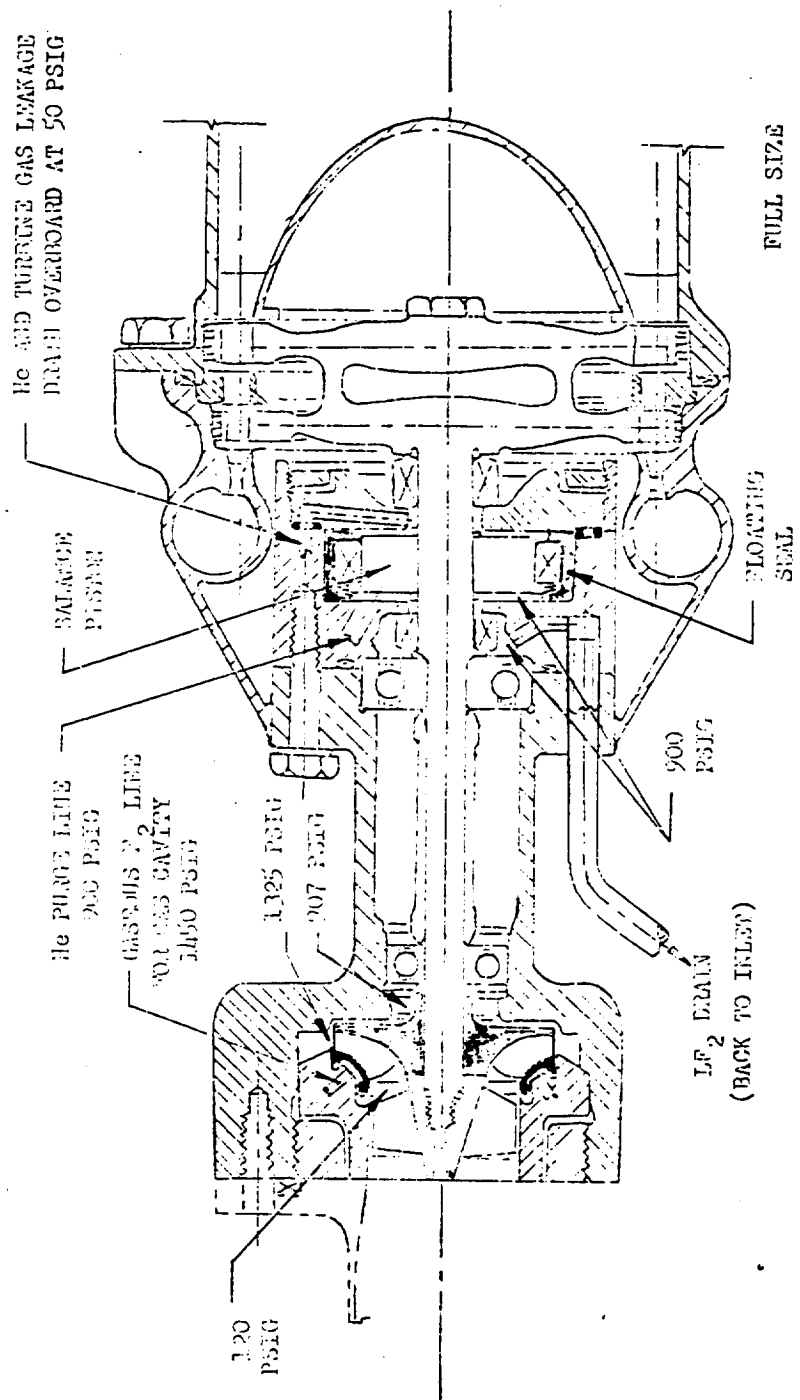


Figure 61. Schematic of a Modified Mark 36, 12-gpm Centrifugal Pump Utilizing a Gas Cavity on Impeller Front Shroud and a Balance Piston

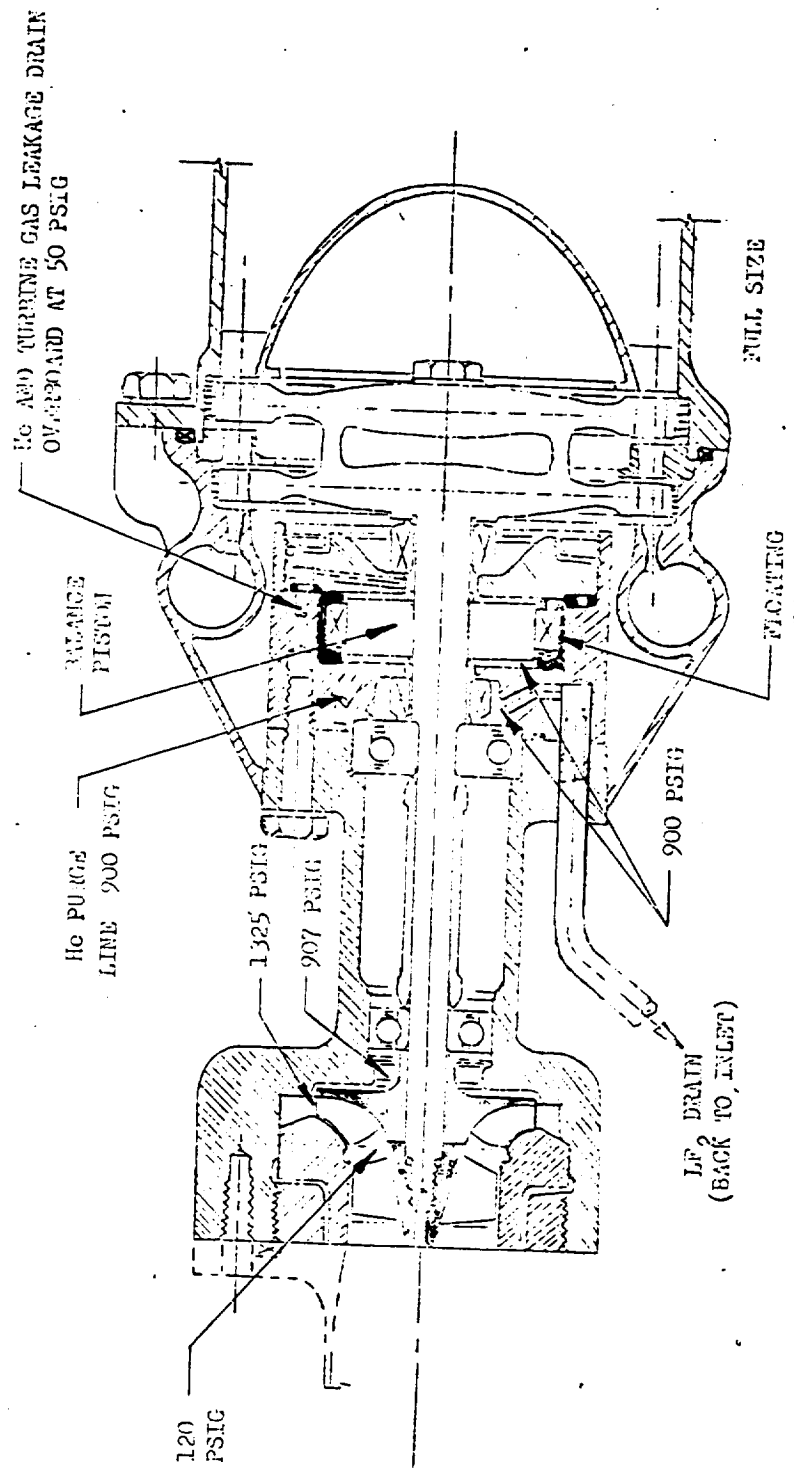


Figure 62. Schematic of a Modified Mark 36, 12-gpm Centrifugal Pump Utilizing an Open-Face Impeller and Balance Piston

TABLE IX. CENTRIFUGAL PUMP POWER BREAKDOWN

Power	Present Pump Design		Balance Piston Pump				
			Open Face Impeller (Fig. 62)		Gas Cavity on Front Shroud (Fig. 61)		
	hp	(kw)	hp	(kw)	hp	(kw)	
Delivered Fluid Power	10.40	(7.76)	10.40	(7.76)	10.40	(7.76)	
Power Loss From Leakage of Impeller Seals	2.69	(2.01)	0.43	(0.32)	0.38	(0.28)	
Power Loss From Disk Friction on Impeller Shrouds	1.77	(1.32)	0.91	(0.68)	1.07	(0.80)	
Other Pump Power Losses:							
Skin Friction, Incidence, Diffusion, and Momentum Loss	3.09	(2.31)	3.50	(2.61)	1.71	(1.28)	
Hydraulic Power	17.95	(13.39)	15.24	(11.37)	13.56	(10.12)	
Friction Power							
Face Seals	0.93	(0.69)	0.23	(0.17)	0.23	(0.17)	
Shaft Seal	0.66	(0.49)	--	--	--	--	
Bearings	0.08	(0.06)	0.08	(0.06)	0.08	(0.06)	
Floating Seal	--		0.05	(0.04)	0.03	(0.02)	
Balance Piston	--		0.02	(0.01)	0.01	(0.01)	
Net Required Pump Power	19.62	(14.64)	16.62	(12.40)	13.91	(10.38)	
Overall Pump Efficiency, percent	53.0		62.6		74.6		
Additional Helium Purge Flow Required for Balance Piston				lb/sec (g/s)	lb/sec (g/s)		
				0.004 (1.816)	0.004 (1.816)		

where

- P_{loss} = power loss due to frictional resistance
D = seal face diameter
P = differential pressure across the seal
N = rotational speed of the seal

Table X presents torque values and power loss values for face and shaft seals at several speeds, diameters, and cavity pressures. These values are scaled from test data in dry GN_2 .

An equivalent friction coefficient K can be expressed for a bearing which will allow calculation of frictional torque that resists shaft rotation. The torque T can be expressed by the relation:

$$T = KDF \quad (44)$$

where

- K = equivalent friction coefficient
D = bearing bore diameter
F = axial bearing load

The equivalent friction coefficient used here is 0.004, and bearing friction torque and power loss values are presented in Table X (Ref. 21). The relationships shown are used to determine the power requirements of the bearing and seal package. The friction loss due to bearing coolant fluid churning was calculated as 0.01 in.-lb (0.001 Nm), which is negligible.

TABLE X. POWER LOSS VALUES DUE TO FRICTION IN SEALS AND BEARINGS

Diameter, in. (cm)	Face Seal Friction Torque			Friction Horsepower, hp (kw)
	Pressure, psi (N/m ² × 10 ⁻⁶)	Speed, rpm	Friction Torque* in.-lb (Nm)	
0.5 (1.27)	150 (1.03)	75,000	0.39 (0.04)	0.46 (0.34)
0.5 (1.27)	150 (1.03)	50,000	0.39 (0.04)	0.31 (0.23)
1.5 (3.81)	150 (1.03)	30,000	3.51 (0.40)	1.67 (1.25)
1.5 (3.81)	150 (1.03)	14,000	3.51 (0.40)	0.78 (0.58)

*Source: Dry GN₂ pressure torque tests of Mark 15F primary seal corrected for seal size

Diameter, in. (cm)	Shaft Riding Seal Friction Torque			Friction Horsepower, hp (kw)
	Pressure, psi (N/m ² × 10 ⁻⁶)	Speed, rpm	Friction Torque* in.-lb (Nm)	
0.375 (0.953)	150 (1.03)	75,000	0.55 (0.06)	0.66 (0.49)
0.375 (0.953)	150 (1.03)	50,000	0.55 (0.06)	0.44 (0.33)
1.87 (4.75)	150 (1.03)	30,000	13.77 (1.56)	6.55 (4.89)
1.87 (4.75)	150 (1.03)	14,000	13.77 (1.56)	3.06 (2.28)

*Source: Dry GN₂ pressure torque tests of Mark 15F shaft riding seal corrected for seal size

Bore, mm	Bearing Friction Torque			Friction Horsepower Loss Each Bearing, hp (kw)
	Load, 1b (N)	Speed, rpm	Friction Torque in.-lb (Nm)	
8	25	111	75,000	0.3* (0.003)
12	25	111	75,000	0.5* (0.006)
20	60	267	50,000	0.19** (0.02)
30	175	778	30,000	0.83** (0.09)

*Source: A. B. Jones bearing analysis

**Use of equivalent friction coefficient at bore of 0.004

NOTE: Friction loss due to fluid churning is not included in bearing losses

TASK V: POSITIVE DISPLACEMENT PUMP EVALUATION

Design evaluations of a number of positive displacement pumps were made which led to the selection of a gear pump as the concept best suited to meet the same requirements as the rotating pump which are as follows:

Pump inlet pressure, psia	35 ($2.41 \times 10^5 \text{ N/m}^2$)
Pump inlet temperature, R	159 (88.5 K) (LF_2 saturated at 20 psia) ($1.4 \times 10^5 \text{ N/m}^2$)
Pump exit pressure, psia	1500 ($1.03 \times 10^7 \text{ N/m}^2$)
Design flowrate, gpm	12 ($7.57 \times 10^{-4} \text{ m}^3/\text{s}$)
Pumped fluid	LF_2 (capability of FLOX operation)

To select the most suitable positive displacement pump, evaluation criteria and rating system similar to those used to evaluate the rotating pumps were devised. As shown in Table XI, it consists of four major categories--performance life, reliability, and cost:

Performance Criteria:

1. Volumetric efficiency
2. Hydraulic efficiency
3. Overall efficiency
4. Size and weight
5. Friction

Life Criteria:

1. Seal loads
2. Seal speeds
3. Bearing loads
4. Material compatibility

TABLE XI. POSITIVE DISPLACEMENT PUMP RATING CHART

Performance (total points = 25)

Volumetric Efficiency, η_v	5
Hydraulic Efficiency, η_h	5
Overall Efficiency, η_o	5
Size and Weight	5
Friction ;	5

Life (total points = 20)

Seal Loads	5
Seal Speeds	5
Bearing Leads	5
Material Compatability	5

Reliability (total points = 30)

Clearances	10
External Leakage	10
Valve Factor	5
Pump Discharge Pressure Oscillations	5

Costs (total points = 25)

Development Costs	15
Unit Costs	10

Reliability Criteria:

1. Clearances (same as rotating pump)
2. External leakage (same as rotating pump)
3. Valve factor (accounts for increase in design complexity if valves are required)
4. Pump discharge pressure oscillations (same as rotating pump)

Cost Criteria:

1. Development costs
2. Unit costs

The pump concepts to be evaluated were selected as representative of the types currently in use and deemed capable of meeting the flow, head, and efficiency requirements. Pumps selected to be evaluated were:

1. Gear
2. Piston (axial)
3. Piston (radial)
4. Vane
5. Diaphragm
6. Helirotor

A discussion of each of the positive displacement pump concepts follows.

GEAR PUMP

Introduction

Fluid in a gear pump is pumped in the open spaces between the gear teeth and the casing. The teeth coming out of mesh create a suction which draws liquid from the inlet line, filling the tooth spaces. Rotation of the gears carries the fluid in

the tooth spaces from the inlet to the discharge side. The teeth mesh at the discharge, displacing the fluid in the spaces and forcing it into the discharge line.

Gear pumps have an inherent advantage over other positive displacement pumps because of their simplicity. Inlet and discharge valves are not required, but a relief valve is normally included to limit the maximum pressure in the system.

Analysis

The gear pumps considered consisted of two meshing gears. Units containing three or more gears have lower volumetric efficiencies, and in the flow range of interest have no advantage over the two gear units. To simplify the pump and to minimize manufacturing costs, the configuration studies contained open gears of equal diameter.

In establishing the performance of the gear pump, a significant parameter is the volumetric efficiency, which is a measure of the leakage losses. Volumetric efficiency (η_v) is defined as:

$$\eta_v = 1 - \frac{Q_L}{Q_{TH}} \quad (45)$$

where Q_L is the leakage (also referred to as "slip") in the pump, and Q_{TH} is the theoretical displacement of the pump, with zero leakage. For preliminary analysis it is assumed that the fluid recirculated by the pump is the amount trapped between the tip of a gear tooth and the root circle of the tooth space when fully meshed. The equation for the theoretical displacement then becomes:

$$Q_{TH} = \frac{(D_{O.D.}^2 - D_{I.D.}^2) \pi LN}{(4)(60)} \quad (46)$$

where

Q_{TH} is expressed in ft^3/sec

$D_{O.D.}$ = outside diameter of gear teeth, ft

$D_{I.D.}$ = working depth diameter ($D_{O.D.} - 4x$ addendum), ft

L = axial length of gear teeth, ft

N = rpm

The theoretical volume of liquid delivered per revolution, is given by:

$$q = \frac{(D_{O.D.}^2 - D_{I.D.}^2) \pi L}{4} \quad (47)$$

where the terms are as defined above and q is expressed in ft^3 per revolution.

Equation 46 can then be expressed as:

$$Q_{TH} = \frac{qN}{60} \quad (48)$$

Substituting Eq. 48 into 45 will yield:

$$\eta_V = 1 - \frac{60 Q_L}{q N} \quad (49)$$

To calculate the internal leakage, Q_L , the Reynolds number in the gear to housing clearances has to be established. The expression for the Reynolds number for the laminar flow region is (derivation given Appendix A):

$$R_e = \frac{\Delta p \rho \delta^3}{6 \mu^2 l} \quad (50)$$

where

Δp = differential pressure across leak path (lb/ft^2)

ρ = mass density ($\text{lb sec}^2/\text{ft}^4$)

δ = clearance (ft)

μ = absolute viscosity ($\text{lb sec}/\text{ft}^2$)

l = leak path length parallel flow (ft)

To have a condition of laminar flow, the Reynolds number must be less than 4000. Solving the above equation for the clearance, δ , it is found that the condition of laminar flow ($R_e < 4000$) is satisfied only if the clearance is smaller than 0.00015 inch (3.8×10^{-6} m). Since the gear-to-housing clearances in the pump are expected to be higher, the leakage flow will be of turbulent type.

In the turbulent flow regime the volumetric leakage flow is expressed by the following relationship (see Appendix A for derivation):

$$Q_L = 4.6 \frac{\Delta p^{.57} g^{.43} w \delta^{1.72}}{\gamma^{.43} \mu^{.143} l^{.57}} \quad (51)$$

where the terms are as defined above, and

- Q = volumetric flow, ft^3/sec
- g = gravitational constant (32.2 ft/sec^2)
- w = leak path width, ft
- γ = specific weight, lb/ft^3

Rewriting this equation to account for the various leakage paths in the gear pump results in:

$$Q_L = 4.6 \frac{\Delta p^{.57} g^{.43}}{\gamma^{.43} \mu^{.143}} \left[\frac{2w_1 \delta_1^{1.72}}{l_1^{.57}} + \frac{1.674D \delta_2^{1.72}}{D^{.57}} + \frac{w_2 \delta_2^{1.72}}{l_3^{.57}} \right] \quad (52)$$

where the terms are as defined above, and

- w_1 = gear tooth width, ft
- δ_1 = gear tip clearance (radial), ft
- l_1 = leak path length along gear tip, ft
- D = gear diameter, ft
- δ_2 = axial clearance, ft
- l_2 = leak path length at mesh, ft
- w_2 = leak path width at mesh, ft

The first term in the parenthesis reflects the leak path at the gear tip, the second term at gear side and the third term at the gear mesh.

When this expression for leakage is substituted into Eq. 49, an expression for volumetric efficiency in terms of pump geometry is obtained:

$$\eta_v = 1 - \frac{4.6 \Delta P \cdot .57 g \cdot .43}{\gamma \cdot .43 \mu \cdot 143 qN} \left[\frac{2w_1 \delta_1^{1.72}}{\ell_1^{.57}} + \frac{1.67 D \delta_2^{1.72}}{D^{.57}} + \frac{w_2 \delta_2^{1.72}}{\ell_3^{.57}} \right] \quad (53)$$

Using this equation, the plot of diameter versus axial clearance shown in Fig. 63 can be constructed. Ninety percent volumetric efficiency can be obtained with an axial clearance of 0.0009 inch (2.286×10^{-5} m), assuming that the radial clearance is held constant at 0.0005 inch (1.27×10^{-5} m).

The effect of axial clearance on volumetric efficiency is shown in Fig. 64. This plot is based on Eq. 53, using a fixed gear geometry with only the axial clearance of the gear changing. The volumetric efficiency improves if the axial location of the gears is such that the total axial clearance is split on either side of the gears. This effect also is indicated in Fig. 64.

As can be seen from Fig. 63 and 64, close axial clearances must be maintained. Due to these clearances, shaft bending must be held to a minimum. To minimize shaft bending, the bearings for each gear must be placed one above the other as close to the gears as possible. The anticipated high radial loads together with bearing stiffness (pounds load divided by radial deflection) and life requirements indicate roller bearings are required.

Bearing radial load is obtained by:

$$F = (D_{OD}) (L) (\Delta P) \quad (54)$$

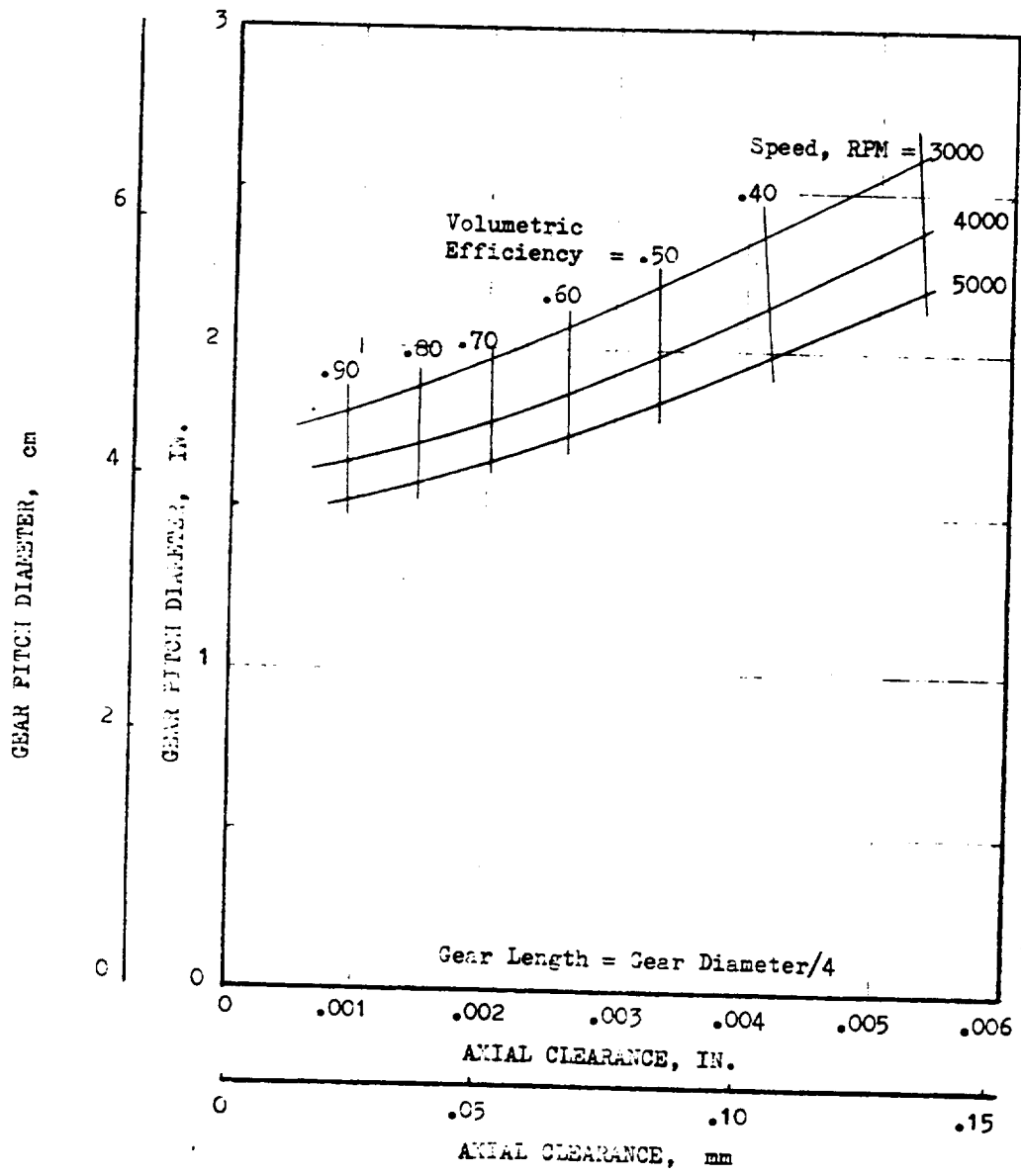


Figure 63. Rotor Diameter as a Function of Axial Clearance

R-8494-1

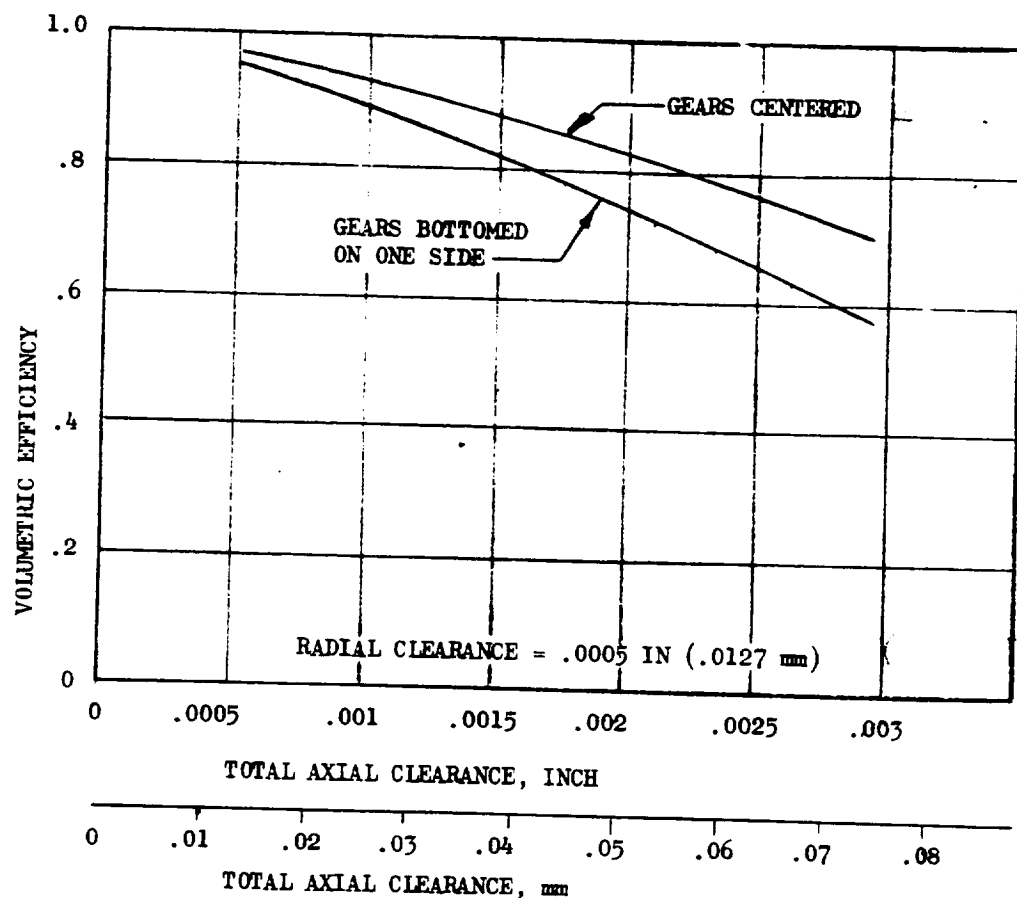


Figure 64. Clearance Effect on Gear Pump Efficiency

R-8494-1

where

- F = radial load, lb
D_{OD} = outside diameter of gear, ft
L = axial length of gear, ft
 ΔP = delta pressure across gear, lb/ft²

The radial load on the bearings can be reduced by increasing the pump speed and thereby reducing the required gear diameter. However, a maximum satisfactory operating speed exists above which the possibility of cavitation occurring in the pumping cavity is theoretically possible. According to Wilson (Ref.22), cavitation results if the liquid cannot keep up with the moving element. The inlet pressure to the pump provides the only energy available to accelerate the fluid. Thorough tests on gear pumps have indicated a consistent relationship for cavitation occurring (Ref. 22):

$$\frac{Q_{LC}}{Q_{TH}} = 1 - \left(\frac{P_a g}{\gamma C V_p^2} \right) \left(\frac{P_i - P_v}{P_a} \right) \quad (55)$$

where

- Q_{LC} = flow loss due to cavitation, ft³/sec
Q_{TH} = theoretical pump flow, ft³/sec
P_a = atmospheric pressure, lb/ft²
P_i = pump inlet pressure, lb/ft²
P_v = vapor pressure of fluid, lb/ft²
V_p = velocity of gear tip, ft/sec
 γ = specific weight, lb/ft³
C = cavitation factor $(V_2 - V_1)/V_p$

If zero cavitation is assumed, then $Q_{LC}/Q_T = 0$, and the equation can be rewritten:

$$\left(\frac{P_a g}{\gamma C V_p^2} \right) \left(\frac{P_i - P_v}{P_a} \right) = 1 \quad (56)$$

Again according to Wilson (Ref.22), the cavitation factor, C , for a well-designed gear pump is about 0.4. Using this and known values for P_a , P_i , P_v , and γ , Eq. 56 can be solved for V_p . Then, for a given gear diameter, only one rotational speed satisfied the relationship:

$$V = \frac{N}{60} \pi D_{OD} \quad (57)$$

where

$\frac{N}{60}$ = rotational speed, rev/sec

D_{OD} = gear diameter, ft

V = velocity, ft/sec

This speed is the maximum speed at which a pump with a given gear diameter can be operated without cavitation occurring. This maximum speed then establishes the amount of bearing radial load by setting the minimum diameter of the gear.

The relationship of gear tip diameter and gear width (axial length) to the required speed to meet a delivered flow of 12 gpm is shown in Fig. 65. Also plotted are bearing radial loads and the cavitation limit line. Operation at speed to the right of this line will result in cavitation unless the inlet pressure to the pump is increased above the present 15 psi above the fluid vapor pressure.

The losses in a gear pump are slip (or leakage) losses and torque losses. The leakage losses have been discussed above. The torque losses are of three types:

1. Those that result from viscous shear in the leak paths at the gear tips and ends.

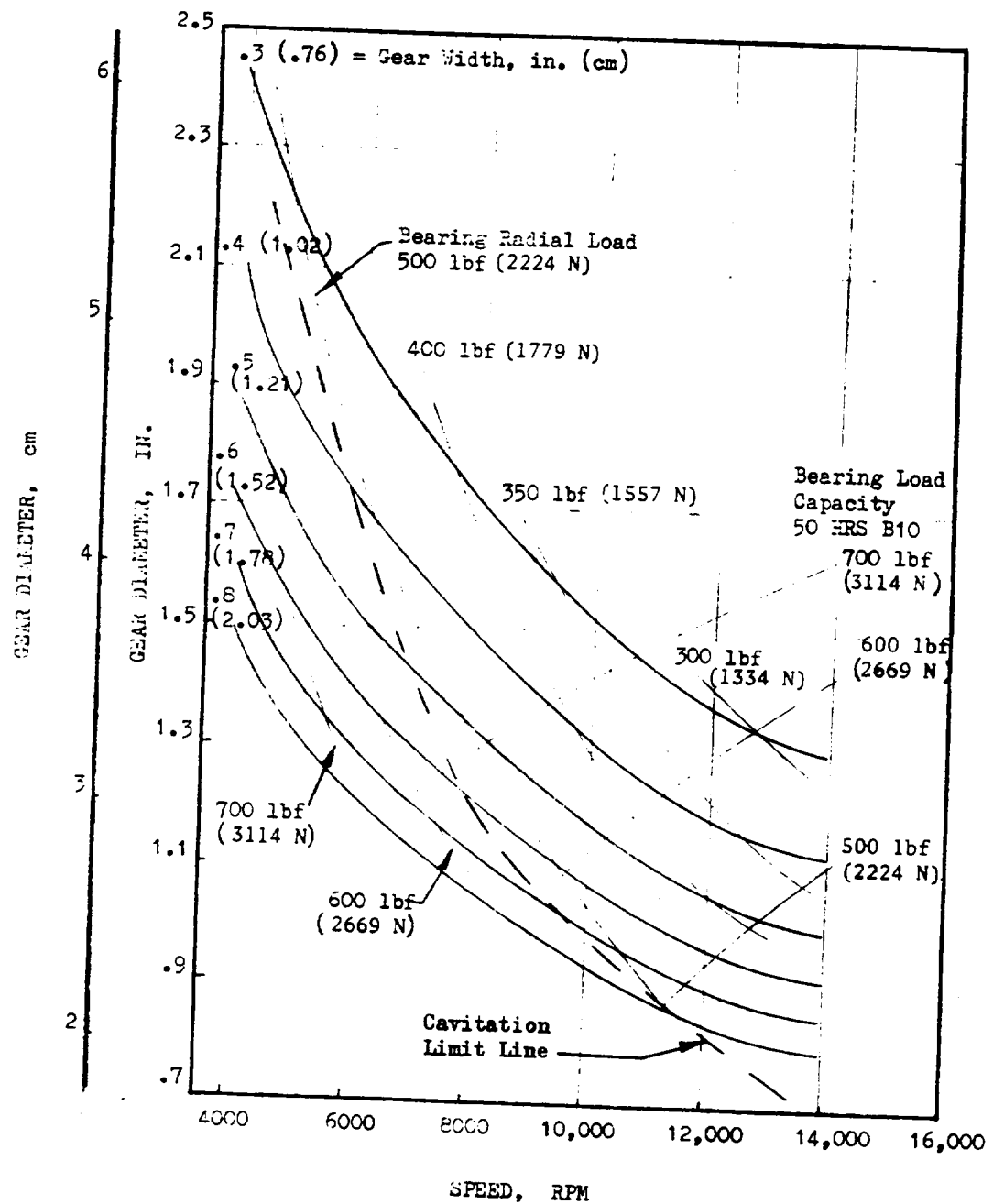


Figure 65. Gear Diameter as a Function of Speed

R-8494-1

154

2. Those due to friction originating at the contact of surfaces moving relative to each other. These occur where deflections are of the same order of magnitude as clearances between adjacent parts.
3. Those that arise on surfaces that are in close contact but which are independent of the unbalanced pressure forces, e.g., shaft seals. In many practical cases this force is small compared to the other torque losses, and for the purposes of this analysis was considered equal to zero.

Viscous torque is defined as:

$$T_V = C_D q \mu N \quad (58)$$

Friction torque is defined as:

$$T_f = C_f \frac{q}{2\pi} \Delta P \quad (59)$$

Ideal torque is defined as:

$$T_i = \frac{\Delta P q}{2\pi} \quad (60)$$

where:

C_D = viscous drag coefficient

C_f = friction coefficient

q = displacement, ft^3/rev

μ = viscosity, $\text{lb sec}/\text{ft}^2$

N = rotational speed, rev/sec

T = torque, ft-lb

ΔP = differential pressure, lb/ft^2

The total torque can then be stated as,

$$T = \frac{\Delta P q}{2\pi} + C_D q \mu N + C_f \frac{q}{2\pi} \Delta P \quad (61)$$

The problem then arises as to the value of the viscous drag coefficient. The work done by Wilson assumes that all flow is in the laminar flow region. However, it has previously been determined that all flow paths, including leakage paths when pumping LF_2 are in the turbulent flow region. Because of problems encountered in calculating viscous drag with turbulent flow, the viscous drag coefficient was calculated for first approximation by assuming laminar flow was present. This is a conservative assumption since the fluid friction factor for smooth walls is lower for turbulent flow. The various losses are presented in Fig. 66.

There are two potential mechanical problem areas associated with this pump. The first is running roller bearings in LF_2 with a high radial load. Since little experience has been accumulated relative to this, the determination of the extent of the problem will have to await actual testing.

The second potential problem is running gears in LF_2 . This problem centers around sliding contact between the gear sides and the stationary housing and between the meshing gear teeth. According to Schmidt (Ref.23), in the presence of pure fluorine metals form a fluoride film on the surface. Fluoride films, like the oxide films that form on aluminum in air, are so closely bonded to the metal surface that they are considered "in" rather than "on" the surface of the metal. This film acts to inhibit further attack of the base metal. As wear occurs, this film is replaced. However, the film thickness is usually measured in angstroms and may not be replaced as rapidly as the wear rate.

Studies have indicated that platings such as aluminum oxide (Al_2O_3) have been used satisfactorily for dynamic seal noses. However, the material is extremely brittle and should be applied as a thin coating only. The Al_2O_3 coating appears to be the best solution for plating the housing opposite the gear sides. The extent of the

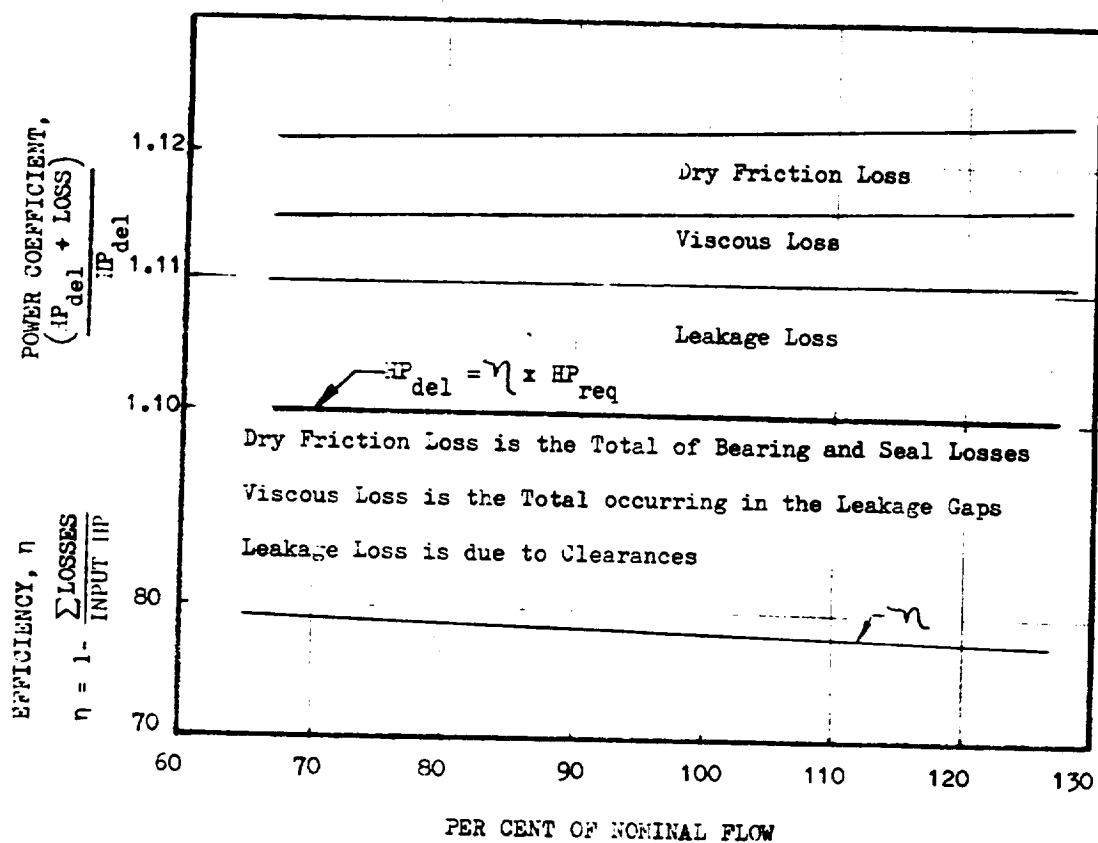


Figure 66. Gear Pump Loss Isolation

problem in the meshing gear teeth is not known. The gears will be lightly loaded with a relatively low Hertz stress, but whether this is low enough to preclude the loss of the protective fluoride film that forms upon contact with pure fluorine also will have to be determined by testing.

A preliminary layout of the gear pump is shown in Fig. 67.

VANE PUMP

Introduction

In a typical vane pump, the fluid is pumped between vanes which form part of the rotor and which are free to slide radially relative to the rotor. The fluid is admitted to the cavity formed by adjacent vanes through an inlet port. The rotor is positioned eccentrically with respect to the housing in such a manner that when the vanes sweep past a discharge port the volume enclosed between adjacent vanes is reduced and the trapped fluid is forced into the discharge port. The vanes are kept in contact with the housing by centrifugal force. In addition, the roots of the vane guides are subjected to high pressure from the discharge to provide additional contact load, if required.

No valves are required for the inlet and discharge ports but a relief valve is usually installed for over-pressure protection. This relief valve vents the discharge flow to the suction side of the pump.

Analysis

Due to the low viscosity of liquid fluorine a fluid wedge hydrodynamic bearing cannot be set up between the sliding vane and the cam ring of a vane pump while pumping LF_2 . Therefore, the friction at this contact location will be of the dry friction type. This requires the vanes to be radially pressure balanced so a proper trade off between friction loss and slip loss (leakage flow) will be obtained. This design is also restricted by the radial load that can be tolerated by the vane and the heat generation caused by friction.

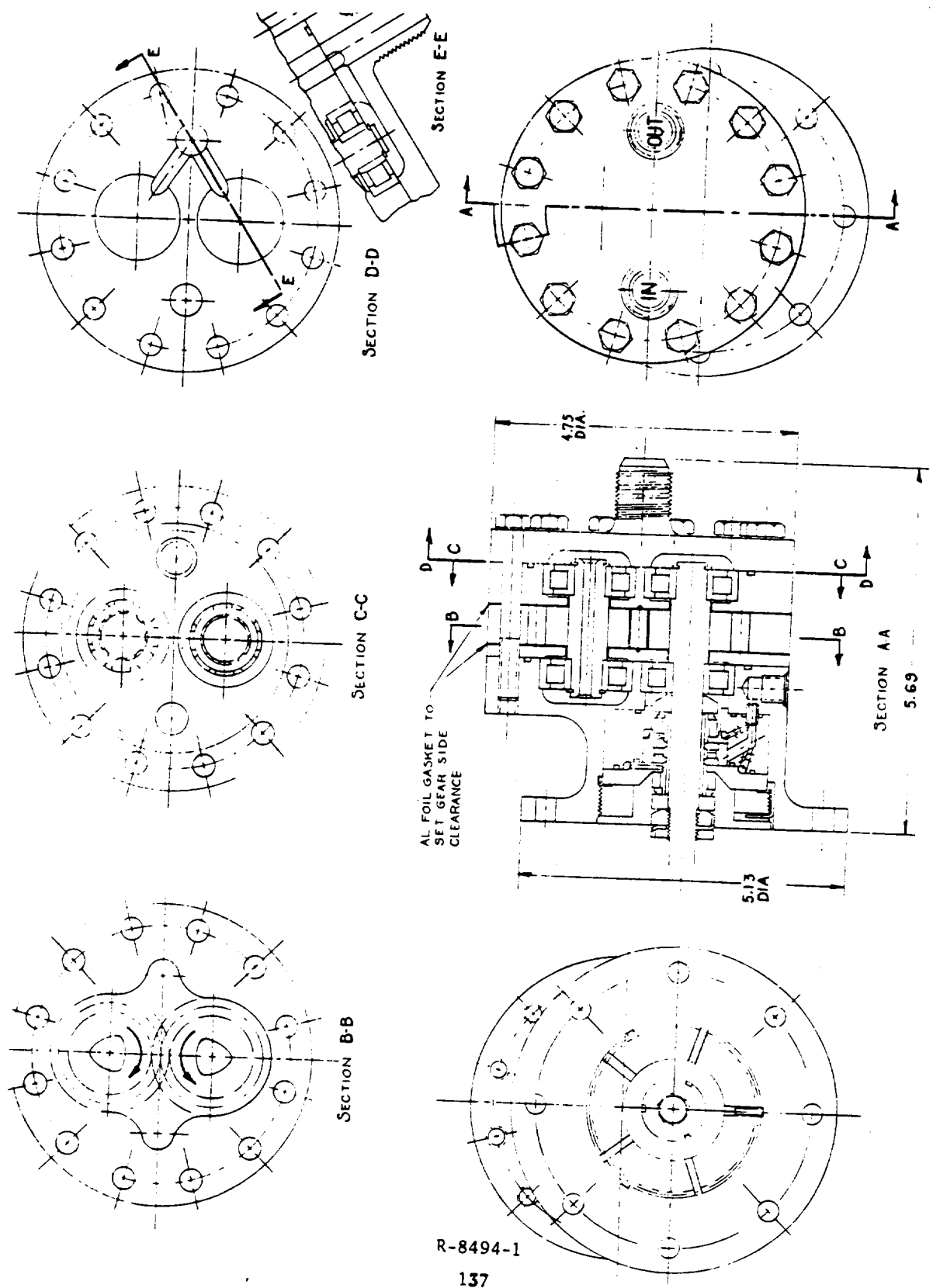


Figure 67. Preliminary Layout of Gear Pump

The magnitude of the frictional heat generation is assumed to be proportional to the vane radial load against the cam ring. These frictional forces produce a resistive torque that converts input power to frictional heat. The friction heat generation in the vanes and cam ring is estimated to be 1.1×10^{-2} Btu/sec (11.6 watt) based on radial vane loads of 2 pounds (8.9 N) and a coefficient of friction of 0.12 (Ref.23). This amount of heat generation would increase the fluid temperature about 0.1 F (0.18 K) at the nominal pump flow if all the energy was transferred to the fluid.

The above estimates are based on data from Ref. 23, assuming the use of Kentanium sliding against aluminum oxide. Because of the presence of fluorine a fluoride film coating is formed on the surfaces which improves the dry lubricating properties of the materials. However, it is imperative to achieve proper load balancing of the sealing vanes to prevent high or uneven face loading, which can cause excessive seal wear and local fragmentation. One criteria that can be used to evaluate the severity of loading is the "pV" factor, the product of contacting load per unit area and sliding relative velocity. This product is proportional to the heat generated if the coefficient of friction is assumed independent of load and velocity. Using this criteria, it appears that the greatest problems would be encountered in balancing the vane radial loads.

Analysis of the flow conditions for the gear pump disclosed that for clearances in excess of 0.00015 inch (0.00038 mm) the leakage flow would be of the turbulent type. This analysis is also applicable for the vane pump, and since the clearances are expected to be higher than 0.00015 inch for the vane pump, the leakage flows will be calculated using turbulent flow relationships. The general expression for turbulent flow between two parallel plates is (see Appendix A for derivation):

$$Q_L = 4.6 \frac{\Delta P^{.57}}{\mu^{.143}} \frac{g^{.43}}{\gamma^{.43}} \frac{w}{\lambda^{.57}} \delta^{1.72} \quad (61)$$

where

Q_L = volumetric leakage, ft^3/sec

ΔP = pressure differential, lb/ft^2

g = gravitational constant, ft/sec²

δ = clearance, ft

w = width of leak path, ft

μ = viscosity, lb sec/ft²

l = length of leak path, ft

Adapting the above expression for the actual leak paths in a vane pump and substituting into the equation for volumetric efficiency,

$$\eta_v = 1 - \frac{60Q_L}{qN}$$

yields the following relationship:

$$\eta_v = 1 - \frac{4.6 \Delta P^{.57} g^{.43} 60}{\gamma^{.43} \mu^{.143} qN} \left[\frac{w_1 \delta_1^{1.72}}{l_1^{.57}} + \frac{2w_2 \delta_2^{1.72}}{l_2^{.57}} + \frac{1.67 D \delta^{1.72}}{D^{.57} 3} \right] \quad (62)$$

Where the first term in the bracket accounts for leakage around the ends of the vanes, the second represents leakage at the dividing seals and the third at the rotor ends. The second term is assumed constant. This assumption is made because the effect of the clearance at this location is secondary to the influence of the other two. The dividing seals separate the inlet and discharge ports. They are the minimum radial clearance between the rotor and the eccentric cam ring which minimizes the leakage from the high- to the low-pressure side of the pump.

Equation 62 is presented graphically in Fig. 68. As shown, with the assumptions made, an efficiency of better than 90 percent can be obtained with 0.00035 inch (8.89×10^{-6} m) axial clearance. Figure 69 shows the effect of rotor axial clearance on performance. If the rotor moves from the center to a position of zero clearance on one end, the efficiency will decrease 5 percent. The loss in efficiency due to axial wear is 4 percent per 0.0001 inch (2.54×10^{-6} m), whereas the vane wear in the radial direction is not expected to cause a performance change due to a clearance increase since the vanes move out radially as wear occurs thereby keeping the leakage rate constant.

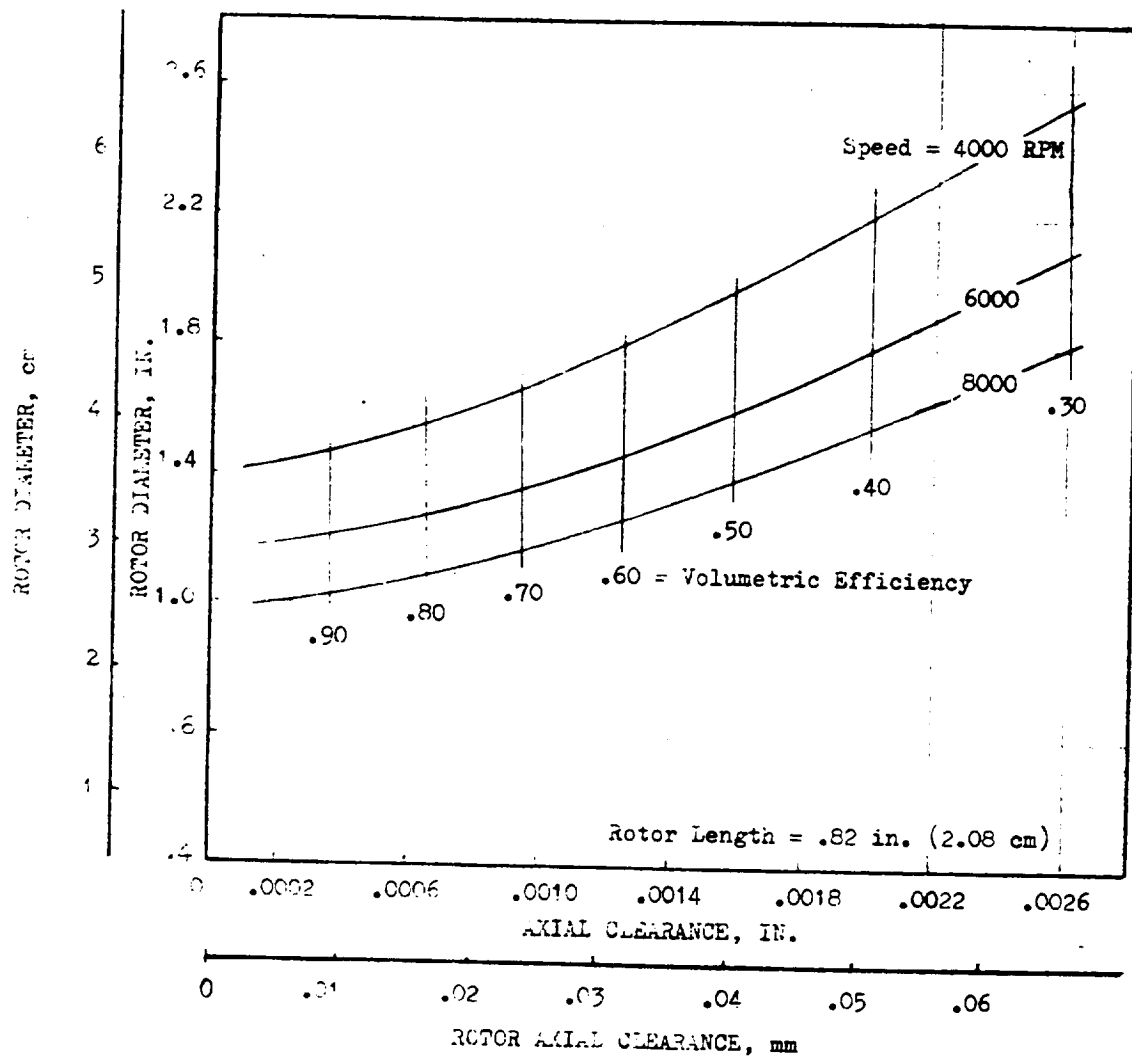


Figure 68. Vane Pump Rotor Diameter as a Function of Axial Clearance

R-8494-1

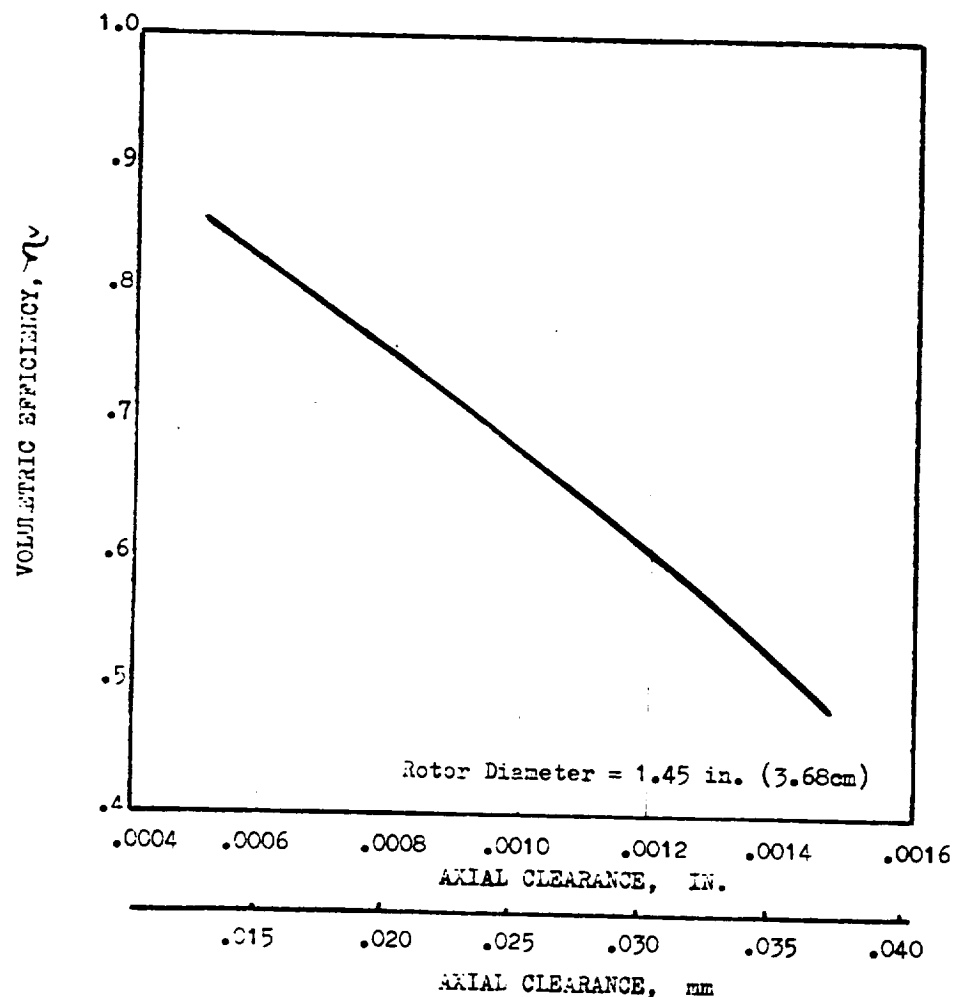


Figure 69. Clearance Effect on Vane Pump Efficiency

R-8494-1

The various hydraulic and mechanical losses are presented in Fig. 70. The dry friction loss is based on the best available loss estimates of seal and bearing drag with vane radial loads set at 3 pounds (13.3 N). The viscous loss was estimated by the same method used for the gear pump.

Expected problem areas for this pump concept include balancing of vane radial loads. This must be a compromise between high contact loads with the cam ring (with attendant wear and heat generation) and a high leakage rate at the vane tips (with attendant volumetric efficiency loss). The vane speed is expected to be so low that centrifugal forces will be negligible. Therefore, balancing radial forces could be accomplished by bleeding high pressure fluid into the cavity at the base of each vane or by using springs between the rotor and each vane. Careful analysis in this area is required, for without being able to generate a hydrodynamic bearing, the materials themselves must provide the lubrication and using the thin fluoride film generated by the presence of fluorine.

A preliminary layout of the vane pump is shown in Fig. 71.

PISTON PUMP

Two types of piston pumps were analyzed. They are the radial outflow and axial configuration.

Axial Piston Pump

The reciprocating action of the pistons in the axial pump is obtained by rotating the shaft and the cylinder block simultaneously on separate center lines that intersect at a low angle. Since the high axial thrust load of the cylinder block cannot be transmitted through the universal joint conventionally used in this type of pump, this required that the load be transmitted through a large single ball the center of which is located at the centerline intersection point. The cylinder block is then driven by a set of bevel gears.

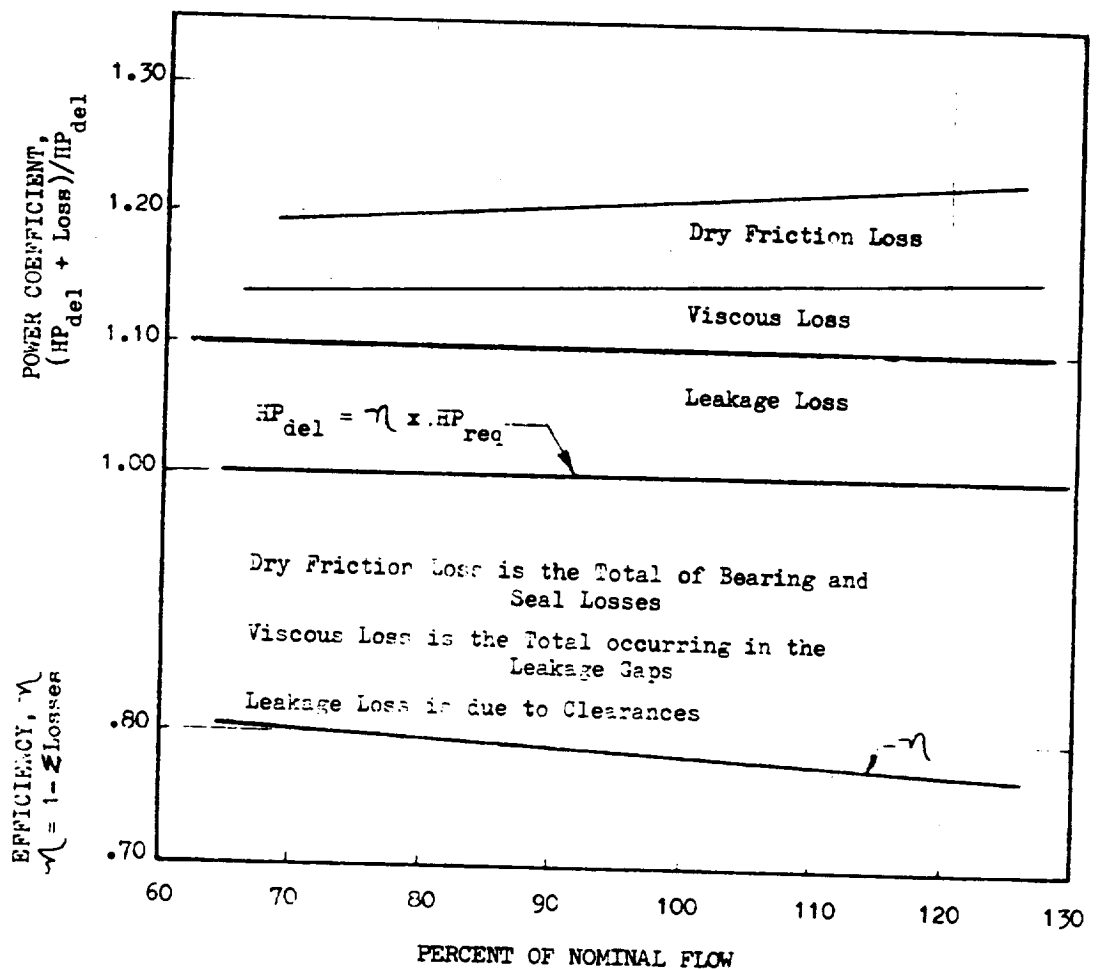


Figure 70. Vane Pump Loss Isolation

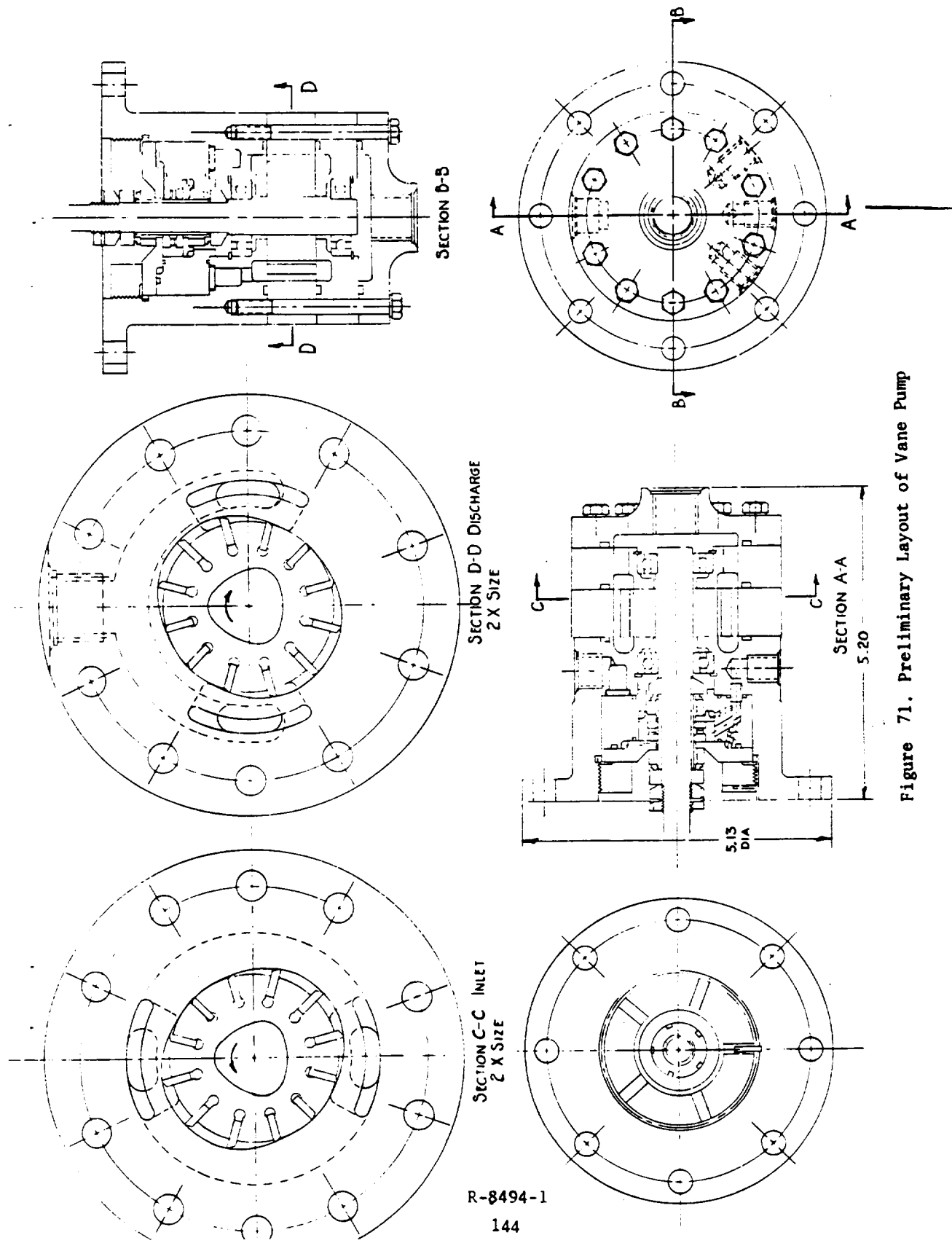


Figure 71. Preliminary Layout of Vane Pump

The valving for the intake and discharge is obtained in the conventional manner for this type of pump. The cylinder block with its port slots rotates past stationary inlet and discharge ports. The rotating port slots are aligned with the stationary intake and discharge ports during the intake and discharge strokes of the pistons, respectively.

The main thrust bearings on the shaft are lubricated and cooled by high pressure fluid from the discharge port. The two bearings on the rotating cylinder block and the thrust ball are lubricated and cooled by high pressure leakage past the pistons in the cylinder head. The gears are submerged in fluid and the gear case vents to the inlet port.

Radial Outflow Piston Pump

The pistons in the radial outflow pump receive their reciprocating motion from an eccentric bearing machined as an integral part of the shaft. The pistons are assembled to a split clevis type ring. The two ring halves are riveted together and this piston and clevis ring assembly is pressed on the outer race of the eccentric bearing. The outer race of this bearing, with clevis ring pressed on, acts as a cam to produce the reciprocating motion of the piston.

The cylinder head includes a double check valve. The inlet and discharge portions of this valve are pressure actuated.

The bearings are lubricated by the pumped fluid. A bleed port is drilled from the discharge collecting manifold to the cavity between the primary seal and the adjacent bearing. The fluid from this cavity flows through all three bearings and combined with the piston leakage cools and lubricates all internal moving parts.

Performance

Leakage in the piston pumps is in the turbulent flow regime; this weight flow is defined by:

$$w_l = \frac{4.6(\Delta P \gamma)^{0.57} \pi D_p N \delta^{1.72} g^{.43}}{\ell^{0.57} \mu^{0.143}} \quad (63)$$

The theoretical weight flow is described by:

$$w_{TH} = \frac{\pi D_p^2 S \gamma N n}{240} \quad (64)$$

Volumetric efficiency is defined:

$$\eta_v = 1 - \frac{w_l}{w_{TH}} \quad (65)$$

Therefore, upon substituting Eq. 63 and 64 into 65:

$$\eta_v = 1 - \frac{1105 \delta^{1.72} (\Delta P)^{0.57} L^* g^{.43}}{\ell^{0.57} D_p^{0.143} \mu^{0.43} \gamma^{0.43} n S} \quad (66)$$

Where L^* accounts for the percentage of time when ΔP exists.

The graphical presentation of volumetric efficiency is shown in Fig. 72 for the axial pump and Fig. 73 for the radial outflow. As shown, there appears to be no advantage of one above the other from a volumetric efficiency standpoint. The dependency of efficiency on piston clearance is presented in Fig. 74 for fixed geometry pumps. This figure shows that wear affects the radial outflow pump slightly more than the axial pump. However, there still appears to be no significant performance advantage of one over the other.

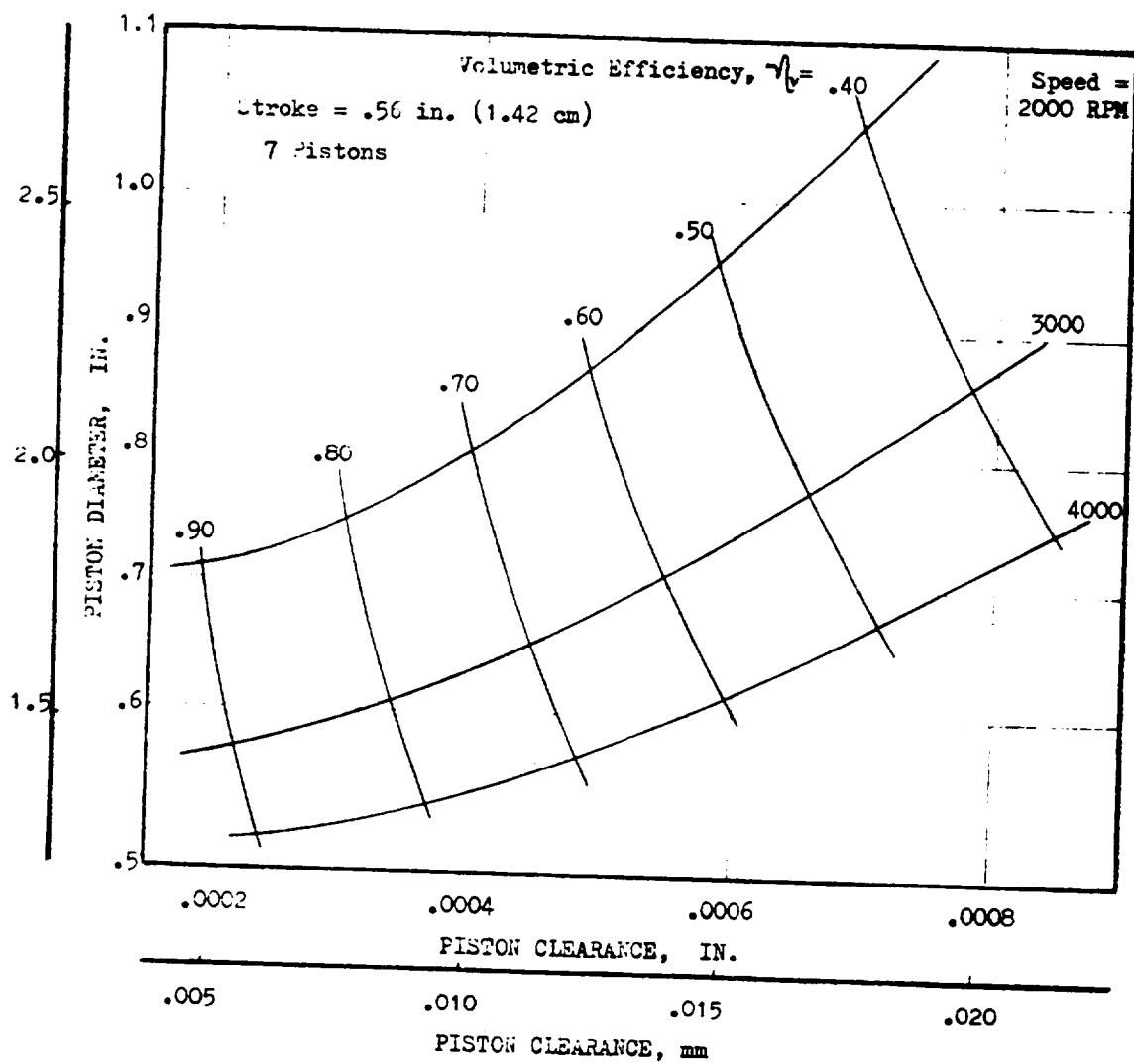


Figure 72. Effects of Speed, Piston Clearance, and Piston Diameter on Axial Piston Pump Efficiency

R-8494-1

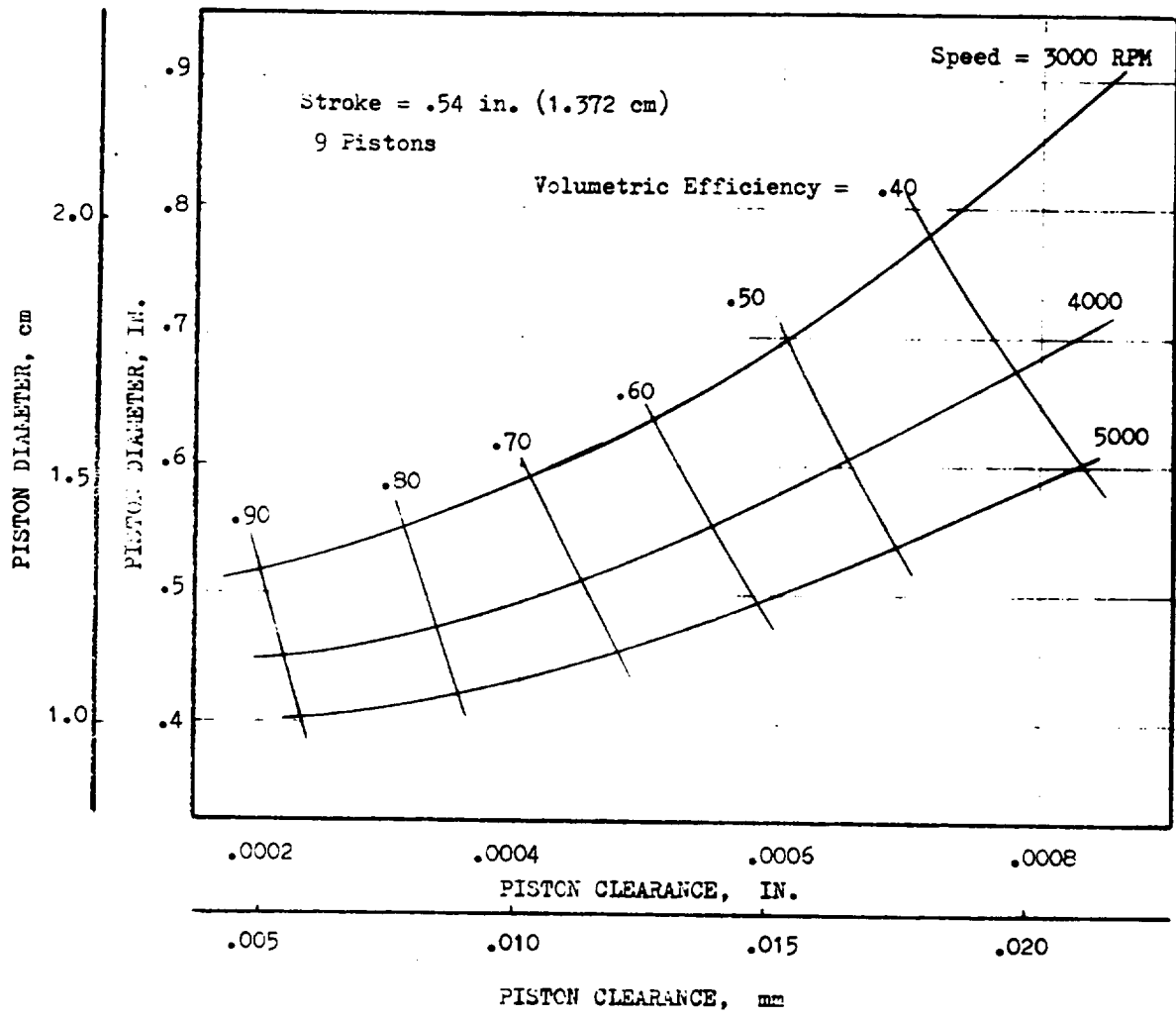


Figure 73. Effect of Speed, Piston Clearance, and Piston Diameter on Radial Piston Pump Efficiency

R-8494-1

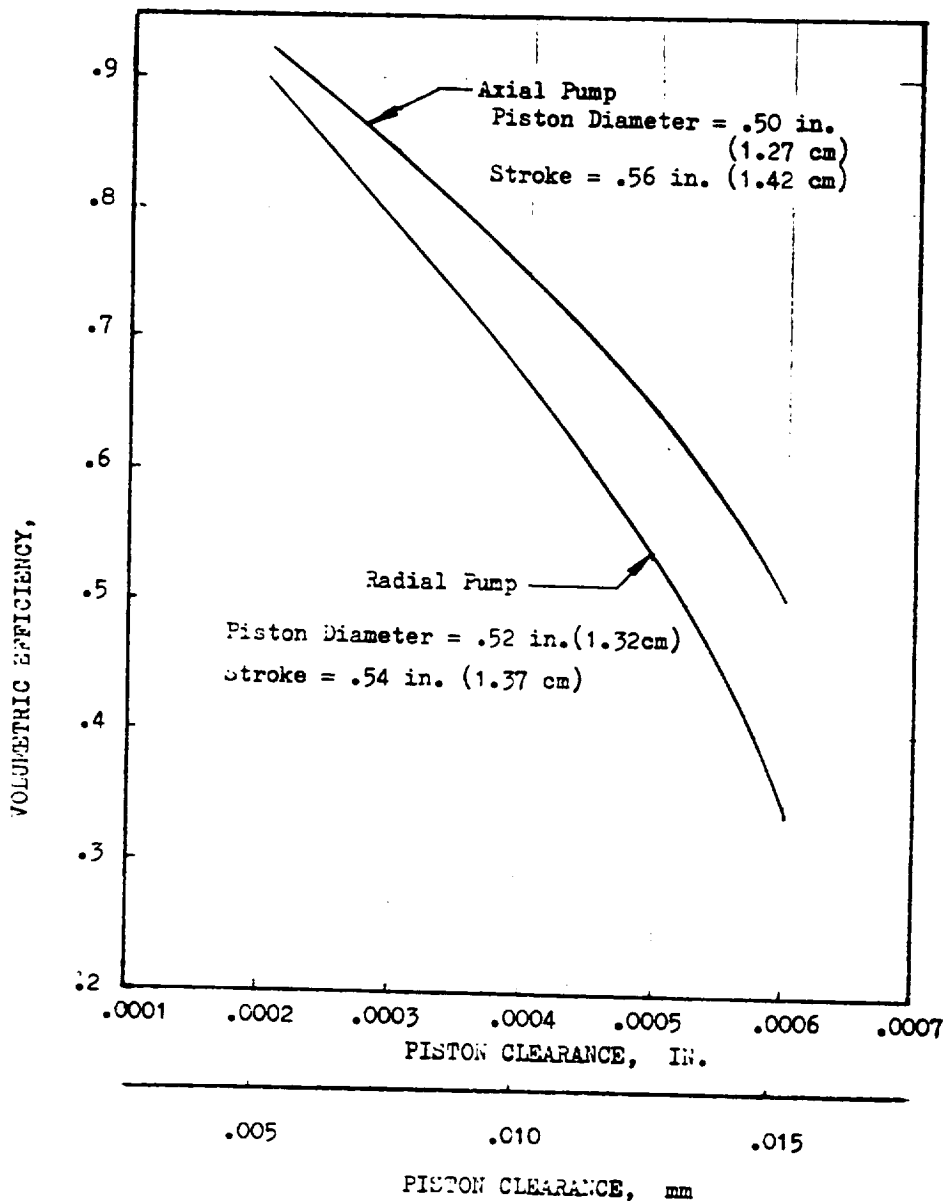


Figure 74. Clearance Effect on Piston Pump Efficiency

R-8494-1

149

Figures 75 and 76 present losses and overall efficiencies for the two piston pump configurations. The dry friction loss is shown for the axial pump with the assumption that the cylinder barrel is pressure balanced.

The potential problem areas associated with the radial outflow piston pump are valves, piston rubbing, side loads due to the cam, and weight. When valves are introduced into a design, their reliability becomes important. This is related to wear of sealing and seat surfaces and seizure or failure. These may be minimized by maintaining low loads and simplicity of design. Piston rubbing may be tolerated only with reduced loads.

The axial pump has high axial loads which require pressure balancing for some of the components. This must be accomplished otherwise intolerable high wear rates may result. Side loads on the pistons must also be minimized in order to reduce wear.

Preliminary layout of the axial piston pump is shown in Fig. 77, and the radial piston pump in Fig. 78.

HELIOTOR PUMP

The moving elements of this type of pump consist of two rotors with helical lobes, intermeshing with each other and placed in a housing, such that a number of separate interlobe spaces are formed. The fluid is admitted at one end through a properly located port opening, filling each open helical interlobe space completely from inlet to outlet end, there confined by the end plate.

As the moving elements rotate, the intake to the interlobe space is closed off by the inlet-end plate and, with further rotation, the rotors intermesh so that the length and volume of the interlobe space is progressively reduced, resulting in a positive displacement of fluid.

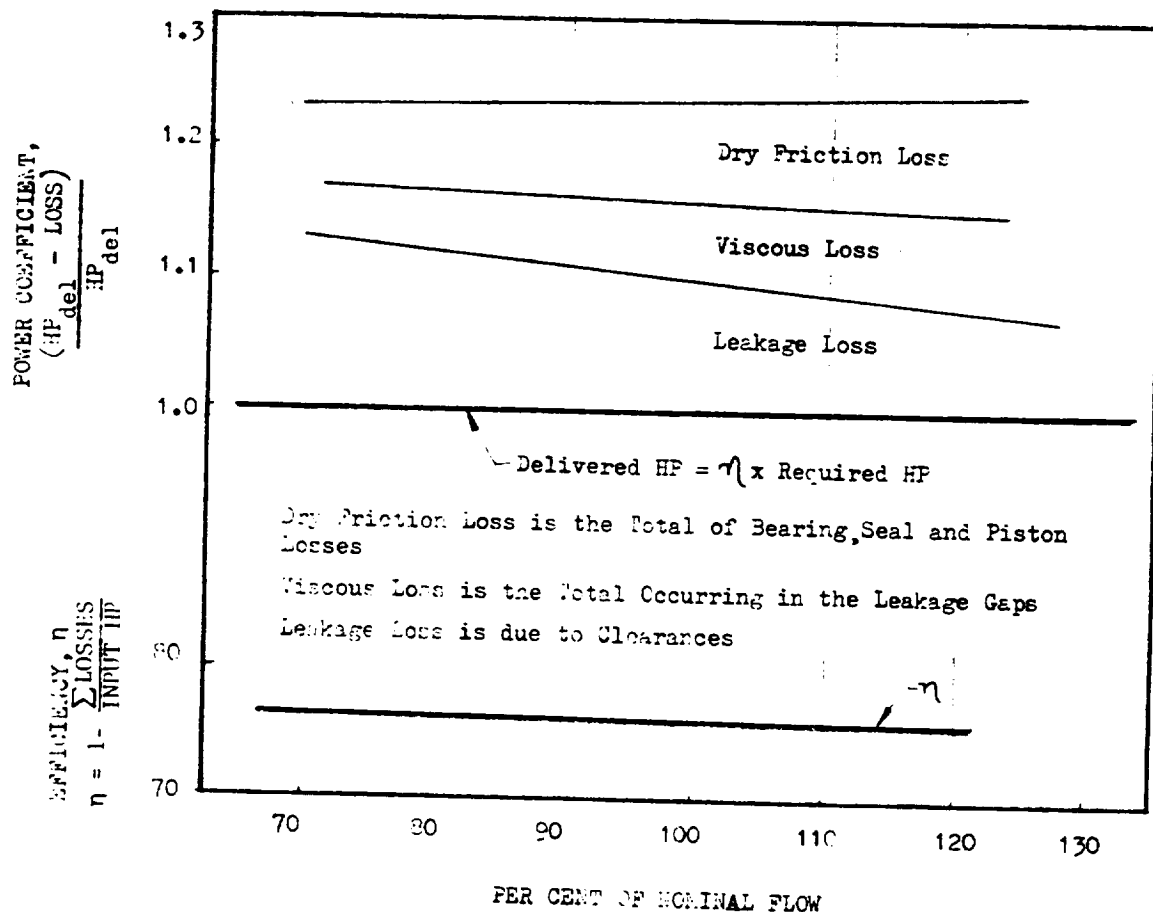


Figure 75. Axial Piston Pump Loss Isolation

R-8494-1

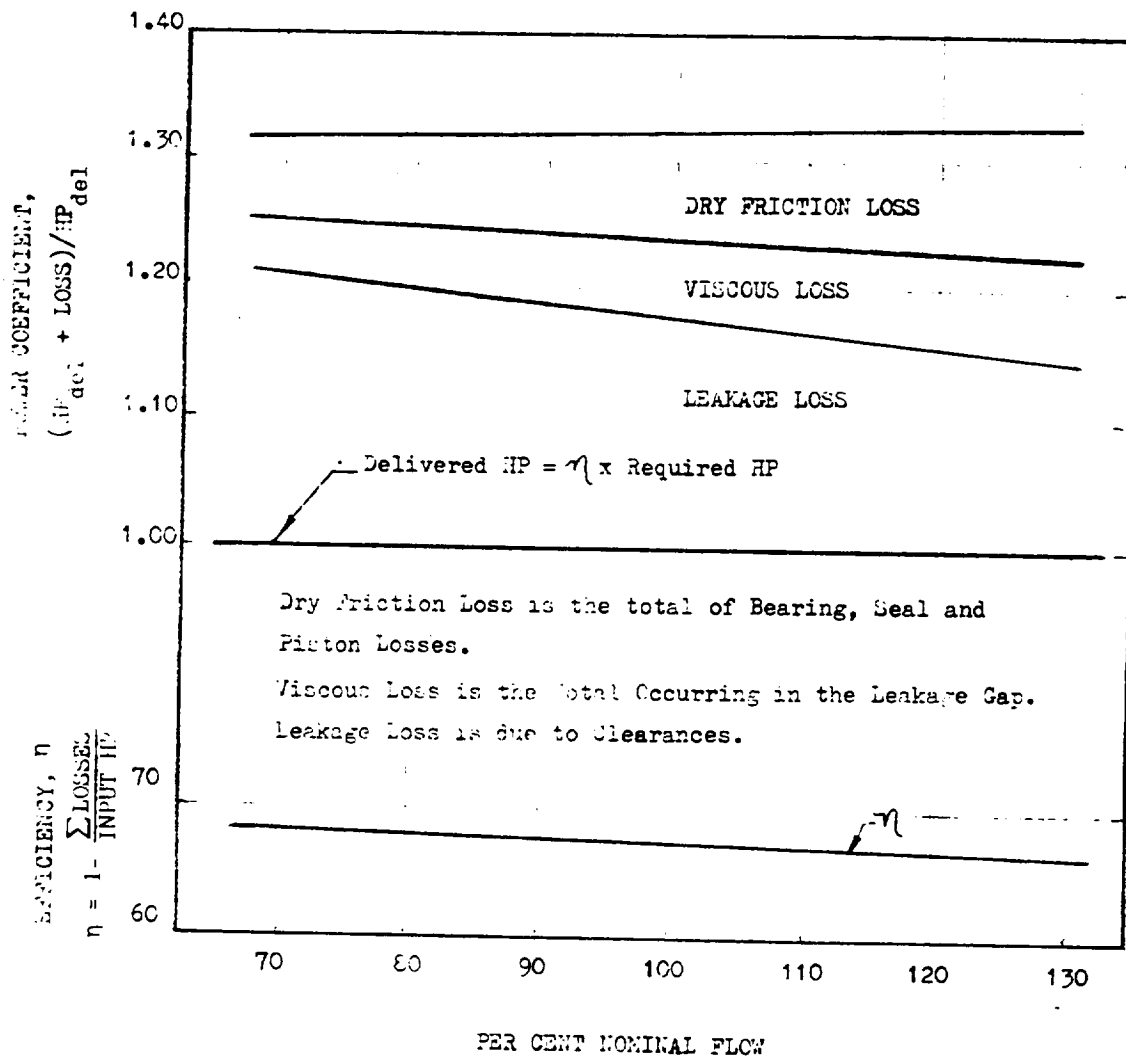


Figure 76. Radial Piston Pump Loss Isolation

R-8494-1

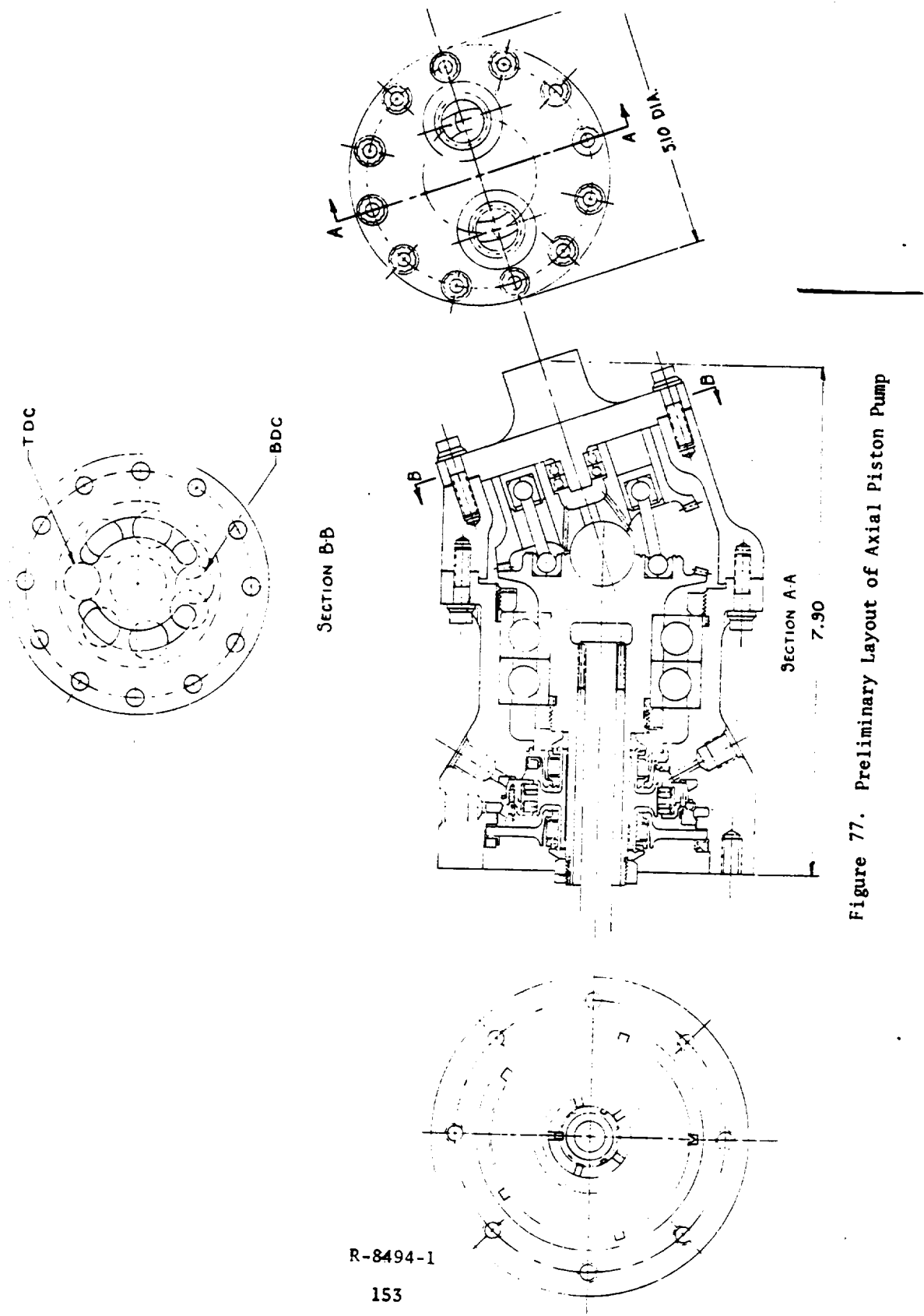


Figure 77. Preliminary Layout of Axial Piston Pump

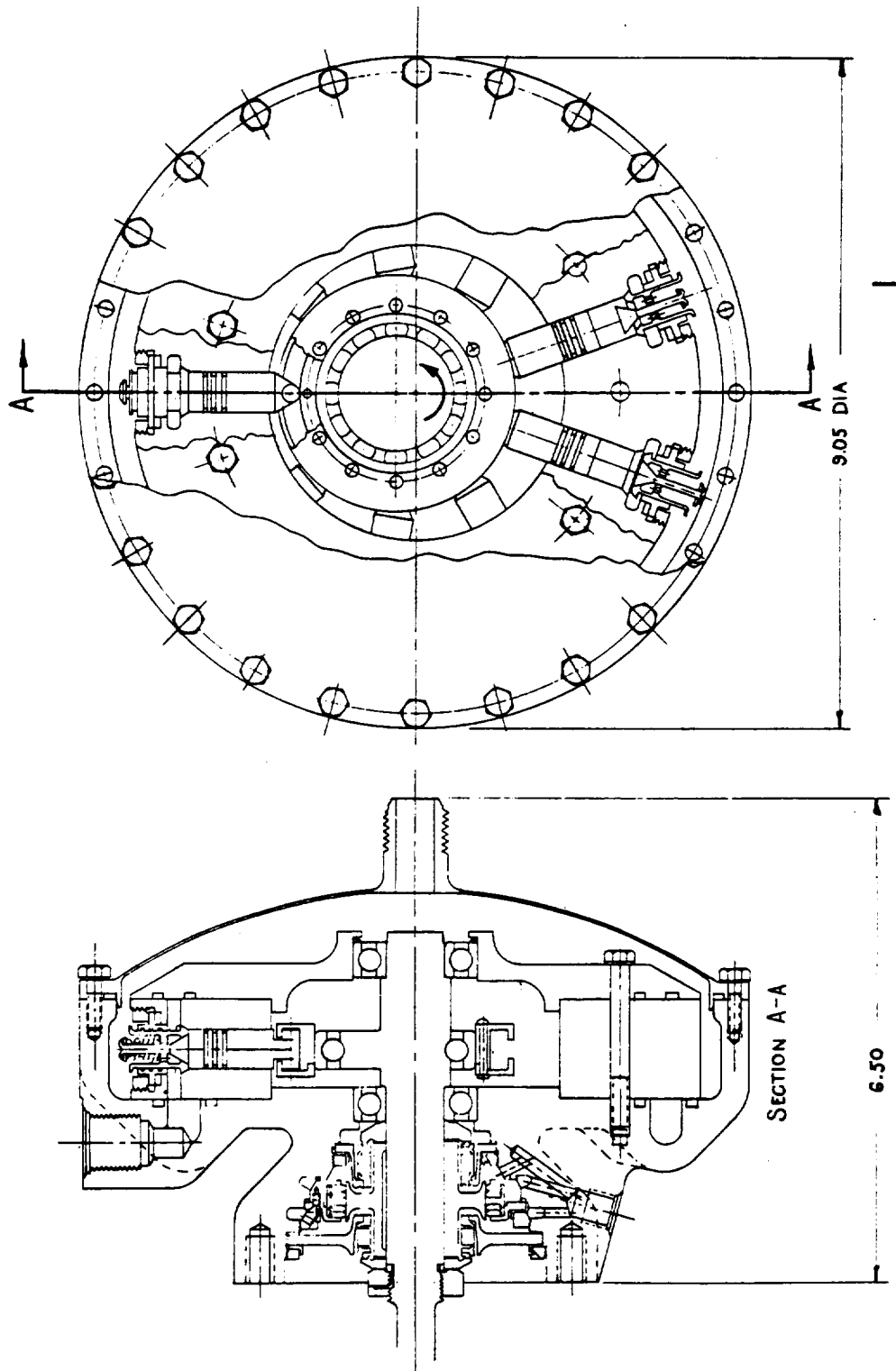


Figure 78. Preliminary Layout of Radial Piston Pump

Several design configurations for helirotor pumps can be considered, Fig. 79 (Ref.24). Conventional designs have male rotors with three to four lobes coupled with female rotors having four to six lobes. A small lobe number allows a great depth of the pumping passages, i.e., gives large capacity for given rotor diameters. But if the number of lobes is reduced, the root of the female rotor becomes small so that excessive deflections of the lobes at high pressure differentials can be expected. Since a comparatively large pressure ratio is required for the subject design, a high number of female and male lobes is desired. It appears that a combination of four male lobes coupled with six female lobes placed on rotors which have the same outer diameter, and with a speed ratio of the male to the female rotor of 3 to 2 is a suitable combination. To relieve the torque on the timing gear to the maximum possible degree, it appears advantageous to use the lobe geometry specified in the Nilsson patent (U.S. patent No. 2622787 issued December 23, 1942, Ref. 25). This geometry also allows use of a sealing strip at the tip of the lobe, thus relieving tolerance requirements for the fabrication of the male and female rotor. With wraparound angles of the male lobe from 150 (2.62 rad) to 300 (5.24 rad), the ratio of rotor width to diameter should be unity to reduce the radial load to a minimum.

The calculations for the geometry are made on the following basis:

The theoretical flowrate follows the relation

$$Q_{TH} = \frac{A_e LN}{60} \quad (67)$$

where A_e denotes the effective pumping area, L the length of the rotor and N the rotational speed. The effective area can be calculated based on geometry as a percentage of the square of the diameter, when holding the number of lobes constant. For the selected configuration this relationship is:

$$\frac{A_e}{D^2} = 0.462 \approx C^* \quad (68)$$

	ADDENDUM	MAXIMUM BUILT-IN VOLUME RATIO MAX.	MAXIMUM WRAP ANGLE MAX.	GEOMETRIC COEFFICIENT $C^* = A_e/D_2$	DIAMETER RATIO MALE/FEMALE	SPEED RATIO MALE/FEMALE
	STD	3.38	300°	.482	1/1	3/2
	FULL	3.38	300°	.563	1/1.1	3/2
	STD	3.00	295°	.462	1/.82	5/4
	FULL	3.00	295°	.604	1/1	5/4
	STD	2.60	290°	.524	1/.81	4/3
	FULL	2.60	290°	.602	1/.88	4/3

Figure 79. Typical Helirotor Configurations

The leakage flow through a gap for turbulent flow condition can be presented in the form:

$$Q_L = 4.6 \delta^{1.72} \left[\frac{\Delta P}{\ell} \right]^{0.57} \left[\frac{\pi D_m g^{0.43}}{\mu^{0.143} \gamma^{0.43}} \right] \quad (69)$$

where δ denotes the gap, ℓ the length of the leakage path, D_m the mean diameter of the leakage gap, and μ the absolute viscosity. The volumetric efficiency then follows the relation:

$$\eta_v = 1 - \frac{Q_L}{Q_{TH}} = 1 - \frac{4.6 \delta^{1.72} (\Delta P)^{0.57}}{\mu^{0.143} \ell^{0.57} C^* D^2 L N \gamma^{0.43}} \quad (70)$$

For the convenience of the calculations, Eq. 70 can be simplified by letting ($\ell = L$) and unifying powers which are approximately the same:

$$\eta_v = 1 - \frac{\sqrt{\Delta P g} \left(\frac{\delta}{L} \right)^{1.6}}{DN \mu^{0.143} C^*} \frac{\psi^* \pi}{60} \times 4.6 \quad (71)$$

where ψ^* denotes a restriction factor which depends on the particular configuration of the leakage path. Available test data indicate that this restriction factor will have a numerical value of $\psi^* = 0.38$. Equation 71 shows that for a given pressure rise, the volumetric efficiency depends on the ratio of clearance to flow path length, or since $L/D = 1$, on the ratio of clearance to rotor diameter, the rotative speed and the diameter itself. Introducing the design specifications into Eq. 71, the final equation for the volumetric efficiency reads ($L = D$):

$$\eta_v = 1 - \frac{1.88 \times 10^6 (\delta/D)^{1.6}}{ND} \quad (72)$$

where N is expressed in rpm and D in ft.

Assuming different rotative speeds, the required rotor diameter can be calculated as function of the clearance and, thus, as function of rotor diameter. Figure 80 is a plot of the calculated data and shows that a clearance of 0.0023 in. (5.842×10^{-5} m) is required when a volumetric efficiency of 80 percent is desired, and that a clearance of 0.005 in. (1.27×10^{-4} m) reduces the obtainable volumetric efficiency to values in the range of 52 to 58 percent. The rotor diameter increases with decreasing rotative speed and increasing clearance, as was to be expected. Checking the Reynolds Number of the leakage flow in the rotor clearances it is found that in all cases the leakage flow is in the turbulent flow regime.

Previous correspondence with the Stratos Corporation, a licensee of the Svenska Rotor Maskiner Company, indicates that the minimum feasible rotor diameter is about 1.2 in. (3.048×10^{-2} m). This limit is also implied in Ref. 24. Projecting this fabrication limit into Fig. 80, it becomes apparent that a comparatively low speed of 4000 rpm and small rotor clearances will have to be selected to obtain high volumetric efficiencies, and that higher rotative speeds and rotor clearances reduce the maximum obtainable efficiency significantly.

Figure 81 shows the calculated radial and axial load per rotor when the simplifying assumption is made that the full pressure differential is effective on the projected thrust areas of the male and female rotor. This diagram shows that comparatively high loads, 1650 lb (7340 N) to 1850 lb (8230 N), are generated for rotors with a diameter of 1.2 inch (3.048×10^{-2} m). The axial load increases with the square of the diameter, while the radial load increases as a linear function of diameter. Thus, considerably smaller loads can be obtained if rotor diameters of less than 1.2 in. (3.048×10^{-2} m) can be fabricated.

The third curve shown in Fig. 81 is the capacity limit curve for roller bearings. As evidenced from the relation of this curve to the load curves, the diameter of the helirotor pump must be much less than 1.2 in. (3.048×10^{-2} m). Therefore, with 1500 psia (103.42×10^5 N/m²) discharge pressure, the bearing loads are too high to be carried satisfactorily. Because the high bearing loads require too large a bearing relative to the rotor diameter, this pump configuration is eliminated from further consideration.

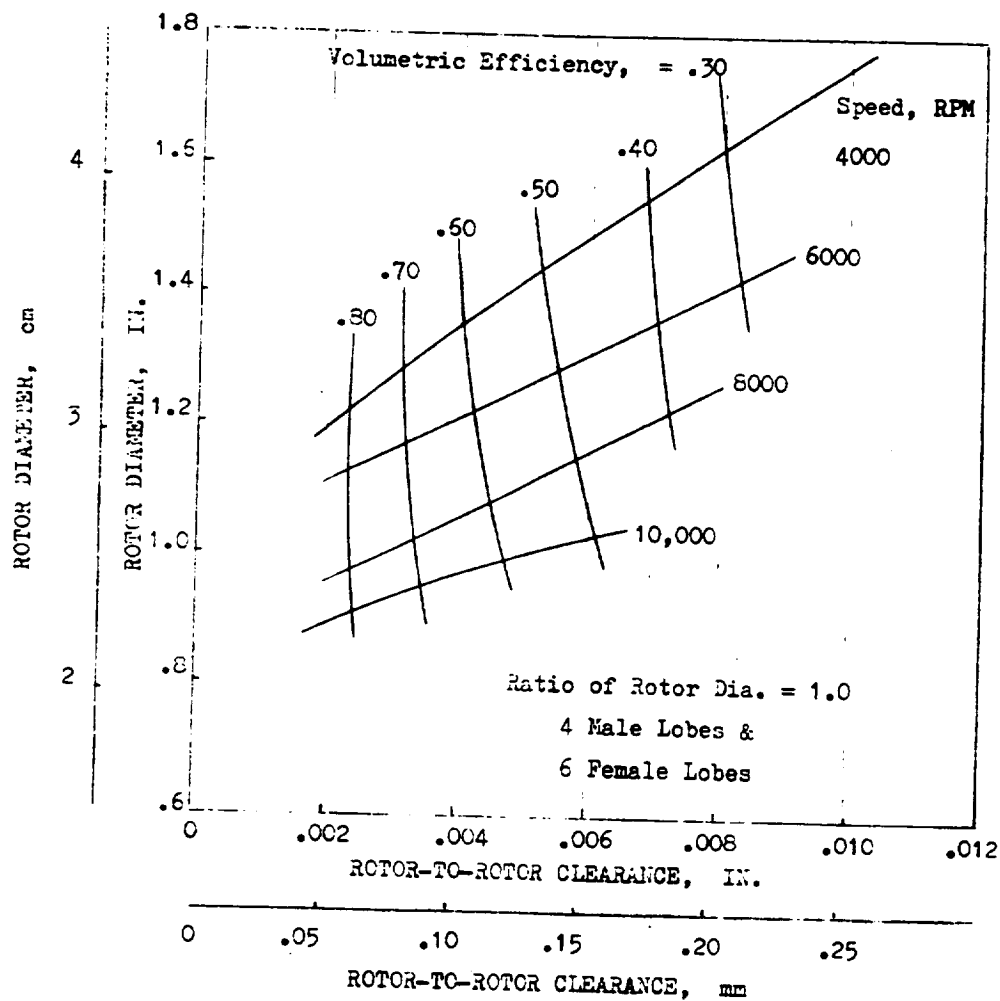


Figure 80. Effects of Speed, Rotor to Rotor Clearance, and Rotor Diameter in Helirotor Pump Efficiency

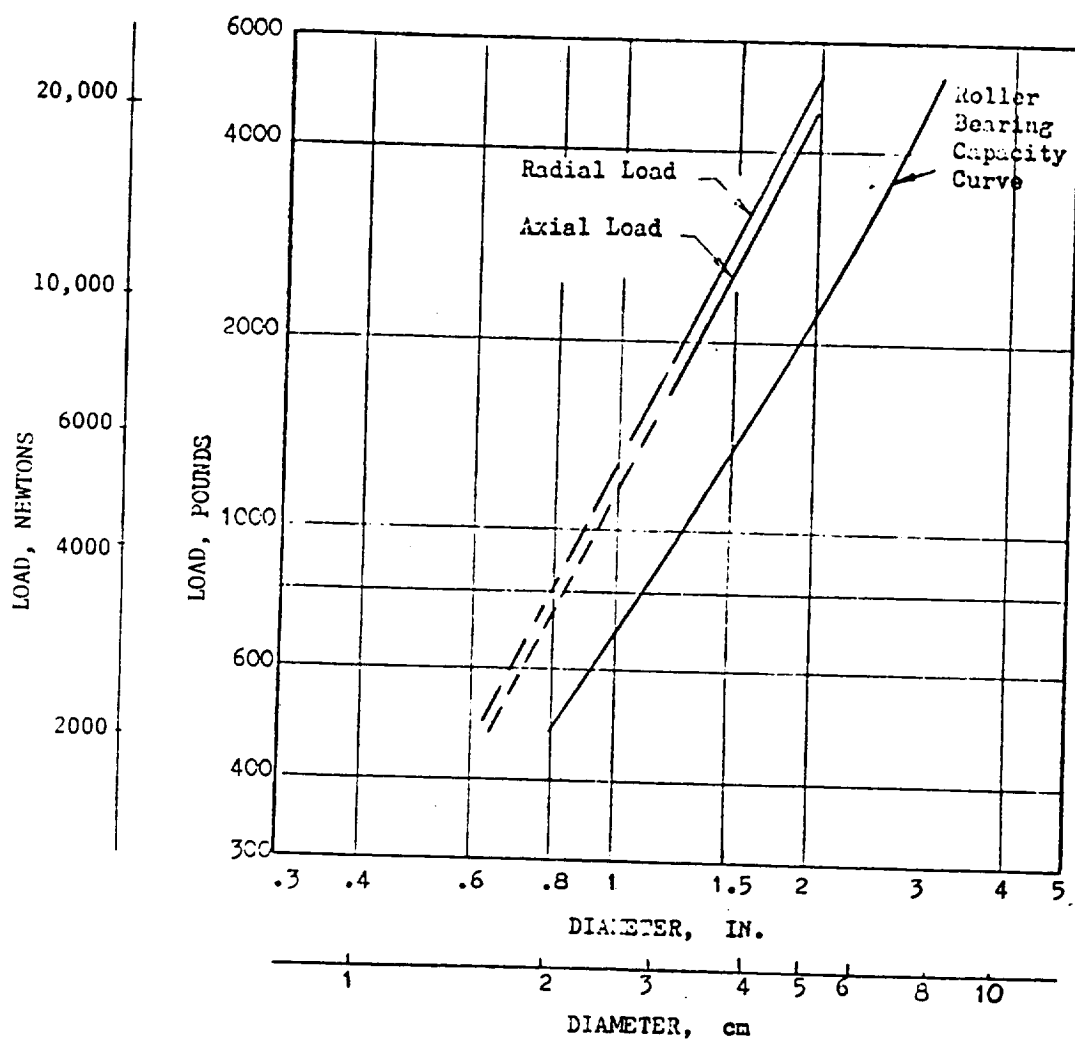


Figure 81. Calculated (Maximum) Loads on Helirotor Pump

DIAPHRAGM PUMP

Introduction

A diaphragm pump achieves its pumping from displacement of fluid by flexing a metal diaphragm. It has the advantage of minimum moving contact between parts in the fluid being pumped. If the valve poppets are supported on flexures so that valve guides are not required, the only moving contact part exposed to the pumped fluid would occur at the valve seats.

In a typical arrangement, diaphragms are arranged in pairs around an eccentric and operate in the same way as double-acting cylinders. A diaphragm is attached to each side of the reciprocating bodies. Each radially outward stroke of the reciprocating body is a discharge stroke for the outer diaphragm and a suction stroke for the inner diaphragm, while each radially inward stroke of the reciprocating body is a discharge stroke for the inner diaphragm and a suction stroke for the outer diaphragm.

During the initial investigation of this pump concept, it became apparent that this concept would be somewhat larger in overall size and considerably heavier than other positive displacement pump concepts. It also appeared that procurement and development costs would be higher than less complex pumps. These factors lead to the conclusion that the diaphragm pump would end up at the bottom of the positive displacement pump rating scale. As a result, only a minimum design and analysis effort was expended to allow a higher degree of effort on more promising concepts.

Analysis

From the standpoint of mechanical complexity, specific speed, specific diameter and weight, five double acting diaphragms or cylinders appears to be a maximum practical number. Using this as a basis, the following design results for a 12 gpm, 1500 psia discharge pressure pump (Ref. 26):

Stroke	0.015 in. max (3.81×10^{-4} m)
Number of cylinders	5, double acting

Clearance volume (max)	0.007 in. ³ ($1.1471 \times 10^{-7} \text{ m}^3$)
Stroking speed	3000 cycles/min or 30,000 total strokes/min
Estimated volumetric efficiency	85%
Estimated mechanical efficiency	30%
Diaphragm thickness	0.008 in. ($2.032 \times 10^{-4} \text{ m}$)
Piston diameter	3 in. ($7.62 \times 10^{-2} \text{ m}$)
Diaphragm convolution radius	0.25 in. ($6.35 \times 10^{-3} \text{ m}$)
Specific Speed	0.48
Specific Diameter	33.2
Hydraulic power	10.3 hp (7680.709 w) 7.7 kw
Input power	34.2 hp (25502.936 w) 25.5 kw
Maximum envelope diameter	16 in. ($4.064 \times 10^{-1} \text{ m}$)
Length	8 in. ($2.032 \times 10^{-1} \text{ m}$)

This design results in comparatively high specific speed and specific diameter. This in turn results in a large diaphragm load. The diaphragm suggested for this pump is a single convolution type often used in pressure-actuated control mechanisms. All of the flexure occurs in the convolution and the center portion of the diaphragm can be rigid. The convolution has a disadvantage in that it can withstand high differential pressure in one direction only but has an advantage of having a rigid center. The stress in the diaphragm is given by the equation:

$$\sigma = \frac{\Delta p b}{h} + k E f \left[\frac{h}{[ab(1-u^2)]^2} \right]^{1/3} \quad (73)$$

where

- Δp = differential pressure, lb/in.²
- b = radius of convolution, in.
- h = thickness of diaphragm, in.
- k = constant
- E = modulus of elasticity, lb/in.²
- f = deflection from flat position, in.
- a = diaphragm effective radius, in.
- u = Poisson's ratio

For this design, a bending stress in the diaphragm of 37,000 psi ($2.551 \times 10^8 \text{ N/m}^2$) is calculated, yielding a combined stress of 74,000 psi ($5.102 \times 10^8 \text{ N/m}^2$). It would be expected that a life of 5 hours can be obtained even if it is considered that surge pressure loading due to valve response time could cause the combined stress to reach values of 80,000 to 90,000 psi ($5.5 \times 10^8 \text{ N/m}^2$ to $6.2 \times 10^8 \text{ N/m}^2$).

The bearing loads in the diaphragm pump are extremely high due to the large bore and short stroke. The force opposing stroking is about 10,600 lbs (47,100 N) and may reach values of 12,000 to 13,000 lbs (53,400 to 57,800 N) due to surge overpressures. These forces can be coped with only when a very large diameter ball or roller bearing are used.

Another effect of using a large bore and short stroke is that the ratio of the clearance volume to the displacement volume must be large in comparison to conventional piston pumps. Because of heat transfer and pump inefficiency, the fluid that remains in the pump chamber after the exhaust stroke has a higher temperature than the fluid in the inlet line. After a large number of strokes, the temperature of the remaining fluid may have risen to the point that its vapor pressure is greater than the inlet pressure and vapor may form during the inlet stroke. This will restrict the flow on succeeding exhaust strokes as the fluid is no longer incompressible. A minimum clearance volume is therefore essential.

The low mechanical efficiency is due mainly to the high bearing losses. They are estimated to contribute about 65 percent of the mechanical losses, the remaining 35 percent being caused by cam lift losses.

This type of pump would be better suited if the discharge pressure were decreased because this would decrease the bearing loads and make the unit more reliable and decrease the weight. A decrease in both pressure and flow would be reflected in smaller size and lighter weight.

A preliminary layout of the diaphragm pump is shown in Fig. 82.

FOLDOUT FRAME 1

FOLDOUT FRAME 2

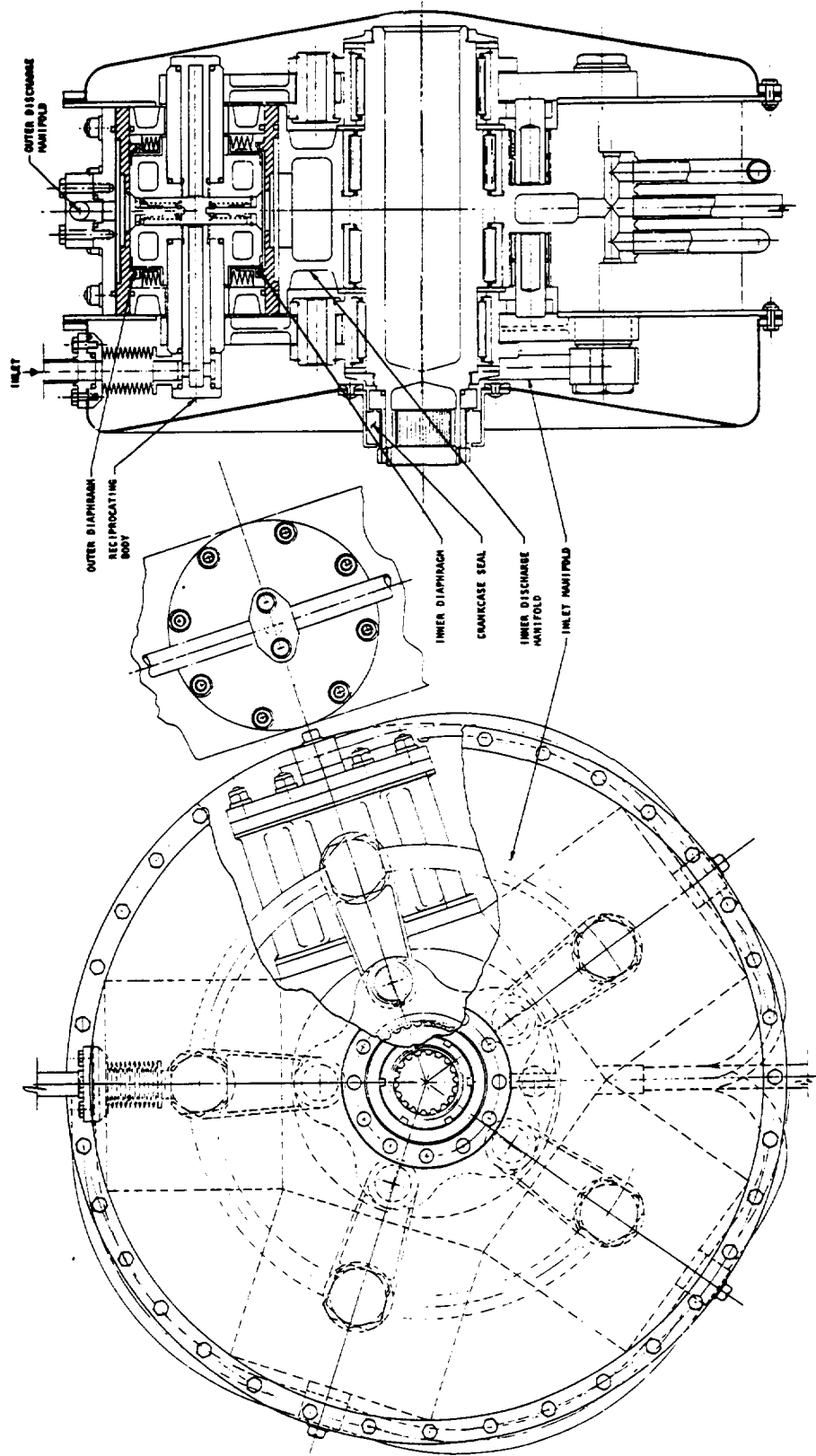


Figure 82. Preliminary Layout of
Diaphragm Pump

R-8494-1

164

PUMP EVALUATION

Preliminary analysis was completed on all six of the pump concepts. The analysis consisted of establishing operating speeds, estimating volumetric, hydraulic and overall efficiencies, and analytically determining cavitation performance. Preliminary layouts were then made of each concept which established design criteria including bearing size, bearing loads, seal configuration and seal rubbing speed. The layouts were also used to calculate the overall weight of each. On the basis of this analysis the heliotor pump was dropped from further consideration because of the difficulty of providing sufficient bearing capacity consistent with the rotor diameter and because of the problem of maintaining the required clearances to stay within a reasonable efficiency.

The analysis and design data for the other concepts is summarized in Table XII and from this data the rating matrix of Table XIII was generated. As can be seen, the gear and the vane pump had the highest overall rating. These results were reviewed with NASA-Lewis Research Center and as a result of the review, a decision was made to study high speeds for the gear pump and the axial piston pump.

Higher Speed Axial Piston Pump

Increasing the rotating speed of the axial piston pump from 4000 rpm to 10,000 rpm resulted in offsetting criteria effects such that the overall rating was increased by only one point. The rating went from 70 to 71 (see Table XIII). The criteria which had an effect on the rating were overall efficiency which decreased from 76 percent to 72 percent mainly due to increased churning losses at the higher speed. The face seal rubbing velocity which increased from 24.5 ft/sec (7.4676 m/s^2) to 61.2 ft/sec (18.654 m/s^2) and the shaft seal rubbing velocity which increased from 32.5 ft/sec (9.906 m/s^2) to 81.3 ft/sec (24.78 m/s^2). The increased rubbing velocities, which have an adverse effect on the rating, are due to a combination of the increased rotating speed and the inability, because of design and mechanical restrictions, to reduce the seal and shaft size inversely and proportionally as the speed increases. The bearing axial load on the other hand was

TABLE XII. DESIGN OPERATING CONDITIONS POSITIVE DISPLACEMENT PUMPS

Parameter	Gear	Piston Axial	Piston Radial	Vane	Diaphragm	Revised Configuration	
						Gear	Piston Axial
Speed, rpm	4,000	4,000	3,000	4,000	1,000	10,000	10,000
Bearing, DN	48,000	160,000	90,000	60,000	50,000	*	*
Face Seal Rubbing Velocity, ft/sec	13.1	24.5	18.4	13.1	6.1	3.3	61.2
Shaft Seal Rubbing Velocity, ft/sec	9.8	32.5	24.4	9.8	8.1	24.5	81.3
Minimum Axial Clearance, inch	0.0009	0.0002	0.0002	0.0004	0	*	*
Minimum Radial Clearance, inch	0.0005	NA	NA	0.0005	0	*	*
Bearing Axial Load, pounds	0	1,100	Neg.	0	0	0	400 to 550
Bearing Radial Load, pounds	932	Neg.	450	0	15,000	400	0
Efficiency (overall)	78	76	67	78	26	78	72
Cavitation No., ft/sec/limit	0.75	0.19	0.14	0.56	Neg.	0.91	0.51
Weight, pounds	19.7	26.2	41.7	13.6	165	*	*
High-Pressure Static Seals	2	1	0	3	6	2	1
Low-Pressure Static Seals	2	1	1	0	7	2	1

*Did not change sufficiently to affect rating matrix

TABLE XIII. RATING MATRIX POSITIVE DISPLACEMENT PUMPS

Criteria	Points Allowed	Gear	Piston Axial	Piston Radial	Vane	Diaphragm
Performance (total points = 25)						
Volumetric	5	5	5	3	5	4
Hydraulic	5	5	4	3	5	1
Overall	5	5	4	3	5	1
Size and Weight	5	4	3	2	5	1
Friction	5	4	2	3	2	5
Life (total points = 20)						
Seal Loads	5	5	5	5	5	5
Seal Speed	5	4	2	3	4	5
Bearing Load	5	3	1	4	5	1
Cavitation Performance	4	1	3	4	2	5
Reliability (total points = 30)						
Clearances	10	2	6	6	2	10
External Leakage	10	6	8	10	4	2
Valve Factor	5	5	5	2	5	2
Pressure Oscillation	5	4	2	3	4	2
Cost (total points = 25)						
Development Costs	15	15	12	9	15	6
Unit Costs	10	10	8	6	10	6
Total	100	78	70	66	78	56

markedly reduced (from 1100 lb (4900 N) to approximately 475 lb (2110 N)) which was enough to offset, on the rating matrix, the adverse effects of the efficiency decrease and increase in rubbing velocities. The effect of speed on axial load for various piston diameters and strokes is shown in Fig. 83. Since the overall rating of the higher speed axial piston pump increased by only one point, it did not alter its position on the rating matrix with respect to the other concepts.

Higher Speed Gear Pump

The effects of increasing the rotating speed of the gear pump were also investigated and the relationship of performance and gear geometry is presented in Fig. 84. A cavitation limit line is also presented in the figure and is based on the amount of energy required to accelerate the fluid up to the gear tip speed with an inlet static pressure of 15 psi (1.03×10^5 N/m²) above vapor pressure. Operation to the right of this line will require a boost pump. This figure indicates that to obtain high efficiency the larger gear diameters are required.

According to Fig. 84 to maintain efficiencies in excess of 85 percent without a boost pump, and to allow some margin from the cavitation limit line, a speed on the order of 6000 rpm would be a maximum. The geometry required would be a gear diameter of 1.47 in. (3.7338×10^{-2} m) and a width of .40 in. (1.016×10^{-2} m). This configuration (Fig. 85) would weigh 11.9 lbm (5.40 kg). In the boost pump region of operation, as shown in Fig. 84, an efficiency of 85 percent can be maintained at a speed of 9000 rpm. A pump of this configuration is shown in Fig. 86. A boost pump configuration designed to operate at 9000 rpm with a gear geometry of 0.3 in. (7.62×10^{-3} m) width and 1.40 in. (3.556×10^{-2} m) diameter will weigh 11.6 lbm (5.26 kg).

Considering the pump by itself indicates that the weight reduction of 0.3 lbm (0.136 kg) is insufficient to justify the added complexity associated with the boost pump configuration. However, it should be noted that the weight of the drive unit is reduced at higher speeds. Taking these two factors together may increase the weight savings to a point to make the increased complexity of the boost pump configuration justifiable. However, considering the pump only, the configuration without a boost feature is preferable.

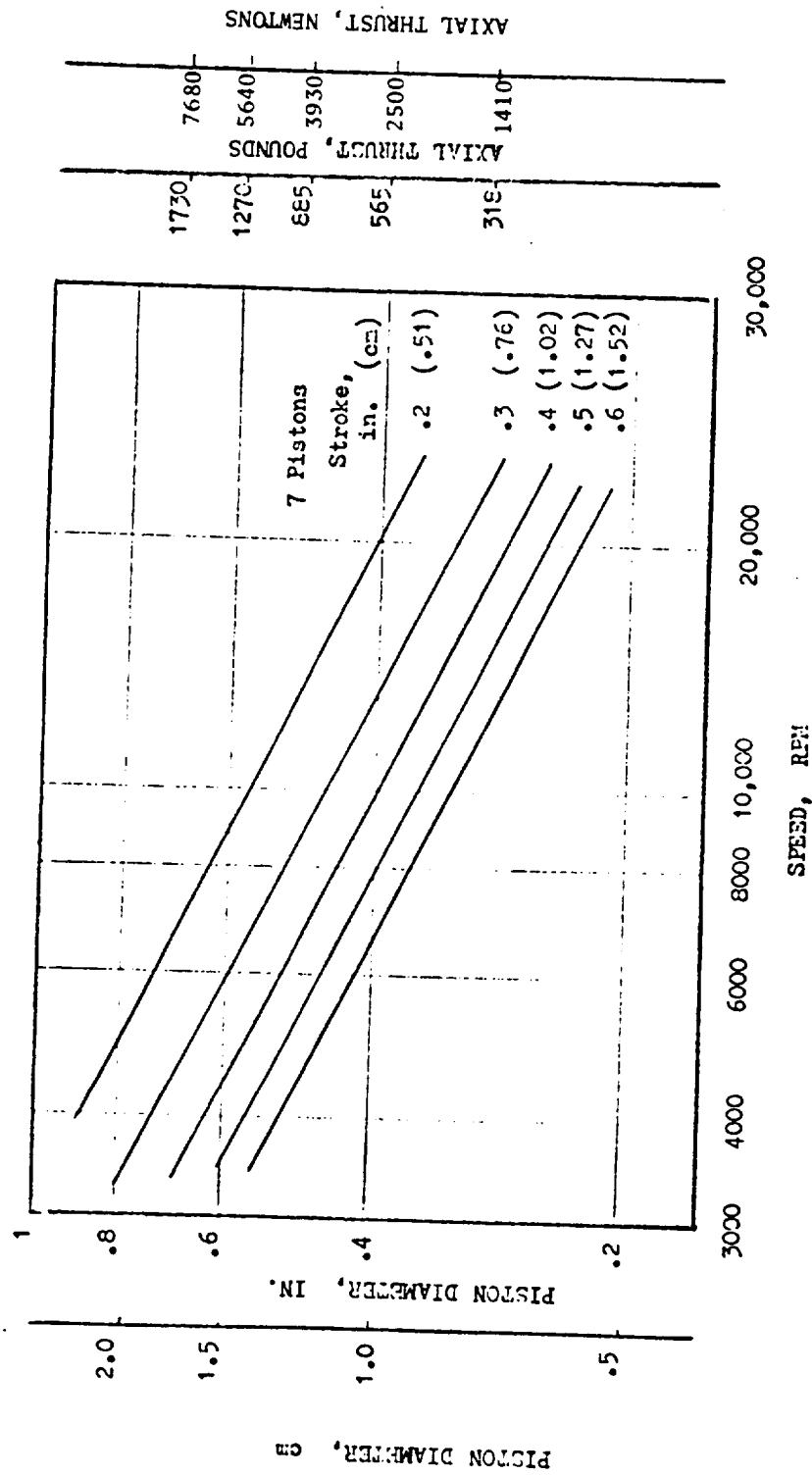


Figure 83. Effects of Speed on Axial Load for Various Piston Diameters and Strokes

R-8494-1

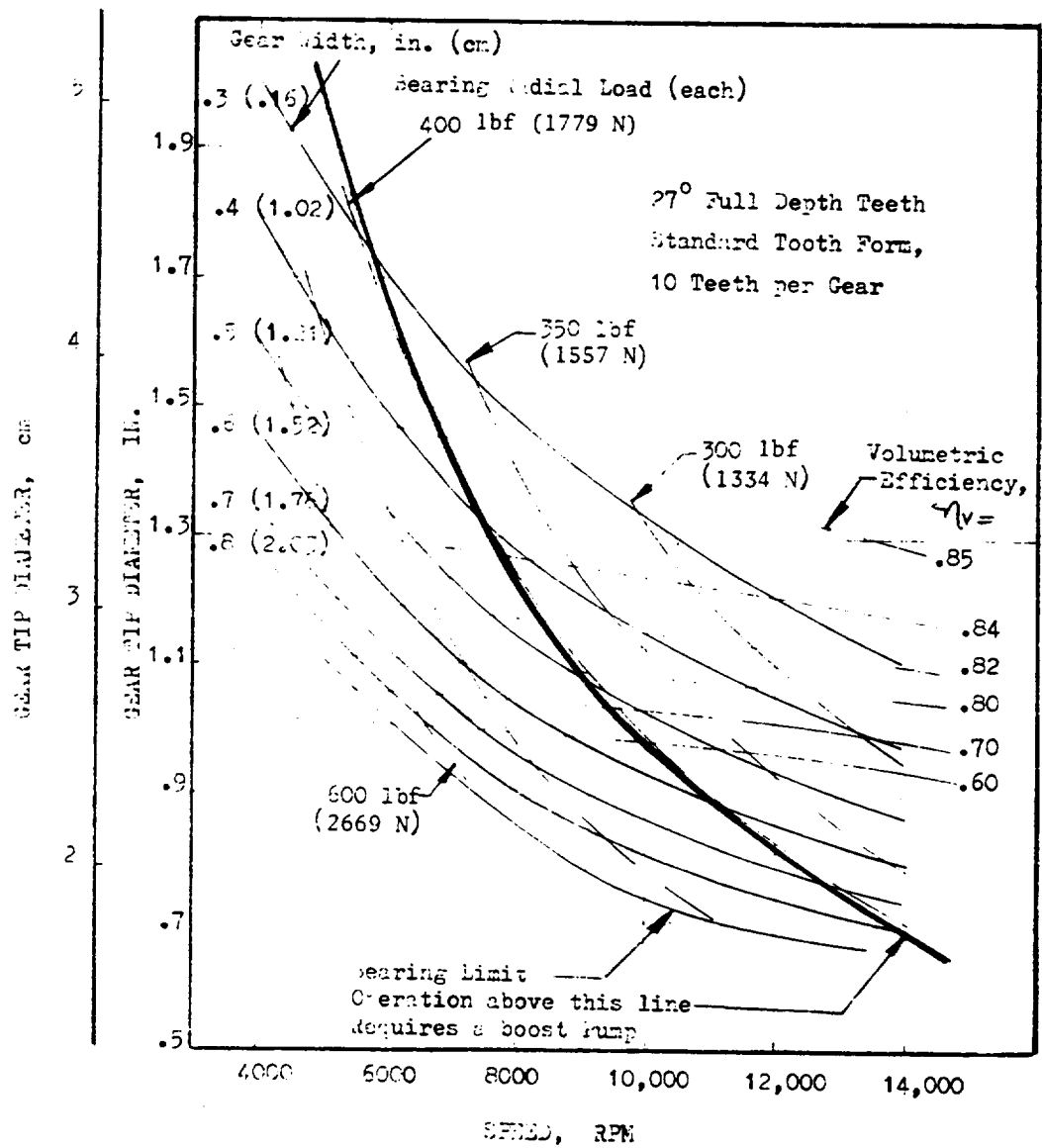


Figure 84. Gear Pump Performance Map

R-8494-1

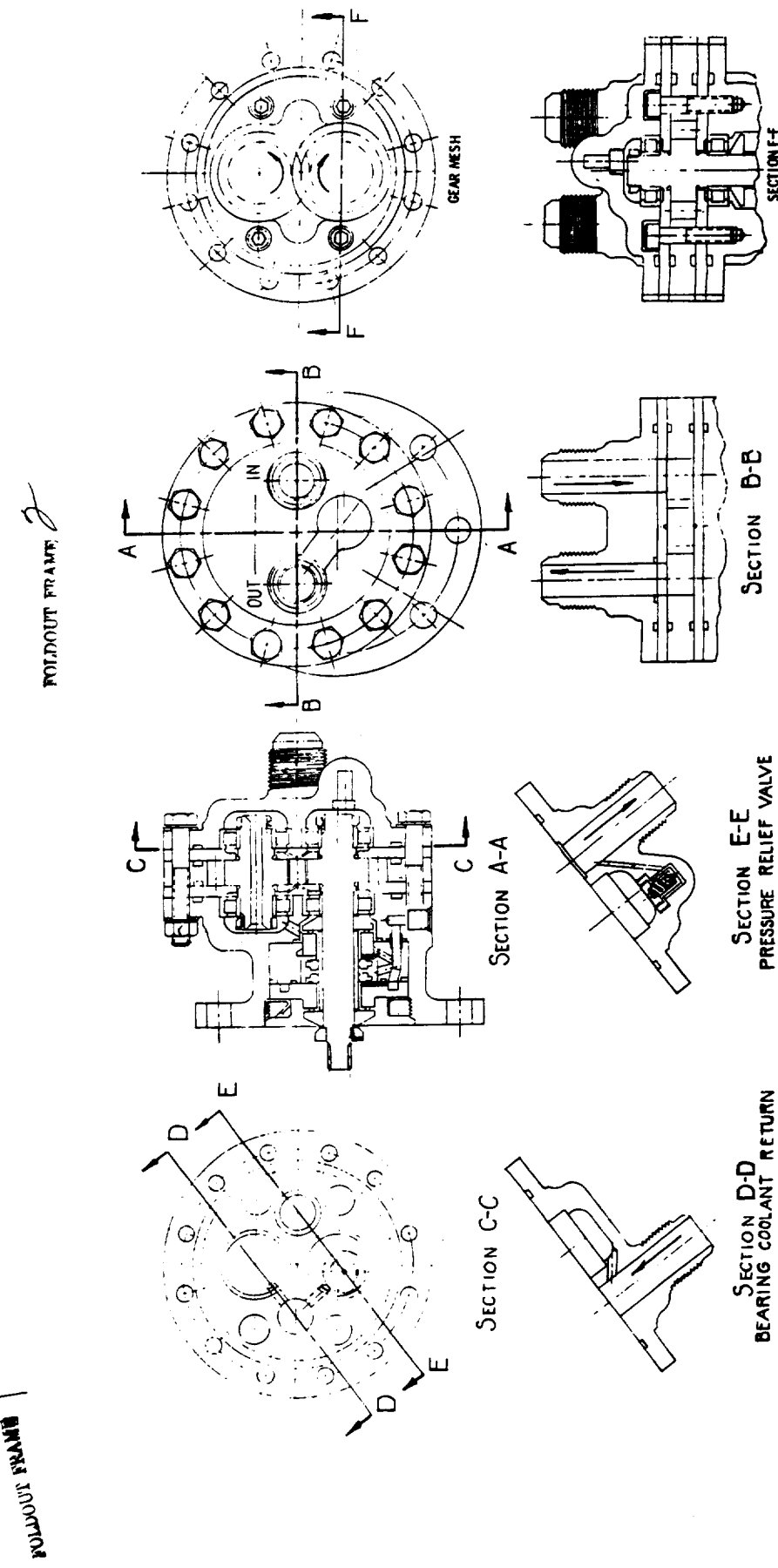


Figure 85. 6000-rpm Gear Pump

R-8494-1
171/172

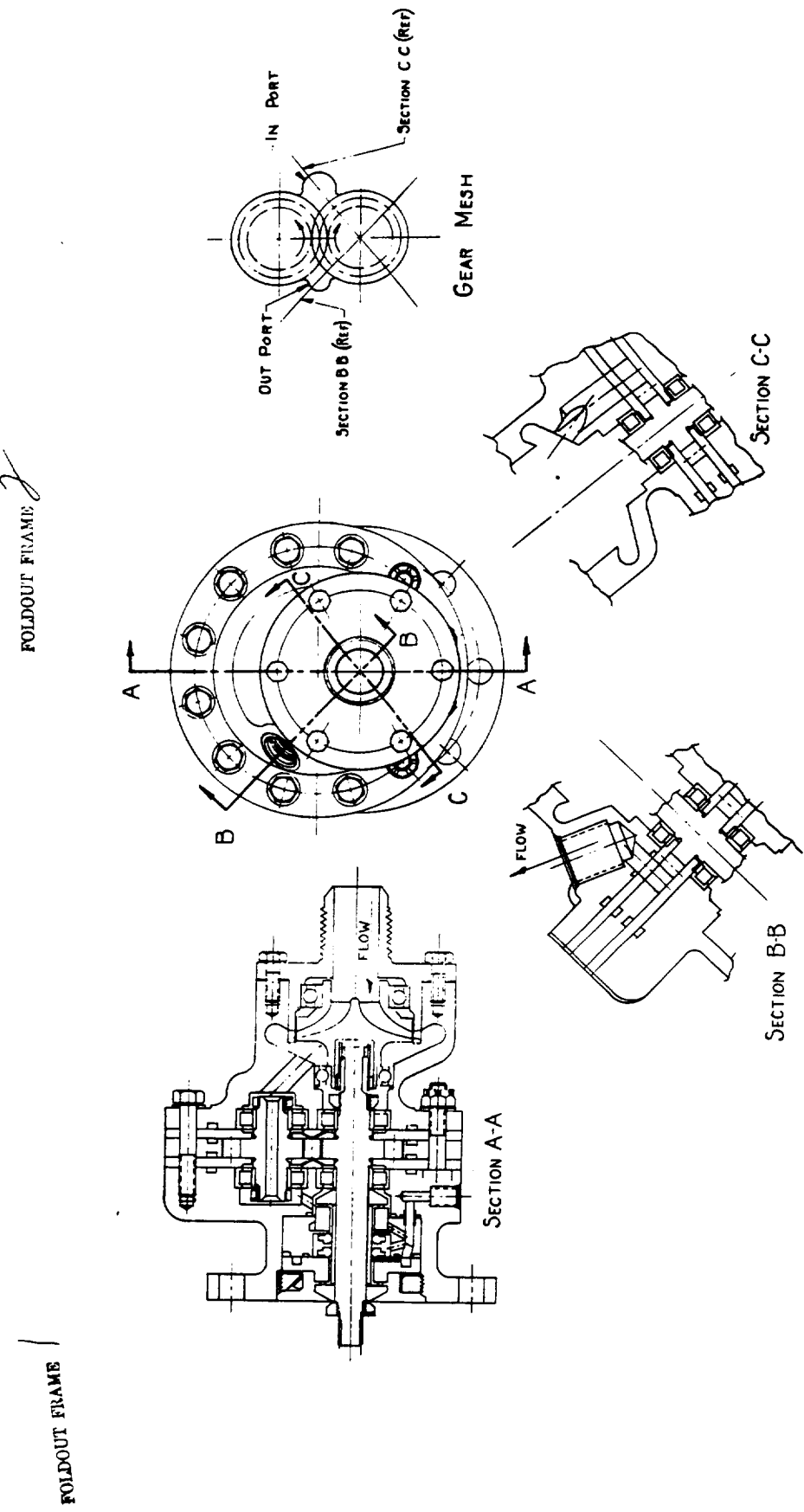


Figure 66. 9000-TPI Gear Pump

R-8494-1
173/

As a result of these studies, a gear pump, unboosted, was selected as the design best suited to this application, and Task VI, the final design of the gear pump, described in the following pages, was undertaken.

TASK VI: POSITIVE DISPLACEMENT PUMP DESIGN

On the basis of the preceding positive displacement pump concept analysis, two configurations, the gear and vane pumps, placed highest on the rating matrix, Table XIV. The results of this analysis were presented to NASA for final review and approval.

The configuration chosen was the gear pump. Therefore the task remaining was to finalize the design. The following reiterates the performance requirements for the pump:

Pump inlet pressure	35 psia	$(2.41 \times 10^5 \text{ N/m}^2)$
Pump inlet temperature	159 R	(88.5 K)
Pump exit pressure	1500 psia	$(1.03 \times 10^7 \text{ N/m}^3)$
Design flowrate	12 gpm	$(7.57 \times 10^{-4} \text{ m}^3/\text{s})$
Pumped fluid	LF ₂	(with capability of FLOX operation)

During the Positive Displacement Pump Evaluation section study of this report (Task V), a number of general conclusions were reached relative to the best configuration of the gear pump:

1. Two spur gears of equal size should be used.
2. Roller bearings with a slight internal interference fit should be used.
3. The bearings for each of the two gears should be placed one above the other to minimize shaft deflections.
4. A maximum rotating speed exists for a given gear diameter in order to preclude cavitation in the pumping cavity.

Using the above as ground rules, the specific design of the pump proceeded.

GEAR DESIGN

A pressure angle of 25 degrees (0.43633 rad) was selected because it will minimize the amount of trapped fluid between the meshing teeth and will provide a larger pumping volume than either a 14-1/2- or 20 degree standard pressure angle.

Nine teeth per gear were selected since a small number of teeth increases the theoretical displacement in relation to the slip (leakage). Further, nine is the minimum number of teeth that can be used without requiring tooth undercutting to prevent tooth-to-tooth interference.

The recommendations of the American Gear Manufacturers Association (AGMA) were followed relative to the relationship of the gear addendum to diametral pitch. The preferred relationship, and the one actually used, was (Ref. 27):

$$\text{Addendum} = 1.25/P_d \quad (74)$$

where

$$P_d = \text{diametral pitch} = \frac{n}{D}$$
$$n = \text{number of teeth}$$
$$D = \text{pitch diameter}$$

From bearing catalogs the relationship of the roller bearing OD's and ID's (also shaft OD) was determined to be

$$D_B = 1.5 D_s + .4 \quad (75)$$

where

$$D_B = \text{bearing diameter, ft}$$
$$D_s = \text{shaft diameter, ft}$$

The shaft diameter is determined by torque considerations. To complete this analysis, design layouts indicated a relationship between the bearings and gear OD's would be,

$$1.34 D_B = D_{OD} = 1.2D \quad (76)$$

where

$$D_{OD} = \text{outside diameter of gear, ft}$$
$$D = \text{pitch diameter, ft}$$

To determine a gear radial tip clearance that will preclude rubbing, the deflections that affect this clearance were required. The shear and bending deformations of the shaft due to the pressure loading on the gears were calculated as:

<u>Radial Deflection</u>		
	<u>In.</u>	<u>mm</u>
Idler Shaft	0.00042	0.0107
Driver Shaft	0.00039	0.0099

In addition, the bearing deflections and detail part stackup tolerance was estimated to be 0.0007 inch (1.778×10^{-5} m). The total of all estimated deflections then are 0.00112 inch (2.84×10^{-5} m) at the idler gear OD and 0.00107 inch (2.72×10^{-5} m) at the driver gear OD.

The design approach used with regard to the axial clearance was to apply a coating of aluminum oxide on the stationary parts adjacent to the gears and set the total clearance to 0.0001 inch (2.54×10^{-6} m) minimum and 0.0003 inch (7.62×10^{-6} m) maximum. It is anticipated that the gears will wear away part of the aluminum oxide during operation; however, this approach is expected to result in smaller internal leakage than if the clearance were set at an arbitrarily larger value.

Performance and overall pump size is dependent on gear size. The relationship of performance and gear geometry, established by the equations developed in the Gear Pump Evaluation section (Eq. 46, 53, and 56), is shown in Fig. 87. A cavitation limit line is also presented in the figure and is based on the amount of energy required to accelerate the fluid up to the gear tip speed with an inlet static pressure of 15 psi (1.03×10^5 N/m²) above vapor pressure. Operation to the right of this line will require a boost pump. This figure indicates that to obtain high efficiency the larger gear diameters are required.

According to Fig. 87, to maintain efficiencies in excess of 85 percent without a boost pump and to allow some margin from the cavitation limit line, a speed on the order of 5,000 rpm is a maximum. The geometry required is a gear diameter of 1.90 inch (4.826×10^{-2} m) and a width of .334 inch (8.484×10^{-3} m). This configuration (Fig. 88) would weigh 11.9 lbm (5.40 kg).

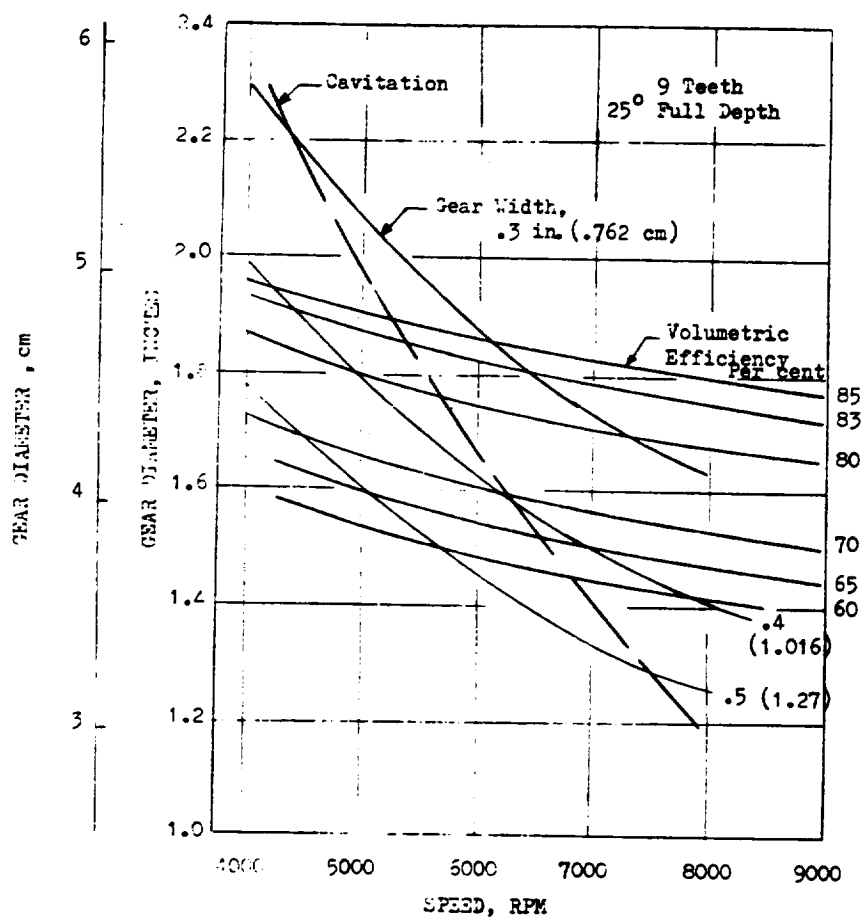


Figure 87. Performance Map of the Gear Pump - Final Design

R-8494-1
178

The meshing teeth trap fluid and return this fluid back to the inlet. This fluid is subcooled. When the trapped fluid returns to the inlet through the relief, the fluid will follow a constant enthalpy process. The temperature of the trapped fluid can be calculated by:

$$\Delta T = \frac{FHP}{C_w\eta} \quad (77)$$

where

FHP = developed fluid horsepower

\dot{w} = mass flowrate, lb/sec

η = overall efficiency

Assuming an overall efficiency of 75 percent results in a ΔT of 11 F (6.12 K). Following a constant enthalpy process from a point 11 F (6.12 K) and 1500 psi (1.034×10^7 N/m²) above inlet conditions to the referenced inlet conditions gives a fluid quality of 0.178. The liquid density returning to the inlet is 91.2 lbm/ft³ (1460 kg/m³); the vapor density is 0.85 lbm/ft³ (13.6 kg/m³). These three conditions lead to a density of the mixture of 46 lbm/ft³ (737 kg/m³). The density of the fluid while it was trapped at 1500 psi (including correction for bulk modulus) was 93 lbm/ft³ (1490 kg/m³). This indicates a density ratio of two. The amount of fluid trapped per tooth space is 0.00225 in.^3 ($3.6871 \times 10^{-8} \text{ m}^3$). The total volume of fluid being pumped in a tooth space is 0.0694 in.^3 ($1.1373 \times 10^{-6} \text{ m}^3$). Since the trapped volume will double when the fluid is exposed to inlet conditions, a full charge will not enter during the inlet cycle. The gear width must then be increased to make up this decrease. The volume increase required will be the ratio of the expanded volume to the total volume, which is 3.3 percent. The gear width now required to meet the required delivered volumetric flow is 0.350 inch ($8.89 \times 10^{-3} \text{ m}$).

MATERIALS SELECTION

The entire pump is manufactured from INCO 718 material with the exception of the bearings and seals. The bearing material is 440C. Past experience and tests indicate that 440C material is superior to other alloys for bearings operating in a cryogenic liquid. AISI 440C was considered for the gears but was rejected because of its brittleness which could result in gear tooth chipping. The dynamic seals are INCO 718 with aluminum oxide (Al_2O_3) flame sprayed on the seal nose. The seal mating rings are K162B (Kennametal).

Since the gears and all housing components are fabricated from the same material, INCO 718, the potential problem of differential thermal contraction between parts in going from ambient to cryogenic temperature has been eliminated. In large pumps, or pumps where minor changes in radial or axial clearance is not significant this differential thermal contraction poses no problem. However, in this pump configuration, a change in clearance of only 1 or 2 ten-thousandths of an inch can be critical.

AXIAL THRUST

Unless compensated for, an axial thrust is generated within the gear pump. This thrust originates from the seal nose loading on the seal mating rings and from the pressure force on the internal end of the drive gear shaft. This latter force is brought about by the fluid leaking past the gear ends and the fluid used to cool the bearings. The maximum axial thrust calculated under these conditions is 18 lbf (80 N). This force on the drive shaft was thought to be excessive due to wear on the aluminum oxide coatings on the side plates opposite the gears.

The method used to eliminate this axial thrust within the pump was to install a pressure balance seal at the opposite end of the drive shaft from the primary and secondary face riding seals. This seal accomplishes two purposes. First, the spring load of the seal against its mating ring equals and opposes the combined spring load of the primary and secondary seals. Secondly, it allows the pressure on the internal end of the drive shaft to approach zero thereby eliminating this pressure force. The leakage from this seal is drained overboard. The positive displacement pump final design is shown in Fig. 88.

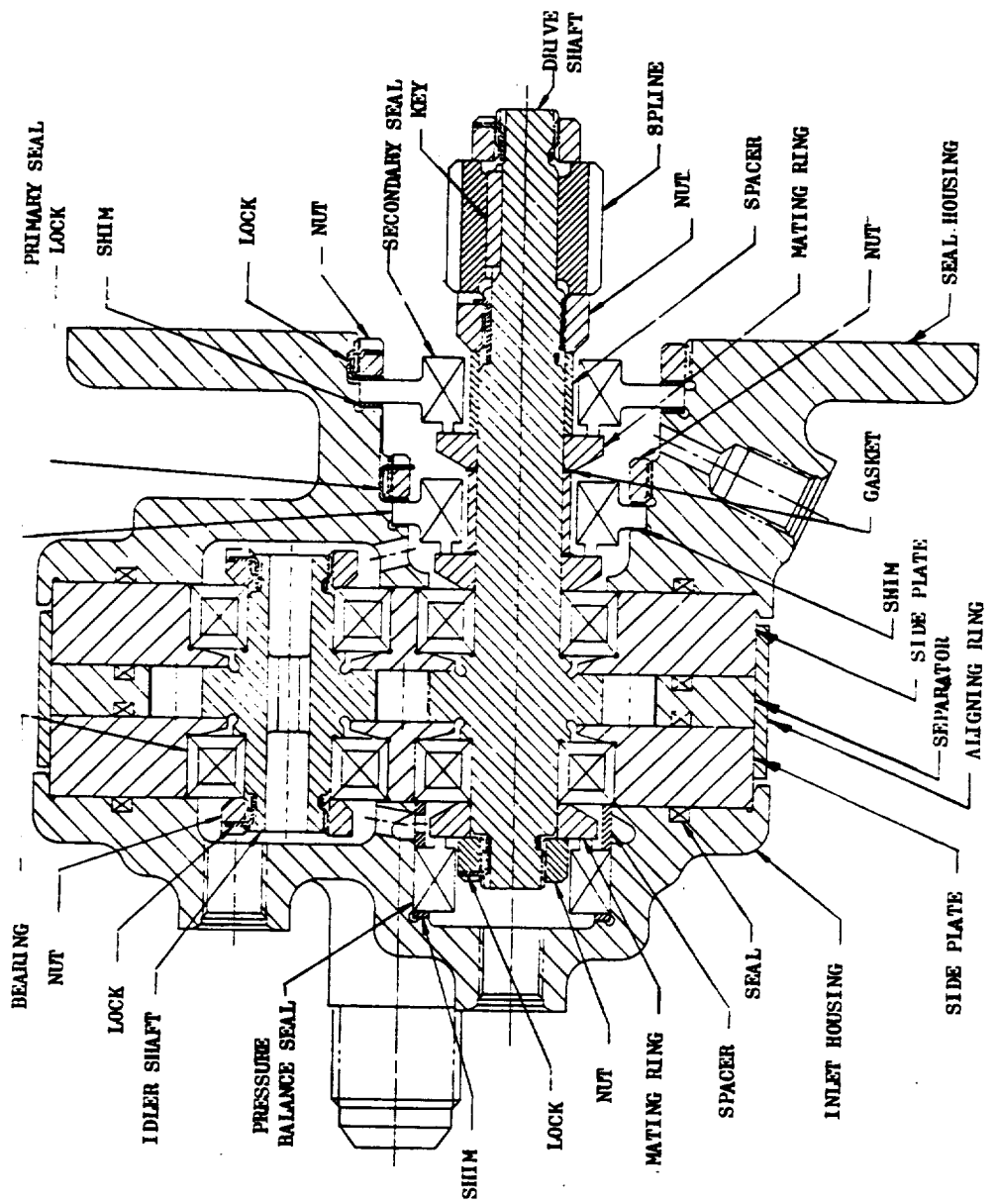


Figure 88. Final Gear Pump Design

MECHANICAL DESIGN

Roller bearings are used because of the high hydraulic loads. The bearings will have an internal interference fit sufficient to cause internal compressive bearing loads that will always exceed the hydraulic loads. This prevents excessive bearing deflections and gives better control on the gear outside diameter running clearance.

A modified 25 degree pressure angle spur gear will be used. The modification changes the gear tooth profile from a true involute form. This modification was required since the small number of teeth (nine) per gear is not consistent with standard gear design for the outer diameter desired. Without modification, a true involute design would have caused in 0.0015-inch (0.0381 mm) interference between a meshing idler tooth and a driver tooth at the tooth root.

The nomenclature location of the following hardware descriptions can be found in Fig. 88.

The internal running clearances must be held to a much smaller value than conventional gear pumps because of the low viscosity of the fluid to be pumped. In order to keep these clearances small the idler gear and the drive gear are machined as an integral part of their respective shafts. The bearing inner races will then be pressed on the gear shaft journals. The bearing inner races will then be ground concentric to the gear outside diameter and normal to the gear face. This will result in only one tolerance between the gear outer diameter and the bearing inner race roller journal thereby allowing closer control of the radial gear-to-housing clearance.

The gear side plates will be flame sprayed with aluminum oxide in the areas where the gear faces will rub. The roller bearings are mounted in the side plates to give a minimum bearing span and reduce shaft gear deflection. The side plates are spaced by a separator which controls the side or face running clearance of the gears. The two side plates and separator will be rough machined and then assembled with a shrink fit ring on the outside diameter with a single indexing dowel pin.

Finish grinding will be accomplished on the three parts as an assembly, thus controlling the bearing alignment and concentricity to within 0.0001 of an inch (0.0254×10^{-4} m).

The inlet housing incorporates both the inlet and discharge ports. It also retains the pressure balance seal for the drive gear. The seal housing retains the dynamic seals for the pump drive shaft. The pump mounting flange is also a part of the seal housing. These two castings are bolted together on the outer periphery and sandwich the gear housing matched assembly, thus restraining the gear side plate deflections.

The bearings run submerged in the pumped fluid. Bearing coolant flow is obtained from the fluid leakage between the gear faces and the side plates. A slight forced coolant is also obtained from the trapped fluid at the gear mesh. This trapped fluid is released by bleed holes in each of the side plates. These bleed holes are located on the gear pitch line. The bleed holes direct the fluid to each of the bearings.

The idler gear shaft has an axial hole through the center of the shaft. This allows the coolant fluid pressure to equalize on both sides of the shaft and bearings which helps to maintain a hydraulic balance of the gear. The drive shaft gear hydraulic balancing is obtained by having two dynamic seals of the same nose diameter--one each side of the gear--outboard of the bearings. These pressure balancing cavities of both gears are cross drilled so equal pressure is obtained on both gears (see Fig. 88). The bearing coolant flow passing through these cavities is returned to the inlet line sufficiently far upstream of the pump to assure that mixed phase flow does not occur at the pump inlet.

Two seals are used on the drive end of the shaft gear. The cavity between these seals will be purged and drained overboard. The seal leakage from the pressure balance seal on the opposite end of the drive gear will be drained into the same overboard drain.

STRESS AND DYNAMIC ANALYSIS

The structural analysis of the positive displacement LF_2 pump was based on the following parameters:

<u>Parameter</u>	<u>Nominal</u>	<u>Maximum</u>
Speed, rpm	5000	5500
Power, hp (watts)	15 (11,185 W)	20 (14,914 W)
Torque, in.-lb (Nm)	189 (21.35 Nm)	252 (28.47 Nm)
Discharge Pressure, psi (N/m^2)	1500 ($1.034 \times 10^7 \text{ N}/\text{m}^2$)	1500 ($1.07 \times 10^7 \text{ N}/\text{m}^2$)

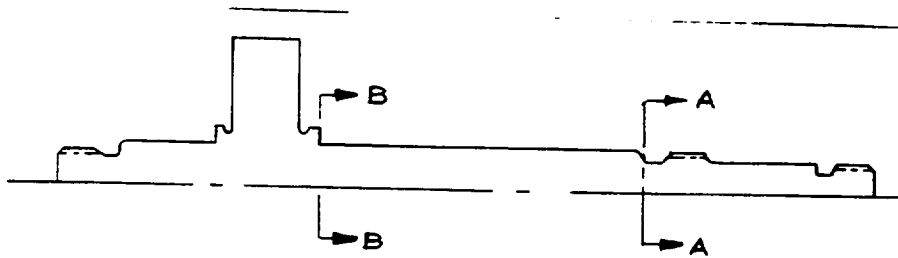
All parts analyzed are structurally adequate. The stresses reported herein are limit stresses, which are 20 percent greater than the predicted maximum operating values. In many areas, material selection and section thicknesses were based on thermal compatibility, or functional and manufacturing requirements, and are more than adequate from a structural standpoint.

Driver Shaft

The driver shaft is made of wrought INCO 718. The centrifugal stresses are insignificant because of the low speed. At the thread relief, the limit shear stress, due to power torque, is 19,370 psi ($1.34 \times 10^8 \text{ N}/\text{m}^2$), and the limit axial stress, which is a function of the nut pretorque, is 53,500 psi ($3.69 \times 10^8 \text{ N}/\text{m}^2$). The factor of safety on limit combined steady and alternating stress is 2.2. A summary of the stresses and factors of safety for locations at the thread relief (Section A-A) and at the bearing shoulder Section B-B) are presented in Fig. 89.

Shaft Radial Deflections

The calculated radial deflections of the driver and idler shafts at the gear center plane are 0.00039 in. (0.0099 mm) and 0.00042 in. (0.0107 mm) respectively. This deflection includes the bending and shear deformation of the shafts only, and is due to pressure-loading on the gear faces. The pressure distribution and directions of deflections are shown in Fig. 90.



P/N RL001430E

Material: Heat-treated, wrought INCO 718.

Material Properties:

<u>Property</u>	<u>Room Temperature</u>	<u>-300 F (88.7 K)</u>
F_{tu} , ksi	180 ($1.241 \times 10^9 \text{ N/m}^2$)	219 ($1.51 \times 10^9 \text{ N/m}^2$)
F_{ty} , ksi	150 ($1.034 \times 10^9 \text{ N/m}^2$)	166 ($1.14 \times 10^9 \text{ N/m}^2$)
F_{te} , ksi	42 ($2.896 \times 10^9 \text{ N/m}^2$)	56 ($3.86 \times 10^8 \text{ N/m}^2$)

Limit Stress at Section A-A:

Axial Preload Stress	53500 psi	($3.69 \times 10^8 \text{ N/m}^2$)
Steady Torsional Stress	19370 psi	($1.34 \times 10^8 \text{ N/m}^2$)
Alternating Torsional Stress	3480 psi	($2.40 \times 10^7 \text{ N/m}^2$)

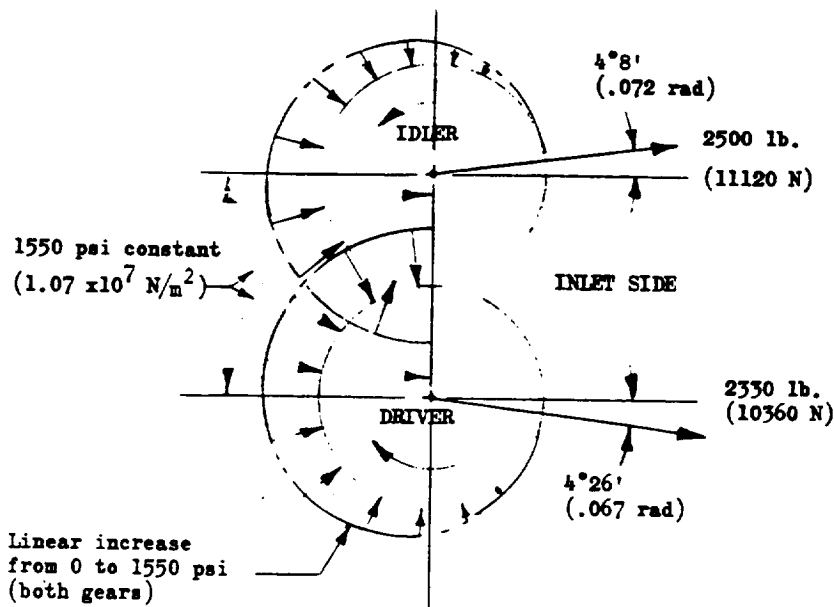
Factor of safety on combined steady and fatigue stresses: 2.2

Limit Stress at Section B-B:

Axial Preload Stress	28460 psi	($1.96 \times 10^8 \text{ N/m}^2$)
Pressure Bending Stress	15160 psi	($1.05 \times 10^8 \text{ N/m}^2$)
Steady Torsional Stress	7500 psi	($5.17 \times 10^7 \text{ N/m}^2$)
Alternating Torsional Stress	1880 psi	($1.30 \times 10^7 \text{ N/m}^2$)

Factor of safety on combined steady and fatigue stress: 2.4

Figure 89. Summary of Stresses and Factors of Safety at Thread Relief and at the Bearing Shoulder for the Driver Shaft



The pressure distribution and resultant shaft loads are as shown.
The shaft radial deflections are:

$$\text{for the idler: } S_R = 0.00042 \text{ in. (0.0107 mm)}$$

$$\text{for the driver: } S_R = 0.00039 \text{ (0.0099 mm)}$$

These include shear and bending deformations of the shaft, due to the pressure loading on the gears. They occur at the center plane of the gears.

Figure 90. Gear Pump Pressure Distribution and Deflections

Gear Housing

The gear housing plates are made of wrought INCO 718. The stresses in the housings are low, 20,700 psi ($1.43 \times 10^8 \text{ N/m}^2$) maximum. The main concern is the deflection of the plates away from the gear faces. The calculated deflection is 0.0004 in. (0.0102 mm) at the center of the plates, where the gears mesh. This deflection calculation is based on a simplified model. A summary of the stresses and deflections is presented in Fig. 91.

Pump Casings

The pump casings are cast INCO 718. The pressure stresses in the casings are small, less than 15,000 psi ($1.03 \times 10^8 \text{ N/m}^2$). These should present no structural problems.

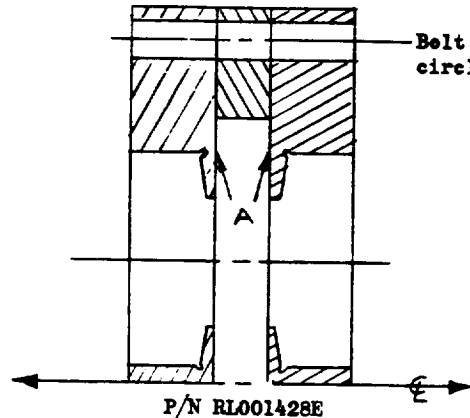
Miscellaneous

All the fasteners and other miscellaneous components have been selected to provide adequate factors of safety.

Critical Speed Analysis

The gear pump was modeled to obtain a critical speed analysis. The results (shown in Fig. 92) indicate that a critical speed could exist in the operating range of the pump for very low values of the bearing radial spring rates. However due to the internal interference fit of the roller bearings the actual bearing radial spring rates ($>10^6 \text{ lb/in.}$ ($1.75 \times 10^8 \text{ N/m}$) with 0.0001 (0.00254 mm) inch internal interference) are large enough to raise the lowest critical speed well above the operating range. Thus, no critical speeds are in the operating range of the pump.

The pump was modeled by 22 mass stations connected by 21 elastic springs. The shaft is supported by two bearings at the pump itself and two bearings in the torquemeter. The results of the calculation are shown in Table XIV.



Material: Heat treated wrought INCO 718.

Material Properties:

<u>Property</u>	<u>Room Temperature</u>
F_{tu}	180 ksi (1.24×10^9 N/m 2)
F_{ty}	150 ksi (1.03×10^9 N/m 2)

Pressure bending stress:

Limit stress at bolt circle 20700 psi (1.43×10^8 N/m 2)

Limit stress at point A 9500 psi (6.55×10^7 N/m 2)

Factor of safety - high

Deflection at Centerline:

Each plate deflects 0.0004 in. (0.0102 mm) in the direction indicated by the arrows.

Figure 91. Summary of Gear Housing Stresses and Deflections

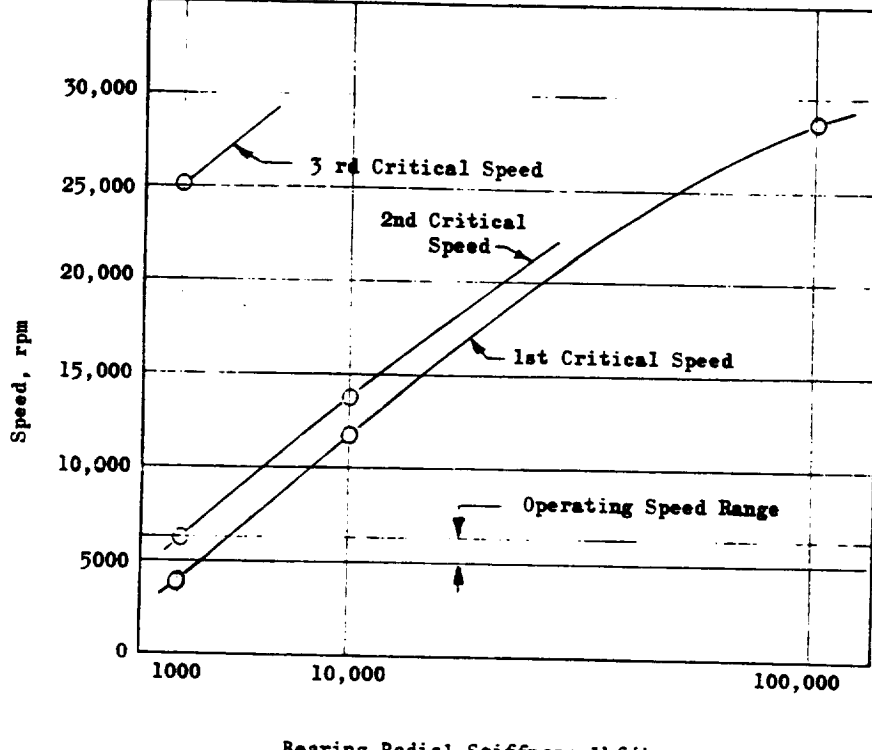


Figure 92. Gear Pump Critical Speed vs Bearing Stiffness

TABLE XIV. CRITICAL SPEEDS

Mode	Bearing Stiffness, lbf/in.	Critical Speed, rpm
1	1,000	3,800
2		6,160
3		25,100
1	10,000	11,800
2		13,700
1	100,000	28,600

R-8494-1

190

NOMENCLATURE

ROTATING PUMP

A	Amplification factor $1/\gamma_B$
A^*	Flow factor
a	Spacing between vanes or disks, feet
B	Axial extension of rotating pitot drum, feet
b	Vane height, feet
C_p	Pitot pickup velocity, feet/sec.
C_u	Tangential fluid velocity, feet/sec.
C_m	Fluid meridional velocity, feet/sec.
D_s	Specific diameter
D	Diameter, feet
D^*	Proportionality factor, D/δ
d	Characteristic diameter, feet
F	Axial force, lbs.
F_{te}	Endurance limit (fatigue strength), psi
F_{tu}	Tensile ultimate strength, psi
F_{ty}	Tensile yield strength, psi
g	Gravitational constant, ft^2/sec^2
H	Head rise, feet
H_{ad}	Actual developed head, feet
K_1, K_2, \dots, K_n	Constants
k	Proportionality factor, d/Δ
m	Slip factor
NPSH	Net positive suction head, feet
N_s	Specific speed
N	Rotative speed, rpm
n	Proportionality factor, B/δ
P	Power, ft-lb/sec.
P_L	Friction power loss, ft-lb/sec.
P_{th}	Theoretical power, ft-lb/sec.
P_c	Power coefficient
p	Static pressure, lbs/ ft^2
Q	Volumetric flow rate, gpm

R-8494-1

q	Head coefficient
q_L	Pitot drum blading head loss coefficient
q_p	Internal ducting head loss coefficient
q_{ad}	Actual developed head coefficient
q_{th}	Theoretical head coefficient
q_D	Pitot probe drag head loss coefficient
q_w	Wheel disk friction head loss coefficient
R	Radius, feet
Re	Reynolds number, Ud/ν
r	Ratio of free area to total area due to boundary layers
S	Emission ratio
T	Torque, ft-lbs
U	Rotor tangential velocity, ft/sec.
w	Weight flow rate, lb/sec.
x	Proportionality factor, Δ/δ
y	Proportionality factor, a/δ
Z	Blade or disk number
 β	Parameter relating blade number to specific speed
β_w	Wheel friction loss coefficient
γ_g	Specific weight of gas, lb/ft^3
γ_f	Specific weight of fluid, lb/ft^3
ξ	Pitot pickup diameter, feet
ξ_R	Pitot pump loss coefficient
ξ_p	Internal duction loss coefficient
ξ_D	Drag coefficient
η	Efficiency, %
η_B	Pitot vane efficiency
λ	Blade spacing parameter
λ	Drag ratio casing to rotor
ν	Kinematic viscosity, $\text{ft}^2/\text{sec.}$
ξ_R	Pressure recovery coefficient
ξ_m	Disk friction moment coefficient
π	Circumference to diameter ratio

ρ	Mass density, slugs/ft ²
σ	Thoma cavitation parameter, NPSH/H _{ad}
ϕ	Flow coefficient, C _m /U
ψ	Head coefficient, Hg/U ²
χ	Velocity ratio, 1/φ
ω	Rotational speed, radians/sec.
Δ	Diameter of pitot body, feet

Subscripts

1	Section 1 or inlet
2	Section 2 or discharge
TOT	Total
Static	Static
Local	Local parameter
tip	tip or outer diameter
Max.	Maximum

POSITIVE DISPLACEMENT PUMP

a	Diaphragm effective radius (in.)
A _e	Effective pumping area of helirotor pump
b	Radius of convolution in diaphragm (in.)
BHP	Brake horsepower
C	Cavitation factor
C _D	Viscous drag coefficient
C _f	Friction coefficient
C _p	Specific heat at constant pressure (BTU/lb-F)
D	Pitch diameter (ft)
D _B	Diameter of bearing (ft)
D _{ID}	Inside diameter (ft) Working depth diameter for gear (ft)
D _{OD}	Outside diameter (ft)
D _p	Diameter of piston (ft)
D _s	Diameter of shaft (ft)
d _m	Mean diameter (ft)
d _t	Radial height of gear teeth (ft)
d _v	Gear tooth tip width (or crown) in direction of rotation (ft)
E	Modulus of elasticity
F	Radial load (lb)
f	Deflection of diaphragm from flat position (in.)
FHP	Fluid horsepower
F _{te}	Endurance limit (fatigue strength) (lb/in ²)
F _{tu}	Tensile ultimate strength (lb/in ²)
F _{ty}	Tensile yield strength (lb/in ²)
g	Acceleration due to gravity (32.2 ft/sec ²)
h	Thickness of diaphragm (in.)
H _{P_{DEL}}	Horsepower delivered
H _{P_{REQ}}	Horsepower required
k, k ₁ , k ₂ ...	Constants
L	Axial length (ft)
L*	Percentage of time when ΔP exists in piston pump
L _{av}	Average width of gear teeth in direction of rotation (ft)

l_s	Pitot pump strut length (ft)
l	Leak path length parallel flow (ft)
N	Rotational speed (rev./min.); also Newton
n	Number of teeth or number of pistons
P_d	Diametral pitch (ft^{-1})
ΔP	Differential pressure (lb/ft^2)
P_a	Atmospheric pressure (lb/ft^2)
P_i	Inlet pressure (lb/ft^2)
P_v	Vapor pressure of fluid (lb/ft^2)
Q_L	Leakage (slip) flow (ft^3/sec)
Q_{LC}	Flow loss due to cavitation (ft^3/sec)
Q_{TH}	Theoretical flow (ft^3/sec)
q	Displacement, ft^3/rev
R_e	Reynolds number
S	Stroke (ft)
t	Thickness (ft)
T	Torque (ft-lb)
ΔT	Differential temperature ($^{\circ}\text{F}$)
T_f	Friction torque (ft-lb)
T_i	Ideal torque (ft-lb)
T_v	Viscous torque (ft-lb)
u	Poisson's ratio
V	Velocity (ft/sec)
V_p	Velocity at tip (ft/sec)
w	Leak path width (ft)
w_l	Leakage flow, (lb/sec)
w_m	Average velocity in clearance (ft/sec)
w	Mass flowrate (lb/sec)
δ	Clearance (ft)
η	Overall efficiency
η_v	Volumetric efficiency
μ	Absolute or dynamic viscosity ($\text{lb}\cdot\text{sec}/\text{ft}^2$)
ν	Kinematic viscosity (ft^2/sec)
ρ	Density ($\text{lb}\cdot\text{sec}^2/\text{ft}^4$)
σ	Stress (lb/in^2)
γ	Specific weight (lb/ft^3)
γ^*	Restriction factor

REFERENCES

1. R-6363, MA-5 Flex Sustainer Engine Feasibility Test Program, Contract NAS3-3241, Rocketdyne, a division of North American Rockwell, 28 February 1966.
2. Kittredge, C. P.: Estimating the Efficiency of Prototype Pumps from Model Tests, ASME Paper No. 67-WA/FE-6.
3. Hildebrand, P. et al.: Centrifugal Pump (High Pressure) for Power Transmissions, AiResearch Technical Report No. AFAPL-TR-66-12, USAF Contract No. AF33(657)-10151, January 1966.
4. Eckert, B. Q. and E. Schnell: Axial and Radial Kompressoren, Verlag, Berlin, 1961.
5. Hoerner, Sighard F.: Fluid-Dynamic Drag, published by Author, 1958.
6. Pfleiderer, C.: Die Kreiselpumpen Fur Flussigkeiten Und Gase, Springer-Verlag, Berlin, Germany, 1955.
7. Balje, O. E., et al.: Study of Turbine and Turbopump Design Parameters, Final Report, Vol. 4, Low Specific Speed Turbopump Study, S/TD No. 1735, Dept. of the Navy, Office of Naval Research, Contract No. NONR 2292(00) Task No. NR 094-343.
8. Barske, U. M.: Formulae and diagrams for the Calculation of Open Impeller Centrifugal Pumps, Royal Aircraft Establishment, Tech Note No. R.P.D. 127, Great Britain, September 1955.
9. Daugherty & Ingersoll, Fluid Mechanics, McGraw Hill, 1954.
10. Study, Design, and Test of Experimental Liquid Hydrogen Pump for Use in Flight Systems, Rocketdyne, a division of North American Rockwell, Final Report, Tech. Doc. Report No. ASD-TDR-63-114, February 1963.
11. Hasinger, S. H. and L. Kehrt, Investigation of a Shear Force Pump, Aeronautical Research Lab, Wright Air Development Center, 1962.
12. Brester, M.D. and Pohlhausen, Laminar Flow Between Two Parallel Rotating Disks, Applied Mathematics Research Lab, Wright Air Development Center, 1959.

13. Barske, U. M., "Development of Some Unconventional Centrifugal Pumps," Proceedings of the Institutions of Mechanical Engineers, Vol. 174, No. 11, Fig. 25, p. 452, 1960.
14. Balje, O. E., "Drag-Turbine Performance," ASME Paper No. 56-AV-6, p. 1302-1304.
15. Myagi and Mizadzu, Tohoku Imperial University, Reports, Vol. 13, No. 1, pp 264-288, 1939.
16. Rocketdyne Internal Report, Tamm 3115-2079, Design of Mark 10 Turbopump Impellers to Reduce Discharge Pressure Oscillations, R. M. Cook, November 1963.
17. R-7405, Design Criteria Monograph - Centrifugal Flow Pumps, R. B. Furst, Rocketdyne, a division of North American Rockwell, 22 March 1968 (revised 21 October 1968).
18. Daily, J. W. and R. E. Nece, "Chamber Dimension Effects on Induced Flow and Frictional Resistance of Enclosed Disks," ASME Trans., March 1960.
19. Pratt and Whitney Aircraft, Investigation of Pressure Prediction Methods for Low-Flow Radial Impellers, PWA FR-1716, 13 January 1966.
20. Schlichting, H., Boundary Layer Theory, 4th Ed., McGraw-Hill, p. 549, 1960.
21. Jones, A. B., "A General Theory for Elastically Constrained Ball and Radial Roller Bearings Under Arbitrary Load and Speed Conditions," Trans. ASME, Series D, J. Basic Eng., Vol. 82, pp. 309-320, June 1960.
22. Wilson, W. E., Cavitation in Positive Displacement Pumps, Product Engineering, March 1959.
23. Schmidt, H. W., Fluorine and Fluorine-Oxygen Mixtures in Rocket Systems, NASA SP 3037.
24. Wichert, K. E., Characteristics of Helical Rotary Positive Displacement Compressors, ASME No. 61-HYD-18, 1961.

25. Fisher, W. C., Production Design of a Modern Axial Flow Positive Displacement Rotary Compressor, ASME No. 49-OGP-3, 1959.
26. Balje, O. E., Engineering Consultant, consultations during September 1968.
27. AGMA Standard, USAS B6.1-1968.
28. Advanced Maneuvering Propulsion System A.F. Contract No. F04611-67-C-0116.

APPENDIX A

DERIVATIONS

REYNOLDS NUMBER FOR CLEARANCE GAP

General Reynolds number equation:

$$R_e = \frac{\rho V D}{\mu} \quad (I)$$

$$D = 4R_H = \frac{4W\delta}{2W + 2\delta} = \frac{2W\delta}{W + \delta}$$

If we assume that $W \gg \delta$, then

$$W + \delta \approx W$$

and the expression for D becomes:

$$D = 2\delta \quad (II)$$

For the laminar region the flow through a clearance gap is given by (Ref. 7):

$$Q = \frac{W\delta^3 \Delta P}{12\mu l}$$

where

W = clearance width normal to the flow

δ = clearance gap normal to flow

ΔP = pressure differential across leak path

μ = absolute viscosity

l = leak path length parallel to flow

Solving for average velocity in the above equation yields:

$$v = \frac{\Delta P \delta^2}{12 \mu l} \quad (\text{III})$$

Substituting the expressions derived in equations II and III into equation I results in:

$$R_e = \frac{\Delta P \rho \delta^3}{6 \mu^2 l}$$

where ρ is mass density.

FLOW THROUGH CLEARANCE GAP
TURBULENT FLOW REGIME

Head loss in a circular cross section is given by the Darcy-Weisbach equation:

$$H_L = f \frac{\ell}{d} \frac{V^2}{2g} \quad (IV)$$

where

$$\begin{aligned} H_L &= \text{head loss (ft)} \\ f &= \text{friction factor} \\ \ell &= \text{length parallel flow (ft)} \\ d &= \text{cross section diameter (ft)} \\ V &= \text{average velocity (ft/sec)} \\ g &= \text{gravitational constant (32.2 ft/sec}^2) \end{aligned}$$

For a noncircular cross section "d" can be replaced by a term including the hydraulic radius (R_H)

$$\begin{aligned} d &= 4R_H \\ R_H &= \frac{\text{Area}}{\text{Wetted Perimeter}} \\ &= \frac{w\delta}{2(w-\delta)} \\ d &= \frac{2w\delta}{w+\delta} \end{aligned}$$

or if $w \gg \delta$

$$d = 2\delta$$

Substituting the above expression into equation (IV) yields:

$$H_L = f \frac{\ell}{4\delta} \frac{V^2}{g} \quad (V)$$

According to Blasius (Ref. 9) for turbulent flow with smooth conduit walls the value of friction factor can be expressed as:

$$f = \frac{0.316}{(R_e)^{0.25}} \quad (VI)$$

Furthermore

$$R_e = \frac{\rho V d}{\mu} = \frac{\rho V 4 R_h}{\mu} = \frac{2 \rho V w \delta}{\mu (w + \delta)}$$

where

ρ = mass density

R_h = hydraulic radius

μ = absolute viscosity

Assuming that $w \gg \delta$ and therefore $w \approx w + \delta$ will modify the above to:

$$R_e = \frac{2 \rho V \delta}{\mu} \quad (VII)$$

Substituting the expression of equation VI into equation VII yields:

$$f = \frac{0.316 \mu^{0.25}}{(2 \rho V \delta)^{0.25}} \quad (VIII)$$

This expression for friction factor can then be substituted into equation V, resulting in:

$$H_L = .0664 \frac{\mu^{0.25} \rho V^{1.75}}{\rho^{0.25} \delta^{1.25} g} \quad (IX)$$

Substituting the expressions

$$H_L = \frac{\Delta P}{L}$$

and

$$\rho = \frac{F}{g}$$

into equation IX and solving for velocity VIII gives:

$$V = \frac{4.7 \Delta P^{.57} g^{.43} \delta^{.72}}{\mu^{.143} \gamma^{.43} \ell^{.57}} \quad (\text{X})$$

then

$$q_L = AV = W\delta V = \frac{4.7 \Delta P^{.57} g^{.43} W \delta^{1.72}}{\mu^{.143} \gamma^{.43} \ell^{.57}} \quad (\text{XI})$$

where

q_L = leakage flow (ft^3/sec)

ΔP = pressure drop (lb/ft^2)

g = gravitational constant (ft/sec^2)

δ = clearance (ft)

W = width of leak path (ft)

μ = viscosity ($\text{lb sec}/\text{ft}^2$)

γ = specific weight (lb/ft^3)

ℓ = length of leak path (ft)